Graphitic Carbon Nitride and Its Derivative Toward Energy Conversion

Xiaochun Gao

Supervisors:

Prof. Guoxiu Wang & Dr. Dawei Su

This thesis is presented as part of the requirement for the conferral of the degree:

DOCTOR OF PHILOSOPHY

University of Technology Sydney

Faculty of Science

School of Mathematical and Physical Sciences

Centre for Clean Energy Technology

July 2020

Abstract

This Ph.D. project focus on graphitic carbon nitride (g-C_3N_4) and its derivatives toward energy conversion applications, including the photocatalytic hydrogen evolution and lithium sulfur (Li-S) batteries. Bulk g-C_3N_4 materials suffer from the insufficient supply of valid photocarriers due to the low surface area, poor visible light absorption, and fast photocarrier recombination. While Li-S batteries have been severely impeded by fast capacity fading and severe electrochemical polarization. Therefore, a rational morphology, defect, or hybrid modification on g-C_3N_4 and its derivatives is designed to boost the photocatalytic H_2 evolution or battery performance.

A facile structure and doping engineering strategy is proposed to obtain the atomic-thin mesoporous C/O-doped g-C_3N_4 nanosheets via an acid-assisted exfoliation route without any hard templates. The theoretical calculations reveal that C/O atoms would boost the charge transfer rate and charge separation efficiency due to the enhanced electronic polarization effect and shortened bond lengths. Additionally, the electronic conductivity is enhanced due to the formation of delocalized π-bonding. The synergic contribution of textural and electronic features renders an excellent photoelectrochemical (PEC) performance and superior H_2 evolution rates.

A broadband photocatalyst composed of defect engineered g-C_3N_4 (DCN) and upconversion $NaYF_4$: Yb^{3+}, Tm^{3+} (NYF) nanocrystals is proposed to boost

the utilization of solar energy. The simultaneous introduction of S dopants and C vacancies renders DCN with defect states to effectively extend its visible light absorption to 590 nm and provide a moderate electron-trapping ability, thus facilitating the re-absorption of upconverted photons and boosting photocarrier separation efficiency. Through the defect engineering, a promoted interfacial charge polarization between DCN and NYF is achieved, which favors the upconverted excited energy transfer from NYF onto DCN as verified both theoretically and experimentally. With the optimization of a 3D framework architecture, the NYF@DCN catalyst exhibits a superior solar H_2 evolution rate.

We report a strategy to trap polysulfides and boost Li-S redox kinetics by embedding, the g-C_3N_4 derivative, surface oxidized quantum-dot-size TiN (TiN-O) into the highly ordered mesoporous carbon matrix. While the carbon scaffold offers sufficient electrical contact to the insulate sulfur, benefiting the full usage of sulfur and physical confinement of polysulfides. The surface oxygen defects render TiN-O with a stronger charge polarization effect for polysulfides via the S-O-Ti bond as verified experimentally and theoretically. Remarkably, TiN-O based coin cells and prototype soft-package cells exhibit excellent cycling stability with great flexibility, demonstrating their potential for practical applications.

Acknowledgments

Time flies, and my three and a half year's Ph.D. study will finish soon. I would like to express my sincere gratitude to my principal supervisor Prof. Guoxiu Wang, who offers me a Ph.D. position with a full scholarship in UTS. It is his professional guidance, critical thinking, and warm encouragement that help me move forward. I would also like to thank my co-supervisor, Dr. Dawei Su, for his constructive suggestions, skillful experience to help address my research problems. He is very knowledgeable in both physics and chemistry, and I always learn a lot when discussing with him. Besides, I would also like to thank Dr. Jane Yao, who mangers everything well in our team. Without her support, the research work cannot be completed smoothly. Thanks for her insistence on journal club where I improve my academic presentation skills significantly.

I want to thank my colleagues at UTS, Dr. Bing Sun, Dr. Hao Liu, Dr. Dong Zhou, Dr. Pan Xiong, Dr. Liubin Dong, Dr. Huajun Tian, Dr. Xin Guo, Dr. Jinqiang Zhang, Dr. Yufei Zhao, Dr. Jing Xu, Dr. Weizhai Bao, Dr. Lin Liu, Shaoqi Hou, Xingxing Yu, Jiayan Liao, Yi Chen, Shijian Wang, Xiao Tang, Kang Yan, Fan Zhang, Javad Safaei, Shuoqin Zhao, Tianyi Wang, Wang Yang, Wu Yang, Min Luo, Ziqi Guo, Anastasia Tkacheva, Tuhin Subhra Sahu, Pauline Jaumaux, and Yuhan Xie for all your kind assistance and collaboration during my Ph.D. study and life.

I am also grateful for the kind help from Prof. Jintao Zhang at Shandong University, who always gives me useful suggestions on planning my research. Thanks to A/Prof. Dr. Jin Feng for her help with the theoretical calculations.

I appreciate the excellent technical support from Dr. Ronald Shimmon, Dr. Linda Xiao, Alexander Angeloski, Katie McBean, Herbert Yuan, Mark Berkahn, Mark Lockrey, and Geoff McCredie.

The financial support from UTS and Australian Research Council (ARC) through the Discovery Project (DP170100436), ARENA 2014/RND106 are gratefully acknowledged.

Last, I would like to express my sincerest thanks to my four parents, my brother, my sister, my grandparents, who always support me selflessly. Endless thanks and apologies to my beloved, Shaoqi, thanks for giving up all but understanding, encouraging, and supporting me. Without you, my Ph.D. study cannot be so smooth, happy, and enjoyable.

CERTIFICATE OF AUTHORSHIP

I, Xiaochun Gao, certify that the work presented in this thesis has not previously been submitted for a degree nor has been submitted as part of requirements for a degree except as fully acknowledged within the text.

I also certify that the thesis has been written by me. Any help that I have received in my research work, and the preparation of the thesis itself has been acknowledged. In addition, I certify that all information sources and literature used are indicated in the thesis.

This research is supported by an Australian Government Research Training Program.

Xiaochun Gao

Production Note:
Signature removed prior to publication.

Sydney, Australia

8 July 2020

Lists of Nomenclature

Abbreviations

g-C_3N_4	graphitic carbon nitride
Li-S batteries	lithium sulfur batteries
PEC	photoelectrochemical
DCN	defect engineered g-C_3N_4
NYF	$NaYF_4$: Yb^{3+}, Tm^{3+}
TiN-O	surface oxidized TiN (TiN-O)
CB	conductive band
VB	valence band
SHE	standard hydrogen electrode
NIR	near-infrared
UV	ultraviolet
2D	two dimensional
IPA	isopropanol
NMP	N-methy-pyrrolidone
AAO	anodic aluminum oxide
AQE	apparent quantum efficiency
DOSs	density of states
DFT	density functional theory

SEM	scanning electron microscopy
STEM	scanning transmission electron microscopy
TEM	transmission electron microscopy
AFM	atomic force microscopy
XRD	X-ray diffraction
XPS	X-ray photoelectron spectroscopy
FT-IR	Fourier-transform infrared spectroscopy
EPR	electron paramagnetic resonance
UV-vis DRS	UV-vis diffusion-reflectance spectra
PL	photoluminescence
TGA	Thermal Gravimetric analysis
CV	cycling voltammogram
EIS	electrochemical impedance spectra
XANES	X-ray absorption near-edge structure

List of Symbols

θ	Angle of incidence with the lattice plane	degree
d	Lattice spacing	nm
λ	Wavelength	nm
τ	Decay time	s
I	Current density	mA cm^{-2}
E	Voltage	V
η	Overpotential	V
γ	Stretch constant	a.u.
C	Concentration	a.u.

List of Organisations

ISEM	Institute for Superconducting and Electronic Materials
NSW	The New South Wales
ARENA	Australian Renewable Energy Agency
UTS	University of Teehnology Sydney
ARC	Australian Research Council

Table of Contents

List of Figures

List of Tables

Chapter 1

1. Introduction

1.1. Research Background

The steadily deteriorated global energy crisis and environmental issues caused by the irreversible consumption of fossil fuels have posed an unprecedented urgent request for clean energy, particularly on the applications of energy generation and storage.[1–4] Since the pioneering work reported by Fujishima and Honda in 1972 that water can be split into hydrogen by TiO_2 under solar irradiation,[5] photocatalytic hydrogen evolution has been regarded as one of the most efficient and economical energy solutions to address these concerns. In addition, the commercialization of lithium-ion batteries has provided people with new sights on clean energy conversion and storage.[6] Recently, graphite carbon nitride (g-C_3N_4), a metal-free photocatalyst, has firstly attracted extensive attention in hydrogen production due to its merits of perfect band structure, stable physicochemical properties, low-cost, and environmental benignity.[7] Also, its derivatives have been demonstrated to be promising materials for electrochemical energy conversion and storage applications.[8,9] In this regard, this thesis will first mainly summarize recent development on g-C_3N_4 nanomaterials for photocatalytic hydrogen evolution and then introduce my research work on this project. Finally, my research work on g-C_3N_4 derivative toward other energy applications (lithium sulfur batteries) will also be discussed.

1.1.1. Photocatalytic hydrogen evolution

Solar energy is feeding all kinds of lives on the earth via the photosynthesis process that absorbs

CO_2 and H_2O and produces glucose and O_2.[10] Inspired by this, scientists have made enormous investigations seeking high-efficient solar photocatalysts to produce clean energy, particularly employing the naturally abundant resources as starting materials. In this respect, solar hydrogen production has attracted extensive research interest as its only combustion product is H_2O. In the first four decades, metal oxides/sulfides/selenide (e.g., TiO_2, ZnO, CdS),[11,12] visible-responsive plasmonic metals (Au, Ag, Cu),[13,14] and quantum dots (CdSe)[15,16] are the most widely studied photocatalysts due to their electronic structure or light harvesting ability. However, these semiconductors /metals/quantum dots are generally confronted with large bandgap or detrimental photo corrosion, setting a hurdle for solar photocatalysis. In this case, carbon-based nanomaterials are considered as good candidates due to the superior electronic conductivity and optical properties.[17,18] Nevertheless, graphene, quantum dots, carbon nanotube, the most widely investigated energy materials, have the problem of the inappropriate bandgap, elusive control on electronic structure and synthetic technique, which restrain them from being a core photocatalyst. Recently, graphitic carbon nitrides (g-C_3N_4), a metal-free semiconductor, has attracted extensive research interest due to its tailorable electronic structure, environmental benignity, stable physicochemical properties, and low cost.[19] In particular, its unique band structure with a bandgap of 2.7 eV (conductive band (CB) minimal and valence band (VB) maximal of -1.13 and 1.57 V *vs*. standard hydrogen electrode (SHE)) not only enables the absorbance of solar spectrum (λ<450 nm) but also satisfy the criteria of H_2/O_2 evolution, making it a promising catalyst for pollutant removal and water splitting.[20–22] Despite significant progress has been made, bulk g-C_3N_4 still suffers from the poor solar light utilization caused by the insufficient absorbance of long wavelength light and fast recombination of

charge carriers.[23] To tackle these problems, many strategies have been proposed, including the defects creation,[24,25] hetero(homo)junction formation,[26] and structure modification.[27]

Defect engineering is an important strategy to tune the band structure of semiconductors, which is the key to determinate light absorbance, redox activity, and recombination rate of charge carriers.[28] Dopants such as C, N, O, P, S, and F can be easily incorporated into the tri-s-triazine ring or substitute the tertiary amino group because the polymerization of g-C_3N_4 is extensively affected by precursors, additives, temperature, and atmosphere.[29–32] These dopant-induced defects are effective in narrowing the bandgap or even form the defect states to accommodate the photo-excited electrons, giving rise to an enhancement on light harvesting and charge carrier separation.[32] For instance, the P-doped macroporous g-C_3N_4 extends its visible light absorption to 557 nm with a superior hydrogen evolution rate of 1.6 mmol h^{-1} g^{-1}.[32] A similar phenomenon is also observed on the vacancy defective g-C_3N_4, which mainly due to its abundant localized electrons.[24,33] For example, Niu *et al.* reported that N vacancy-related C^{3+} electronic states result in partial overlap with the CB, leading to a narrow bandgap and improved light absorption.[33] Xu *et al.* also found g-C_3N_4 nanosheets with tunable N vacancies can induce midgap states to maximize the separation efficiency of photogenerated electron-hole pairs.[34] Furthermore, C vacancies were effective in facilitating the charge transfer from CB to the surface adsorbed O_2, boosting the photocatalytic oxidation of NO via superoxide radicals ($O_2^{\bullet-}$) under visible light irridiation.[24] Therefore, it is crucial to find approaches via modulating the dopants or vacancies within g-C_3N_4 to produce solar-driven renewable energy.

Furthermore, hybriding with other semiconductors such as TiO_2, ZnO, BiClO, CdS, graphene, and carbon dots provides a new approach to improve the photocatalytic performance of g-C_3N_4.[23] However, due to the wide bandgaps, these semiconductors show inferior absorption ability towards near-infrared (NIR) light, which occupies 44% of the solar energy. It is well known that the upconversion particles, lanthanide-ions-doped $NaYF_4$, can emit ultraviolet (UV) and visible light after absorbing the low-energy NIR light, endowing them to be a promising material with wide photoresponse for photocatalysis.[35] Therefore, integrating defective g-C_3N_4 with upconversion nanoparticles could be an efficient strategy to simultaneously harvest UV, visible and NIR light, and supress the recombination of charge carriers from enhancing the photocatalytic performance of hydrogen evolution.

Optimizing the geometrical structure of g-C_3N_4 materials is another important strategy to boost the photocatalytic H_2 evolution activity due to the significantly increased active sites, shortened photocarriers diffusion pathway, and facilitated mass/charge transfer process.[20] Constructing advanced architecture such as nanowires, nanocolumns, nanospheres, or exfoliating the bulk aggregates into ultrathin nanosheets has been widely investigated and demonstrated to be effective toward solar hydrogen evolution.[23] Thus, the solar hydrogen evolution rate of g-C_3N_4 or its hybrids will be significantly enhanced if both defect engineering/hybrid creation and morphology manipulation can be taken into consideration.

1.1.2. Li-S batteries

Rechargeable battery technology has emerged as the most important energy storage approach, which is critical in the applications of portable electronic devices and automobiles. Notably,

Li-ion batteries are strongly competitive due to its merits of low-cost, light-weight, as well as the high energy and power density.[36–40] However, intercalation-based Li-ion batteries technology is limited by the specific capacities of anode and cathode materials.[41] To overcome these charge-storage limitations, materials that enable chemical reactions and can accommodate abundant ions and electrons are the first promising options. At this point, Li-S batteries with significantly improved energy density are widely investigated.[42–50] Despite the considerable advantages of Li-S batteries, the poor cycle stability and low sulfur utilization caused by the insulated sulfur, polysulfides shutting effect, and large volume expansion have been the biggest challenge for its commercialization.

Developing a functional polar sulfur host is one of the most important strategies to alleviate above-deteriorated issues.[51] Carbonaceous materials with abundant pores and high pore volume show the capacity for the physical confinement of polysulfides.[52] However, the binding affinity is too weak to solve the polysulfides shutting effect.[53] Recently, the surface chemistry between polar sulfur hosts and polysulfides has been intensively studied as its critical role in trapping the diffused polysulfides and catalyzing the conversion between S and Na_2S.[54] Thus, a rational design on structure and surface chemistry by employing a porous and conductive carbon matrix with a polar sulfur host is a promising approach to improve the capacity and cycling stability of Li-S batteries.

1.2. Objectives of the Research

In this Ph.D. thesis, I firstly synthesized the porous C/O-doped g-C_3N_4 photocatalyst via a facile and green precursor modification followed by a thermal annealing procedure. Meanwhile, the

morphology was designed to an atomic-thick nanosheets structure. Based on this investigation, theoretical calculations show that the C-doping can assist the formation of delocalized π-bonding, which is favorable to the enhancement of conductivity. While the ectra-O dopants can facilitate the charge transfer progress and improve the sepearation efficiency of photocarriers because of the enhanced electronic polarization effect (Bader Charge) and shortened bond lengths. As a result, the synergic contribution of textural and electronic features renders C/O-doped g-C_3N_4 with an excellent photoelectrochemical (PEC) performance and high solar hydrogen evolution. For my second work, the defect engineered g-C_3N_4 is coupled with hexagonal upconversion NaYF4, Yb^{3+}, Tm^{3+} (NYF) nanocrystals to form a broadband photocatalyst following a post-heat treatment. The defective porous g-C_3N_4 nanocolumns with S dopants and C vacancies can extend the solar light absorption region to 590 nm and facilitate charge separation efficiency via the induced defect states. While the NYF can upconvert NIR light to UV/visible light, further boosting the solar utilization. Moreover, due to the induced defect states, the upconverted energy transferring from NYF to g-C_3N_4 is also boosted. As a result, the hybrid shows a super solar hydrogen evolution rate among the existing upconversion systems. My third work is inspired by previously reported work that g-C_3N_4 can act as an N source to prepare metal nitrides.[55] Thus, the surface oxidized TiN, a g-C_3N_4 derivative, was chosen as the sulfur host for Li-S batteries. The result shows that surface oxidized TiN plays an important role in suppressing polysulfides shutting effect and boosting the conversion dynamics. When tested in soft-package cells, the cathodes show high capacity and excellent cycling performance compared to the pure TiN cathodes. These results indicate that engineering on defects, hybrid structure, and morphology of g-C_3N_4 is effective to improve the

solar hydrogen evolution activity. Additionally, g-C_3N_4 is a promising energy material for the preparation of cathodes for other electrochemical energy storage systems.

1.3. Thesis Structure

To boost the photocatalytic hydrogen evolution rate, g-C_3N_4 with defects (C, O, S dopants, and C vacancies), upconverted hybrid structure, and unique morphology was fabricated in this thesis. Moreover, to understand the influence of these defects, upconverted hybrid structure in solar energy conversion applications, detailed experimental synthesis, material characterizations, photoelectrochemical and photocatalytic properties were performed. Furthermore, the theoretical calculations were also discussed in depth. The g-C_3N_4 derivative, surface oxidized TiN, is used as the cathodic material for Li-S batteries. The scope of this thesis work is briefly outlined as follows:

Chapter 1 introduces the background of a) g-C_3N_4 based photocatalysts; b) cathodic materials for Li-S batteries, and expounds on the importance and significance of this work.

Chapter 2 presents a literature review mainly on recent progress in g-C_3N_4 based photocatalysts toward H_2 evolution by morphology control, defect engineering, and hybrid structure. The g-C_3N_4 derivatives toward other energy applications is also discussed.

Chapter 3 presents the detailed preparation methodology, material, and photocatalytic characterization techniques, coin cell test measurements.

Chapter 4 investigates the effect of C/O dopants on the photocatalytic properties of g-C_3N_4

nanosheets.

Chapter 5 introduces the fabrication of broadband photocatalyst enabled by defect engineered g-C_3N_4 and upconversion $NaYF_4$, Yb^{3+}, Tm^{3+} (NYF) nanocrystals, and studies the synergistic effect of defect states and upconversion on the photocatalytic properties.

Chapter 6 introduces a g-C_3N_4 derivative, surface oxidized TiN and elucidates its critical role on the strong charge polarization effect for high performance Li-S batteries.

Chapter 7 summarizes the work in this thesis and provides some suggestions for the design and synthesis of other materials and applications in other areas.

1.4. References

(1) Vitousek, P. M.; Mooney, H. A.; Lubchenco, J.; Melillo, J. M. Human Domination of Earth's Ecosystems. *Urban Ecol. An Int. Perspect. Interact. Between Humans Nat.* **2008**, *277* (5325), 3–13.

(2) Gruber, N.; Galloway, J. N. An Earth-System Perspective of the Global Nitrogen Cycle. *Nature* **2008**, *451* (7176), 293–296.

(3) Dresselhaus, M. S.; Thomas, I. L. Alternative Energy Technologies. *Nature* **2001**, *414* (6861), 332–337.

(4) Armaroli, N.; Balzani, V. The Future of Energy Supply: Challenges and Opportunities. *Angew. Chemie Int. Ed.* **2007**, *46* (1-2), 52–66.

(5) Fujishima, A.; Honda, K. Electrochemical Photolysis of Water at a Semiconductor Electrode. *Nature* **1972**, *238* (5358), 37–38.

(6) Yoshino, A. Development of the Lithium-Ion Battery and Recent Technological Trends; Pistoia, G. B. T.-L.-I. B., Ed.; Elsevier: Amsterdam, **2014**, 1–20.

(7) Ong, C. B.; Ng, L. Y.; Mohammad, A. W. A Review of ZnO Nanoparticles as Solar Photocatalysts: Synthesis, Mechanisms and Applications. *Renew. Sustain. Energy Rev.* **2018**, *81*, 536–551.

(8) Liu, J.; Zhang, Y.; Zhang, L.; Xie, F.; Vasileff, A.; Qiao, S. Graphitic Carbon Nitride ($g\text{-}C_3N_4$)-Derived N-Rich Graphene with Tuneable Interlayer Distance as a High-Rate Anode for Sodium-Ion Batteries. *Adv. Mater.* **2019**, *31* (24), 1901261.

(9) Ye, C.; Jiao, Y.; Jin, H.; Slattery, A. D.; Davey, K.; Wang, H.; Qiao, S. 2D MoN-VN Heterostructure To Regulate Polysulfides for Highly Efficient Lithium-Sulfur Batteries. *Angew. Chemie Int. Ed.* **2018**, *57* (51), 16703–16707.

(10) Witt, H. T.; Müller, A.; Rumberg, B. Experimental Evidence for the Mechanism of Photosynthesis. *Nature* **1961**, *191* (4784), 194–195.

(11) Chilkalwar, A. A.; Rayalu, S. S. Synergistic Plasmonic and Upconversion Effect of the (Yb, Er) NYF-TiO_2/Au Composite for Photocatalytic Hydrogen Generation. *J. Phys. Chem. C* **2018**, *122* (46), 26307–26314.

(12) Guo, X.; Song, W.; Chen, C.; Di, W.; Qin, W. Near-Infrared Photocatalysis of β-$NaYF_4$: Yb^{3+}, Tm^{3+}@ ZnO Composites. *Phys. Chem. Chem. Phys.* **2013**, *15* (35), 14681–14688.

(13) Tian, Q.; Yao, W.; Wu, W.; Liu, J.; Wu, Z.; Liu, L.; Dai, Z.; Jiang, C. Efficient UV-Vis-NIR Responsive Upconversion and Plasmonic-Enhanced Photocatalyst Based on Lanthanide-Doped $NaYF_4$/SnO_2/Ag. *ACS Sustain. Chem. Eng.* **2017**, *5* (11), 10889–10899.

(14) Feng, W.; Zhang, L.; Zhang, Y.; Yang, Y.; Fang, Z.; Wang, B.; Zhang, S.; Liu, P. Near-Infrared-Activated $NaYF_4:Yb^{3+}$, Er^{3+}/Au/CdS for H_2 Production: Via Photoreforming of Bio-Ethanol: Plasmonic Au as Light Nanoantenna, Energy Relay, Electron Sink and Co-Catalyst. *J. Mater. Chem. A* **2017**, *5* (21), 10311–10320.

(15) Bednarkiewicz, A.; Nyk, M.; Samoc, M.; Strek, W. Up-Conversion FRET from Er^{3+}/Yb^{3+}:$NaYF_4$ Nanophosphor to CdSe Quantum Dots. *J. Phys. Chem. C* **2010**, *114* (41), 17535–17541.

(16) Malik, M.; Padhye, P.; Poddar, P. Graphene Quantum Dots-Driven Multiform Morphologies of β-$NaYF_4:Gd^{3+}/Tb^{3+}$ Phosphors: The Underlying Mechanism and Their Optical Properties. *ACS Omega* **2018**, *3* (2), 1834–1849.

(17) Yan, X.; Yao, X. Defective Carbons for Electrocatalytic Oxygen Reduction. *Carbon-Based Met. Catal. Des. Appl.* **2018**, *1–2* (20), 59–75.

(18) Rahman, M. Z.; Davey, K.; Qiao, S. Z. Carbon, Nitrogen and Phosphorus Containing Metal-Free Photocatalysts for Hydrogen Production: Progress and Challenges. *J. Mater. Chem. A* **2018**, *6* (4), 1305–1322.

(19) Wang, X.; Maeda, K.; Thomas, A.; Takanabe, K.; Xin, G.; Carlsson, J. M.; Domen, K.; Antonietti, M. A Metal-Free Polymeric Photocatalyst for Hydrogen Production from Water under Visible Light. *Nat. Mater.* **2009**, *8* (1), 76–80.

(20) Sun, J.; Zhang, J.; Zhang, M.; Antonietti, M.; Fu, X.; Wang, X. Bioinspired Hollow Semiconductor Nanospheres as Photosynthetic Nanoparticles. *Nat. Commun.* **2012**, *3* (1), 1–7.

(21) Lau, V. W. H.; Moudrakovski, I.; Botari, T.; Weinberger, S.; Mesch, M. B.; Duppel, V.;

Senker, J.; Blum, V.; Lotsch, B. V. Rational Design of Carbon Nitride Photocatalysts by Identification of Cyanamide Defects as Catalytically Relevant Sites. *Nat. Commun.* **2016**, *7*, 12165.

(22) Liu, J.; Liu, Y.; Liu, N.; Han, Y.; Zhang, X.; Huang, H.; Lifshitz, Y.; Lee, S. T.; Zhong, J.; Kang, Z. Metal-Free Efficient Photocatalyst for Stable Visible Water Splitting via a Two-Electron Pathway. *Science (80).* **2015**, *347* (6225), 970–974.

(23) Ong, W.-J. J.; Tan, L.-L. L.; Ng, Y. H.; Yong, S.-T. T.; Chai, S.-P. P. Graphitic Carbon Nitride (g-C_3N_4)-Based Photocatalysts for Artificial Photosynthesis and Environmental Remediation: Are We a Step Closer to Achieving Sustainability? *Chem. Rev.* **2016**, *116* (12), 7159–7329.

(24) Li, Y.; Ho, W.; Lv, K.; Zhu, B.; Lee, S. C. Carbon Vacancy-Induced Enhancement of the Visible Light-Driven Photocatalytic Oxidation of NO over g-C_3N_4 Nanosheets. *Appl. Surf. Sci.* **2018**, *430*, 380–389.

(25) Huang, Z.-F. F.; Song, J.; Pan, L.; Wang, Z.; Zhang, X. X.; Zou, J.-J. J.; Mi, W.; Zhang, X. X.; Wang, L. Carbon Nitride with Simultaneous Porous Network and O-Doping for Efficient Solar-Energy-Driven Hydrogen Evolution. *Nano Energy* **2015**, *12*, 646–656.

(26) Zhang, Y.; Mori, T.; Niu, L.; Ye, J. Non-Covalent Doping of Graphitic Carbon Nitride Polymer with Graphene: Controlled Electronic Structure and Enhanced Optoelectronic Conversion. *Energy Environ. Sci.* **2011**, *4* (11), 4517–4521.

(27) Liang, Q.; Li, Z.; Yu, X.; Huang, Z. H.; Kang, F.; Yang, Q. H. Macroscopic 3D Porous Graphitic Carbon Nitride Monolith for Enhanced Photocatalytic Hydrogen Evolution. *Adv. Mater.* **2015**, *27* (31), 4634–4639.

(28) Tay, Q.; Kanhere, P.; Ng, C. F.; Chen, S.; Chakraborty, S.; Huan, A. C. H.; Sum, T. C.; Ahuja, R.; Chen, Z. Defect Engineered g-C_3N_4 for Efficient Visible Light Photocatalytic Hydrogen Production. *Chem. Mater.* **2015**, *27* (14), 4930–4933.

(29) Dong, G.; Zhao, K.; Zhang, L. Carbon Self-Doping Induced High Electronic Conductivity and Photoreactivity of g-C_3N_4. *Chem. Commun.* **2012**, *48* (49), 6178-6180.

(30) Li, J.; Shen, B.; Hong, Z.; Lin, B.; Gao, B.; Chen, Y. A Facile Approach to Synthesize Novel Oxygen-Doped g-C_3N_4 with Superior Visible-Light Photoreactivity. *Chem. Commun.* **2012**, *48* (98), 12017–12019.

(31) Wang, Y.; Zhang, J.; Wang, X.; Antonietti, M.; Li, H. Boron- and Fluorine-Containing Mesoporous Carbon Nitride Polymers: Metal-Free Catalysts for Cyclohexane Oxidation. *Angew. Chemie - Int. Ed.* **2010**, *49* (19), 3356–3359.

(32) Ran, J.; Ma, T. Y.; Gao, G.; Du, X. W.; Qiao, S. Z. Porous P-Doped Graphitic Carbon Nitride Nanosheets for Synergistically Enhanced Visible-Light Photocatalytic H2 Production. *Energy Environ. Sci.* **2015**, *8* (12), 3708–3717.

(33) Niu, P.; Liu, G.; Cheng, H.-M. M. Nitrogen Vacancy-Promoted Photocatalytic Activity of Graphitic Carbon Nitride. *J. Phys. Chem. C* **2012**, *116* (20), 11013–11018.

(34) Tu, W.; Xu, Y.; Wang, J.; Zhang, B.; Zhou, T.; Yin, S.; Wu, S.; Li, C.; Huang, Y.; Zhou, Y.; et al. Investigating the Role of Tunable Nitrogen Vacancies in Graphitic Carbon Nitride Nanosheets for Efficient Visible-Light-Driven H_2 Evolution and CO_2 Reduction. *ACS Sustain. Chem. Eng.* **2017**, *5* (8), 7260–7268.

(35) Gnach, A.; Bednarkiewicz, A. Lanthanide-Doped up-Converting Nanoparticles: Merits and Challenges. *Nano Today* **2012**, *7* (6), 532–563.

(36) Yoshio, M.; Brodd, R. J.; Kozawa, A. *Lithium-Ion Batteries*; Springer, 2009; Vol. 1.

(37) Goriparti, S.; Miele, E.; De Angelis, F.; Di Fabrizio, E.; Proietti Zaccaria, R.; Capiglia, C. Review on Recent Progress of Nanostructured Anode Materials for Li-Ion Batteries. *J. Power Sources* **2014**, *257*, 421–443.

(38) Li, Y.; Gong, M.; Liang, Y.; Feng, J.; Kim, J. E.; Wang, H.; Hong, G.; Zhang, B.; Dai, H. Advanced Zinc-Air Batteries Based on High-Performance Hybrid Electrocatalysts. *Nat. Commun.* **2013**, *4*, 1805.

(39) Liu, J.; Song, K.; Van Aken, P. A.; Maier, J.; Yu, Y. Self-Supported $Li_4Ti_5O_{12}$-C Nanotube Arrays as High-Rate and Long-Life Anode Materials for Flexible Li-Ion Batteries. *Nano Lett.* **2014**, *14* (5), 2597–2603.

(40) Zhang, C. (John); Kim, S. J.; Ghidiu, M.; Zhao, M. Q.; Barsoum, M. W.; Nicolosi, V.; Gogotsi, Y. Layered Orthorhombic Nb_2O_5@$Nb_4C_3T_x$ and TiO_2@$Ti_3C_2T_x$ Hierarchical Composites for High Performance Li-Ion Batteries. *Adv. Funct. Mater.* **2016**, *26* (23), 4143–4151.

(41) Banerjee, A.; Shilina, Y.; Ziv, B.; Ziegelbauer, J. M.; Luski, S.; Aurbach, D.; Halalay, I. C. Review-Multifunctional Materials for Enhanced Li-Ion Batteries Durability: A Brief Review of Practical Options. *J. Electrochem. Soc.* **2017**, *164* (1), A6315–A6323.

(42) Lu, J.; Li, L.; Park, J. B.; Sun, Y. K.; Wu, F.; Amine, K. Aprotic and Aqueous Li-O_2 Batteries. *Chem. Rev.* **2014**, *114* (11), 5611–5640.

(43) Sun, L.; Wang, D.; Luo, Y.; Wang, K.; Kong, W.; Wu, Y.; Zhang, L.; Jiang, K.; Li, Q.; Zhang, Y.; et al. Sulfur Embedded in a Mesoporous Carbon Nanotube Network as a Binder-Free Electrode for High-Performance Lithium-Sulfur Batteries. *ACS Nano* **2016**,

10 (1), 1300–1308.

(44) Johnson, L.; Li, C.; Liu, Z.; Chen, Y.; Freunberger, S. A.; Ashok, P. C.; Praveen, B. B.; Dholakia, K.; Tarascon, J. M.; Bruce, P. G. Erratum: The Role of Li-O_2 Solubility in O_2 Reduction in Aprotic Solvents and Its Consequences for Li-O_2 Batteries. *Nat. Chem.* **2015**, *7* (1), 87.

(45) Zhai, D.; Lau, K. C.; Wang, H. H.; Wen, J.; Miller, D. J.; Lu, J.; Kang, F.; Li, B.; Yang, W.; Gao, J.; et al. Interfacial Effects on Lithium Superoxide Disproportionation in Li-O_2 Batteries. *Nano Lett.* **2015**, *15* (2), 1041–1046.

(46) Li, Q.; Xu, P.; Gao, W.; Ma, S.; Zhang, G.; Cao, R.; Cho, J.; Wang, H. L.; Wu, G. Graphene/Graphene-Tube Nanocomposites Templated from Cage-Containing Metal-Organic Frameworks for Oxygen Reduction in Li-O_2 Batteries. *Adv. Mater.* **2014**, *26* (9), 1378–1386.

(47) Zhai, D.; Wang, H. H.; Yang, J.; Lau, K. C.; Li, K.; Amine, K.; Curtiss, L. A. Disproportionation in Li-O_2 Batteries Based on a Large Surface Area Carbon Cathode. *J. Am. Chem. Soc.* **2013**, *135* (41), 15364–15372.

(48) Liu, Z.; Feng, N.; Shen, Z.; Li, F.; He, P.; Zhang, H.; Zhou, H. Carbon-Free O_2 Cathode with Three-Dimensional Ultralight Nickel Foam-Supported Ruthenium Electrocatalysts for Li-O_2 Batteries. *ChemSusChem* **2017**, *10* (13), 2714–2719.

(49) Rosenman, A.; Markevich, E.; Salitra, G.; Aurbach, D.; Garsuch, A.; Chesneau, F. F. Review on Li-Sulfur Battery Systems: An Integral Perspective. *Adv. Energy Mater.* **2015**, *5* (16).

(50) Wu, C.; Fu, L.; Maier, J.; Yu, Y. Free-Standing Graphene-Based Porous Carbon Films

with Three-Dimensional Hierarchical Architecture for Advanced Flexible Li-Sulfur Batteries. *J. Mater. Chem. A* **2015**, *3* (18), 9438–9445.

(51) Pang, Q.; Liang, X.; Kwok, C. Y.; Nazar, L. F. Advances in Lithium-Sulfur Batteries Based on Multifunctional Cathodes and Electrolytes. *Nat. Energy* **2016**, *1* (9), 16132.

(52) Li, Z.; Jiang, Y.; Yuan, L.; Yi, Z.; Wu, C.; Liu, Y.; Strasser, P.; Huang, Y. A Highly Ordered Meso@microporous Carbon-Supported Sulfur@smaller Sulfur Core-Shell Structured Cathode for Li-s Batteries. *ACS Nano* **2014**, *8* (9), 9295–9303.

(53) Liu, S.; Li, J.; Yan, X.; Su, Q.; Lu, Y.; Qiu, J.; Wang, Z.; Lin, X.; Huang, J.; Liu, R.; et al. Superhierarchical Cobalt-Embedded Nitrogen-Doped Porous Carbon Nanosheets as Two-in-One Hosts for High-Performance Lithium–Sulfur Batteries. *Adv. Mater.* **2018**, *30* (12), e1706895.

(54) Zhong, Y.; Yin, L.; He, P.; Liu, W.; Wu, Z.; Wang, H. Surface Chemistry in Cobalt Phosphide-Stabilized Lithium-Sulfur Batteries. *J. Am. Chem. Soc.* **2018**, *140* (4), 1455–1459.

(55) Fischer, A.; Antonietti, M.; Thomas, A. Growth Confined by the Nitrogen Source: Synthesis of Pure Metal Nitride Nanoparticles in Mesoporous Graphitic Carbon Nitride. *Adv. Mater.* **2007**, *19* (2), 264–267.

Chapter 2

2. Literature Review

2.1. Introduction

The irreversible consumption of fossil fuels and ever-increasing energy demand have proposed human society with unprecedented environmental and energy crises.[1] So far, researchers have made great efforts in exploiting and storing renewable energy via a sustainable and eco-friendly manner.[2,3] Among the myriad clean energy technologies, photocatalytic hydrogen evolution has shown its potential to address these concerns by employing the eco-friendly solar and water resource to produce the high calorific valued (143 KJ g^{-1}), storable and transportable H_2.[4] In addition, since the first commercialization of lithium-ion batteries in 1991, technological revolution on new-type batteries have inspired people with new thinking on clean energy conversion and storage.[5] Recently, graphite carbon nitride (g-C_3N_4), a metal-free photocatalyst, has firstly attracted extensive attention in hydrogen production due to its merits of perfect band structure, stable physicochemical properties, low-cost, and environmental benignity.[6] Also, its derivatives have been demonstrated to be promising materials for electrochemical energy conversion and storage applications.[7,8] In this regard, this chapter will first mainly summarize recent development on g-C_3N_4 nanomaterials for photocatalytic hydrogen evolution and then briefly introduce recent development of g-C_3N_4 derivatives on other electrochemical storage applications.

2.2. Photocatalytic hydrogen evolution

Since the landmark discovery of Honda-Fujishima effect in the early 1970s,[9] the photocatalytic

hydrogen evolution has been significantly flourishing as reflected by the dramatically increasing number of related publications searched in Web of Science (**Figure 1a**). Being the core component of the photocatalytic system, a variety of photocatalysts have been investigated, including the metallic oxide/sulfides/nitrides,[10,6,11,12] carbonaceous materials (carbon dots/quantum dots)[13,14] and metal clusters.[15] However, these materials still suffer from severe photo corrosion,[16,17] inferior light absorption, or difficulty in preparation,[18] which restrict their practical applications. Recently, a metal-free polymer, graphitic carbon nitride (abbreviated as g-C_3N_4) has boosted a surge of interest since the seminal work reported by Wang et al. in 2009 (**Figure 1a**).[19] Considering its exceptional electronic structure with a bandgap of 2.7 eV and perfect band positions for water splitting (conductive band (CB) minimal and valence band (VB) maximal of -1.13 and 1.57 V vs. standard hydrogen electrode (SHE)),[19,20] g-C_3N_4 has been regarded as the most promising next-generation candidate for photocatalytic H_2 evolution as evidenced by the relative high publications and citations since 2009 (**Figure 1b**).

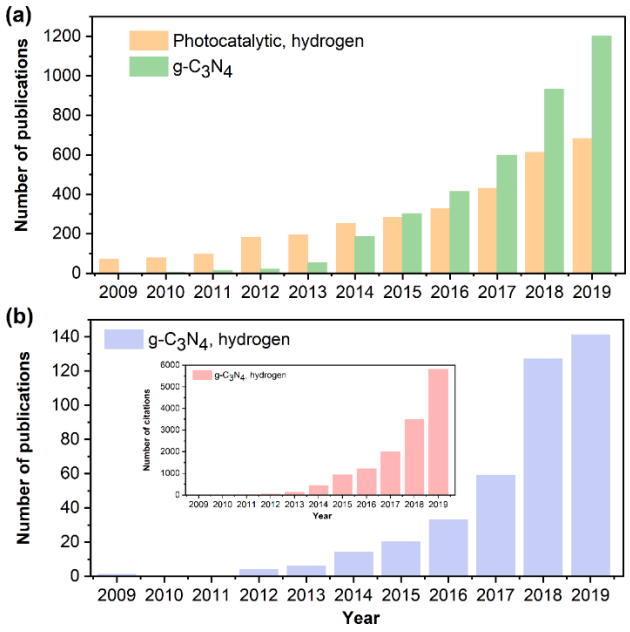

Figure 2.1 Number of annual publications using **a)** "photocatalytic, hydrogen" "g-C_3N_4" and

b) "g-C_3N_4, hydrogen" as title key words since 2008 (insert: number of citations of "g-C_3N_4, hydrogen"). Data from Institute for Scientific Information (ISI) Web of Science on 25th February 2020.

2.2.1. Principles and challenges for g-C_3N_4

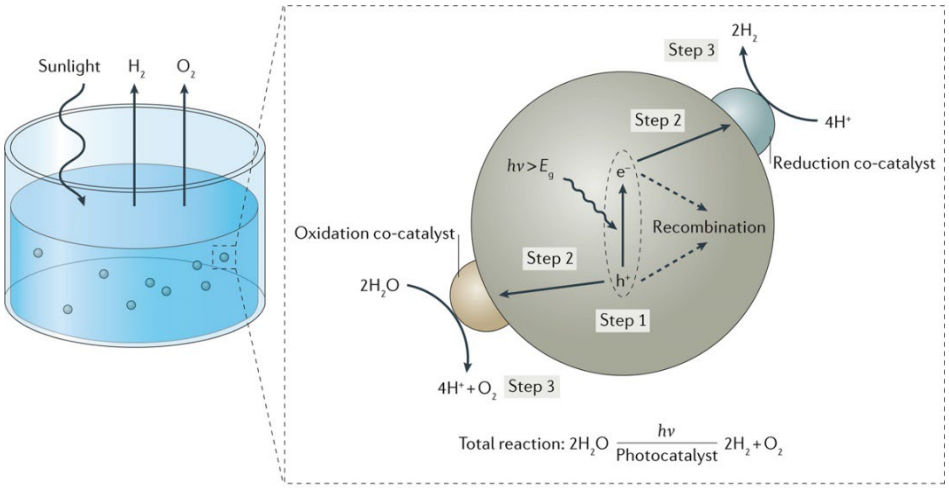

Figure 2.2 Illustration of the basic principle of photocatalytic water splitting.[21]

As is known to all that the H_2 evolution via water splitting is an uphill chemical reaction with a high Gibbs free energy of 237 kJ mol^{-1}.[22] Thus, external solar light with appropriate wavelength must be provided to excite the photocarriers inside the photocatalyst, which is generally regarded as the first step for photocatalytic H_2 evolution (**Figure 2**).[21] For ideal g-C_3N_4, the excited wavelength should be shorter than ~ 459 nm according to its bandgap of 2.7 eV.[19] After irradiation, the negative charged electrons are migrated to CB while the positive charged holes are left in VB. Next, these photocarries diffuse randomly from bulk to surface of photocatalyst or co-catalyst. It is worth to mention that the photocarrier transfer can also be seriously hindered by the recombination of photogenerated electron-hole pairs. Finally, the

photocarriers participate in the redox chemical reactions, respectively. Importantly, this only happens in the condition that the CB or VB level is more negative or positive than the standard H^+/H_2 or O_2/H_2O evolute potential. For g-C_3N_4, the CB is about 1.13 V more negative than standard H^+/H_2 evolute potential, and thus H_2 can be thermal-dynamically produced. This review will mainly focus on the half-reaction of water splitting, namely, the reductive H_2 evolution, for g-C_3N_4 relative materials.

Despite the success of g-C_3N_4 for photocatalytic H_2 evolution, bulk g-C_3N_4 materials still suffer from the insufficient supply of valid photocarriers, which can be ascribed to the following aspects. First, in a typical synthetic procedure, the cyanamide, dicyandiamide, or melamine is often annealed in a semi-closed crucible at 550°C for 4 h (hours), which gives g-C_3N_4 a severely stacked lamellar structure with a low surface area. On one hand, the lamellar structure offers limited active sites involved in the aqueous solution, resulting in a poor mass transfer. On the other hand, these bulk aggregates barely block the photons on the surface without scattering them into directions, which leads to a poor light absorption ability. Second, bulk g-C_3N_4 shows the maximum light absorption to 459 nm, disabling to utilizing most of the visible and infrared light. The poor light absorption toward long wavelength light leads to a poor H_2 evolution rate. Thirdly, the fast recombination of photocarriers in the bulk and surface of g-C_3N_4 dramatically reduces the amount of valid electrons, further lowering the photocatalytic activity.[23] To this point, we aim to deliver a comprehensive review on the recent development of g-C_3N_4-based materials in photocatalytic H_2 evolution in the following aspects: 1) morphology control, 2) defect engineering, as well as 3) hybrid coupling on g-C_3N_4. At last, we would also add a mini description of 4) the g-C_3N_4 derivatives for batteries energy

applications.

2.2.2. Development of morphology controls on g-C_3N_4

Generally, the textural properties of g-C_3N_4 are easily affected by each condition of the annealing procedure, including the precursors, annealing temperature, atmosphere, time and space, post-treatment of final products. Therefore, flooding of research work has been worked in this area. Herein, we summarize the preparing method in the following sections:

2.2.2.1. Ultrasonic method

In the early research stage of g-C_3N_4, many research groups have proposed ultrasonic method to exfoliate the bulk g-C_3N_4 aggregates into two dimensional (2D) g-C_3N_4 nanosheets (**Figure 2. 3**).[24] Many solvents such as isopropanol (IPA), water, and N-methy-pyrrolidone (NMP), ethanol, and acetone were chosen as the exfoliated liquid to disperse the bulk g-C_3N_4 powder.[24] Ajayan et al. found that IPA and NMP show the best exfoliated ability after sonication for 10 h with a thickness of 2.0 nm of g-C_3N_4 nanosheets (**Figure 2. 3a, b**). As a result, g-C_3N_4 shows a high surface area of 384 m^2 g^{-1} with a superior H_2 evolution rate of 93 μmol h^{-1}, 9 times higher than that of pristine g-C_3N_4. The atom-thick ultrathin g-C_3N_4 nanosheets were prepared via a similar liquid exfoliation method using water as a dispersing solvent with an ultra-sonication time of 16 h (**Figure 2. 3c-f**).[25] Apart from the ordinary ultrasonic instrument, the pulsed ultrasonic cell disruptor was also employed to exfoliated the bulk g-C_3N_4 aggregates (**Figure 2. 3g**).[26] But the main challenge of this method are the time/energy consuming, low yield, and

difficulty in collecting the solid samples. Thus, facile and efficient methods are still in great demand for future applications.

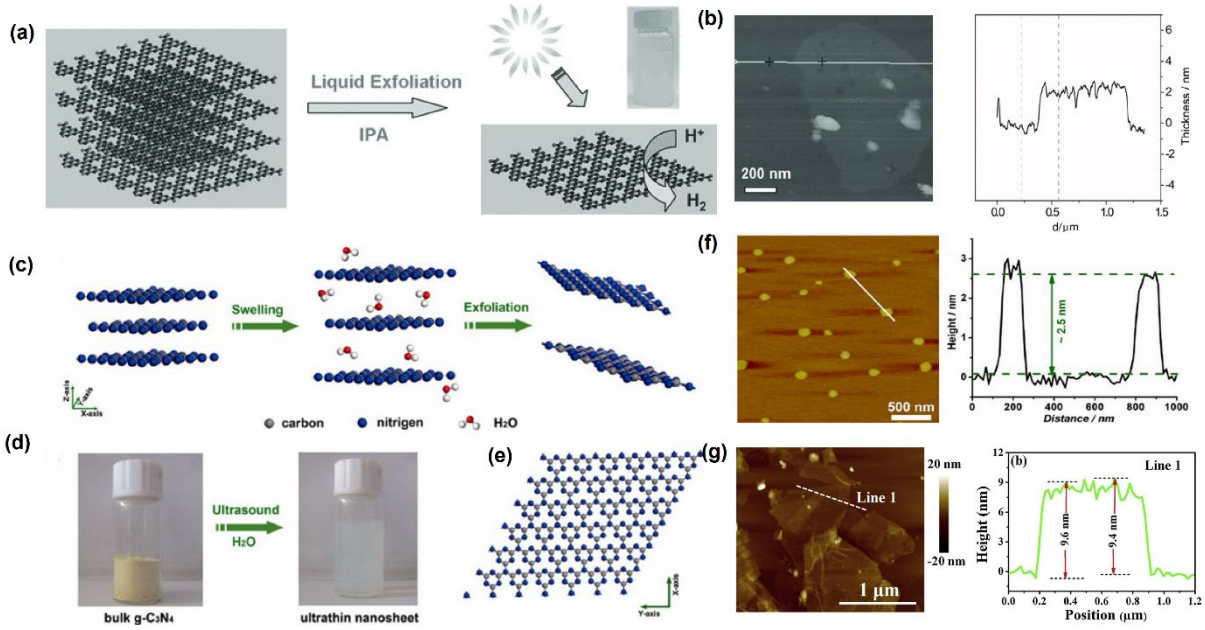

Figure 2.3 (a) Liquid exfoliation of g-C_3N_4 nanosheets in IPA,[24] and **(b)** the corresponding AFM with a thickness of around 2.0 nm. [24] **(c-e)** Liquid exfoliation of g-C_3N_4 nanosheets in H_2O[25] and **(f)** the corresponding AFM with a thickness of around 2.5 nm. **(g)** AFM image of exfoliated g-C_3N_4 nanosheets the thickness of ~9 nm.[26]

2.2.2.2. Template method

The template (hard and soft template) method is an important approach to obtain advanced nanostructure. For the hard template method, silica (SBA-15,[27] nanosphere colloid solutions[27, 28]), $CaCO_3$ particles,[29] and anodic aluminum oxide (AAO)[30] are the most widely used templates due to their high thermal stability and anti-corrosion property. In a typical synthetic route, cyanamide is chosen as the precursor because of its molten state at higher temperature (70-

80 °C). In addition, this fluidity can make a perfect filtering process under vacuum followed by centrifugation. After the thermal polymerization at 550 °C and acid/alkali etching process, a new g-C_3N_4 replica can be copied. Following this strategy, a series of g-C_3N_4 materials with advanced nanostructures such as mesoporous ordered nanorods,[27] nanospheres,[27, 31] and nanoarrays[30] were obtained (**Figure 2. 4**). Unfortunately, the hard templates method is usually time/energy-consuming, complex, or even dangerous due to the use of toxic HF.

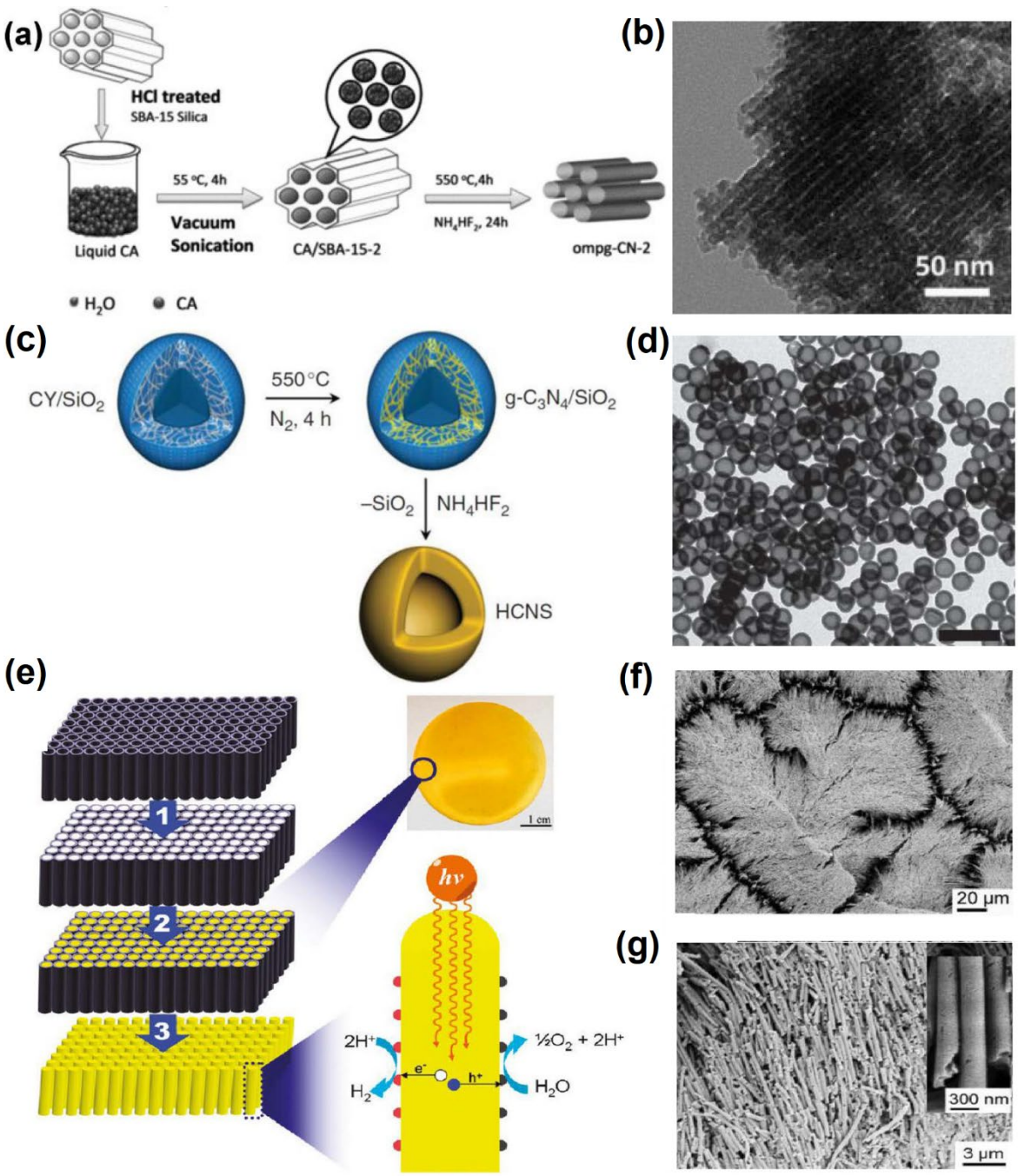

Figure 2.4 Synthesis diagrams and electronic microscopy images of g-C_3N_4 with (**a, b)** mesoporous ordered nanorods structure (ompg-CN-2 indicates ordered mesoporous g-C_3N_4, the scale bar equals 1 μm), [27] (**c, d)** nanoshpere structure (CY and HCNS indicate cyanamide and hollow carbon nitride spheres), [27,31] and (**e-g)** nanoarray nanostructure. [30]

Comparing to the hard template method, the soft template method shows great superiority

of facile preparation, excluding the synthesis of the hard template and the template rinsing process. Surfactants such as Triton X-100, P123, F127, Brij30, Brij58, and Brij76 are widely used to with the N-containing precursors (melamine, dicyanamide, and urea) optimize the physical structure of g-C_3N_4.[23] However, these chemicals should be discreetly chosen as some surfactants are decomposed at low departure, and the pores will be sealed again in higher temperature. Among them, the Pluronic P123 and melamine are the ideal matches due to the higher decomposed temperature and less reactive property of melamine compared to other precursors. As a result, both will go through their own ways without inter-crossing too much, which leads to a low carbon content of final porous g-C_3N_4 products with a significantly improved surface area up to 90 m^2 g^{-1}, 10 times higher than bulk material.[32] The commercially accessible 1-butyl-3-methylimidazolium tetrafluoroborate ($BmimBF_4$) also shows a unique role in alternating the morphology of bulk g-C_3N_4. Li et al. reported an enriched mesoporous g-C_3N_4 with an ultra-high surface area and large pore volume of 4 m^2 g^{-1} and 0.32 m^2 g^{-1}, respectively.[33]

Apart from the “inert” /insoluble hard and soft templates, the accessible, abundant, and easy-to-remove NaCl can also act as a template, giving g-C_3N_4 a variety of morphologies such as nanoribbons, nanorods, and nanoflowers.[34] Due to the electronegativity of the surface of NaCl and dicyandiamide, assemblies were generated after the grounding and mixing process. After the high temperature annealing at 600°C for 1 h, g-C_3N_4 nanoribbons were obtained with abundant cyano groups. Interestingly, when dispersing these exfoliated nanoribbons in different alcohols such as methanol, ethanol, and n-propanol, the nanobelts, nanobundles/nanoflowers, and nanorods/nanotubes can be formed, correspondingly. This is

owing to the different structure and steric hindrance of alcohols that affect the hydrogen bond formation between cyano groups and the hydroxyl of alcohols. Similar easy-to-remove templates such as LiCl and LiCl/KCl salts were also reported.[35]

The gas template method, which relies on the generated gas inside the polymerized intermediators also gives a porous structure of g-C_3N_4. The typical regents are the low melting sulfur,[36] easy-to-decomposed NH_4Cl[37], and the inorganic acid.[38] These templates are easy to sublimate or decompose at a higher temperature, which blows abundant bubbles and finally result in loosen and porous structures. He and co-authors reported facile sulfur mediated synthesis of uniform g-C_3N_4 with abundant pores around 50 nm.[36] When increasing sulfur content (melamine/sulfur mass ratio of 1/1), the surface area becomes larger as more bubbles were generated. The highest surface area and H_2 evolution rate can reach 46.0 $m^2 g^{-1}$ and 50.1 μmol h^{-1}, which is about 2.7 and 6.1 times higher than the bulk g-C_3N_4 materials. Other easy-to-decomposed precursors such as NH_4Cl and protonated precursors have recently drawn much attention. [37] For the former, NH_4Cl can release the corrosive NH_3 and HCl molecules which is effective to etch the bulk g-C_3N_4 agglomerates into smaller nanosize composed of ultrathin porous nanosheets. [37] For the latter one, the inorganic acid such as HCl, HNO_3, and H_2SO_4 all display an active role in exfoliating the bulk aggregates into porous few-layer g-C_3N_4 nanosheets. [38] Due to the weak binding (hydrogen bonding network) between acid and melamine, the self-assembled melamine-acid derivatives tend to decompose into corrosive NO, NO_2, and SO_2, giving rise to a porous texture of g-C_3N_4. In some cases, the g-C_3N_4 can exist in a loosen foam shaped formation.[38] Thus, a significant surface area can be achieved to 212.5 $m^2 g^{-1}$, which is 13.1 times higher than bulk materials.

2.2.2.3. Post treatment method

Besides the physical ultra-sonication, post treatment such as thermal etching, acid etching, and strong chemical oxidation on bulk g-C_3N_4 materials is another universe strategy to improve the surface area. Niu et al. first proposed a repeated thermal etching process that can exfoliate the bulk lamellar structure to wrinkle ultra-thin g-C_3N_4 nanosheets.[39] This is operated based on the instability of the interlayered hydrogen-bond, which can be gradually oxidized and removed by O_2 in the air as shown in **Figure 2. 5a**. Additionally, the thickness can be adjusted by the thermal conditions, such as the time, temperature. As a result, this method can deliver g-C_3N_4 nanosheets with a thickness of 2 nm (**Figure 2. 5b**) and a high surface area up to 306 m^2 g^{-1}. Compared to other prepared approaches, this method has the advantages of low-cost, easy scale up, and environmental friendliness. However, the biggest limitation is the low yield of ~ 6%. Chemical oxidization that mimics the Hummer's method on exfoliating graphite to graphene was also successfully processed by employing the $K_2Cr_2O_7/H_2SO_4$ as oxidants (**Figure 2. 5c**).[40] This acid oxidation can create abundant hydroxyl and carboxyl groups and induce the formation of pores. As a result, the specific surface area reaches 235.2 m^2 $g^{-1,}$ and the water solubility is significantly increased to 3 mg mL^{-1}. While using mild acid (Brønsted acid H_3PO_4) is another strategy to exfoliate the bulk material to porous 2D g-C_3N_4 nanosheets without destroying its basic tri-s-triazine building block.[41] Different from other exfoliation method, H_3PO_4 can be directly intercalated into the interlayer of bulk g-C_3N_4 stacks and selectively interact with the strand nitrogen atoms via the Brønsted acid-base interaction (**Figure 2. 5d**). Via this protonation-exfoliation process, the porous 2D g-C_3N_4 nenosheets was obtained with

a 8 time higher surface area and much thinner thickness of 1.1 nm compared with the bulk material (**Figure 2. 5e-g**).

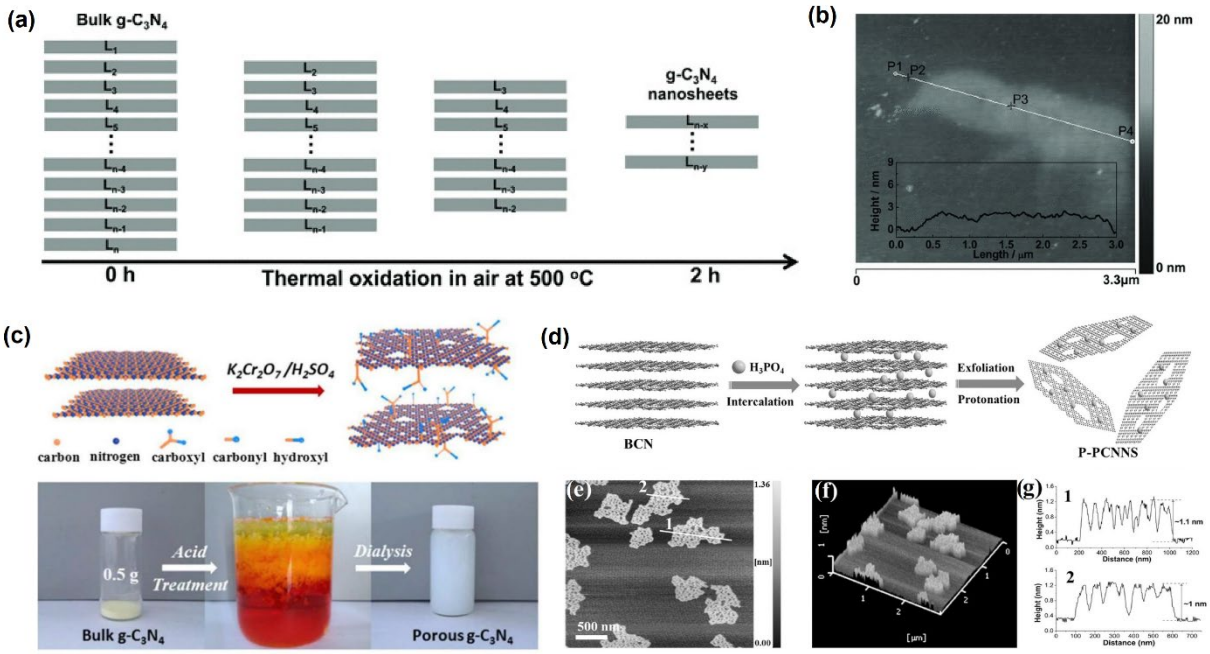

Figure 2.5 Preparation process of g-C_3N_4 nanosheets using **(a)** thermal etching method and **(b)** the corresponding AFM image; [39] **(c)** chemical oxidation method;[40] **(d)** acid protonation-exfoliation and the corresponding **(e-f)** AFM and **(g)** thickness plot images.[41]

2.2.3. Development of defect engineering on g-C_3N_4

As is known to all that the ultimate photocatalytic performance of g-C_3N_4 is closely relative to its electronic properties, which holds the critical role in determining the light absorption and charge transfer progress. g-C_3N_4 is an organic polymer with its polymerization process being easily affected by the annealing conditions, and thus the atoms in the basic tri-s-triazine unit can be replaced by foreign atoms such as the non-metal elements (C, O, S, P, etc.), vacancies, and metals (Na, K, Cu, Fe, Co, Ni, etc.). Generally speaking, the heteroatoms of higher periodic

elements tend to exhibit narrower bandgaps and lower HOMO (highest occupied molecular orbital) levels, endowing g-C_3N_4 with enhanced visible light absorption and fast electron mobility.[42] Therefore, defect engineering based on introducing the purities (dopants, vacancies) into the g-C_3N_4 matrix has drawn extensive attention. Regarding this, we summarize recent progress in the development of defective g-C_3N_4 toward photocatalytic H_2 evolution.

2.2.3.1. C-doping

Zhang et al. first reported the C self-doped g-C_3N_4 (C-g-C_3N_4) material that was prepared by annealing the alcohol-modified melamine at 520 °C with a heating rate of 20 °C min^{-1} in air.[43] The density functional theory (DFT) calculations reveal that C atoms prefer to substitute the bridging N atoms and result in the formation of delocalized big π bonds with the neighboring atoms, which would improve the conductivity and thus facilitate the charge transfer process. This was further confirmed by the dramatically reduced charge transfer resistance and lower bandgap of C-g-C_3N_4. As a result, the H_2 evolution rate increases by 1.4 times under visible light irradiation. The bio-templated porous microtubular C-doped (BTPMC) was prepared to employ urea and kapok fiber as g-C_3N_4 and C sources. Due to the electrostatic interaction and hydrogen network between urea and kapok fiber, the final BTPMC reserved the previous morphology of kapok fiber of nanotubes. Due to the C-doping, the bandgap can be narrowed to 1.68 eV, revealing the significant visible light absorption to 738 nm.[44] A similar work was also proposed by using the b-Cyclodextrin and dicyandiamide as starting materials. The C dopants induced the formation of Urbach tail due to the activation of n-π* electronic transition,[45,46,47] thus extend the visible light absorption to 590 nm and boost a 5-fold increase

in H_2 evolution rate.[48]

2.2.3.2. O-doping

Chen et al. first fabricated the O-doped g-C_3N_4 via a facile H_2O_2 hydrothermal approach with extended visible light absorption to 498 nm and enhanced photoreactivity towards methyl blue (MB) degradation and H_2 evolution under visible light irradiation.[49] According to the X-ray photoelectron spectroscopy (XPS) results, one can infer that the O atoms directly bonded to sp^2-hybridized carbon and replaced the two-coordinated N atoms, resulting in the C-O and N-C-O bond. The O dopants significantly tune the electronic structure of g-C_3N_4 with its bandgap reducing by 0.21 eV. However, the VBM (valence band maximum) remains the same, indicating the VBM of the O-doped g-C_3N_4 primarily depends on the N 2p orbitals. Due to the more negative electronegativity of O than N, extra electrons would be redistributed and cause additional defect-related surface below the CBM (conductive band maximum). This will result in an accelerated charge transfer and separation in the O-doped g-C_3N_4. Thus it witnessed a superior photodegradation of MB (methyl blue) and an improved H_2 evolution rate of 37.5 μmol h^{-1}.

Deeper discussion on O-doping g-C_3N_4 toward photocatalytic activity was analyzed by Zhang's group who synthesized O-doped g-C_3N_4 ultrathin nanosheets by annealing the H_2O_2 treated melamine at 550°C for 2h (**Figure 2. 6a**).[50] Controlled samples of MCN-1 and MCN-2 were obtained with 1:4 and 1:8 mass ratio of melamine and H_2O_2. Compared to bulk g-C_3N_4, MCN-1 shows the lowest PL intensity (**Figure 2. 6b**), indicating the suppressed recombination of photocarriers, and thus it exhibits the highest H_2 evolution rate of 60.2 μmol h^{-1} (**Figure 2.**

6c). The experimental and theoretical results demonstrate that O atoms prefer to substitute the two-coordinated N position. In-depth DFT calculations indicate that the O dopants can shorten the C-N/C=N bonds, which is beneficial to the charge transfer due to the shorter charge diffusion pathway from bulk to the surface. Additionally, the bandgap was calculated to narrow, extending the visible light to a longer wavelength (**Figure 2. 6d**). Interestingly, electronic polarization is also observed as seem from the differential charge density diagram (**Figure 2. 6e**). This acts like the "inner electric field" which propels the electron transfer from more negative sites to less negative areas. Based on the above statement, the synergic effect of textural and electronic merits, the target material demonstrated an enhanced mass and charge transfer, enhanced visible light absorption, as well as a high charge separation efficiency, thus 6.1 and 3.1 times higher superior H_2 evolution rate and AQE (apparent quantum efficiency), respectively.

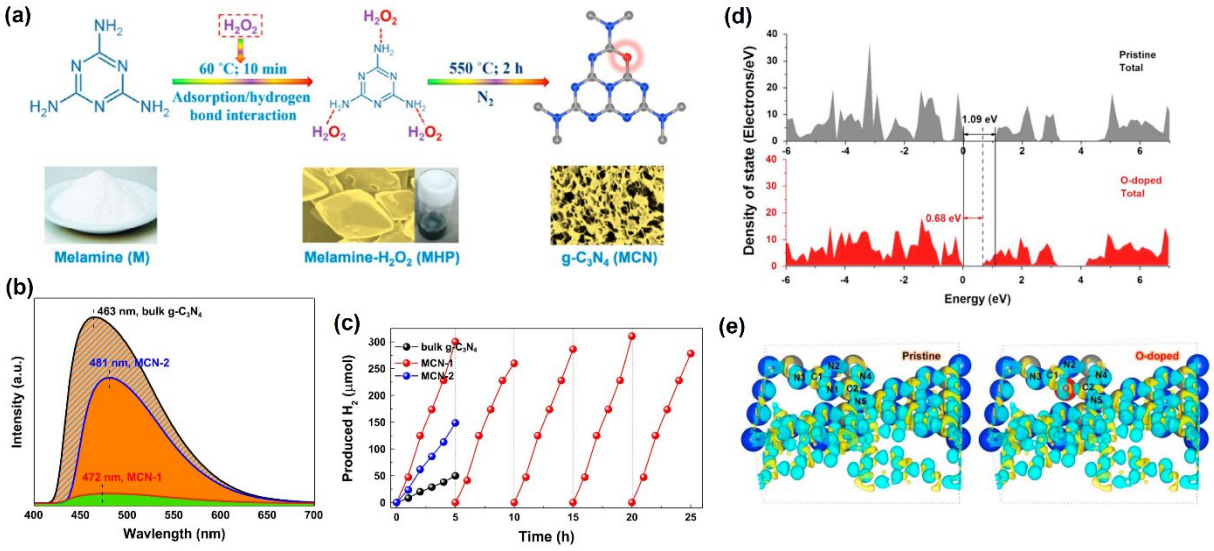

Figure 2.6 (a) Synthetic route of O-doped mesoporous g-C_3N_4 nanosheets. **(b)** PL spectra and **(c)** H_2 evolution rates of bulk g-C_3N_4, MCN-1, and MCN-2. **(d)** Calculated DOSs (density of

states) and **(e)** differential charge density of pristine g-C_3N_4 and O-doped g-C_3N_4 (decrease in electrons: olive; increase in electrons: cyan).[50]

2.2.3.3. S-doping

The pioneering work on S-doping g-C_3N_4 ($C_3N_{4-x}S_x$) was reported by Cheng et al. in 2010.[51] The S atoms were doped into the g-C_3N_4 matrix via a post heat treatment of g-C_3N_4 in H_2S flow at 450 °C for 1 h. The XPS and XANES (X-ray absorption near-edge structure) results show that S was successfully doped and formed C-S bonding by replacing the two-coordinated N atoms. As seen from DFT calculations that S dopants are effective in narrowing the bandgap by the interaction of S 3p states with N 2p states (**Figure 2. 7a-c**). Noticeably, due to the QCE (quantum confinement effect) induced by the decreased particle size, a broaden bandgap was witnessed with the CB and VB shifting oppositely (**Figure 2. 7d**). Moreover, the homogenous doping of sulfur has endowed $C_3N_{4-x}S_x$ with a larger VB width, leading to faster electron mobility. Strikingly, due to this unique electronic structure, $C_3N_{4-x}S_x$ shows a superior oxidation ability that can remove phenol under $\lambda > 400$ nm while it is impossible for bulk g-C_3N_4 under $\lambda > 300$ nm. Other precursors such as thiourea,[52,53,54] urea/benzyl disulfide[55,56] have been reported to work as S source, which is much "green" that the toxic and corrosive H_2S gas.

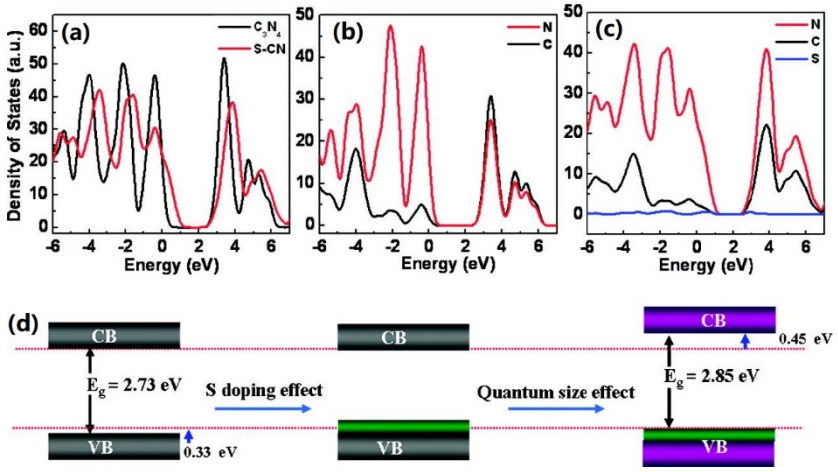

Figure 2.7 (a) Total DOSs (density of states) of g-C_3N_4 and $C_3N_{4-x}S_x$. **(b)** Projected DOSs of N and C for C_3N_4. **(c)** Projected DOSs of N, C, and S for $C_3N_{4-x}S_x$. **(d)** Schematic diagram of of band structure evolution for C_3N_4 by S-doping and quantum confinement effect.[51]

2.2.3.4. P-doping

A series of P-doped g-C_3N_4 have been successfully prepared using different phosphorus sources with varied doping positions, and consequently, the significantly changed photocatalytic properties.[57] The most presentative work was reported by Qiao's group by annealing the mixture of melamine and 2-aminoethlyphosphonic acid (AEP, **Figure 2. 8a**).[58] Following the annealing procedure, additional thermal exfoliation was applied to bulk P-doped g-C_3N_4 (PCB-B), thus resulted in a final porous ultrathin P-doped g-C_3N_4 nanosheets (PCN-S). This combination of P-doping and thermal exfoliation method has the merits of environmental benignity, easy scale up, as well as high efficiency. The DFT calculations identified that P atoms prefer to appear in C1, which would enlarge the in-planar distance of nitride pores from 6.95 Å to 7.04 Å and distort the tri-s-triazine unit (**Figure 2. 8b**). The interplanar spacing of PCN-B is larger than CN-B due to the bulk peeling process of nanosheets. However, after the

additionally thermal etching process, the particle size was smaller and the thickness was thinner, therefore would result in the QCE. As a result, compared to PCN-B, PCN-S exhibits a weaker visible light absorption but still much stronger than the bulk CN-B and CN-S (**Figure 2. 8c**). Strikingly, a new electronic state appears under CBM, which is called midgap state (**Figure 2. 8d-e**). The authors claimed that the midgap state can boost the photocatalytic H_2 evolution mainly in the following two ways: 1) allowing electron excitation with energy lower than its bandgap at 2.24 eV, and extending visible light absorption to 557 nm; 2) accommodating electrons migrated from the CB, thus lowering the recombination rate of photogenerated electron-hole pairs. Along with the optimization of texture, the ultrathin and porous g-C_3N_4 nanosheets favor the photocarrier transport in both in-plane and interior direction, accelerating the charge transfer process. Finally, a high visible-light photocatalytic H_2-production activity of 1596 mmol h^{-1} g^{-1} and an apparent quantum efficiency of 3.56% at 420 nm were achieved, respectively. This superior performance ranks the top of the current pure g-C_3N_4-based photocatalytic system.[57,59,60,61,62,63]

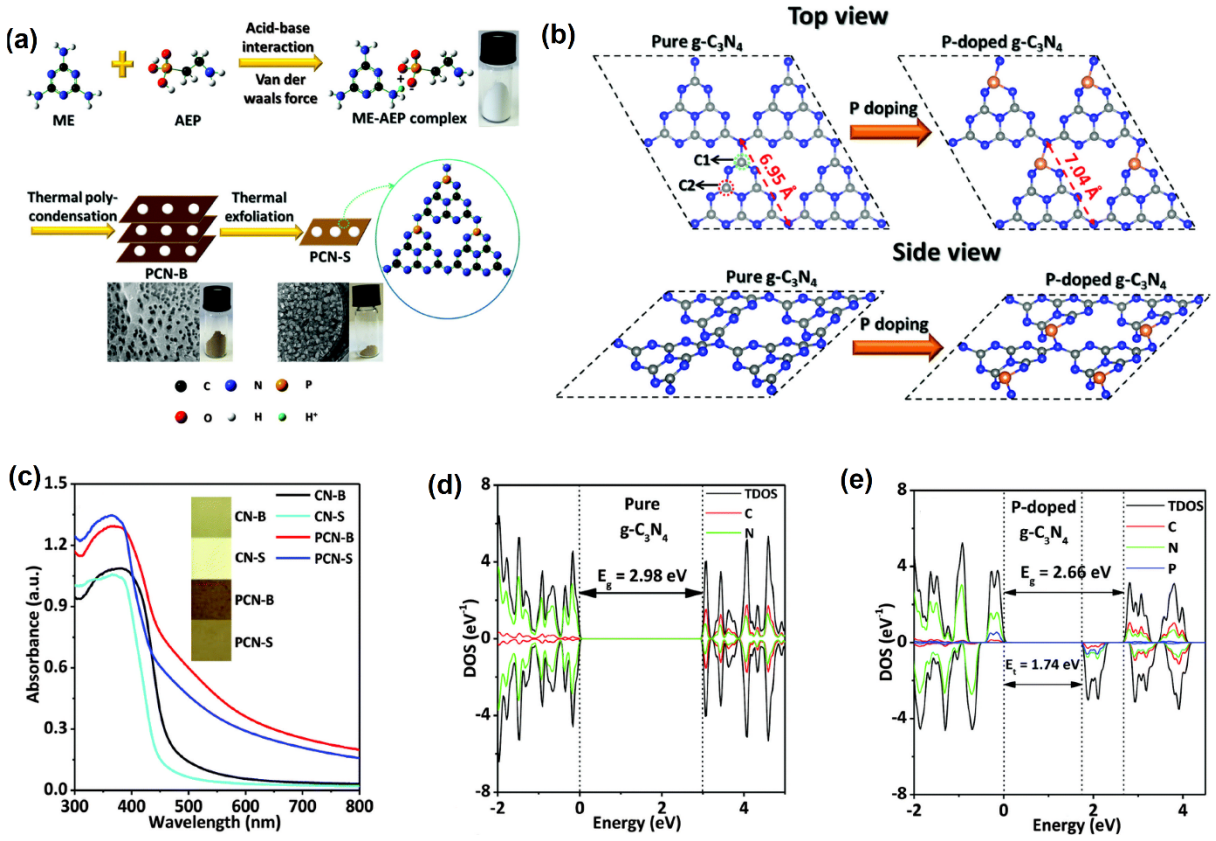

Figure 2.8 (a) Synthetic route of porous PCN-S (ME indicate melamine). **(b)** DFT calculaions models of ideal g-C_3N_4 and PCN-S. Gray, blue, and orange balls are C, N, and P, respectively. **(c)** UV−vis diffusion reflectance spectra of as-prepared photocatalysts (CN-B: bulk g-C_3N_4; CN-S: g-C_3N_4 nanosheets). **(d)** TDOS and **(e)** PDOS of ideal g-C_3N_4 and P-doped g-C_3N_4. [58]

2.2.3.5. Other doping

Halogen-doping (F, Cl, I, Br) has also attracted worldwide research interest.[64] Zhu et al. performed the DFT calculations to study how halogen doping affects the electronic structure, light absorption, and work function of g-C_3N_4. [64] By calculating the formation energy of the five possible doping positions and one interstitial position, the author claimed that both of F and Cl prefer to occupy the interstitial space due to the positive and large formation energy in

the original C/N positions. Compared to Cl, F is more easily to be doped into g-C_3N_4 matrix because of its smaller atomic radii. A similar observation is witnessed by the much larger Br and I atoms with a positive formation energy of 3.67 and 3.36 eV. The bandgaps, in increasing order, are F-C_3N_4 (0.64 eV), I-C_3N_4 (0.95 eV), Br-C_3N_4 (1.13 eV), and Cl-C_3N_4 (1.14 eV), which are smaller than that of bulk g-C_3N_4 (1.18 eV). This implies an enhanced visible light absorption, which benefits the utilization of solar energy. Moreover, the reduced work functions of halogen-doped g-C_3N_4 indicate that uplifted Fermi levels and facilitate electron transfer from the g-C_3N_4 surface, leading to a boosted charge transfer process. The experimental research work reported in recent years agree well with this founding, implying the promising applications of halogen-doping on g-C_3N_4 for improving the photocatalytic performance.[65,66,65,67]

2.2.3.6. Vacancies

Similar to dopants, vacancies, both C and N vacancies, are able to tune the electronic structure and the photocarrier transfer properties of g-C_3N_4.[68,69,70,71] The N vacant g-C_3N_4 was first synthesized by Liu et al. via annealing dicyandiamide in an opened crucible at 550-600°C for 4h.[72] The XPS result indicated N vacancies prefer to appear in the two-coordinated N sites (N_{2c}) because of their unsaturated coordination and higher amount (**Figure 2. 9a**). The resultant N vacant g-C_3N_4 exhibited a slightly narrower bandgap (2.66 eV vs. 2.74 eV) and extended visible light absorption in the range of 450-600 nm due to the existence of C^{3+} states in the bandgap. Furthermore, the recombination process of electron-hole pairs was suppressed with the decreasing short-lived photocarriers and increasing long-lived photocarriers, respectively.

Therefore, enhanced photocatalytic performance on producing OH radials and photodegradation of Rhodamine B (RhB) was obtained.

Another similar research is the C vacant g-C_3N_4 (Cv-gCN) synthesized by simply annealing the mixture of bulk g-C_3N_4 and $NaHCO_3$ at 550°C for 2 h.[73] The successful formation of C vacancies can be confirmed by the electron paramagnetic resonance (EPR) with a reduced intensity at g=2.0043, resulting from the decreased unpaired electrons on the C atoms of the tri-s-triazine. According to the DFT calculations, Cv-gCN displays a larger bandgap of 1.395 eV than bulk g-C_3N_4 of 1.175eV, leading to inferior visible light absorption. The experimental result keeps good in accordance with this, mainly due to the QCE. Notably, the C vacancies uplift the CBM of Cv-gCN, which could generate much more active $O_2^{\cdot-}$ radicals to remove the toxic NO pollutant (**Figure 2. 9b**).

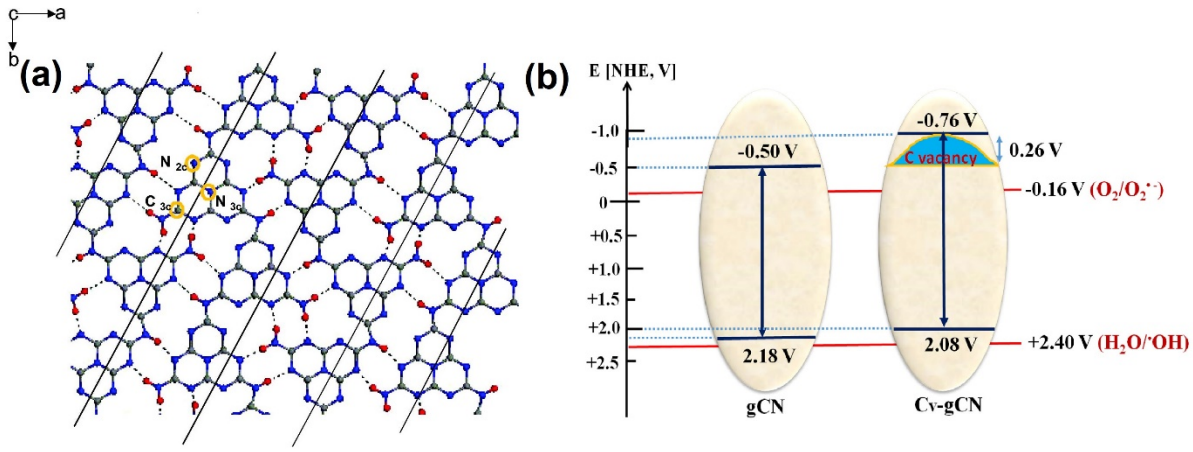

Figure 2.9 (a) DFT calculation model of C vacant g-C_3N_4 (N_{2c}, N_{3c}, and C_{3c} indicate two-coordinated N, three-coordinated N, and three-coordinated C). [72] **(b)** Comparison of the band structures of g-C_3N_4 before and after the introduction of C vacancy.[73]

2.2.4. Development of hybrid coupling on g-C_3N_4

Apart from morphology and defect engineering, coupling g-C_3N_4 with other semiconductors, metals, or carbonaceous materials is another effective approach to boost the photocarrier separation and suppress the recombination of photocarriers.[74] One typical example of hybrid structure is the MP_x (M=Fe, Co, or Ni)/g-C_3N_4/MoS_2 heterojunctions, which MoS_2 was designed to act as a cocatalyst while MP_X as an interfacial electronic bridge to facilitate the charge transfer process.[75] The heterojunctions were prepared by a phosphorization of MP_x on the surface of g-C_3N_4, followed by a physical mixing with MoS_2 nanosheets under ultra-sonication (**Figure 2. 10a**). When irradiated under simulated light, g-C_3N_4-1%Ni_2P-1.5% MoS_2 shows the highest H_2 evolution rate of 532.4 μmol h^{-1} g^{-1} and a high AQE (apparent quantum efficiency) of 1.45% at 405 nm (**Figure 2. 10b-d**).

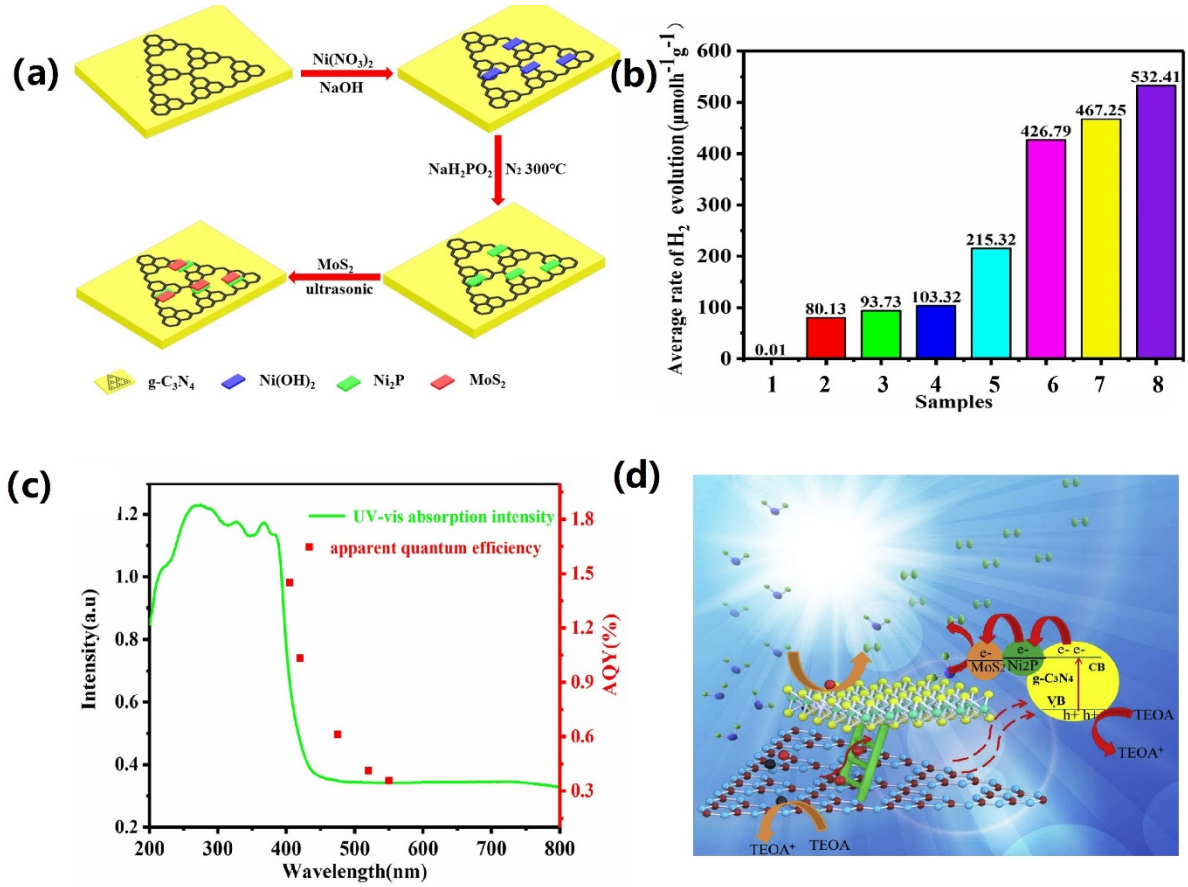

Figure 2.10 (a) Synthetic diagram of tenary g-C_3N_4/MPx/MoS_2. **(b)** Hydrogen evolution rate of (1) g-C_3N_4, (2) g-C_3N_4-1%Fe_2P, (3) g-C_3N_4-1%CoP, (4) g-C_3N_4-1%Ni_2P (5)g-C_3N_4-1.5%MoS_2, (6) g-C_3N_4-1%Fe_2P-1.5%MoS_2, (7) g-C_3N_4-1%CoP-1.5%MoS_2, (8) g-C_3N_4-1%Ni_2P- 1.5%MoS_2. **(c)** AQE of g-C_3N_4-1%Ni_2P-1.5% MoS_2. **(d)** Schematic representation of photocatalytic H_2 evolution reaction over ternary g-C_3N_4-Ni_2P-MoS_2 photocatalyst.[75]

In order to enhance the long-wavelength light absorption of g-C_3N_4, a series of broadband response semiconductor have been synthesized to constructing the hybrid structures, including the Ag_2O/g-C_3N_4[76], Sb_2S_3/g-C_3N_4/g-C_3N_4 quantum dots,[77] BiOBr/carbon dots/g-C_3N_4,[78] g-C_3N_4/Cs_xWO_3 [79] as well as upconversion nanoparticles with g-C_3N_4 materials.[80,81,82]

2.3. g-C_3N_4 derivatives for other energy applications

As is known to all that g-C_3N_4 consists of earth-abundant C, N elements, which has been demonstrated to be a precursor for the N-doped carbon materials at high temperature due to the similarity between g-C_3N_4 and graphene.[82] The doped N can manipulate the electronic structure of adjacent carbon atoms and cause charge redistribution, which is widely introduced into carbon matrix and used in many research fields such as fuel cells, [83] Zn-air batteries, [84], and water splitting.[85] In addition, due to the N=C-N in the tri-s-triazine units, metal-N might be formed in high temperature annealing,[86,87] and thus metal nitrides can be used in batteries applications.[88] The typical examples are introduced as follows:

2.3.1. Zn-air batteries

Since the pioneering work by Dai and co-workers in 2009,[89] the oxygen electrocatalysis has attracted extensive research attention. As g-C_3N_4 contains N and C, and shares similarities with graphene, and thus N-doped carbon and metal carbides can be obtained in higher annealing temperature. The N atoms are able to tune the electronic structure of their adjacent carbon atoms and induce the charge distribution. As a result, the electrocatalytic performance on oxygen evolution and reduction is significantly improved. Niu et al. proposed a novel method to obtain the Fe_7C_3 nanoparticles embedded in an interconnected porous graphene-like Fe-/N-doped carbon matrix (Fe_7C_3@FeNC).[88] Particularly, g-C_3N_4 was used as the sacrificial template and dopamine was used mainly as the carbon sources. After the self-assembly process and high temperature annealing, Fe and N-doped carbon were achieved as a supporting matrix, while Fe_3C_3 as dispersing co-catalyst (**Figure 2. 11a**). As is seen from Figure 2. 11b, the Fe_7C_3

nanoparticles were covered by the multiple layers of carbon (**Figure 2. 11b**). When testing its oxygen evolution reaction (OER) and oxygen reduction reaction (ORR) performance in alkaline solution, the Fe_7N_3@FeNC electrode showed a low overpotential of 358 mV for reaching the current density of 10 mA cm^{-2} and an impressive halfwave potential of 0.83 V, respectively. Liu and co-workers employed dicyandiamide as a precursor and polymerized dopamine as a carbon source to obtain a series of DA-derived graphene-like carbon nanosheets (DCN-T, T indicates temperature ranging from 800-1100° C, **Figure 2. 11c**).[90] The controlled sample PDCN-1000 used polydopamine instead of dopamine as a carbon source. Compared to PDCN-1000, DCN-1000 shows a thinner carbon nanosheets structure of only 0.6-2 nm, indicating dopamine is easier to carbonized and confined by the plate-like g-C_3N_4. With an N-doping level of 20.1%, DCN-800 exhibits the best ORR activity with the lowest overpotential and highest diffusion limit the current density of 4.23 mA cm^{-2} (**Figure 2. 11d**). Zhang et al. presented the important role of the N-C catalyst for Zn-air batteries by pyrolyzing g-C_3N_4 embedded in carbon.[91] The template g-C_3N_4 decomposed at high annealing temperature and release NH_3 to assist the N-doping, leaving its original position with pores, which can be seen on **Figure 2. 11e**.[91] Further modification with Fe metals rendered the formation of Fe and N-doped carbon materials (Fe-N-C), and the authors tested the corresponding Zn-air batteries performance in comparison with N-C (**Figure 2. 11f-g**). Obviously, Fe-N-C electrodes show both suppressed polarization and higher power density than N-C, indicating metal-N might be superior over pure N-doped carbon materials.

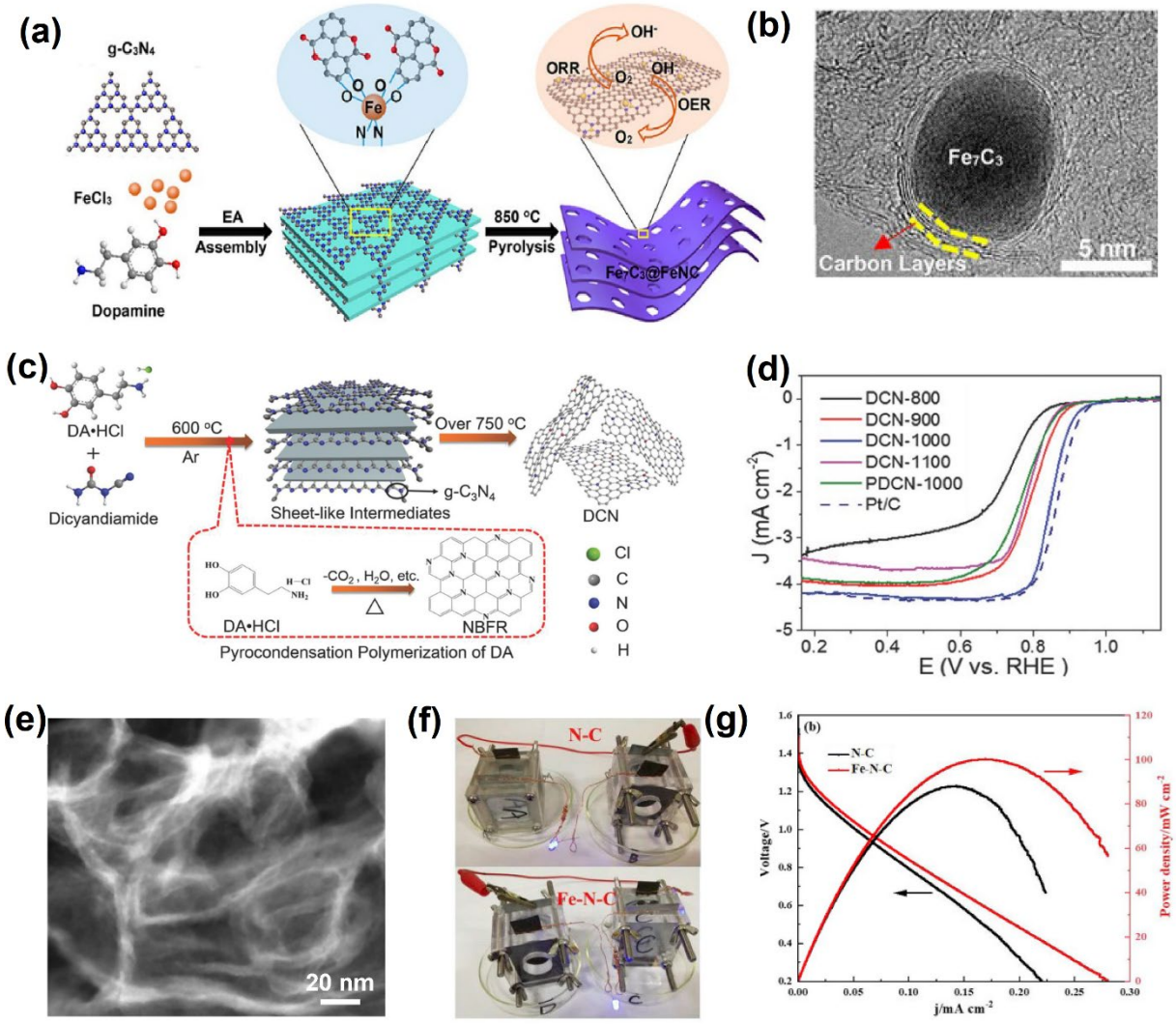

Figure 2.11 **(a)** Synthetic diagram of Fe_7N_3@FeNC, and **(b)** HR-TEM diagram of Fe_7N_3@FeNC.[88] **(c)** Synthetic routine of DCN and **(d)** linear sweep voltammetry (LSV) of DCN-T and Pt/C.[90] **(e)** TEM of Fe-N-C, **(f)** digital photos, and **(g)** polarization and power density curves of Fe-N-C and N-C. [91]

2.3.2. Metal (lithium, sodium) ion batteries

Metal (lithium, sodium) ion batteries are among the best cost-effective energy storage applications as the abundant Na and Li resources in the earth.[92] Graphite has been the widely investigated anode as its interlayer space can accommodate Li-ion. However, its limited

interlayer distance (～0.34 nm) fails to provide enough space for Na ion.[93] Thus advanced materials with expanded interlayer distance have gained enormous attention. Hou and his colleagues have found that P-doped carbon nanosheet can reach an expanded interlayer spacing of 0.42 nm, allowing for the insertion of Na ion with good rate performance and excellent cycling stability.[94] Inspired by this, Qiao's group successfully tune the expanded N-rich few-layer graphene (N-FLG) with a large interlayer distance of 0.51 nm by annealing g-C_3N_4 and Zn catalyst at 800° C (**Figure 2. 12a**).[7] The annealing temperature was optimized with the largest interlayer distance and N content of 19.3 at. % with highest pyrrolic N. More significantly, comparing to the pyridinic N, pyrrolic N owns superiority on expanding interlayer spacing as the lone pair of electrons perpendicular to the graphene layer (**Figure 2. 12b-c**). When testing the rate performance, N-FLG-800 shows the highest discharge capacity of 264.3 mA h g^{-1} at 0.1 C and excellent capacity to recover ability (**Figure 2. 12d**). Recently, Tang et al. reported a similar experiment that employed g-C_3N_4 and polypyrrole as the N source and template. After template removal, mesoporous N-doped graphene-like carbon was obtained, showing the wrinkle-shape (**Figure 2. 12e**).[95] The counter sample was PDC, which was synthesized without g-C_3N_4 template, showing dramatically reduced N content from 17.54% to 7.57 %. Although both samples show similar N 1s XPS spectra (**Figure 2. 12f**), NGC shows almost twice the discharge capacity than PDC when testing their lithium-ion battery performance **(Figure 2. 12g-h)**.

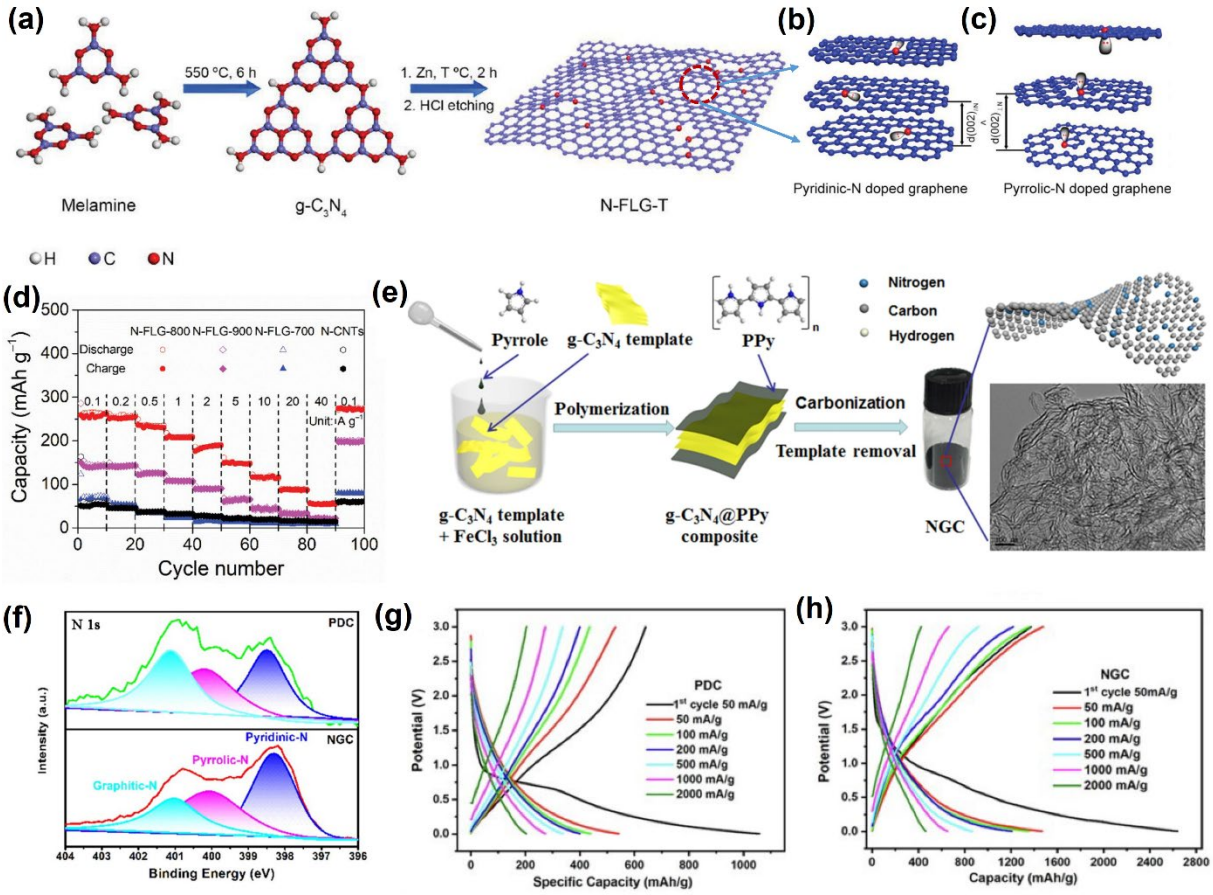

Figure 2.12 (a) Preparation of N-FLG-T (T indicates temperature), schematic illustration for the effect of **(b)** pyridinic and **(c)** pyrrolic N on the enlargement of graphene interlayer distance, **(d)** rate performance of N-FLG-T and N-doped carbon nanotubes (N-CNTs). [7] **(e)** Synthesis of NGC, **(f)** XPS comparison, discharge-charge plots of **(g)** PDC and **(h)** NGC. [95]

2.3.3. Li-S batteries

Apart from the traditional metal ion batteries and Zn-air batteries, Li-S batteries have attracted worldwide attention due to their high theoretical capacity (1673 mA h g^{-1}) and energy density.[96] However, Li-S batteries have met great challenges such as fast capacity fading, inferior rate performance, as well as low Coulombic efficiency. The main reason is the notorious "shuttling effect" of lithium polysulfides (LiPS).[97] The most effective approach is to construct advanced

polar cathode materials with strong physical and chemical trapping ability to LiPS.[98] The polar materials include heteroatom doped carbon materials, metal oxides, metal sulfides, metal cluster, metal nitrides and so on.[99]

Metal nitrides such as TiN, VN, GaN have been successfully obtained by employing the g-C_3N_4 as N precursor and their M-$(OEt)_4$ or MCl_6 as metallic source followed by a high temperature annealing. [87] The most represented work was carried out by Thomas'ss group which using hard template-derived mesoporous g-C_3N_4 as a structure confined agent. After the filling of $Ti(OEt)_4$/ethanol solution and followed air hydrolysis into g-C_3N_4, the mixture was heated at 800° C and TiN/C was finally obtained (**Figure 2. 13a**).[87] As seen from the HR-TEM images in Figure 2. 13b,c, we can observe the successful morphology reserve of ordered mesoporous g-C3N4 for TiN/C composites (**Figure 2. 13b, c**). Recently, it is very exciting to found reports on TiN toward Li-S batteries. One typical synthetic strategy is that using the resorcinol formaldehyde-derived carbon (RF) as a supporting matrix to absorb titanium tetraisopropoxide to load TiO_2 nanoparticles. [100] After an NH_3 nitridation and S infiltration, finally, the RF-TiN was obtained with abundant pores (**Figure 2. 13d**). The loading of TiN is extremely beneficial to the improvement of Li-S batteries performance, as reflected by the enhanced discharge capacity (**Figure 2. 13e**) and excellent rate performance (**Figure 2. 13f**). The enhancement battery performance of S@RF-TiN is not only due to the appearance of TiN but the overall architecture, as the barely S@TiN nanoparticles (S@TiN-NP) show an inferior batteries performance (**Figure 2. 13e**).

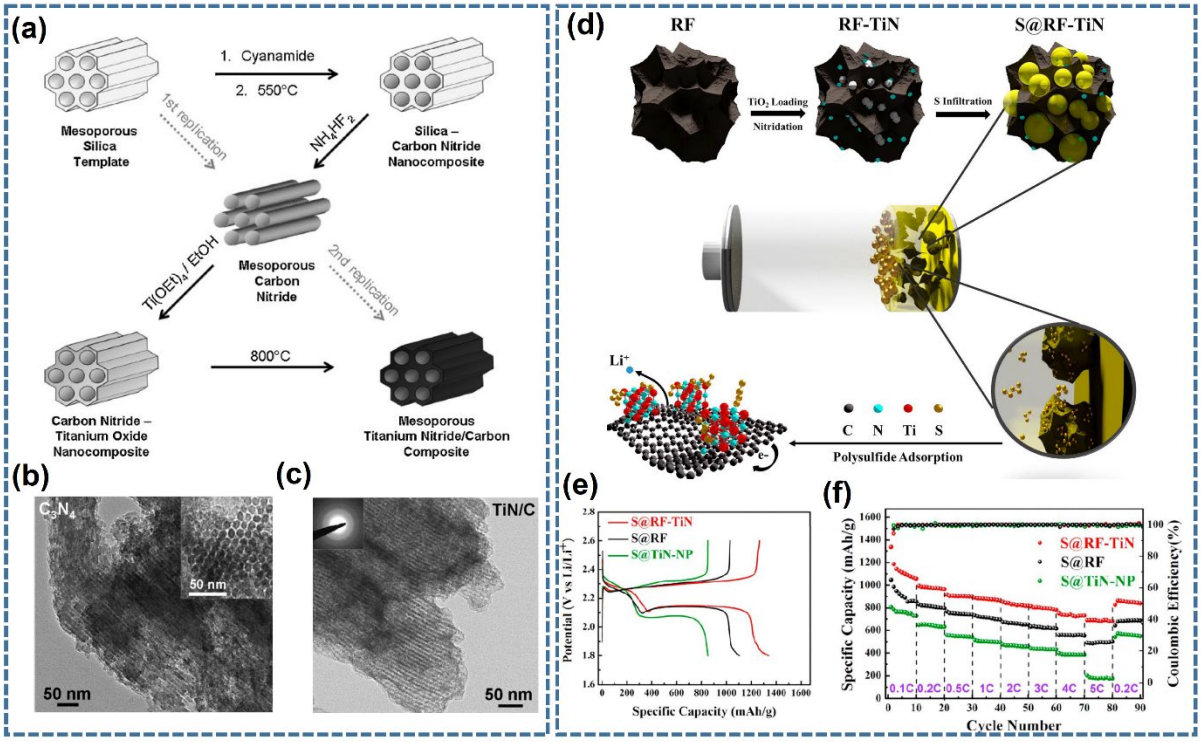

Figure 2.13 (a) Schematic for the synthesis of TiN/C using g-C_3N_4 as a template, TEM images of **(b)** g-C_3N_4 and **(c)** TiN/C. [87] **(d)** Schematic for the synthesis of S@RF-TiN, **(e)** discharge and charge plots and **(f)** rate performance and Coulombic efficiency of S@RF-TiN, S@RF, and S@TiN-NP.[100]

Considering most of these g-C_3N_4 derivatives, particularly metallic nitrides, have been reported with higher electron conductivity, higher polarity, and considerably excellent electrocatalytic activity. [100] All these merits satisfy the requirements of the cathodic sulfur materials for the blooming research area of Li-S batteries: 1) good conductivity to optimize the insulating property of sulfur; 2) high polarity to efficiently trap the diffused lithium polysulfide and improve the cycling performance; 3) excellent catalytic performance to boost the conversion between S and Li_2S. Thus, applying the g-C_3N_4 derivatives as the cathodic sulfur hosts in Li-S batteries might provide people with new thinking on the electrochemical energy

conversion and storage technology.

2.4. Conclusion

Based on the above literature review, one can learn that the photocatalytic of g-C_3N_4-based materials can be optimized via structure modification, defect engineering, as well as hybrid coupling. While its derivatives, such as heteroatom-doped carbon, metallic carbides, and metallic nitrides, are promising materials for electrochemical energy storage and conversion applications. Particularly, metallic nitrides are excellent candidates for future cathode materials for Li-S batteries. The following research work was inspired by the above literature analysis, and both photocatalytic H_2 evolution and Li-S batteries on g-C_3N_4 and its derivatives would be introduced separately.

2.5. References

(1) Bruce, P. G.; Freunberger, S. A.; Hardwick, L. J.; Tarascon, J. M. Li-O_2 and Li-S Batteries with High Energy Storage. *Nat. Mater.* **2012**, *11* (1), 19–29.

(2) Suzuki, M. Identifying Roles of International Institutions in Clean Energy Technology Innovation and Diffusion in the Developing Countries: Matching Barriers with Roles of the Institutions. *J. Clean. Prod.* **2015**, *98*, 229–240.

(3) Bosetti, V.; Lubowski, R.; Golub, A.; Markandya, A. Linking Reduced Deforestation and a Global Carbon Market: Implications for Clean Energy Technology and Policy Flexibility. *Environ. Dev. Econ.* **2011**, *16* (4), 479–505.

(4) Cortright, R. D.; Davda, R. R.; Dumesic, J. A. Hydrogen from Catalytic Reforming of

Biomass-Derived Hydrocarbons in Liquid Water. *Nature* **2002**, *418* (6901), 964–967.

(5) Yoshino, A. 1 - Development of the Lithium-Ion Battery and Recent Technological Trends; Pistoia, G. B. T.-L.-I. B., Ed.; Elsevier: Amsterdam, 2014; pp 1–20.

(6) Ong, C. B.; Ng, L. Y.; Mohammad, A. W. A Review of ZnO Nanoparticles as Solar Photocatalysts: Synthesis, Mechanisms and Applications. *Renew. Sustain. Energy Rev.* **2018**, *81*, 536–551.

(7) Liu, J.; Zhang, Y.; Zhang, L.; Xie, F.; Vasileff, A.; Qiao, S. Graphitic Carbon Nitride ($g\text{-}C_3N_4$)-Derived N-Rich Graphene with Tuneable Interlayer Distance as a High-Rate Anode for Sodium-Ion Batteries. *Adv. Mater.* **2019**, *31* (24), 1901261.

(8) Ye, C.; Jiao, Y.; Jin, H.; Slattery, A. D.; Davey, K.; Wang, H.; Qiao, S. 2D MoN-VN Heterostructure To Regulate Polysulfides for Highly Efficient Lithium-Sulfur Batteries. *Angew. Chemie Int. Ed.* **2018**, *57* (51), 16703–16707.

(9) Fujishima, A.; Honda, K. Electrochemical Photolysis of Water at a Semiconductor Electrode. *Nature* **1972**, *238* (5358), 37–38. https://doi.org/10.1038/238037a0.

(10) Daghrir, R.; Drogui, P.; Robert, D. Modified TiO_2 for Environmental Photocatalytic Applications: A Review. *Ind. Eng. Chem. Res.* **2013**, *52* (10), 3581–3599.

(11) Zong, X.; Yan, H.; Wu, G.; Ma, G.; Wen, F.; Wang, L.; Li, C. Enhancement of Photocatalytic H_2 Evolution on CdS by Loading MoS_2 as Cocatalyst under Visible Light Irradiation. *J. Am. Chem. Soc.* **2008**, *130* (23), 7176–7177.

(12) Hara, M.; Takata, T.; Kondo, J. N.; Domen, K. Photocatalytic Reduction of Water by TaON under Visible Light Irradiation. *Catal. Today* **2004**, *90* (3–4), 313–317.

(13) Yu, H.; Shi, R.; Zhao, Y.; Waterhouse, G. I. N.; Wu, L.; Tung, C.; Zhang, T. Smart

Utilization of Carbon Dots in Semiconductor Photocatalysis. *Adv. Mater.* **2016**, *28* (43), 9454–9477.

(14) Han, M.; Zhu, S.; Lu, S.; Song, Y.; Feng, T.; Tao, S.; Liu, J.; Yang, B. Recent Progress on the Photocatalysis of Carbon Dots: Classification, Mechanism and Applications. *Nano Today* **2018**, *19*, 201–218.

(15) Li, Q.; Guo, B.; Yu, J.; Ran, J.; Zhang, B.; Yan, H.; Gong, J. R. Highly Efficient Visible-Light-Driven Photocatalytic Hydrogen Production of CdS-Cluster-Decorated Graphene Nanosheets. *J. Am. Chem. Soc.* **2011**, *133* (28), 10878–10884.

(16) Zhang, H.; Zong, R.; Zhu, Y. Photocorrosion Inhibition and Photoactivity Enhancement for Zinc Oxide via Hybridization with Monolayer Polyaniline. *J. Phys. Chem. C* **2009**, *113* (11), 4605–4611.

(17) Huang, M.; Yu, J.; Deng, C.; Huang, Y.; Fan, M.; Li, B.; Tong, Z.; Zhang, F.; Dong, L. 3D Nanospherical $Cd_xZn_{1-x}S$/Reduced Graphene Oxide Composites with Superior Photocatalytic Activity and Photocorrosion Resistance. *Appl. Surf. Sci.* **2016**, *365*, 227–239.

(18) Dong, Y.; Wang, R.; Li, H.; Shao, J.; Chi, Y.; Lin, X.; Chen, G. Polyamine-Functionalized Carbon Quantum Dots for Chemical Sensing. *Carbon N. Y.* **2012**, *50* (8), 2810–2815.

(19) Wang, X.; Maeda, K.; Thomas, A.; Takanabe, K.; Xin, G.; Carlsson, J. M.; Domen, K.; Antonietti, M. A Metal-Free Polymeric Photocatalyst for Hydrogen Production from Water under Visible Light. *Nat. Mater.* **2009**, *8* (1), 76–80.

(20) Zhang, J.; Sun, J.; Maeda, K.; Domen, K.; Liu, P.; Antonietti, M.; Fu, X.; Wang, X.

Sulfur-Mediated Synthesis of Carbon Nitride: Band-Gap Engineering and Improved Functions for Photocatalysis. *Energy Environ. Sci.* **2011**, *4* (3), 675–678.

(21) Chen, S.; Takata, T.; Domen, K. Particulate Photocatalysts for Overall Water Splitting. *Nat. Rev. Mater.* **2017**, *2* (10), 17050.

(22) Yang, J.; Wang, D.; Han, H.; Li, C. Roles of Cocatalysts in Photocatalysis and Photoelectrocatalysis. *Acc. Chem. Res.* **2013**, *46* (8), 1900–1909.

(23) Ong, W.-J. J.; Tan, L.-L. L.; Ng, Y. H.; Yong, S.-T. T.; Chai, S.-P. P. Graphitic Carbon Nitride (g-C_3N_4)-Based Photocatalysts for Artificial Photosynthesis and Environmental Remediation: Are We a Step Closer to Achieving Sustainability? *Chem. Rev.* **2016**, *116* (12), 7159–7329.

(24) Yang, S.; Gong, Y.; Zhang, J.; Zhan, L.; Ma, L.; Fang, Z.; Vajtai, R.; Wang, X.; Ajayan, P. M. Exfoliated Graphitic Carbon Nitride Nanosheets as Efficient Catalysts for Hydrogen Evolution under Visible Light. *Adv. Mater.* **2013**, *25* (17), 2452–2456.

(25) Zhang, X.; Xie, X.; Wang, H.; Zhang, J.; Pan, B.; Xie, Y. Enhanced Photoresponsive Ultrathin Graphitic-Phase C3N4 Nanosheets for Bioimaging. *J. Am. Chem. Soc.* **2013**, *135* (1), 18–21.

(26) Yuan, Y. J.; Shen, Z.; Wu, S.; Su, Y.; Pei, L.; Ji, Z.; Ding, M.; Bai, W.; Chen, Y.; Yu, Z. T.; et al. Liquid Exfoliation of g-C_3N_4 Nanosheets to Construct 2D-2D MoS_2/g-C_3N_4 Photocatalyst for Enhanced Photocatalytic H_2 Production Activity. *Appl. Catal. B Environ.* **2019**, *246*, 120–128.

(27) Zhang, J.; Guo, F.; Wang, X. An Optimized and General Synthetic Strategy for Fabrication of Polymeric Carbon Nitride Nanoarchitectures. *Adv. Funct. Mater.* **2013**,

23 (23), 3008–3014.

(28) Zheng, D.; Huang, C.; Wang, X. Post-Annealing Reinforced Hollow Carbon Nitride Nanospheres for Hydrogen Photosynthesis. *Nanoscale* **2015**, *7* (2), 465–470.

(29) Jun, Y.; Lee, E. Z.; Wang, X.; Hong, W. H.; Stucky, G. D.; Thomas, A. From Melamine-cyanuric Acid Supramolecular Aggregates to Carbon Nitride Hollow Spheres. *Adv. Funct. Mater.* **2013**, *23* (29), 3661–3667.

(30) Li, X.-H.; Zhang, J.; Chen, X.; Fischer, A.; Thomas, A.; Antonietti, M.; Wang, X. Condensed Graphitic Carbon Nitride Nanorods by Nanoconfinement: Promotion of Crystallinity on Photocatalytic Conversion. *Chem. Mater.* **2011**, *23* (19), 4344–4348.

(31) Sun, J.; Zhang, J.; Zhang, M.; Antonietti, M.; Fu, X.; Wang, X. Bioinspired Hollow Semiconductor Nanospheres as Photosynthetic Nanoparticles. *Nat. Commun.* **2012**, *3* (1), 1–7.

(32) Yan, H. Soft-Templating Synthesis of Mesoporous Graphitic Carbon Nitride with Enhanced Photocatalytic H_2 Evolution under Visible Light. *Chem. Commun.* **2012**, *48* (28), 3430–3432.

(33) Wang, Y.; Zhang, J.; Wang, X.; Antonietti, M.; Li, H. Boron-and Fluorine-containing Mesoporous Carbon Nitride Polymers: Metal-free Catalysts for Cyclohexane Oxidation. *Angew. Chemie Int. Ed.* **2010**, *49* (19), 3356–3359.

(34) Yuan, B.; Chu, Z.; Li, G.; Jiang, Z.; Hu, T.; Wang, Q.; Wang, C. Water-Soluble Ribbon-like Graphitic Carbon Nitride (g-C_3N_4): Green Synthesis, Self-Assembly and Unique Optical Properties. *J. Mater. Chem. C* **2014**, *2* (39), 8212–8215.

(35) Wirnhier, E.; Döblinger, M.; Gunzelmann, D.; Senker, J.; Lotsch, B. V; Schnick, W.

Poly (Triazine Imide) with Intercalation of Lithium and Chloride Ions [$(C_3N_3)_2$ (NH_xLi_{1-x}) 3· LiCl]: A Crystalline 2D Carbon Nitride Network. *Chem. Eur. J.* **2011**, *17* (11), 3213–3221.

(36) He, F.; Chen, G.; Yu, Y.; Zhou, Y.; Zheng, Y.; Hao, S. The Sulfur-Bubble Template-Mediated Synthesis of Uniform Porous GC 3 N 4 with Superior Photocatalytic Performance. *Chem. Commun.* **2015**, *51* (2), 425–427.

(37) Wu, X.; Gao, D.; Wang, P.; Yu, H.; Yu, J. NH_4Cl-Induced Low-Temperature Formation of Nitrogen-Rich g-C_3N_4 Nanosheets with Improved Photocatalytic Hydrogen Evolution. *Carbon N. Y.* **2019**, *153*, 757–766.

(38) Gao, X.; Feng, J.; Su, D.; Ma, Y.; Wang, G.; Ma, H.; Zhang, J. In-Situ Exfoliation of Porous Carbon Nitride Nanosheets for Enhanced Hydrogen Evolution. *Nano Energy* **2019**, *59*, 598–609.

(39) Niu, P.; Zhang, L.; Liu, G.; Cheng, H. M. Graphene-like Carbon Nitride Nanosheets for Improved Photocatalytic Activities. *Adv. Funct. Mater.* **2012**, *22* (22), 4763–4770.

(40) Li, H.-J.; Sun, B.-W.; Sui, L.; Qian, D.-J.; Chen, M. Preparation of Water-Dispersible Porous g-C3N4 with Improved Photocatalytic Activity by Chemical Oxidation. *Phys. Chem. Chem. Phys.* **2015**, *17* (5), 3309–3315.

(41) Shi, L.; Chang, K.; Zhang, H.; Hai, X.; Yang, L.; Wang, T.; Ye, J. Drastic Enhancement of Photocatalytic Activities over Phosphoric Acid Protonated Porous g-C_3N_4 Nanosheets under Visible Light. *Small* **2016**, *12* (32), 4431–4439.

(42) Ma, X.; Lv, Y.; Xu, J.; Liu, Y.; Zhang, R.; Zhu, Y. A Strategy of Enhancing the Photoactivity of G-C3N4 via Doping of Nonmetal Elements: A First-Principles Study.

J. Phys. Chem. C **2012**, *116* (44), 23485–23493.

(43) Dong, G.; Zhao, K.; Zhang, L. Carbon Self-Doping Induced High Electronic Conductivity and Photoreactivity of g-C_3N_4. *Chem. Commun.* **2012**, *48* (49), 6178–6180.

(44) Mohamed, M. A.; Zain, M. F. M.; Minggu, L. J.; Kassim, M. B.; Amin, N. A. S.; Salleh, W. N. W.; Salehmin, M. N. I.; Nasir, M. F. M.; Hir, Z. A. M. Constructing Bio-Templated 3D Porous Microtubular C-Doped g-C_3N_4 with Tunable Band Structure and Enhanced Charge Carrier Separation. *Appl. Catal. B Environ.* **2018**, *236*, 265–279.

(45) Cao, S.; Zhou, N.; Gao, F.; Chen, H.; Jiang, F. All-Solid-State Z-Scheme 3,4-Dihydroxybenzaldehyde-Functionalized Ga2O3/Graphitic Carbon Nitride Photocatalyst with Aromatic Rings as Electron Mediators for Visible-Light Photocatalytic Nitrogen Fixation. *Appl. Catal. B Environ.* **2017**, *218*, 600–610.

(46) Chen, Y.; Wang, B.; Lin, S.; Zhang, Y.; Wang, X. Activation of N→ π* Transitions in Two-Dimensional Conjugated Polymers for Visible Light Photocatalysis. *J. Phys. Chem. C* **2014**, *118* (51), 29981–29989.

(47) Jorge, A. B.; Martin, D. J.; Dhanoa, M. T. S.; Rahman, A. S.; Makwana, N.; Tang, J.; Sella, A.; Corà, F.; Firth, S.; Darr, J. A. H_2 and O_2 Evolution from Water Half-Splitting Reactions by Graphitic Carbon Nitride Materials. *J. Phys. Chem. C* **2013**, *117* (14), 7178–7185.

(48) Da Silva, E. S.; Moura, N. M. M.; Coutinho, A.; Dražić, G.; Teixeira, B. M. S.; Sobolev, N. A.; Silva, C. G.; Neves, M. G. P. M. S.; Prieto, M.; Faria, J. L. B-Cyclodextrin as a Precursor to Holey C-Doped g-C_3N_4 Nanosheets for Photocatalytic Hydrogen Generation. *ChemSusChem* **2018**, *11* (16), 2681–2694.

(49) Li, J.; Shen, B.; Hong, Z.; Lin, B.; Gao, B.; Chen, Y. A Facile Approach to Synthesize Novel Oxygen-Doped g-C_3N_4 with Superior Visible-Light Photoreactivity. *Chem. Commun.* **2012**, *48* (98), 12017–12019.

(50) Huang, Z.-F. F.; Song, J.; Pan, L.; Wang, Z.; Zhang, X. X.; Zou, J.-J. J.; Mi, W.; Zhang, X. X.; Wang, L. Carbon Nitride with Simultaneous Porous Network and O-Doping for Efficient Solar-Energy-Driven Hydrogen Evolution. *Nano Energy* **2015**, *12*, 646–656.

(51) Liu, G.; Niu, P.; Sun, C.; Smith, S. C.; Chen, Z.; Lu, G. Q.; Cheng, H.-M. M. Unique Electronic Structure Induced High Photoreactivity of Sulfur-Doped Graphitic g-C_3N_4. *J. Am. Chem. Soc.* **2010**, *132* (33), 11642–11648.

(52) Wang, K.; Li, Q.; Liu, B.; Cheng, B.; Ho, W.; Yu, J. Sulfur-Doped g-C_3N_4 with Enhanced Photocatalytic CO_2-Reduction Performance. *Appl. Catal. B Environ.* **2015**, *176–177*, 44–52.

(53) Ge, L.; Han, C.; Xiao, X.; Guo, L.; Li, Y. Enhanced Visible Light Photocatalytic Hydrogen Evolution of Sulfur-Doped Polymeric g-C_3N_4 Photocatalysts. *Mater. Res. Bull.* **2013**, *48* (10), 3919–3925.

(54) Lu, C.; Zhang, P.; Jiang, S.; Wu, X.; Song, S.; Zhu, M.; Lou, Z.; Li, Z.; Liu, F.; Liu, Y.; et al. Photocatalytic Reduction Elimination of UO_2^{2+} Pollutant under Visible Light with Metal-Free Sulfur Doped g-C_3N_4 Photocatalyst. *Appl. Catal. B Environ.* **2017**, *200*, 378–385.

(55) Ke, L.; Li, P.; Wu, X.; Jiang, S.; Luo, M.; Liu, Y.; Le, Z.; Sun, C.; Song, S. Graphene-like Sulfur-Doped g-C_3N_4 for Photocatalytic Reduction Elimination of UO_2^{2+} under Visible Light. *Appl. Catal. B Environ.* **2017**, *205*, 319–326.

(56) Sun, C.; Zhang, H.; Liu, H.; Zheng, X.; Zou, W.; Dong, L.; Qi, L. Enhanced Activity of Visible-Light Photocatalytic H_2 Evolution of Sulfur-Doped g-C_3N_4 Photocatalyst via Nanoparticle Metal Ni as Cocatalyst. *Appl. Catal. B Environ.* **2018**, *235*, 66–74.

(57) Zhou, Y.; Zhang, L.; Liu, J.; Fan, X.; Wang, B.; Wang, M.; Ren, W.; Wang, J.; Li, M.; Shi, J. Brand New P-Doped g-C_3N_4: Enhanced Photocatalytic Activity for H_2 Evolution and Rhodamine B Degradation under Visible Light. *J. Mater. Chem. A* **2015**, *3* (7), 3862–3867.

(58) Ran, J.; Ma, T. Y.; Gao, G.; Du, X. W.; Qiao, S. Z. Porous P-Doped Graphitic Carbon Nitride Nanosheets for Synergistically Enhanced Visible-Light Photocatalytic H_2 Production. *Energy Environ. Sci.* **2015**, *8* (12), 3708–3717.

(59) Zhou, Y.; Zhang, L.; Huang, W.; Kong, Q.; Fan, X.; Wang, M.; Shi, J. N-Doped Graphitic Carbon-Incorporated g-C_3N_4 for Remarkably Enhanced Photocatalytic H_2 Evolution under Visible Light. *Carbon N. Y.* **2016**, *99*, 111–117.

(60) She, X.; Liu, L.; Ji, H.; Mo, Z.; Li, Y.; Huang, L.; Du, D.; Xu, H.; Li, H. Template-Free Synthesis of 2D Porous Ultrathin Nonmetal-Doped g-C_3N_4 Nanosheets with Highly Efficient Photocatalytic H_2 Evolution from Water under Visible Light. *Appl. Catal. B Environ.* **2016**, *187*, 144–153.

(61) Hong, Y.; Liu, E.; Shi, J.; Lin, X.; Sheng, L.; Zhang, M.; Wang, L.; Chen, J. A Direct One-Step Synthesis of Ultrathin g-C_3N_4 Nanosheets from Thiourea for Boosting Solar Photocatalytic H_2 Evolution. *Int. J. Hydrogen Energy* **2019**, *44* (14), 7194–7204.

(62) Yang, J.; Liang, Y.; Li, K.; Yang, G.; Wang, K.; Xu, R.; Xie, X. One-Step Synthesis of Novel K^+ and Cyano Groups Decorated Triazine-/Heptazine-Based g-C_3N_4 Tubular

Homojunctions for Boosting Photocatalytic H_2 Evolution. *Appl. Catal. B Environ.* **2020**, *262*, 118252.

(63) Lin, B.; Yang, G.; Wang, L. Stacking-Layer-Number Dependence of Water Adsorption in 3D Ordered Close-Packed g-C_3N_4 Nanosphere Arrays for Photocatalytic Hydrogen Evolution. *Angew. Chemie Int. Ed.* **2019**, *58* (14), 4587–4591.

(64) Zhu, B.; Zhang, J.; Jiang, C.; Cheng, B.; Yu, J. First Principle Investigation of Halogen-Doped Monolayer g-C_3N_4 Photocatalyst. *Appl. Catal. B Environ.* **2017**, *207*, 27–34.

(65) Wang, Y.; Di, Y.; Antonietti, M.; Li, H.; Chen, X.; Wang, X. Excellent Visible-Light Photocatalysis of Fluorinated Polymeric Carbon Nitride Solids. *Chem. Mater.* **2010**, *22* (18), 5119–5121.

(66) Hong, J.; Hwang, D. K.; Selvaraj, R.; Kim, Y. Facile Synthesis of Br-Doped g-C_3N_4 Nanosheets via One-Step Exfoliation Using Ammonium Bromide for Photodegradation of Oxytetracycline Antibiotics. *J. Ind. Eng. Chem.* **2019**, *79*, 473–481.

(67) Zhang, G.; Zhang, M.; Ye, X.; Qiu, X.; Lin, S.; Wang, X. Iodine Modified Carbon Nitride Semiconductors as Visible Light Photocatalysts for Hydrogen Evolution. *Adv. Mater.* **2014**, *26* (5), 805–809.

(68) Tay, Q.; Kanhere, P.; Ng, C. F.; Chen, S.; Chakraborty, S.; Huan, A. C. H.; Sum, T. C.; Ahuja, R.; Chen, Z. Defect Engineered g-C_3N_4 for Efficient Visible Light Photocatalytic Hydrogen Production. *Chem. Mater.* **2015**, *27* (14), 4930–4933.

(69) Li, S.; Dong, G.; Hailili, R.; Yang, L.; Li, Y.; Wang, F.; Zeng, Y.; Wang, C. Effective Photocatalytic H_2O_2 Production under Visible Light Irradiation at g-C_3N_4 Modulated by Carbon Vacancies. *Appl. Catal. B Environ.* **2016**, *190*, 26–35.

(70) Tu, W.; Xu, Y.; Wang, J.; Zhang, B.; Zhou, T.; Yin, S.; Wu, S.; Li, C.; Huang, Y.; Zhou, Y.; et al. Investigating the Role of Tunable Nitrogen Vacancies in Graphitic Carbon Nitride Nanosheets for Efficient Visible-Light-Driven H_2 Evolution and CO_2 Reduction. *ACS Sustain. Chem. Eng.* **2017**, *5* (8), 7260–7268.

(71) Choudhury, B.; Paul, K. K.; Sanyal, D.; Hazarika, A.; Giri, P. K. Evolution of Nitrogen-Related Defects in Graphitic Carbon Nitride Nanosheets Probed by Positron Annihilation and Photoluminescence Spectroscopy. *J. Phys. Chem. C* **2018**, *122* (16), 9209–9219.

(72) Niu, P.; Liu, G.; Cheng, H.-M. M. Nitrogen Vacancy-Promoted Photocatalytic Activity of Graphitic Carbon Nitride. *J. Phys. Chem. C* **2012**, *116* (20), 11013–11018.

(73) Li, Y.; Ho, W.; Lv, K.; Zhu, B.; Lee, S. C. Carbon Vacancy-Induced Enhancement of the Visible Light-Driven Photocatalytic Oxidation of NO over g-C_3N_4 Nanosheets. *Appl. Surf. Sci.* **2018**, *430*, 380–389.

(74) Shi, X.; Fujitsuka, M.; Kim, S.; Majima, T. Faster Electron Injection and More Active Sites for Efficient Photocatalytic H_2 Evolution in g-C_3N_4/MoS_2 Hybrid. *Small* **2018**, *14* (11), 1703277.

(75) Lu, X.; Xie, J.; Chen, X.; Li, X. Engineering MP_x (M = Fe, Co or Ni) Interface Electron Transfer Channels for Boosting Photocatalytic H_2 Evolution over g-C_3N_4/MoS_2 Layered Heterojunctions. *Appl. Catal. B Environ.* **2019**, *252*, 250–259.

(76) Liang, S.; Zhang, D.; Pu, X.; Yao, X.; Han, R.; Yin, J.; Ren, X. A Novel Ag_2O/ g-C_3N_4 P-N Heterojunction Photocatalysts with Enhanced Visible and near-Infrared Light Activity. *Sep. Purif. Technol.* **2019**, *210*, 786–797.

(77) Wang, H. H.; Yuan, X.; Wang, H. H.; Chen, X.; Wu, Z.; Jiang, L.; Xiong, W.; Zeng, G. Facile Synthesis of Sb_2S_3/Ultrathin g-C_3N_4 Sheets Heterostructures Embedded with g-C_3N_4 Quantum Dots with Enhanced NIR-Light Photocatalytic Performance. *Appl. Catal. B Environ.* **2016**, *193*, 36–46.

(78) Zhang, M.; Lai, C.; Li, B.; Huang, D.; Zeng, G.; Xu, P.; Qin, L.; Liu, S.; Liu, X.; Yi, H. Rational Design 2D/2D BiOBr/CDs/ g-C_3N_4 Z-Scheme Heterojunction Photocatalyst with Carbon Dots as Solid-State Electron Mediators for Enhanced Visible and NIR Photocatalytic Activity: Kinetics, Intermediates, and Mechanism Insight. *J. Catal.* **2019**, *369*, 469–481.

(79) Shi, A.; Li, H.; Yin, S.; Zhang, J.; Wang, Y. H_2 Evolution over g-C_3N_4/Cs_xWO_3 under NIR Light. *Appl. Catal. B Environ.* **2018**, *228*, 75–86.

(80) Huang, M.-Z. Z.; Yuan, B.; Dai, L.; Fu, M.-L. L. Toward NIR Driven Photocatalyst: Fabrication, Characterization, and Photocatalytic Activity of β-$NaYF_4$: Yb^{3+}, Tm^{3+}/g-C3N4 Nanocomposite. *J. Colloid Interface Sci.* **2015**, *460*, 264–272.

(81) Liang, S.; He, M.; Guo, J.; Yue, J.; Pu, X.; Ge, B.; Li, W. Fabrication and Characterization of BiOBr: Yb^{3+}, Er^{3+}/g-C_3N_4 Pn Junction Photocatalysts with Enhanced Visible-NIR-Light-Driven Photoactivities. *Sep. Purif. Technol.* **2018**, *206*, 69–79.

(82) Zhang, Q.; Deng, J.; Xu, Z.; Chaker, M.; Ma, D. High-Efficiency Broadband g-C_3N_4 Photocatalysts: Synergistic Effects from Upconversion and Plasmons. *ACS Catal.* **2017**, *7* (9), 6225–6234.

(83) Shui, J.; Wang, M.; Du, F.; Dai, L. N-Doped Carbon Nanomaterials Are Durable

Catalysts for Oxygen Reduction Reaction in Acidic Fuel Cells. *Sci. Adv.* **2015**, *1* (1), e1400129.

(84) Cui, H.; Jiao, M.; Chen, Y.; Guo, Y.; Yang, L.; Xie, Z.; Zhou, Z.; Guo, S. Molten-Salt-Assisted Synthesis of 3D Holey N-Doped Graphene as Bifunctional Electrocatalysts for Rechargeable Zn–Air Batteries. *Small Methods* **2018**, *2* (10), 1800144.

(85) Li, M.; Zhang, L.; Xu, Q.; Niu, J.; Xia, Z. N-Doped Graphene as Catalysts for Oxygen Reduction and Oxygen Evolution Reactions: Theoretical Considerations. *J. Catal.* **2014**, *314*, 66–72.

(86) Zhang, J.; Chen, X.; Takanabe, K.; Maeda, K.; Domen, K.; Epping, J. D.; Fu, X.; Antonieta, M.; Wang, X. Synthesis of a Carbon Nitride Structure for Visible-Light Catalysis by Copolymerization. *Angew. Chemie - Int. Ed.* **2010**, *49* (2), 441–444.

(87) Jun, Y. S.; Hong, W. H.; Antonietti, M.; Thomas, A. Mesoporous, 2D Hexagonal Carbon Nitride and Titanium Nitride/Carbon Composites. *Adv. Mater.* **2009**, *21* (42), 4270–4274.

(88) Niu, Y.; Teng, X.; Wang, J.; Liu, Y.; Guo, L.; Song, W.; Chen, Z. Space-Confined Strategy to Fe_7C_3 Nanoparticles Wrapped in Porous Fe-/N-Doped Carbon Nanosheets for Efficient Oxygen Electrocatalysis. *ACS Sustain. Chem. Eng.* **2019**, *7* (15), 13576–13583.

(89) Gong, K.; Du, F.; Xia, Z.; Durstock, M.; Dai, L. Nitrogen-Doped Carbon Nanotube Arrays with High Electrocatalytic Activity for Oxygen Reduction. *Science* **2009**, *323* (5915), 760–764.

(90) Liu, X.; Kang, J.; Dai, Y.; Dong, C.; Guo, X.; Jia, X. Graphene-Like Nitrogen-Doped

Carbon Nanosheet Prepared from Direct Calcination of Dopamine Confined by g-C_3N_4 for Oxygen Reduction. *Adv. Mater. Interfaces* **2018**, *5* (14), 1800303.

(91) Zhang, L.; Xiong, J.; Qin, Y.-H.; Wang, C.-W. Porous N–C Catalyst Synthesized by Pyrolyzing g-C_3N_4 Embedded in Carbon as Highly Efficient Oxygen Reduction Electrocatalysts for Primary Zn-Air Battery. *Carbon N. Y.* **2019**, *150*, 475–484.

(92) Lin, Y.; Qiu, Z.; Li, D.; Ullah, S.; Hai, Y.; Xin, H.; Liao, W.; Yang, B.; Fan, H.; Xu, J. NiS_2@CoS_2 Nanocrystals Encapsulated in N-Doped Carbon Nanocubes for High Performance Lithium/Sodium Ion Batteries. *Energy Storage Mater.* **2018**, *11*, 67–74.

(93) Balogun, M.-S.; Luo, Y.; Qiu, W.; Liu, P.; Tong, Y. A Review of Carbon Materials and Their Composites with Alloy Metals for Sodium Ion Battery Anodes. *Carbon N. Y.* **2016**, *98*, 162–178.

(94) Hou, H.; Shao, L.; Zhang, Y.; Zou, G.; Chen, J.; Ji, X. Large-area Carbon Nanosheets Doped with Phosphorus: A High-performance Anode Material for Sodium-ion Batteries. *Adv. Sci.* **2017**, *4* (1), 1600243.

(95) Miller, T. S.; Jorge, A. B.; Sella, A.; Corà, F.; Shearing, P. R.; Brett, D. J. L.; McMillan, P. F. The Use of Graphitic Carbon Nitride Based Composite Anodes for Lithium-Ion Battery Applications. *Electroanalysis* **2015**, *27* (11), 2614–2619.

(96) Yuan, Z.; Peng, H. J.; Hou, T. Z.; Huang, J. Q.; Chen, C. M.; Wang, D. W.; Cheng, X. B.; Wei, F.; Zhang, Q. Powering Lithium-Sulfur Battery Performance by Propelling Polysulfide Redox at Sulfiphilic Hosts. *Nano Lett.* **2016**, *16* (1), 519–527.

(97) Zhou, G.; Tian, H.; Jin, Y.; Tao, X.; Liu, B.; Zhang, R.; Seh, Z. W.; Zhuo, D.; Liu, Y.; Sun, J.; et al. Catalytic Oxidation of Li_2S on the Surface of Metal Sulfides for Li-S

Batteries. *Proc. Natl. Acad. Sci. U. S. A.* **2017**, *114* (5), 840–845.

(98) Wang, Z.; Dong, Y.; Li, H.; Zhao, Z.; Bin Wu, H.; Hao, C.; Liu, S.; Qiu, J.; Lou, X. W. D. Enhancing Lithium-Sulphur Battery Performance by Strongly Binding the Discharge Products on Amino-Functionalized Reduced Graphene Oxide. *Nat. Commun.* **2014**, *5*, 5002.

(99) Seh, Z. W.; Sun, Y.; Zhang, Q.; Cui, Y. Designing High-Energy Lithium–Sulfur Batteries. *Chem. Soc. Rev.* **2016**, *45* (20), 5605–5634.

(100) Xing, Z.; Li, G.; Sy, S.; Chen, Z. Recessed Deposition of TiN into N-Doped Carbon as a Cathode Host for Superior Li-S Batteries Performance. *Nano Energy* **2018**, *54*, 1–9.

Chapter 3

3. Experiments and Methodology

3.1. Overview

The general research route of this thesis is shown in **Figure 3.1.** Firstly, the targeted materials were mainly synthesized through three different methods: self-assembly method, template method, and solid phase method. Secondly, the morphology, crystalline structure and surface chemistry of the materials were characterized by a series of techniques, including the electron microscopy (scanning electron microscopy (SEM), transmission electron microscopy (TEM), and atomic force microscopy (AFM)), N_2 sorption/desorption measurement, X-ray diffraction (XRD), X-ray photoelectron spectroscopy (XPS), Fourier-transform infrared spectroscopy (FT-IR), electron paramagnetic resonance (EPR), and density functional theory (DFT) calculations. Thirdly, **a)** For g-C_3N_4-based photocatalysts, their optical properties were examined by UV-vis diffusion-reflectance spectra (UV-vis DRS) and photoluminescence (PL) spectra. The photoelectrochemical (PEC) performance and photocatalytic activity were evaluated by measuring the photocurrent response, electrochemical impedance spectra (EIS), and photocatalytic water splitting. **b)** For TiN-based sulfur hosts, a series of cell tests were also carried out, such as cycling voltammogram (CV) scanning, EIS, and Galvanostatic charge/discharge cycles. Finally, the results were presented in the research articles and this thesis.

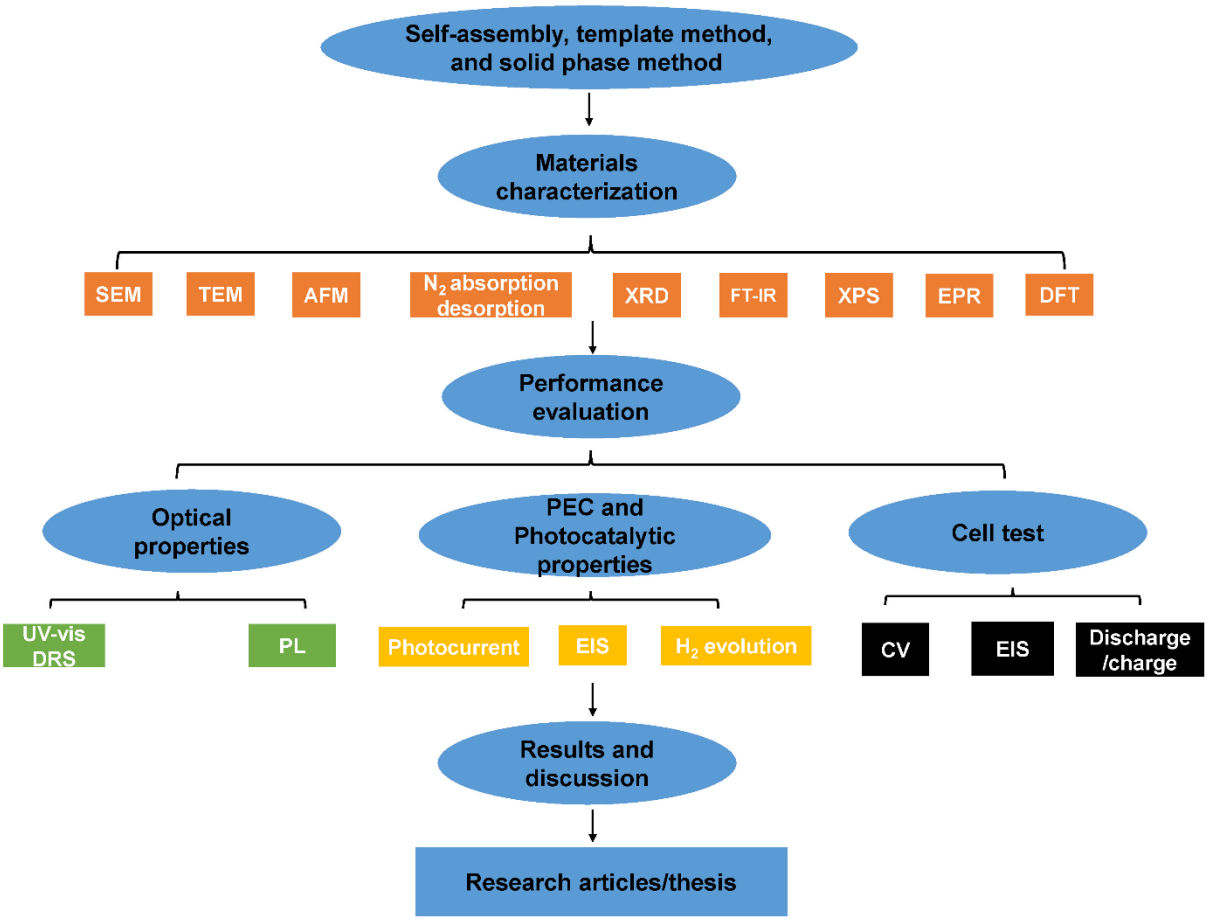

Figure 3.1 The general procedure of this thesis.

3.2. Chemicals and materials

The chemicals used in this thesis, along with their formulas, purity, and suppliers, are listed in **Table 3.1**.

Table 3.1 Chemicals and materials used in the thesis.

Chemicals	Formula	Purity (%)	Supplier
Ethanol	C_2H_5OH	99.8	Sigma-Aldrich
Ethanol	C_2H_5OH	96	Chem-Supply
Nitric acid	HNO_3	70	Sigma-Aldrich
Sulfuric acid	H_2SO_4	95.0-98.0	Sigma-Aldrich
Hydrochloric acid	HCl	37%	Sigma-Aldrich
Glycol	$(HOCH_2CH_2)_2O$	99.0	Sigma-Aldrich
Cyclohexane	C_6H_{12}	>99.5	Sigma-Aldrich
Oleic acid	$CH_3(CH_2)_7CH=CH(CH_2)_7COOH$	90	Sigma-Aldrich
methanol	CH_3OH	99.8	Sigma-Aldrich
1-Octadecene	$CH_3(CH_2)_{15}CH=CH_2$	90	Sigma-Aldrich
Tetraethyl orthosilicate	$Si(OC_2H_5)_4$	99	Sigma-Aldrich
Tetrabutyl titanate	$Ti(OCH_2CH_2CH_2CH_3)_4$	97	Aldrich
Hydrofluoric acid	HF	48	Chem-Supply
1,3-Dioxolane	$C_3H_6O_2$	99.8	Sigma-Aldrich
1,2-Dimethoxyethane	$CH_3OCH_2CH_2OCH_3$	99.5	Sigma-Aldrich
Tetraglyme	$CH_3O(CH_2CH_2O)_4CH_3$	99	Sigma-Aldrich
Melamine	$C_3H_6N_6$	99	Sigma-Aldrich
Cyanuric acid	$C_3H_3N_3O_3$	98	Sigma-Aldrich

Sulfur	S	99	Sigma-Aldrich
Yttrium(III) chloride hexahydrate	$YCl_3 \cdot 6H_2O$	99.9	Sigma-Aldrich
Ytterbium(III) chloride hexahydrate	$YbCl_3 \cdot 6H_2O$	99.998	Sigma-Aldrich
Thulium (III) chloride hexahydrate	$TmCl_3 \cdot 6H_2O$	99.99	Sigma-Aldrich
Sodium hydroxide	NaOH	97	Sigma-Aldrich
Ammonium fluoride	NH_4F	98	Sigma-Aldrich
Hexamethylenetetra-mine	$C_6H_{12}N_4$	99	Sigma-Aldrich
Bis(trifluoromethane) sulfonimide lithium salt	$CF_3SO_2NLiSO_2CF_3$	99	Sigma-Aldrich
Lithium nitrate	$LiNO_3$	99	Sigma-Aldrich
Lithium sulfide	Li_2S	99.98	Sigma-Aldrich

3.3. Materials preparation

The self-assembly method, template method, and solid-phase method were mainly used to prepare the targeted materials in this thesis.

3.3.1. Self-assembly method

Self-assembly is a spontaneous process in which the disordered molecules/atoms/polymers/

colloids/macroscopic particles organize into an ordered structure ranging from submicron to millimeters or larger scales without external direction (**Figure 3.2**).[1] The process can be driven either by inertial, electrical, and magnetic factors, or interfacial energy minimization. Among them, electrical-interaction-driven (hydrogen force, electrostatic charge force) self-assembly has been the most widely investigated in the field of nanomaterials preparation. Interestingly, the morphology of assembles can be tuned by molecules species, pH, temperature, or even the solvents. Due to the facile operation and easy control, the self-assembly has superior advantages toward other synthetic methods. The final products are generally in regular shapes and can act as soft templates for other applications.

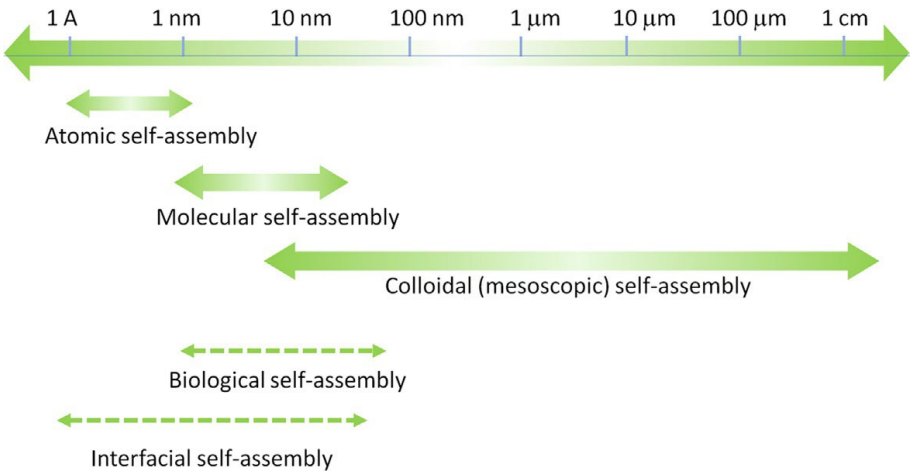

Figure 3.2 Sclae of self-assemblies based on the their size.[1]

3.3.2. Template method

Catalytic activity is significantly influenced by the nanostructures as advanced architectures can provide abundantly accessible catalytic sites. Some of these nanostructures can be prepared via the template method. In general, the template method is classified into the “soft” template method and the “hard” template method. The former one refers to employing the organic

surfactant or block-copolymer micelles as templates, while the latter one refers to using the inorganic silica or aluminum oxide as templates. Soft templates are generally removed by annealing or washing, whereas hard templates are normally etched by acid (HF) or base (NaOH). Both methods can get replicas of their templates.[2]

3.3.3. Solid-phase method

Narrowly speaking, the solid phase method refers to the solid-solid reaction at higher temperatures. This involves the decomposition of organic/inorganic compounds, the recombination of solids as well as replacement reactions. This thesis emphasizes the decomposition of organic precursors to polymers or carbon in air or inert atmosphere.

3.4. Characterization Techniques

3.4.1. Scanning electron microscopy (SEM)

The SEM is a tool to analyze the morphology of materials by scanning the surface with a focused beam of electrons. The basic configuration of SEM is shown in **Figure 3.3**.[3] It consists of three parts: vacuum system, electron beam system, and imaging system. Typically, a tungsten filament cathode is used to thermionically emit the electron beam under high vacuum and voltage. Then, the electron beam is focused by condenser lenses into a small spot (0.4-5 nm), pass through the deflection coils, and finally hit the sample surface. When the electron beam interacts with the sample surface, a series of signals can be produced, including secondary electrons, reflected or back-scatted electrons, characteristic X-ray and light, absorbed current, and transmitted electrons. In this thesis, we chose the Everhart-Thornley detector to collect secondary electrons with their number showing the signal intensity. Thus, the images of morphology are recorded with a theoretical resolution around 1 nm. The models

of SEM used in this thesis are Zeiss Supra 55, Zeiss EVO SEM, and Hitachi SU8100 provided by Microstructural Analysis Unit in UTS and Shandong University.

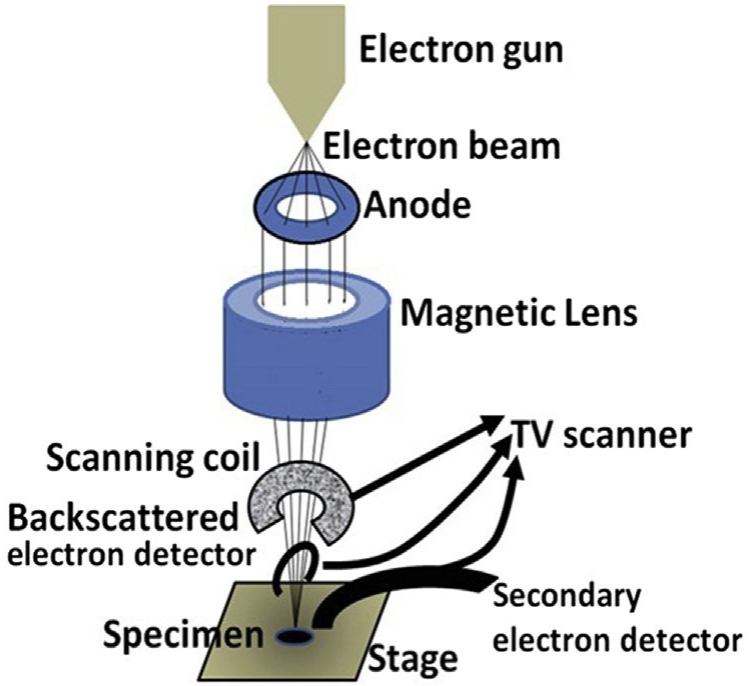

Figure 3.3 Configuration of SEM set-up.[3]

3.4.2. Transmission electron microscopy (TEM)

The TEM measurement is widely used to analyze the morphology of the specimen by allowing the accelerated electrons to transmit through the specimen. The basic TEM set-up is presented in **Figure 3.4**, which consists of five parts: vacuum system, specimen stage, electron gun, electron lens, and aperture. Normally, TEM is used with a high voltage around 200 kV, which requires an ultra-high vacuum in the range of 10^{-7}-10^{-9} Pa to prevent the electrical arc at the TEM cathode. In order to prevent the gas molecule diffusion from the main chamber to the higher vacuum gun, a special isolated vacuum system is designed for the gun using the valves or differential pump aperture. The specimen stage has airlocks to allow the insertion of a specimen holder with the minimizes loss of vacuum in the overall vacuum chambers. The

specimen is generally dispersed in the solution and then dropped onto the grid mesh (copper, molybdenum, gold, or platinum grids), transferred into a specimen holder and specimen stage. The electrons are generated via connecting the filament to the negative component power supply, and then be "pumped" from the electron gun to the anode plate and the TEM column, thus completing the circuit. The electron lens is designed for focusing parallel electrons to a small spot at some constant focal distance. Generally, the electromagnetic coils are also used to generate a convex lens. Because the deviation from the magnetic lens causes aberrations and worsens spherical and chromatic aberration, field produced for the lens must be radially symmetrical. The apertures are used to allow the axial electrons passing through; thus, on the one hand, decrease the beam intensity, which might be applied for the analysis of sensitive samples. On the other hand, the filtering can remove some unwanted scattering electrons to alleviate the spherical or chromatic aberration and diffraction from interaction with the samples.

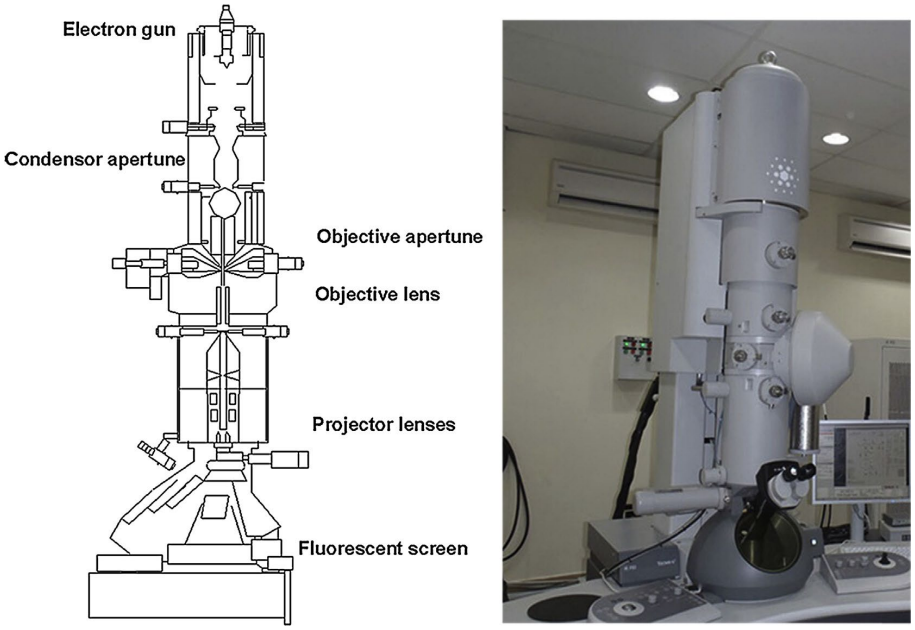

Figure 3.4 Configuration of TEM set-up.[4]

The imaging system has two types of mode: bright field imaging mode and diffraction imaging mode. The former one is widely used in current research as it gives a visual result of

sample morphology: the thicker area scatters electrons at bigger angles and presents darker. In comparison, the thinner area shows a brighter image. This is particularly useful for the non-crystalline, amorphous materials. The TEM used in this thesis includes Tecnai-G2 F30 S-Twin and JEM-2011 at UTS and Yangzhou University.

3.4.3. Atomic force microscopy (AFM)

AFM is a type of scanning probe microscopy, which is intensively used in the field of imaging, measuring and operating nanomaterials in nanoscale. The critical component of AFM is the cantilever with the sharp tip at its end and is used to scan the sample surface. When the tip is brought into proximity of a sample surface, forces between the tip and the sample lead to a deflection of the cantilever according to Hooke's law. The forces are recorded when the tips move in a certain direction, and thus the morphology information is gathered.

The AFM can be manipulated in many modes, of which contact mode, tapping mode, and non-contact mode are most commonly used. This technique has superior advantages toward scanning tunnel microscopy due to the ability for non-conductive sample analysis. In this thesis, Dimension SPM 3000 instrument provided by UTS is used to measure the thickness of nanosheets.

3.4.4. N_2 sorption/desorption measurement

N_2 sorption/desorption measurement is a powerful technique to analyze the physical parameters of porous materials, including specific surface area, pore size distribution, as well as pore volume. Normally, N_2 is used as the absorbent and is cooled to 77 K in liquid form. A known amount of N_2 is then diffused into the measuring tube, and thus a certain quantity of N_2 gas is adsorbed on the sample surface due to the specifical morphology with pores. Finally, the typical

adsorption isotherm plots are given based on that the adsorbed N_2 quantity is as a function of the relative gas pressure P/P_0. The pores can be classified into micropores, mesopores, macropores, which can also be identified from the isotherms according to the International Union of Pure and Applied Chemistry (IUPAC) classification.[5] Additionally, a classic Brunauer-Emmet-Teller (BET) model is commonly used to determine the surface area of samples.[6] The Kelvin equation is used to calculate the pore size distribution. Moreover, the total pore volume can be given by the amount of gas adsorbed at the plateau, assuming that the condensate has the same density as the corresponding bulk liquid at the experimental temperature. In this thesis, a Micrometrics ASAP2020 adsorption analyzer provided in UTS was employed to measure the pore properties.

3.4.5. X-ray diffraction (XRD)

XRD measurement is a useful tool to analyze the crystalline structure based on the interaction of electromagnetic radiation (X-ray with a wavelength of around 10^{-10} meters) with samples. The X-rays are produced in a vacuum X-ray tube, which consists of an anode (normally Cu) and a cathode (normally a tungsten filament). The interaction of the incident radiation with the samples generates constructive interference if the conditions satisfy Bragg's Law:

$$n\lambda=2d \sin \theta,$$

where d is the interplanar spacing, θ is the Bragg angle, n is the order of reflection, and λ is the wavelength of the X-rays irradiation. The crystalline of samples can be indexed by matching the as-obtained XRD patterns to the crystalline database using software (Jade, PDF2019). This thesis employs a Bruker D8 diffractometer with Cu Kα radiation (λ=1.5418 Å) as the tester provided by UTS.

3.4.6. X-ray photoelectron spectroscopy (XPS)

XPS technique is a powerful manner to analyze the surface chemistry of samples, which gives element composition, formula, and chemical state and electronic state of samples. This technique is based on counting the number of emitted inner/valence photoelectrons from atoms and their binding energy. Each element produces a characteristic set of XPS peaks at a given binding energy. XPS technique is applied in many research fields due to its ability to test all kinds of samples in the fields of nanomaterials, photovoltaics, catalysis, energy storage, corrosion science, and inorganic synthesis and so on. In this doctoral study, an EASY ESCA spectrometer (VG ESCA LAB MKII) was used to identify the surface chemistry of samples.

3.4.7. Fourier-transform infrared spectroscopy (FT-IR)

The FT-IR spectroscopy is a valuable approach to identify the functional groups of the specimen. It measures how much the infrared light is absorbed in each wavelength, and the resulting spectrum represents a molecular fingerprint of the sample. In this work, the FT-IR spectrum was characterized by using a Nicolet 6700 Spectrometer in UT with the range from 4000 cm^{-1} to 5000 cm^{-1}.

3.4.8. Electron paramagnetic resonance (EPR)

The EPR measurement, a magnetic resonance technique, that measures the transitions of unpaired electrons in an applied magnetic field. When an external magnetic field is added, the paramagnetic electrons can either orient in a direction parallel or antiparallel to the direction of the magnetic field. It can be used to detect qualitative and quantitative unpaired electrons contained in the atoms or molecules of substances and explore the structural characteristics of the surrounding environment. The test can identify the vacancies, transition metal ions, and

free radicals. In this study, a Bruker A300-10/12 EPR spectrometer with f = 9.853 GHz was used to obtain EPR signals in Yangzhou University.

3.4.9. Density functional theory (DFT) calculations

Density functional theory (DFT) is a very useful computational modeling method used in a variety of subjects, such as physics, chemistry, and materials science, due to its key role in investigating the electronic structure of many-body systems, in particular atoms, molecules, and the condensed phases. DFT calculations give information on the chemical interactions, bond length, Bade Charge, and density of states, which are very constructive for experimental guidance. In this study, the Computational resources have been provided by the National Supercomputing Centers in Jinan and Qufu Normal University.

3.4.10. UV-vis diffusion-reflectance spectra (UV-vis DRS)

The UV-vis DRS measurement is a useful tool to analyze the absorption ability of a photocatalyst and calculates the bandgap of a semiconductor (generally the samples are in solid-state). As the light cannot pass through opaque solid samples, thus the specular reflection is recorded using an integrating spheres with a barium sulfate-coated inside. In this research, a Perkin Elmer Lambda 950 spectrophotometer was used to obtain the UV-vis DRS spectra in UTS.

3.4.11. Photoluminescence (PL) spectroscopy

The PL spectroscopy is a type of electromagnetic spectroscopy that analyses fluorescence from a sample. It is operated using a short wavelength (normally ultraviolent light) to excite the electrons in samples and record the emit light with a much longer wavelength. Considering the samples are analogous, the PL intensity typically indicates the charge separation efficiency:

stronger intensity, lower separation efficiency, vice versa. The time-resolved fluorescence can measure the charge lifetimes. In this research, a Hitachi F7000 instrument was used to record the PL intensity while an Edinburgh Analytical Instrument FLS920 time-resolved spectrofluorometer was employed to record the lifetimes of electrons.

3.4.12. Photoelectrochemical (PEC) performance

The PEC performance of samples was recorded using an electrochemical workstation, which employs a three-electrode cell using the AgCl/Ag electrode as the reference electrode, Pt wire as the counting electrode, and the sample as the working electrode in a given electrolyte. In a typical measurement, the photocurrent was carried out using the current-time technique. The charge transfer resistance was measured using the AC impedance spectroscopy by applying 5 mV alternative signal over the frequency ranged from 100 kHz to 0.01 Hz.

3.4.13. Photocatalytic activity

The photocatalytic activity of the as-prepared samples was evaluated by photocatalytic hydrogen evolution at room temperature. Typically, a given mass of photocatalyst was firstly dispersed in a mixture of triethanolamine and water under sonication. Afterward, a certain amount of H_2PtCl_6 (1 wt% Pt) was added to the solution to act as the co-catalyst. Then the suspension was bubbled with N_2 for 0.5 h to remove the air, and the flask was sealed with silicone rubber and parafilm. A Xe arc lamp (PLS-SXE300C) equipped with an AM 1.5 G filter or UV-cutoff filter ($\lambda > 420$ nm) was employed as the light source to trigger the photocatalytic reaction. The mixture was under continuous magnetic stirring, and the flask was put in front of the lamp where the light intensity was measured at ~ 100 mW cm^{-2}. The amount of generated hydrogen was determined with the gas chromatography (GC2014, Shimadzu) after intermittently taking out 0.2 mL of gas.

3.4.14. Cell tests

For cell tests, the cells were put into the LANDdt Tester or Neware Tester system to record the discharge/charge curves in a given current by calculating the rate and mass of active substances.

3.5. Reference

(1) Lee, Y. S. *Self-Assembly and Nanotechnology: A Force Balance Approach*; John Wiley & Sons, 2008.

(2) Schüth, F. Endo-and Exotemplating to Create High-surface-area Inorganic Materials. *Angew. Chemie Int. Ed.* **2003**, *42* (31), 3604–3622.

(3) Tang, C. Y.; Yang, Z. Membrane Characterization. *Hilal, N* **2017**, 259.

(4) Tang, C. Y.; Yang, Z. Transmission Electron Microscopy (TEM). *Membr. Charact.* **2017**, 145–159.

(5) Sing, K. S. W. Reporting Physisorption Data for Gas/Solid Systems with Special Reference to the Determination of Surface Area and Porosity (Recommendations 1984). *Pure Appl. Chem.* **1985**, *57* (4), 603–619.

(6) Brunauer, S.; Emmett, P. H.; Teller, E. Adsorption of Gases in Multimolecular Layers. *J. Am. Chem. Soc.* **1938**, *60* (2), 309–319.

Chapter 4

4. Atom-thick Defective Carbon Nitride Nanosheets for Efficient Solar-energy-driven Hydrogen Evolution

4.1. Introduction

Graphitic carbon nitride (g-C_3N_4), emerging as a metal-free photocatalyst, has boosted intensive research interest worldwide since it was discovered with a Goldilocks band structure for water splitting by Wang et al. in 2009. [1] Over the past decade, g-C_3N_4 has been widely used in the fields of H_2 evolution, [2] fuel synthesis, [3] pollution removal [4] and energy storage system [5] owing to the merits of its appropriate conduction band (CB) and valence band (VB) positions capable of absorbing solar light in contact with water or other solvents. [6] Despite intensive research, some major challenges arising from the limited surface area (8-16 $m^2\ g^{-1}$), extremely low pore volume (0.1-0.5 $cm^3\ g^{-1}$), inferior electronic conductivity, sluggish charge transport process, as well as the high electron-hole recombination, are urgent to be addressed before large-scale applications.

The commonly employed structure engineering strategy is to expose more active sites by constructing architectures with unique morphology and high surface area. [7–11] The pioneered work was achieved by Antonietti's group using the (ordered) mesoporous, macroporous silica as hard templates via nanocasting or nanocoating.[10,12] Inspired by this, numerous research work on morphology modification, such as g-C_3N_4 hollow spheres, [13,14] nanofibers, [15] and nanobelts, [16] have been presented and demonstrated to be effective to enhance the photocatalytic performance of g-C_3N_4. However, these approaches normally involve either complex

procedures, the extremely toxic precursor (cyanamide), corrosive HF, or harsh experimental conditions. Another strategy directly delaminating the stacking g-C_3N_4 aggregates into porous few-layered 2D nanosheets by post ultrasonication, centrifugation, or repeated thermal etching provides an easier way to accomplish this goal. [17–19] However, the time (energy)-consuming treatments often lead to a rather low yield of g-C_3N_4 nanosheets.

In addition to the physical modifications, surface modulation via doping has been intensively studied to boost the photocatalytic activity of g-C_3N_4. [20] The additional atoms are highly expected to change the electronic structures on extending the light-absorbing ability and facilitating the separation of photocarriers. For instance, Qiao's group introduced phosphorus atoms by using 2-aminomethyl phosphonic acid as a phosphorus source and extended the light-responsive region up to 557 nm. [21] Zhang and co-workers demonstrated that the O-doped porous g-C_3N_4 network allows multiple reflections of the incident light, and the presence of O atoms would narrow the band gap and introduce the lattice strain, thus leading to the enhanced light-harvesting and improving the charge separation. As a result, the hydrogen evolution rate boosted by 6.1 folders in comparison with the bulk material. [22] On the other hand, the self-doping of g-C_3N_4 with carbon atoms would increase the electronic conductivity and thus favors the electron transfer process. [20,23] As is known to all that significant progress has been made toward PEC water splitting by developing efficient catalysts such as ZnO, CdS, and Fe@Ni$(OH)_2$. [24,25] Remarkably, Li *et al.* proposed a photoanode comprising Au@CdS core-shell nanoparticles on ZnO nanowires and the PEC cell produces H_2 at a constant rate of 11.5 μmol h^{-1} for 10 h under AM1.5 light illumination with a bias of 0.4 V. [24] Very recently, g-C_3N_4 has also emerged as a promising photocatalyst for PEC applications owing to its unique band

structure (E_{gap} = 2.75 eV, E_{CB} = -1.13 eV, E_{VB} = 1. 57 eV) which enables the absorbance of solar spectrum (λ<450 nm) and satisfy the criteria of H_2/O_2 evolution. [26] Coupling with other semiconductors such as carbon dots or CdS, the incident-photon-to-current efficiency (IPCE) can be as high as 31 and 42%, respectively. [27,28] To get a high PEC performance, similar to that of photocatalytic water splitting, the charge transfer and separation process is desirable to improve. Thus, it is essential to regulate the photocatalytic and PEC activity of carbon nitrides via the engineering of structure and surface composition.

Herein, we demonstrate an in-situ exfoliation strategy to synthesize the atomic-thick porous carbon nitride with a high pore volume (1.55 cm^3 g^{-1}) by the pyrolysis of protonated melamine. The protonated melamine is obtained by a self-assembly process via the Lewis acid-base neutralization and hydrogen bonding interaction between melamine and inorganic acid (HNO_3, H_2SO_4). Specifically, acids are proved to assist a thermal oxidization and exfoliation progress owing to their stronger oxidizing and corrosive ability. This is of vital importance to tune the morphology as well as embed the dopants into the g-C_3N_4 matrix. In this work, a new C/O-doped g-C_3N_4 model based on our practical XPS results was also proposed to simulate the change of the electronic properties by the DFT calculation. It was found that C-doping can favor the formation of a delocalized π bond, which significantly improves the bulk conductivity while O-doping induces a strong electronic polarization, shortened bond length. Thus, the charge transport and separation are greatly improved, which is further verified by our experimental details. As a result, an excellent PEC performance with 50-60 times larger photocurrent in comparison with the pristine g-C_3N_4 and a high hydrogen evolution rate of 830.1 and 115.5 μmol g^{-1} h^{-1} under the solar- and visible- light irradiation is obtained.

4.2. Experimental Section

4.2.1 Materials

Melamine ($C_3H_6N_6$, 99%), nitric acid (HNO_3, 70%), sulfuric acid (H_2SO_4, 95.0-98.0%) were purchased from Sigma-Aldrich. All chemicals were used as received without further purification.

4.2.2 Preparation of catalyst

HNO_3- assisted pyrolytic g-C_3N_4 (abbreviated as NCN) was prepared via one-step pyrolysis of the self-assembled protonated melamine. Typically, 1 g of melamine was firstly dissolved in 250 mL deionized (DI) water under ultrasonication. Afterward, the solution was pre-cool to 4℃ in the freezer. Then, an appropriate amount of nitric acid was added slowly into the solution under vigorous stirring. White precipitates were generated promptly. The obtained powder was thermally treated at 550 °C for 4 h in a muffle furnace with a certain exposed area to the air. After cooling down to room temperature, the white or light-yellow foams were obtained. H_2SO_4-assisted pyrolytic g-C_3N_4 (SCN) was synthesized by using the same procedure, except nitric acid was replaced with sulfuric acid (H_2SO_4). For comparison, bulk g-C_3N_4 (BCN) was prepared by the same annealing method using melamine as the precursor.

4.2.3 Preparation of photoelectrodes

The photoelectrodes were prepared according to our previous report: [8] (i) 20 mg of as-prepared photocatalysts were first mixed with a certain amount of ethanol/Nafion solution and then were sonicated for 10 min; (ii) the resulting slurry was spread on a 15 mm × 20 mm tin-doped indium oxide (ITO) conducting glass via a spin coater (KW-4A, Chemat Scientific,

United States); (iii) each electrode was dried at 30 °C under vacuum and calcined at 200 °C for 4 h in sequence to enhance the adhesion to the substrate.

4.2.4 Structural Characterizations

The morphology and microstructure of the samples were recorded on a scanning electron microscope (SEM; Hitachi SU8100) at an acceleration voltage of 5 kV and a high-resolution transmission electron microscope (HR-TEM, Tecnai-G2 F30 S-Twin) at an acceleration voltage of 300 kV. The thickness of the catalyst was determined by using atomic force microscopy (AFM; Dimension SPM 3000). Powder X-ray radiation diffraction (XRD) measurements were performed on a Bruker D8 diffractometer with Cu Kα radiation (λ = 1.5418 Å). Nitrogen adsorption and desorption isotherms were collected using a Micrometrics ASAP2020 adsorption analyzer and the pore size distribution was derived from the adsorption branch using the Barrett-Joyner-Halenda (BJH) method. X-ray photoelectron spectroscopy (XPS) measurements were carried out on an EASY ESCA spectrometer (VG ESCA LAB MKII). Elemental analysis was performed on Vario EL Elemental Analysis Instrument (ELEMENTAR Co.). Fourier Transform Infrared Spectroscopy (FTIR) was recorded on a Nicolet 6700 Spectrometer. Photoluminescence (PL) spectra were studied using a Hitachi F7000 fluorescence spectrometer with an excitation wavelength of 325 nm. Time-resolved fluorescence was measured using an Edinburgh Analytical Instrument FLS920 time-resolved spectrofluorometer. UV-vis diffuse-reflectance spectra (UV-vis DRS) were investigated with a UV-visible spectrophotometer (UV-3100, Hitachi) and $BaSO_4$ was used as a reflectance standard.

4.2.5 Photoelectrochemical test

A Xe arc lamp (300 W, 18 A) with a UV-cutoff filter (λ > 420 nm) was employed as the light source. The photocurrents were measured on a CHI 650D electrochemical workstation (CHI Instrument, USA) in a standard three-electrode system, in which the g-C_3N_4-based electrode was used as working electrode, a Pt wire was used as counter one, and an Ag/AgCl (saturated KCl) electrode as reference one. The electrolyte was a 0.35 M Na_2S/0.25M Na_2SO_3 aqueous solution. Photovoltammograms were carried out in the potential range of -0.5 ~ 0.8 V at a scan rate of 10 mV/s. Electrochemical impedance spectroscopy (EIS) was measured by applying 5 mV alternative signal over the frequency ranged from 100 kHz to 0.01 Hz. Mott-Schottky plots were measured at the potential range of −1.6 to −0.4 V in 0.5 M Na_2SO_4 aqueous solution and the frequency of 1000 Hz with an AC voltage magnitude of 10 mV.

4.2.6 Photocatalytic hydrogen evolution

The photocatalytic reactions of hydrogen evolution were performed in a gas-closed system with a top irradiation Pyrex cell. A Xe arc lamp (300 W, 18 A) with a UV-cutoff filter (λ > 420 nm) was employed as a light source (100 mW cm^{-2}) to trigger the photocatalytic reaction. In a typical photocatalytic experiment, 80 mg of the catalyst was firstly dispersed upon constant stirring in a mixed solution of TEOA and water with the volume ratio of 1:9. Afterwards, 1 wt% Pt was deposited on the surface of C_3N_4-based samples via the *in-situ* photo-deposition of H_2PtCl_6 for 0.5 h. Before irradiation, the system was bubbled with nitrogen for 30 min to ensure that the reaction system is under anaerobic conditions. The amount of hydrogen generated was determined with online gas chromatography (GC7900, TCD, nitrogen as a carrier gas and a 5 Å molecular sieve column). All glassware was carefully rinsed with distilled water prior to use.

4.2.7 Computation

DFT calculations are carried out within the local density approximation (LDA) functional using the plane-wave-based Vienna Ab-initio Simulation Package (VASP) code. The vacuum space is set to 30 Å, which has been proven large enough to avoid the layer-to-layer effects. The cutoff energies for plane waves are 500 eV. A 6×6×1 Monkhorst-Pack k-point mesh is used in the geometry optimization and geometries of the composites are optimized separately until the force on each atom is less than 0.05 eV $Å^{-1}$.

4.3. Results and Discussion

4.3.1 Morphology and Structure

Figure 4. 1 illustrates the details of constructing g-C_3N_4 architectures into the porous atomic-thick nanosheets. The porous ultra-thin C/O-doped g-C_3N_4 nanosheets were prepared by two steps: (i) the formation of supermolecules by self-assembly between melamine (pK_b=9.5) and inorganic acid (*e.g.*, HNO_3) via the Lewis base-acid neutralization and hydrogen bonding (O•••H and N•••H). The samples obtained in the presence of HNO_3, H_2SO_4 were named as MNA and MSA. Notably, due to the poor solubility of melamine nitrate ($C_3H_6N_6$•HNO_3, MNA, 0.2 g /100 mL) and melamine sulfate $(C_3H_6N_6)_2$•H_2SO_4•$2H_2O$, MSA, 0.12 g/100 mL), [29] the precursors can be produced in a large scale; and (ii) annealing the protonated precursors at an elevated temperature at 550℃ for 4 h with a certain exposing window to the air. The reason for choosing 550℃ as annealing temperature is that higher than this temperature, g-C_3N_4 continues to decompose, thus the yield will be very low at a long heating time of 4 hours based on our TGA test (**Figure 4.2**). During the precursor polymerization, some decomposed corrosive gases (NO_2, SO_2) would further act as soft templates and pore formers to created few-layered g-C_3N_4 nanosheets with high pore volume. At the same time, the etching and

exfoliating progress alters the atom-rearrangement of tri-s-triazine units allowing more C and O atoms into the polymer matrix and leads to the formation of final porous doped g-C_3N_4 material. It is worth mentioning that the yield (40%) of g-C_3N_4 is much higher than those employing the urea as precursors (4%), owing to the thermal polymerization of pronated melamine does not involve the conversion to biuret. [30,31] Unlike the time/energy-consuming method such as long time ultrasonication or repeated thermal annealing, this strategy proposed a facile, green, and scalable synthesis route of porous ultra-thin g-C_3N_4 nanosheets.

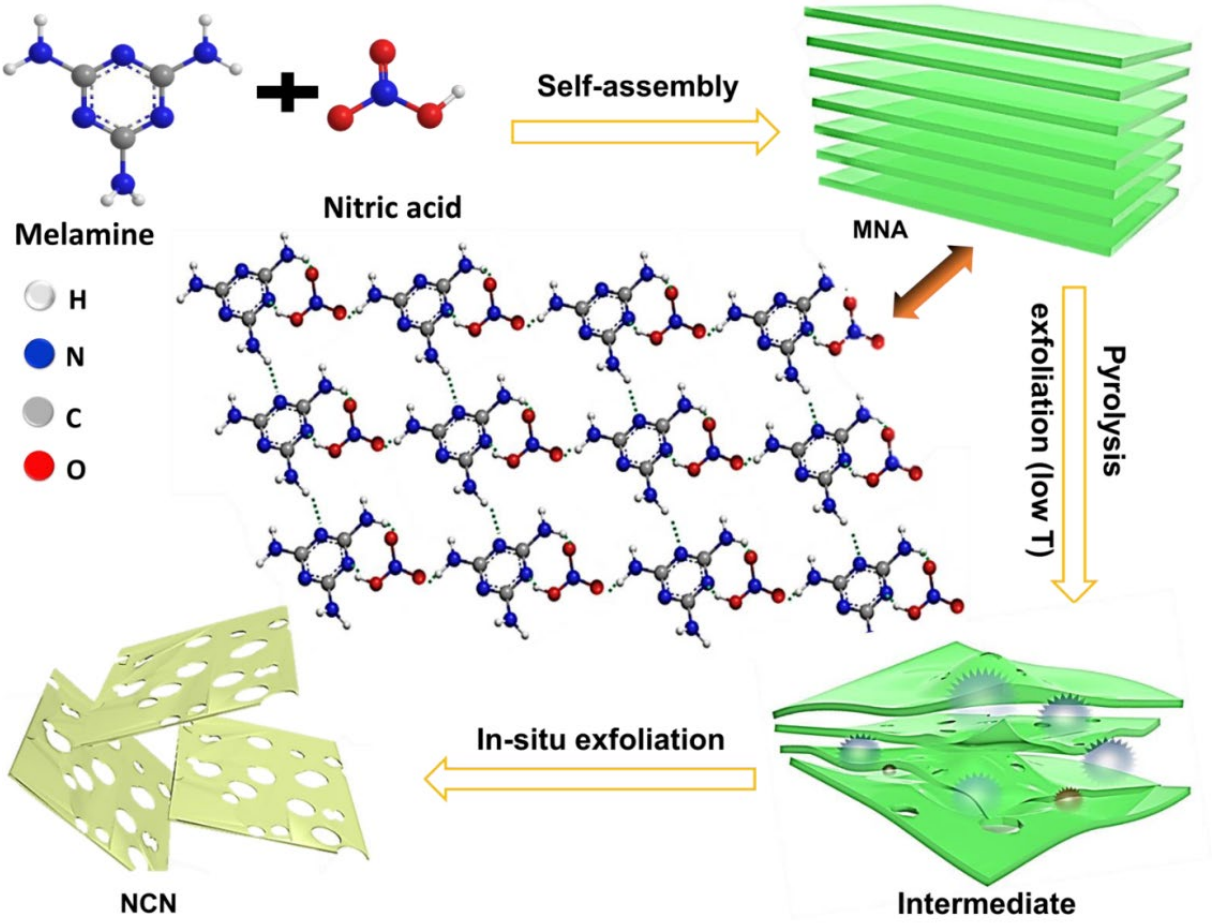

Figure 4.1 The schematic illustration for the preparation of porous ultra-thin g-C_3N_4 nanosheets (NCN).

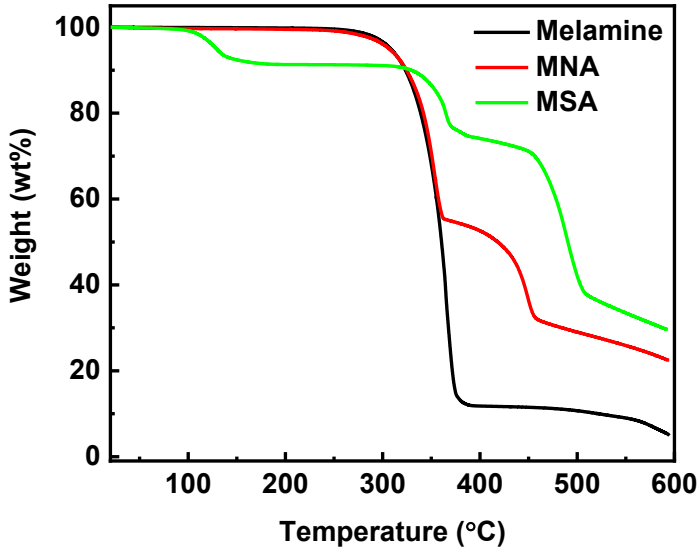

Figure 4.2 TGA test of various precursors: melamine, MNA and MSA.

To gain novel insight into the HNO_3- and H_2SO_4- assisted pyrolytic g-C_3N_4 (NCN and SCN), the microscopes were used to characterize the basic structure and morphology. As shown in SEM images (**Figure 4. 3a, g**), the assembled supermolecules (MNA and MSA) exhibit the regular macrobelt units of 1-3 μm in width and 30-100 μm in length. Furthermore, the macrobelts would continue to assemble into a larger orchid structure (**Figure 4. 3b, h**). However, after thermal treatment, the obtained NCN and SCN exhibit highly porous architecture composed of thin walls with a curved surface (**Figure 4. 3c, e, i, j**). The TEM image of NCN (**Figure 4. 3e**) reveals that the thin and curved shells are interconnected with each other to form a foam-like structure. The pores with various sizes (~5-50 nm) can be seen on the sheets (**Figure 4. 3d**). The porous ultrathin nanosheets with similar pores of SCN can be reflected by the TEM image (**Figure 4. 3k**). According to the atomic force microscopy (AFM) image (**Figure 4. 3f, l**), the thickness of sheets is only around 0.8~1.4 nm, suggesting the atomic-thin layer nature with only 2-4 C-N layers. It has been proven that porous metal

oxides [32] and graphene [33] can be synthesized on the basis of the in-situ production of gas bubbles as templates without any complex template-removal steps. In this work, with the increasing annealing temperature, pronated melamine would be gradually molten and polymerized into carbon nitride. Meanwhile, the corrosive gases such as NO, NO_2, SO_2 would be generated due to the thermal decomposition of counterions (e.g., NO_3^-, SO_4^{2-}) in melamine salts. The in-situ formation and release of gases would blow the molten melamine into bubbles and finally give rise to the formation of porous carbon nitride shells, prevent from layer stacking. The bubble walls neighbored are merged with each other to generate the foam-like architecture (Insert, **Figure 4. 3e, i**). It is worth noting that the counterions would play important roles in the formation of such a porous structure. In the absence of these counterions, the obtained pristine g-C_3N_4 (BCN) shows a thick graphite-like structure with aggregates in a micron-size scale. [8]

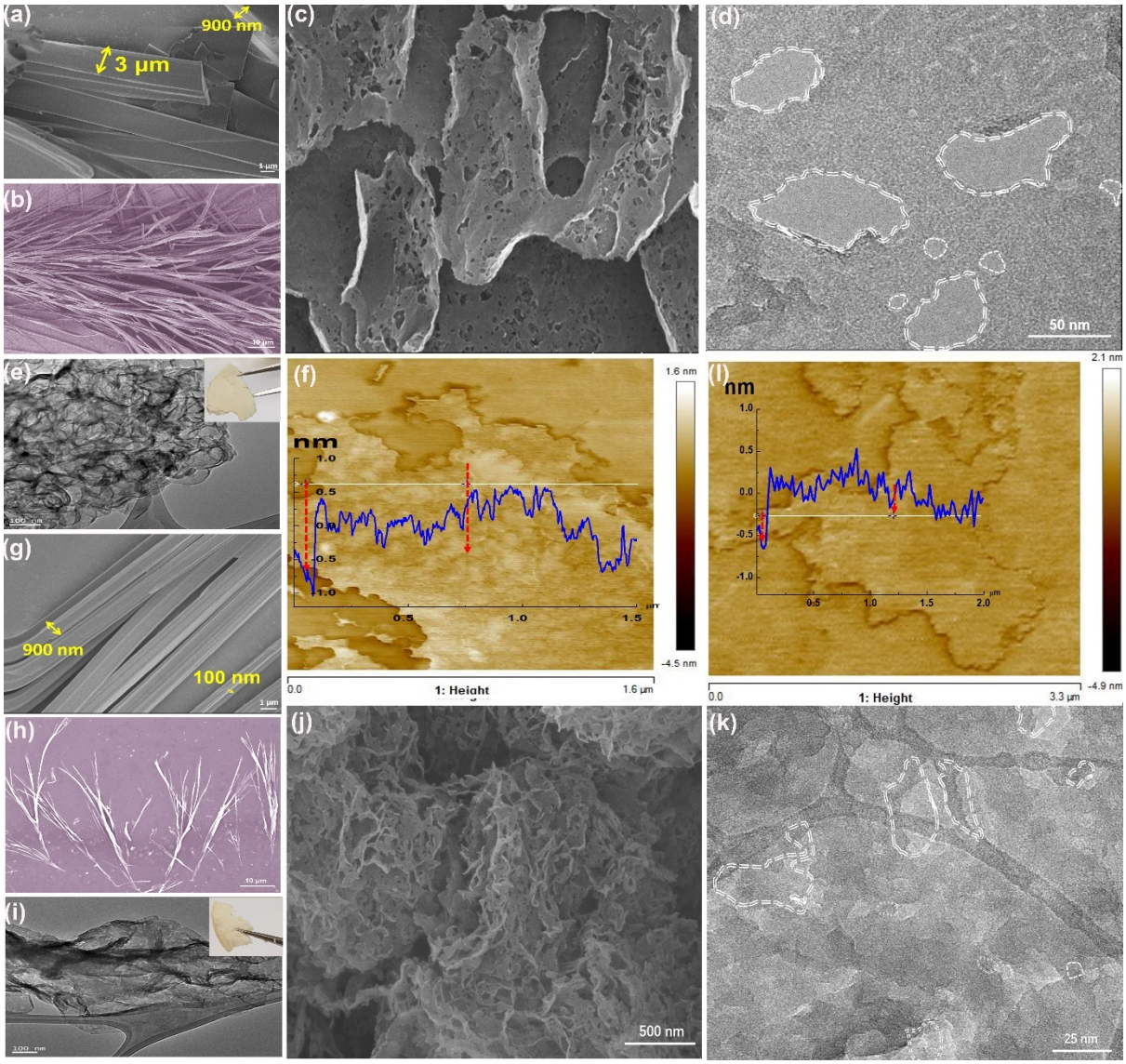

Figure 4.3 SEM images of **(a, b)** melamine nitrate MNA; **(c)** NCN; TEM images of **(d, e)** NCN; AFM image of **(f)** NCN; SEM images of **(g, h)** melamine sulfate MSA; TEM images of **(i, k)** SCN; SEM image of **(j)** SCN; AFM image of **(l)** SCN.

It is also evidenced that the presence of new X-ray diffraction (XRD) peaks for MNA and MSA affords the self-assemble arrangement in comparison with the pure melamine (**Figure 4. 4a**). In addition, the thin layer nature of the as-prepared carbon nitride can be further demonstrated. The characteristic XRD peaks at ~ 13.1 and 27.4° for BCN would be assigned to the (100) and (002) crystal planes.[1] However, the calcination of the organic-inorganic

hybrids (MNA, MSA) at 550 ℃ under the same conditions did not result in the formation of well-crystallized carbon nitride. The broad and weak diffraction peak of (002) plane indicates the loss of ordered crystalline structure in the final products, and the amorphous morphology is further confirmed by the high-resolution TEM (HR-TEM, **Figure 4. 4b-c**) without obvious lattice fringe. This change resembles that bulk graphite is exfoliated into graphene nanosheets. [34] Especially, the absence of diffraction peak of (100) plane corresponding to the in-plane structural packing feature of tri-s-triazine units[35] would be contributed to the preferred exfoliation of g-C_3N_4 in the z-orientation into two-dimensional sheets. [36] This result is in good accordance with that of thin g-C_3N_4 nanosheets exfoliated via the ultrasonication method. [18] Besides, the (002) peak blue shifting of NCN and SCN suggests the increasing interlayer distance, possibly due to the atomic distortion caused by heteroatom doping. [37] At the same time, the amorphous crystalline structures of NCN and SCN will boost an accelerated photocatalytic performance as described elsewhere. [21]

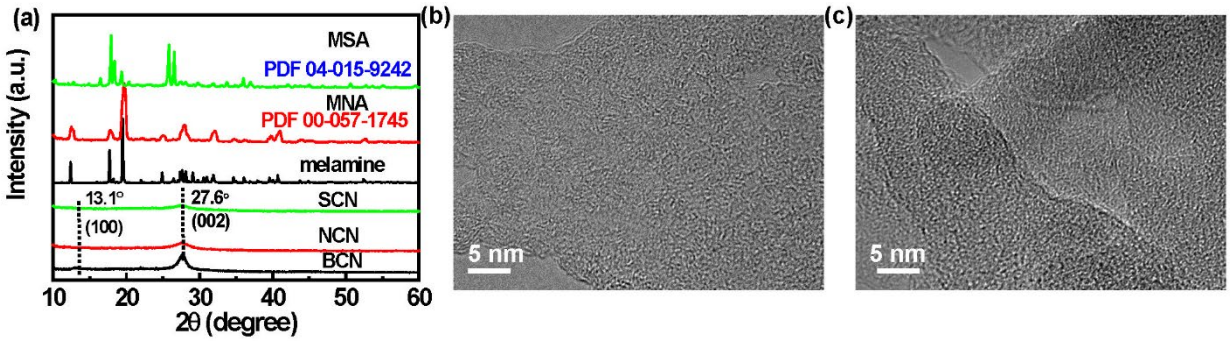

Figure 4.4 (a) XRD patterns of precursors and corresponding carbon nitride samples; High-resolution TEM images of **(b)** NCN and **(c)** SCN.

To probe how our rational structure engineering affects the pore structure, the N_2 adsorption-desorption isotherms were recorded (**Figure 4. 5a**). The isotherms are identified as type III with an H3 hysteresis loop at high P/P_0, revealing the slit-shaped pores caused by the

aggregates of plate-like particles. Notably, the specific surface areas of NCN and SCN are calculated to be 212.5 and 199.0 m^2 g^{-1}, 13 and 12 times larger than that of BCN. A stark contrast can be visually seen from the digital photos in which the foam-like NCN and SCN exhibit much higher volume at the same weight in comparison with BCN (Insert, **Figure 4. 5a**). According to the BJH pore size distribution profiles (Insert, **Figure 4. 5a**), both NCN and SCN show the hierarchically porous structure with obvious mesopores in the range of ~ 2.8 and 45 nm. These pores are supposed to be generated after the release of corrosive gases during the decomposition of protonated melamine. Remarkably, this in-situ acid-assisted exfoliation and etching process dramatically expand the pore volumes of NCN and SCN to 1.55 and 1.18 cm^3 g^{-1}, which are 2.1~40 times larger than those of the previous report (0.08-0.74 cm^3 g^{-1})[7,21,22,38–45] (**Figure 4. 5b**). The enhanced specific surface area favors the reaction rate simply by exposing more active sites to the reactants. While the ultra-large pore volumes do in a different way, namely, higher pore volumes generally could provide more inner voids as nano-reactors to physically confine the reactants in certain spaces, improve the concentrations of active species and thus dynamically facilitate the mass transfer (**Figure 4. 5c**). Based on the above analysis, one can figure out that HNO_3 plays a slightly more positive role than H_2SO_4 in nanosheets exfoliation and textual properties. We ascribe this mainly to the stronger oxidizing property of HNO_3 as a stronger oxidization ability can assist a more favorable thermal exfoliation activity, which has been proven by the repeated O_2 etching experiment. [17] To sum up, our design on structure engineering greatly changes the morphology from stacking aggregates into thin porous nanosheets with several atoms' thickness while exhibiting a defective surface and ultra-large pore volumes.

4.3.2 XPS and FT-IR analysis

Apart from morphology engineering, the surface chemical compositions and doping state are of vital importance to understand the inner mechanism for the photocatalytic reaction. The composition of carbon nitride has an extremely wide interval of $0.55 < C/N < 4.0$. The wide region of homogeneity makes carbon nitride unique because its chemical and electronic characteristics are adjustable by doping with various non-metal atoms in the essential composition expansion. In our case, the surface compositions in **Table 4. 1** reveal that NCN and SCN have high C/N ratios of 1.21 and 0.82, much higher than that of BCN (0.71), suggesting the high doping concentration of C atoms. Specifically, NCN shows the highest C doping level of 10.64%, which is 2.6 times higher than SCN, indicating HNO_3 plays a more profound effect on C-doping than H_2SO_4. We ascribe this to the more corrosive and etching ability of HNO_3, which has been verified in our previous work. [46] Moreover, the successful O-doping for NCN and SCN is confirmed as seen in **Table 4. 1**.

Table 4.1 Surface compositions of the as-prepared catalysts obtained from the XPS analysis (at. %).

Sample	C[1]	N[1]	O[1]	C/N mole ratio
NCN	51.44	42.44	4.83	1.21
SCN	44.06	53.52	2.31	0.82
BCN	40.8	57.12	2.07	0.71

[1] at. %

According to the high-resolution XPS spectra, the structural details can be refined. As shown in **Figure 4. 5d**, the main peak of C 1s for BCN is deconvoluted into three parts assigning to

C-C (C-1, 284.5 eV) and N-C=N (C-3, 288.3 eV), [47] whereas a new peak of C-O-C (C-2, 285.4 eV) is found in NCN and SCN. This further demonstrates the presence of O dopants in the tri-s-triazine units due to the thermal polymerization of protonated melamine and the decomposition of counterions. Based on the fitting result and the specie fractions (**Figure 4. 5g**), NCN witnessed a significant increase of C-C from 9.1 to 37.9 % due to the substitution of N sites with C atoms, explaining the high ratio of C/N. Meanwhile, the proportion of N undergoes an evident decrease from 18.7 (BCN) to 9.8 % (NCN) and 9.4 % (SCN), respectively. The increased C atomic ratio endows the formation of additional C-C bonds instead of N-C=N bonds, in good agreement with the XPS results (**Figure 4. 5d-e**) and species fractions.

As shown in **Figure 4. 5f**, O-doping can also be confirmed by the presence of two new peaks assigned as O-C-N (O-1, 531.4 eV), and C-O-C (O-3, 533.5 eV) in comparison with the non-doped BCN with the only surface absorbed water (O-2, 532.5 eV). Therefore, the acid-assisted strategy plays an important role in O-doping as the generated corrosive gas could assist the partial oxidation of C-N=C aromatic units.[48] Taking account of the total O content, specific surface area, NCN shows a slightly higher fraction, 1.16 times larger than that of SCN, but an overwhelming O-doping level than BCN.

The new species analyzed in the XPS result (C-O-C, C-C) were also detected by the FT-IR technique. As shown in **Figure 4. 5h**, similar to BCN, NCN and SCN display the characteristic peaks around 1200-1700 and 805 cm^{-1}, indicating the stretching mode of the amino group, aromatic C-N heterocycle and the breathing mode of the triazine units.[49] This confirms the basic triazine units of carbon nitride are well reserved after the precursor modification. However, compared with the pristine BCN, two new peaks assigned to the stretching mode of

C-O-C appear at 1010 and 1267 cm^{-1}, [50] which reveals the successful O-doping. Additionally, the other two peaks at 772 and 1429 cm^{-1} can be ascribed to the rocking mode of C-C and bending mode of C-H, suggesting C atoms might substitute the bridging N in the triazine matrix. [51] Thus, based on the above XPS results, we proposed a C/O-doped g-C_3N_4 structure of $C_{28}N_{25}O_2$ in **Figure 4. 5i**.

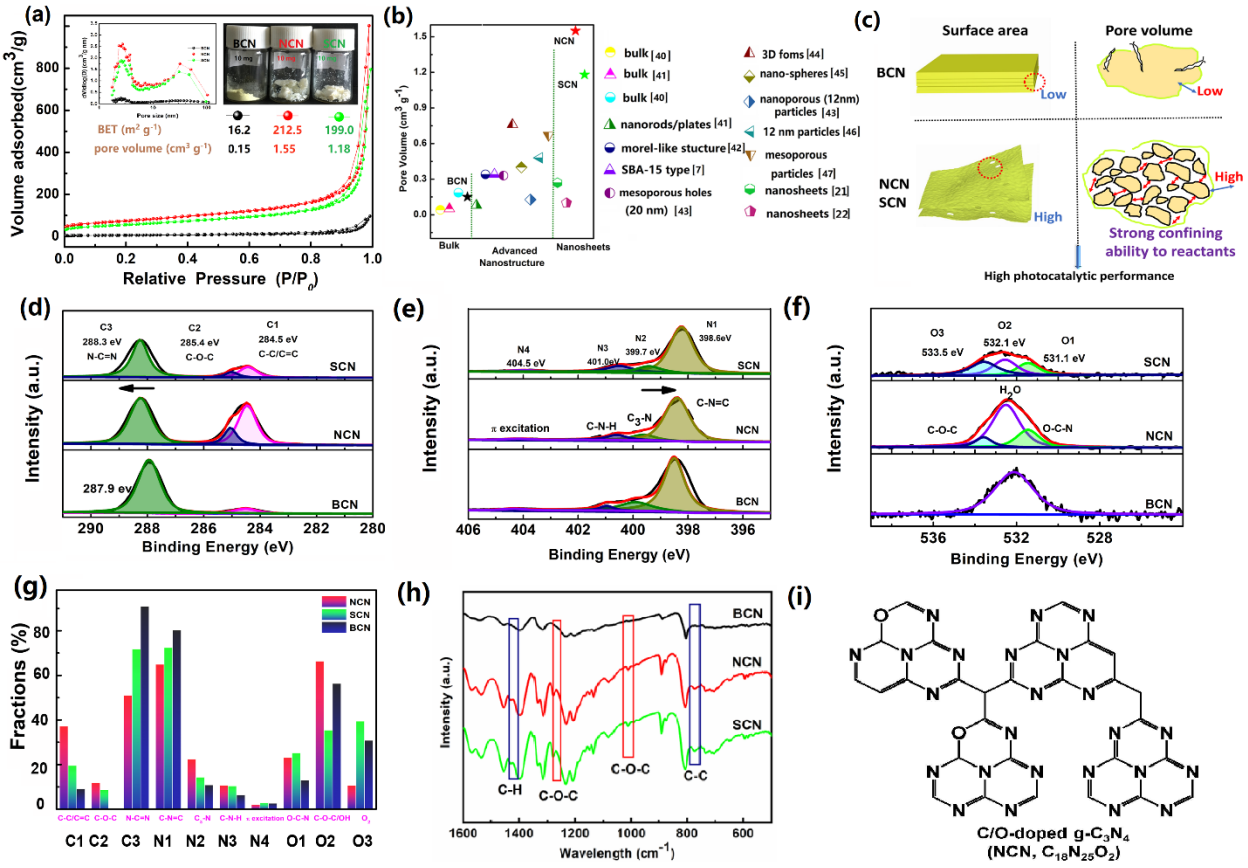

Figure 4.5 (a) N_2 adsorption-desorption isotherms (insert: digital image of carbon nitride samples); **(b)** Schematic illustration of the different roles for surface area and pore volume; **(c)** Literature comparison of pore volumes of BCN, NCN, and SCN. Core-level XPS spectra of **(d)** C 1s; **(e)** N1s; **(f)** O1s; **(g)** Fractions of various species of BCN, NCN, SCN; **(h)** FT-IR spectra of BCN, NCN, and SCN; **(i)** Proposed chemical structure of NCN.

4.3.3 DFT calculation

To gain a deep insight into how the C and O dopants affect the atomic structure and subsequently alter the electronic properties of g-C_3N_4, DFT calculation based on the experimental XPS result was performed, choosing the HNO_3-assisted synthesized NCN ($C_{18}N_{25}O_2$, **Figure 4. 5i**) as an example. The theoretical calculations would be expanded in the following parts: i) the doping positions of C and O dopants; (ii) the enhanced electronic polarization (Bader charge and bong lengths); and iii) the formation of delocalization π bond.

4.3.3.1 Doping positions

Unlike the homogenous carbon materials, the substituted positions of the foreign atoms into the g-C_3N_4 matrix must be considered due to the different chemical environments of C and N atoms. Therefore, the formation energy (E_{form}) of foreign C and O atoms doping to the g-C_3N_4 unit was calculated. Assuming the doping order which N atom is firstly substituted by C (**Figure 4. 6**, route A), and it was found that β is the best position with the lowest E_{form} of 0.59 eV, whereas α and γ positions witness higher energies of 0.75 and 2.21 eV using *Equation 1*:

$$E_{form} = E(C-CN) + mE(C) + nE\ (N) - E(CN) - E(C) \quad (1)$$

where *E(CN)* and *E (C-CN)* are the total energies of the original structure (**Figure 4. 6a'**) and C-substituted structure (**Figure 4. 6b'**), m and n are the numbers of the substituted C and N atom, *E(N)* and *E(O)* are equal to *E(N_2)/2* and *E(O_2)/2*, *E(C)* is obtained from *E(graphene)/2.* The positive values of E_{form} imply that C-CN obtained from initial C-doping is not very stable. Thus the other doping order which O atom is firstly doped is discussed in route B. Obviously, in the first step, the γ' is the most stable position for O atom with the lowest E_{form} of -0.97 eV. After O-doping, 7 potential C-substituted positions are studied, and the foreign C atom prefers the outer bridge position reflecting the lowest E_{form} of -1.41 eV via *Equation 2*:

$$E_{form} = E(OC - CN) + mE(C) + nE\ (N) - E(O - CN) - E(C) \quad (2)$$

where *E(O-CN)* and *E (OC-CN)* are the total energies of the O-substituted CN structure (**Figure 4. 6c'**) and final O/C-doped CN structures (**Figure 4. 6d'**). The negative E_{form} of each doping process indicates that route B is more dynamically favorable than route A. To this end, we mainly choose the outer bridged and two-coordinated N sites for C and O substituted positions, respectively. This result further demonstrates the reasonable chemical structure of NCN proposed in **Figure 4. 5i**.

4.3.3.2 Enhanced electronic polarization

It is of vital significance to boost the charge transport process and charge separation efficiency in the photocatalytic reaction. As we know, a shortened diffusion pathway and strong driving force for electrons (or charge) will expedite the redox kinetics of the active species. In this scenario, we further examined both the change of electronic density (Bader charge) and bond lengths of the bulk material (BCN, **Figure 4. 6b**) and C/O-doped g-C_3N_4 (NCN, **Figure 4. 6c**). After the doping process, as shown in **Figure 4. 6d**, C atoms show lower electronic density (*i.e.,* a 0.18 eV decrease of C4 atom) while N atoms witness an opposite tendency (*i.e.,* a 0.12 eV increase of N4 atom). Namely, the electronic density of C atoms becomes more positive, while N atoms become more negative. This result shows good agreement with the red/blue shift of C-3/N-1 peaks in the XPS spectra (**Figure 4. 6d, e**). The olive and cyan iso-surfaces in **Figure 4. 6e** represent the region of net electron accumulation and deficit, respectively. Obviously, O atoms attract the electron density from C atoms. Therefore, the strong electronic polarization is constructed in the C/O-doped g-C_3N_4, which allows a faster electron transport process from inner space to the bulk surface. [52,53]Additionally, this doping effect further

reduces the bond lengths by ~0.02 Å between the dopant to the neighboring C and N atoms (**Figure 4. 6f**), which further shortens the electronic charge transfer pathway.

4.3.3.3 Delocalization π bond

The formation of the delocalization π bond has been demonstrated to enhances the conductivity of organic compounds.[54] As discussed above, C atoms prefer to substitute the three-coordinated N sites (**Figure 4. 6d'**), which are surrounded by three sp^2 hybridized C=N-C bonds. After C doping, the formation of a new delocalization π bond is corroborated to be formed by the theoretically calculated π orbital distribution diagram (**Figure 4. 6g**). Unlike the original N atoms with poor electrons transmit activity, these new π bonds would act as the electrons "tache" to connect the around heptazine rings, enhance the conductivity and allow the electrons with a more smooth transport pathway. As a result, the charge transfer resistance is predicted to be largely reduced.

Based on the above theoretical calculations, surface engineering induced by the foreign C and O dopants is critical to the electronic property optimization for tri-s-triazine units. In a short conclusion, C-doping favors the formation of the delocalization π bond and improves the conjugated degree of g-C_3N_4 matrix while O-doping imparts the original g-C_3N_4 matrix with stronger electronic polarization effect, shorter bond lengths. The former one is effective to largely reduce the charge transfer resistance, whereas the latter one renders a shorter electron diffusion pathway with larger propelling force. These two factors combine to facilitate the electron transfer rate and favor the separation of electron-hole pairs. Thus, an enhanced catalytic activity is speculated on these advanced carbon nitride catalysts prepared by the in-situ acid-assisted exfoliation strategy.

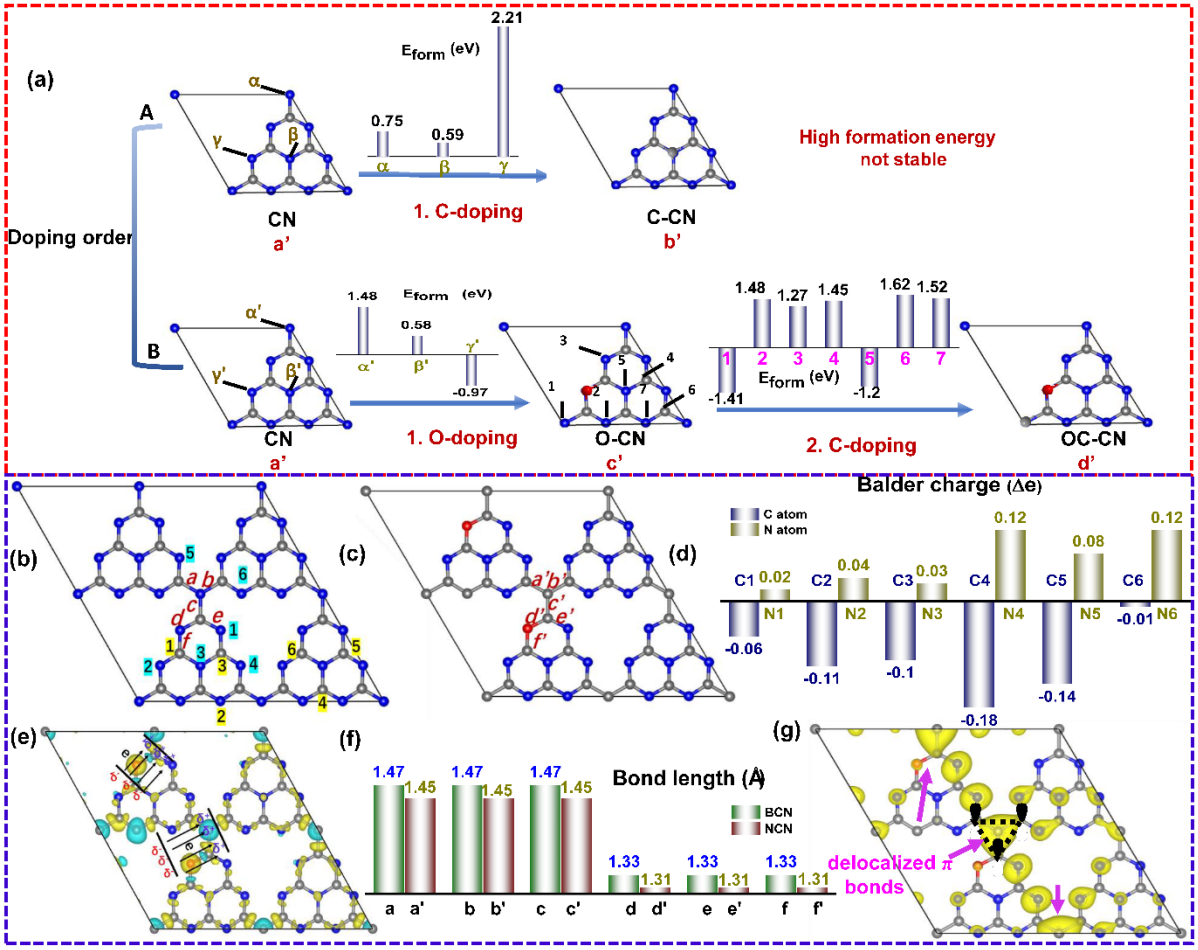

Figure 4.6 (a) The illustration of various C(O)-doped g-C_3N_4 with different doping order: (a') CN; (b') C-CN; (c') O-CN and (d') OC-CN; **(b)** Configuration of original non-doped BCN; **(c)** Optimized configuration of NCN; **(d)** Bader Charge change; **(e)** Differential charge density between BCN and NCN; **(f)** Bond lengths of BCN and NCN and **(g)** π orbital distribution (VBM-5) of NCN in DFT (C, N, and O atoms are shown in grey, blue and red. Olive and cyan illustrate the increase and decrease of electron distributions).

4.3.4 Enhanced photoelectrochemical (PEC) performance

Based on the rational design of the structural and doping strategy discussed above, the PEC performance is expected to be greatly improved. Therefore, a series of experiments were conducted in a typical three-electrode system under a chopped light. Under the same experimental condition in dark, the linear sweep voltammetry (LSV) polarization curves

exhibit that the currents at the NCN and SCN electrodes are around 4-5.5 folders larger than that at the BCN electrode at 0.6 V (**Figure 4. 7a**). It is worth to mention that at the theoretical potential of oxygen evolution reaction (OER) of 0.24 V (*vs.* Ag/AgCl), the current densities under light irradiation are much higher than those in dark. That is, NCN and SCN display the photocurrents of 320, 260 μA cm^{-2}, respectively, around 61 and 50 times larger than that of BCN (2.6 μA cm^{-2}) (**Figure 4. 7b**). The enhanced dark current densities are mainly contributed to the enhanced bulk conductivity induced by the delocalization π bond (**Figure 4. 6g**). The same trend is observed under visible light irradiation.

The reduced bulk charge transfer resistance (R_{ct}) and enhanced PEC charge transport process predicted by our DFT calculation are further demonstrated by the electrochemical impedance spectra (EIS) in dark and illumination conditions. As can be seen from **Figure 4. 7c**, the EIS data matches well with the fitting curves using the R(QR) equivalent circuit. The enhanced bulk conductivity can be reflected by the dramatically decreasing diameters of the semicircle (in the dark) for NCN and SCN. HNO_3-assisted synthesized g-C_3N_4 shows the lowest charge transfer resistance (R_{ct}) of 8.6×10^3 Ω cm^2, one magnitude order smaller than that of BCN (5.57×10^4 Ω cm^2), followed by SCN (2.14×10^4 Ω cm^2) (**Figure 4. 7d**). Notably, the acid-assisted exfoliating strategy favors the PEC performance; that is, under irradiation, the resistances continue to decrease, of which NCN drops from 8.6×10^3 to the lowest value of 5.19×10^3 Ω cm^2. This indicates light irradiation can drive to produce more electrons and facilitates the charge transfer after excitation. Besides, the changed surface electronic state caused by C/O-doping can be further confirmed by the increased charge transfer capacitance (C_{CT}) according to the following Equation: [55–57]

$$C_{CT} = (Q)^{\frac{1}{n}} R_{ct}^{\frac{(1-n)}{n}} \quad (3)$$

where Q and n are the frequency-independent parameters. C_{CT} of NCN and SCN are calculated to be 3.97×10^{-5} and 7.01×10^{-5} μF cm^{-2}, higher than 3.51×10^{-5} μF cm^{-2} of BCN (**Table 4. 2**). Consisting of the DFT calculation, the PEC results mentioned above also demonstrate the improved charge transport, separation process, enhanced bulk conductivity, and electronic surface state.

Table 4.2 EIS results of g-C_3N_4 samples measured in dark and simulated solar light.

Light	Samples	R_{sol} (Ω cm^2) [a]	Q (Ω^{-1} s^n) [b]	n[c]	R_{ct} (Ω cm^2) [d]	C_{CT}[e]
Illumination	BCN	11.68	3.40×10^{-5}	0.8023	3.33×10^{4}	3.51×10^{-5}
	NCN	9.59	4.25×10^{-5}	0.9258	5.19×10^{3}	3.97×10^{-5}
	SCN	10.15	7.19×10^{-5}	0.9319	9.83×10^{3}	7.01×10^{-5}
Dark	BCN	11.72	3.32×10^{-5}	0.9491	5.57×10^{4}	3.43×10^{-5}
	NCN	9.50	3.57×10^{-5}	0.9547	8.59×10^{3}	3.37×10^{-5}
	SCN	10.23	3.41×10^{-5}	0.9062	2.14×10^{4}	3.37×10^{-5}

Note: a: electrolyte solution, b, and c: the frequency-independent parameters, d: surface charge transfer resistance, e: charge transfer capacitance.

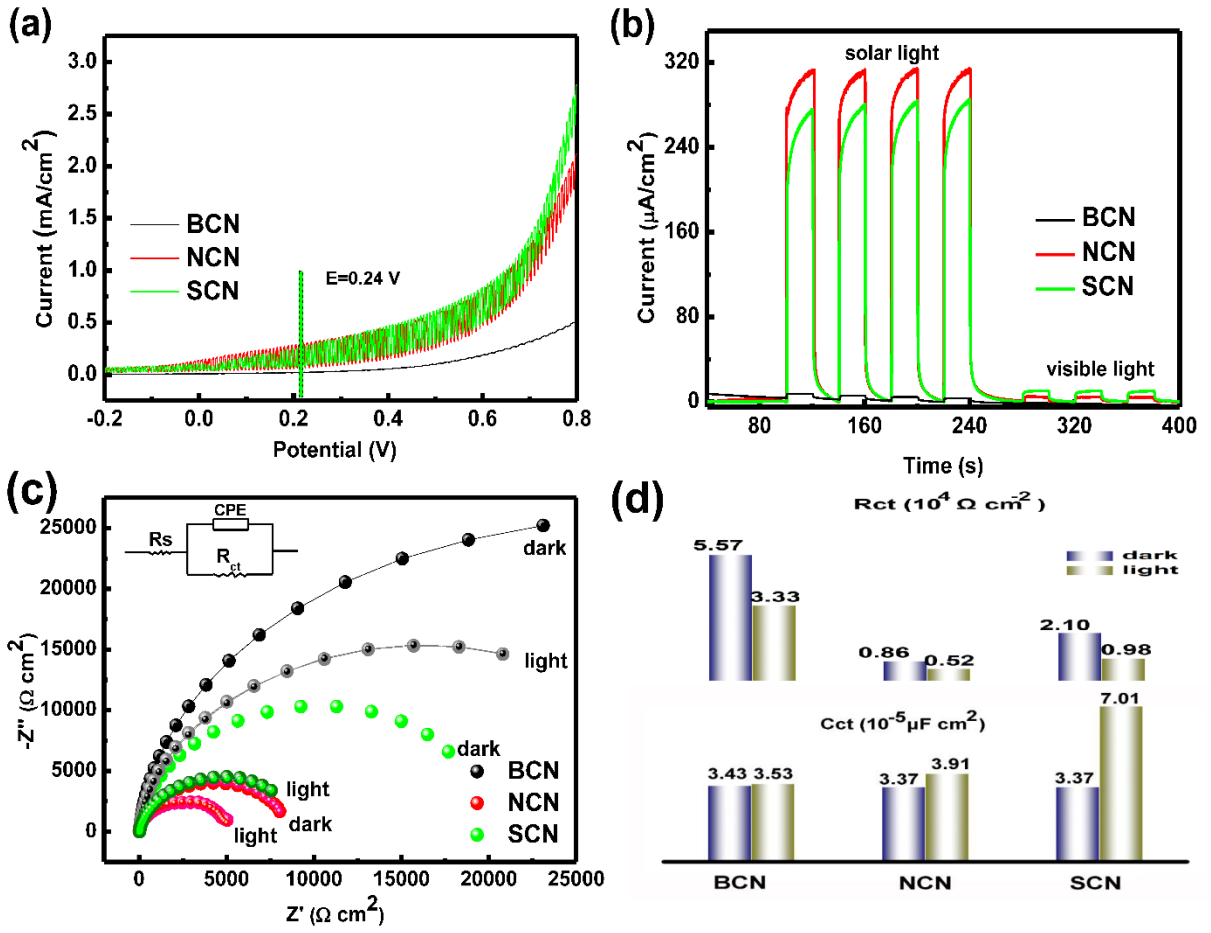

Figure 4.7 (a) The linear sweep voltammetry (LSV); **(b)** Transient photocurrent responses; **(c)** EIS Nyquist plots; Comparison of **(d)** R_{ct} and **(e)** C_{ct} under dark and simulated sunlight in 0.35 M Na_2S/0.25 M Na_2SO_3 aqueous solution (Insert: R(QR) equivalent circuit for Nyquist plots).

4.3.5 Optical properties and band structures

To study the effects of our novel structural and doping strategy have on the optical properties, photoluminescence (PL) spectroscopy was performed to probe the lifetime of the electron-hole pairs (**Figure 4. 8a**). The prolong lifetime was analyzed using the triple-exponential function via the Gaussian instrument response: [58,59]

$$I(t) = A + B_1 \bullet e^{\left(-\frac{t}{\tau 1}\right)} + B_2 \bullet e^{\left(-\frac{t}{\tau 2}\right)} + B_3 \bullet e^{\left(-\frac{t}{\tau 3}\right)} \quad (4)$$

$$R_i = B_i / \sum_{i=1}^{3} B_i \quad (5)$$

$$\tau_{average} = \sum_{i=1}^{3} R_i \cdot \tau_i \ (6)$$

where A, B_1, B_2, and B_3 are constants obtained by fitting each decay curve. The curves fit well with triple-exponential function for the value of χ^2 in an ideal range of 0.9~1.1 (**Table 4. 3**). To accurately depict the decay time, $\tau_{average}$ is used to calculate the lifetime of photocarriers (Formulas 4-6, **Table 4. 3**). Obviously, NCN shows the longest lifetime of 5.64 ns, followed by SCN with a lifetime of 5.59 ns. BCN exhibits the shortest time of only 2.79 ns. The prolonged lifetimes combining with the high photocarriers separation efficiency would endow the electrons with a longer time to be involved in the H_2 reduction reactions.

Table 4.3 The fitting parameters of PL decay curves for various samples.

Sample	τ_1(ns)	τ_2(ns)	τ_3(ns)	B_1	B_2	B_3	R_1(%)	R2(%)	R3(%)	A	χ^2	a_{verage}(ns)
BCN	2.254	8.125	48.469	1.166	0.097	0.004	0.92	0.070	0.003	1.820	1.102	2.79
NCN	3.028	11.967	67.193	0.375	0.087	0.015	0.799	0.185	0.015	9.257	1.082	5.64
SCN	3.678	14.284	78.081	0.471	0.063	0.005	0.873	0.116	0.009	5.485	1.088	5.59

UV-vis diffuse absorbance data (**Figure 4. 8b, c**) and Mott-Schottky plots (**Figure 4. 8d**) were analyzed to explore the change of band structures arising from the exfoliating and doping strategy. Unlike the hetero-atom-doping (C, O, P) described elsewhere, [20,21,60] these C/O-doped g-C_3N_4 nanosheets show an inferior absorbing ability of visible light which can be seen from the 8-10 nm blue shifting of band edge (**Figure 4. 8b**). The calculated band gaps, in decreasing order, are NCN (3.01 eV), NCN (2.96 eV), and BCN (2.78 eV) (**Figure 4. 8c**). The enlarged band gaps are ascribed to the strong quantum effect caused by the ultra-thin atomic-thick g-

C_3N_4 nanosheets. The positions of the valence band (VB) and conduction band (CB) are crucial for the photocatalytic ability. The more negative CB is, the stronger photoreduction ability will be, vice versa. The CB potentials are -1.28, -1.45, and -1.41 V (*vs.* AgCl/Ag, pH=7) for BCN, NCN and SCN according to the Mott-Schottky plots (**Figure 4. 8d**), which can be converted to -0.67, -0.84, -0.80 V (*vs.* NHE, pH=7) via the following equation:

$$E_{RHE} = E_{NHE} + 0.059\,\mathrm{pH} \qquad (7)$$

$$E_{NHE} = E_{vs.Ag/AgCl} + 0.197 \qquad (8)$$

Based on the values of band gaps calculated above, the potentials of CB, VB are given in **Figure 4. 8e**. Though the ability to absorb visible light is weakened, the bigger band gaps extend the reductive ability, giving rise to a more favorable thermodynamic driving force for H_2 evolution.

4.3.6 Photocatalytic performance

The photocatalytic performance of the as-obtained g-C_3N_4 samples for H_2 production was evaluated under UV and visible light irradiation at an intensity of 100 mW cm^{-2}. BCN shows a very low evolution rate of 156.9 μmol g^{-1} h^{-1} under solar light irradiation (**Figure 4. 8f**). In contrast, NCN exhibits a significantly increased evolution rate of 830.1 μmol g^{-1} h^{-1}, 5.4 times higher than that of BCN, and slightly higher than that of SCN (689.4 μmol g^{-1} h^{-1}). Based on the UV-visible diffusion reflectance absorption spectra (**Figure 4. 8b**), all samples exhibit strong light-harvesting ability with a wavelength smaller than 400 nm. However, the weak absorbance in the range of 400-500 nm indicates the poorer light utilization in visible light irradiation than in UV light. As expected, under visible light irradiation (λ>400 nm), NCN, SCN and BCN show a hydrogen evolution rate of *ca.*115.5, 110.5, and 29.7 μmol g^{-1} h^{-1}, 5-7

folder lower than those in UV irradiation. However, NCN and SCN still display a ~ 4 times higher evolution rate in comparison with BCN. Additionally, the H_2 evolution rates of NCN and SCN are comparable and even better than those of reported g-C_3N_4-based materials (**Table 4. 4**). The order of photocatalytic performance is in consistence with those of BET surface area, pore volume, charge transfer resistance, PEC activity as well as PL result. This explains why NCN is superior to SCN as HNO_3 is better than H_2SO_4 in structure and surface engineering. Although the light-yellow color of as-prepared catalysts would result in an inferior ability on absorbing visible light (**Figure 4. 8b**), the shortage could be addressed by the enhanced numbers of active sites, shorten charge diffusion pathway and superior behaviors of photocarriers.

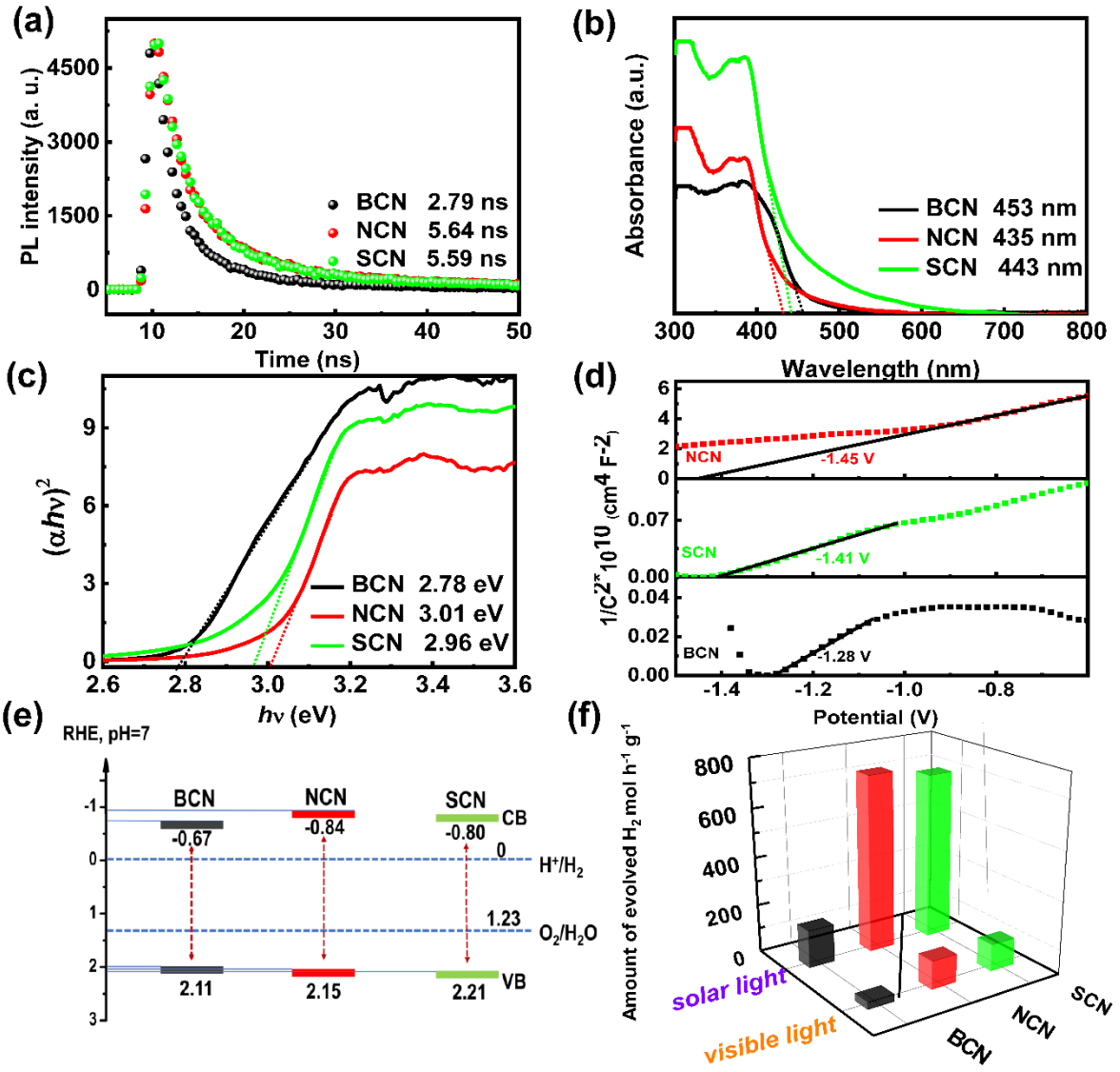

Figure 4.8 (a) Time-resolved PL decay spectra; (b) UV-visible diffusion reflectance adsorption spectra; **(c)** $(\alpha h\nu)^2$ versus *hν* plot obtained from the UV-visible diffusion reflectance adsorption spectra; **(d)** Mott-Schottky plots measured in 0.5 M Na_2SO_4 (vs. Ag/AgCl); **(e)** Band structure diagram of the as-prepared BCN, NCN, and SCN; **(f)** Hydrogen evolution column from water containing 10 vol% TEOA scavengers under simulated sunlight and visible light of BCN, NCN, and SCN.

Table 4.4 Comparison of hydrogen evolution rate under solar and visible light irradiation of g-C_3N_4 based materials and NCN, SCN.

g-C_3N_4-based materials	**H_2 evolution rate under solar light ($\mu mol\ g^{-1}\ h^{-1}$)**	**H_2 evolution rate under visible light ($\mu mol\ g^{-1}\ h^{-1}$)**	**Reference**	**Year published**
black-TiO_2/g-C_3N_4	555.8	N/A	61	2017
g-C_3N_4/monoethanolamine	55.0	28.1	62	2017
AuPd/g-C_3N_4	N/A	107	63	2017
N-deficient g-C_3N_4 nanosheets	N/A	69.0	64	2017
OCNA-6	N/A	68.28	65	2018
$MoSe_2$/g-C_3N_4	N/A	136.8	66	2018
NCN nanosheets	772.1	115.5	this work	----
SCN nanosheets	689.4	110.5	this work	----

4.3.7 Stability of photocatalyst

Figure 4. 9 displays the typical structure and surface stability test of the as-prepared NCN and SCN. As validated from the HR-TEM images (**Figure 4. 9a, b**), thin nanosheets with pores are in good accordance with those of fresh samples (**Figure 4. 9b-c**). For the XRD patterns, the positions of the typical (002) diffraction peak remain unchanged at 27.6°, and the similar intensities are displayed (**Figure 4. 9c**). Therefore, the as-prepared NCN and SCN show robust stability on the morphology and crystalline structure. To further investigate the change of surface chemical compositions, high-resolution core-level XPS spectra were carried out. As

shown in **Figure 4. 9d-i**, the C1s, N1s, and O1s spectra exhibit similar profiles before and after hydrogen evolution reactions, suggesting the ignorable composition changes (**Table 4. 5**). Thus, NCN and SCN exhibit good structure and surface stability for the water splitting.

Table 4.5 Surface compositions of the catalysts obtained from the XPS analysis(at.%).

Sample	C[1]	N[1]	O[1]	C/N mole ratio
NCN	52.78	41.98	5.24	1.25
SCN	44.37	52.20	3.43	0.85

[1] at. %

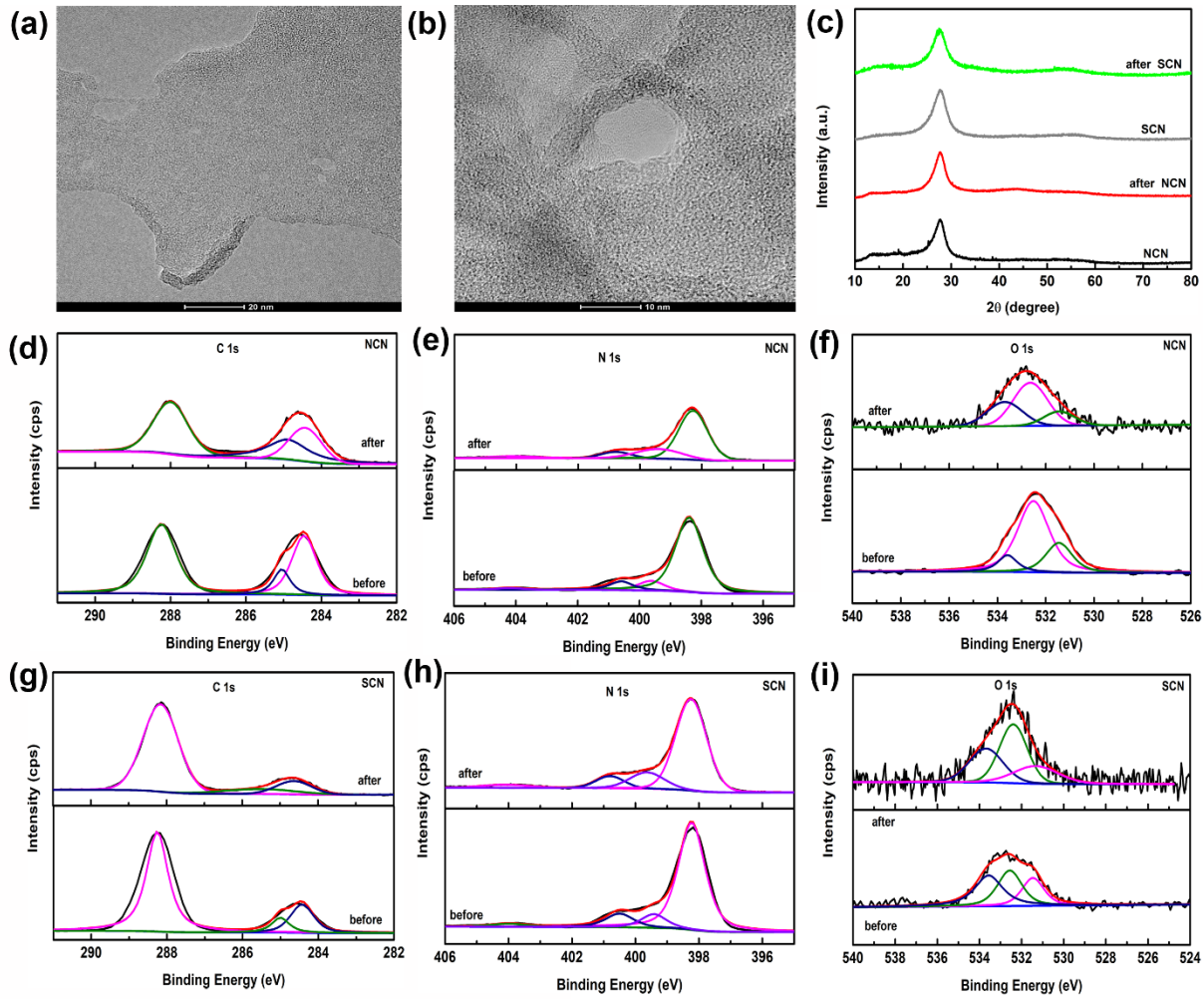

Figure 4.9 HR-TEM images of **(a)** NCN and **(b)** SCN after the hydrogen evolution reaction; **(c)** XRD patterns and **(e-i)** the core-level XPS spectra of C 1s, N 1s, and O 1s of NCN and SCN before and after the hydrogen evolution reaction.

It is widely acknowledged that five sequential steps are involved in various photocatalytic reactions as follows: 1) interface contact; 2) generation of electron-hole pairs via photoexcitation; 3) electron-hole pairs separation; 4) charge transfer and 5) redox reaction.[67–69] These steps are tightly connected with the texture, surface and/or chemical properties of a photocatalyst. Based on the above results, the unique features of NCN would contribute to the enhanced catalytic performance: 1) the porous structure composed of interconnected ultrathin nanowalls provides a large surface area and exceptional high pore volume. Such a texture

feature would facilitate the diffusion of reactants and provide efficient electron transfer pathways; 2) O dopants render efficient generation of photocarriers and charge transfer owing to the electronic polarization effect and shortened bond lengths; 3) C-doping improves the electronic conductivity due to the formation of delocalized π bonds. Therefore, under light irradiation, the electron-hole pairs are readily generated while the photocarriers possess higher reductive activity due to the changed positions of CB. As a result, the recombination of electron-hole pairs is suppressed. Therefore, the efficient redox reaction can be achieved in the triethanolamine (TEOA)/H_2O system, leading to the significantly improved PEC and hydrogen evolution performance.

4.4. Conclusion

In summary, a novel and facile engineering strategy on architecture and surface doping have been developed to prepare the porous ultrathin C/O-doped g-C_3N_4 nanosheets by the protonation of melamine with inorganic acids (HNO_3, H_2SO_4) via self-assembly and subsequent thermal polymerization. The inorganic acid is of vital importance for the formation of porous structure and doping nature. Namely, the thermal decomposition of counterions (NO_3^- and SO_4^{2-}) not only act as the exfoliating agent and generate gas bubbles for the formation of thin nanoshells interconnected to the porous structure but also endows the foreign C and O into carbon nitride matrix. Due to the synergistic contribution of unique porous textural and intrinsically doping features, the enhanced exposing sites, stronger electronic polarization effect and reduced bond lengths caused by the discrepancy of Bader Charge, as well as the enhanced conductivity have shortened the charger diffusion pathway, boosted charge transfer rate either experimentally or theocratically. Thus, a prolonged lifetime and high

charge separation efficiency have been demonstrated. As a result, NCN and SCN with good electronic conductivity exhibit remarkably enhanced PEC performance with high photocurrent density, 60 and 50 times higher than that of BCN. More importantly, the H_2 evolution rates of NCN is around 5.1 and 3.7 folders larger than those of BCN under the solar and visible light irradiation, respectively. This method would pave a new "green" way to synthesize highly efficient carbon nitride-based photocatalyst via the structural modification and doping modulation from the molecular level.

4.5. Reference

(1) Wang, X.; Maeda, K.; Thomas, A.; Takanabe, K.; Xin, G.; Carlsson, J. M.; Domen, K.; Antonietti, M. A Metal-Free Polymeric Photocatalyst for Hydrogen Production from Water under Visible Light. *Mater. Sustain. Energy A Collect. Peer-Reviewed Res. Rev. Artic. from Nat. Publ. Gr.* **2010**, *8* (1), 271–275.

(2) Chen, X.; Zhang, J.; Fu, X.; Antonietti, M.; Wang, X. Fe-g-C3N4-Catalyzed Oxidation of Benzene to Phenol Using Hydrogen Peroxide and Visible Light. *J. Am. Chem. Soc.* **2009**, *131* (33), 11658–11659.

(3) Zhao, L.; Ye, F.; Wang, D.; Cai, X.; Meng, C.; Xie, H.; Zhang, J.; Bai, S. Lattice Engineering on Metal Cocatalysts for Enhanced Photocatalytic Reduction of CO_2 into CH_4. *ChemSusChem* **2018**, *11* (19), 3524–3533.

(4) Wu, F.; Li, X.; Liu, W.; Zhang, S. Highly Enhanced Photocatalytic Degradation of Methylene Blue over the Indirect All-Solid-State Z-Scheme g-C_3N_4-RGO-TiO_2 Nanoheterojunctions. *Appl. Surf. Sci.* **2017**, *405*, 60–70.

(5) Hou, Y.; Li, J.; Wen, Z.; Cui, S.; Yuan, C.; Chen, J. N-doped Graphene/Porous g-C_3N_4 Nanosheets Supported Layered-MoS_2 Hybrid as Robust Anode Materials for Lithium-Ion Batteries. *Nano Energy* **2014**, *8*, 157–164.

(6) Tian, N.; Zhang, Y.; Li, X.; Xiao, K.; Du, X.; Dong, F.; Waterhouse, G. I. N.; Zhang, T.; Huang, H. Precursor-Reforming Protocol to 3D Mesoporous g-C_3N_4 Established by Ultrathin Self-Doped Nanosheets for Superior Hydrogen Evolution. *Nano Energy* **2017**, *38*, 72–81.

(7) Chen, X.; Jun, Y. S.; Takanabe, K.; Maeda, K.; Domen, K.; Fu, X.; Antonietti, M.; Wang, X. Ordered Mesoporous SBA-15 Type Graphitic Carbon Nitride: A Semiconductor Host Structure for Photocatalytic Hydrogen Evolution-with Visible Light. *Chem. Mater.* **2009**, *21* (18), 4093–4095.

(8) Gao, X.; Jiao, X.; Zhang, L.; Zhu, W.; Xu, X.; Ma, H.; Chen, T. Cosolvent-Free Nanocasting Synthesis of Ordered Mesoporous g-C_3N_4 and Its Remarkable Photocatalytic Activity for Methyl Orange Degradation. *RSC Adv.* **2015**, *5* (94), 76963–76972.

(9) Groenewolt, M.; Antonietti, M. Synthesis of g-C_3N_4 Nanoparticles in Mesoporous Silica Host Matrices. *Adv. Mater.* **2005**, *17* (14), 1789–1792.

(10) Li, X. H.; Wang, X.; Antonietti, M. Mesoporous g-C_3N_4 Nanorods as Multifunctional Supports of Ultrafine Metal Nanoparticles: Hydrogen Generation from Water and Reduction of Nitrophenol with Tandem Catalysis in One Step. *Chem. Sci.* **2012**, *3* (6), 2170–2174.

(11) Lin, B.; An, H.; Yan, X.; Zhang, T.; Wei, J.; Yang, G. Fish-Scale Structured g-C_3N_4 Nanosheet with Unusual Spatial Electron Transfer Property for High-Efficiency Photocatalytic Hydrogen Evolution. *Appl. Catal. B Environ.* **2017**, *210*, 173–183.

(12) Portehault, D.; Giordano, C.; Gervais, C.; Senkovska, I.; Kaskel, S.; Sanchez, C.; Antonietti, M. High-Surface-Area Nanoporous Boron Carbon Nitrides for Hydrogen Storage. *Adv. Funct. Mater.* **2010**, *20* (11), 1827–1833.

(13) Bai, X.; Li, J.; Cao, C.; Hussain, S. Solvothermal Synthesis of the Special Shape (Deformable) Hollow g-C_3N_4 Nanospheres. *Mater. Lett.* **2011**, *65* (7), 1101–1104.

(14) Xiao, T.; Tang, Z.; Yang, Y.; Tang, L.; Zhou, Y.; Zou, Z. In Situ Construction of Hierarchical WO_3/g-C_3N_4 Composite Hollow Microspheres as a Z-scheme Photocatalyst for the Degradation of Antibiotics. *Appl. Catal. B Environ.* **2018**, *220*, 417–428.

(15) Tahir, M.; Cao, C.; Mahmood, N.; Butt, F. K.; Mahmood, A.; Idrees, F.; Hussain, S.; Tanveer, M.; Ali, Z.; Aslam, I. Multifunctional g-C_3N_4 Nanofibers: A Template-Free Fabrication and Enhanced Optical, Electrochemical, and Photocatalyst Properties. *ACS Appl. Mater. Interfaces* **2014**, *6* (2), 1258–1265.

(16) Zhao, Y.; Zhao, F.; Wang, X.; Xu, C.; Zhang, Z.; Shi, G.; Qu, L. Graphitic Carbon Nitride Nanoribbons: Graphene-Assisted Formation and Synergic Function for Highly Efficient Hydrogen Evolution. *Angew. Chemie Int. Ed.* **2014**, *53* (50), 13934–13939.

(17) Niu, P.; Zhang, L.; Liu, G.; Cheng, H. M. Graphene-like Carbon Nitride Nanosheets for Improved Photocatalytic Activities. *Adv. Funct. Mater.* **2012**, *22* (22), 4763–4770.

(18) Yang, S.; Gong, Y.; Zhang, J.; Zhan, L.; Ma, L.; Fang, Z.; Vajtai, R.; Wang, X.; Ajayan, P. M. Exfoliated Graphitic Carbon Nitride Nanosheets as Efficient Catalysts for Hydrogen Evolution under Visible Light. *Adv. Mater.* **2013**, *25* (17), 2452–2456..

(19) Zhang, X.; Xie, X.; Wang, H.; Zhang, J.; Pan, B.; Xie, Y. Enhanced Photoresponsive Ultrathin Graphitic-Phase C_3N_4 Nanosheets for Bioimaging. *J. Am. Chem. Soc.* **2013**, *135* (1), 18–21.

(20) Dong, G.; Zhao, K.; Zhang, L. Carbon Self-Doping Induced High Electronic Conductivity and Photoreactivity of g-C_3N_4. *Chem. Commun.* **2012**, *48* (49), 6178–6180.

(21) Ran, J.; Ma, T. Y.; Gao, G.; Du, X. W.; Qiao, S. Z. Porous P-Doped Graphitic Carbon Nitride Nanosheets for Synergistically Enhanced Visible-Light Photocatalytic H_2 Production. *Energy Environ. Sci.* **2015**, *8* (12), 3708–3717.

(22) Huang, Z. F.; Song, J.; Pan, L.; Wang, Z.; Zhang, X.; Zou, J. J.; Mi, W.; Zhang, X.; Wang, L. Carbon Nitride with Simultaneous Porous Network and O-Doping for Efficient Solar-Energy-Driven Hydrogen Evolution. *Nano Energy* **2015**, *12*, 646–656.

(23) Zhao, Z.; Sun, Y.; Dong, F.; Zhang, Y.; Zhao, H. Template Synthesis of Carbon Self-Doped g-C_3N_4 with Enhanced Visible to near-Infrared Absorption and Photocatalytic Performance. *RSC Adv.* **2015**, *5* (49), 39549–39556.

(24) Guo, C. X.; Xie, J.; Yang, H.; Li, C. M. Au@CdS Core–Shell Nanoparticles-Modified ZnO Nanowires Photoanode for Efficient Photoelectrochemical Water Splitting. *Adv. Sci.* **2015**, *2* (12), 1500135.

(25) Guo, C. X.; Li, C. M. Room Temperature-Formed Iron-Doped Nickel Hydroxide on Nickel Foam as a 3D Electrode for Low Polarized and High-Current-Density Oxygen Evolution. *Chem. Commun.* **2018**, *54* (26), 3262–3265.

(26) Volokh, M.; Peng, G.; Barrio, J.; Shalom, M. Carbon Nitride Materials for Water Splitting Photoelectrochemical Cells. *Angew. Chemie Int. Ed.* **2019**, *58* (19), 6138–6151.

(27) Wei, Y.; Wang, Z.; Su, J.; Guo, L. Metal-Free Flexible Protonated g-C_3N_4/Carbon Dots Photoanode for Photoelectrochemical Water Splitting. *ChemElectroChem* **2018**, *5* (19), 2734–2737.

(28) Wang, R.; Yan, J.; Zu, M.; Yang, S.; Cai, X.; Gao, Q.; Fang, Y.; Zhang, S.; Zhang, S. Facile Synthesis of Interlocking g-C_3N_4/CdS Photoanode for Stable Photoelectrochemical Hydrogen Production. *Electrochim. Acta* **2018**, *279*, 74–83.

(29) Bann, B.; Miller, S. A. Melamine and Derivatives of Melamine. *Chem. Rev.* **1958**, *58* (1), 131–172.

(30) She, X.; Liu, L.; Ji, H.; Mo, Z.; Li, Y.; Huang, L.; Du, D.; Xu, H.; Li, H. Template-Free Synthesis of 2D Porous Ultrathin Nonmetal-Doped g-C_3N_4 Nanosheets with Highly Efficient Photocatalytic H_2 Evolution from Water under Visible Light. *Appl. Catal. B Environ.* **2016**, *187*, 144–153.

(31) Liu, J.; Zhang, T.; Wang, Z.; Dawson, G.; Chen, W. Simple Pyrolysis of Urea into Graphitic Carbon Nitride with Recyclable Adsorption and Photocatalytic Activity. *J. Mater. Chem.* **2011**, *21* (38), 14398–14401.

(32) Lu, K.; Xu, J.; Zhang, J.; Song, B.; Ma, H. General Preparation of Three-Dimensional Porous Metal Oxide Foams Coated with Nitrogen-Doped Carbon for Enhanced Lithium Storage. *ACS Appl. Mater. Interfaces* **2016**, *8* (27), 17402–17408.

(33) Wang, X.; Zhang, Y.; Zhi, C.; Wang, X.; Tang, D.; Xu, Y.; Weng, Q.; Jiang, X.; Mitome, M.; Golberg, D.; et al. Three-Dimensional Strutted Graphene Grown by Substrate-Free Sugar Blowing for High-Power-Density Supercapacitors. *Nat. Commun.* **2013**, *4* (1), 1–8.

(34) Guoxiu, W.; Juan, Y.; Jinsoo, P.; Xinglong, G.; Bei, W.; Hao, L.; Jane, Y. Facile Synthesis and Characterization of Graphene Nanosheets. *J. Phys. Chem. C* **2008**, *112* (22), 8192–8195.

(35) Yuan, B.; Chu, Z.; Li, G.; Jiang, Z.; Hu, T.; Wang, Q.; Wang, C. Water-Soluble Ribbon-like Graphitic Carbon Nitride (g-C_3N_4): Green Synthesis, Self-Assembly and Unique Optical Properties. *J. Mater. Chem. C* **2014**, *2* (39), 8212–8215.

(36) McCrory, C. C. L.; Jung, S.; Peters, J. C.; Jaramillo, T. F. Benchmarking Heterogeneous Electrocatalysts for the Oxygen Evolution Reaction. *J. Am. Chem. Soc.* **2013**, *135* (45), 16977–16987.

(37) Jia, L.; Li, J.; Fang, W.; Song, H.; Li, Q.; Tang, Y. Visible-Light-Induced Photocatalyst Based on C-Doped $LaCoO_3$ Synthesized by Novel Microorganism Chelate Method. *Catal. Commun.* **2009**, *10* (8), 1230–1234.

(38) Jin, X.; Balasubramanian, V. V.; Selvan, S. T.; Sawant, D. P.; Chari, M. A.; Lu, G. Q.; Vinu, A. Highly Ordered Mesoporous Carbon Nitride Nanoparticles with High Nitrogen

Content: A Metal-Free Basic Catalyst. *Angew. Chemie - Int. Ed.* **2009**, *48* (42), 7884–7887.

(39) Dong, F.; Sun, Y.; Wu, L.; Fu, M.; Wu, Z. Facile Transformation of Low Cost Thiourea into Nitrogen-Rich Graphitic Carbon Nitride Nanocatalyst with High Visible Light Photocatalytic Performance. *Catal. Sci. Technol.* **2012**, *2* (7), 1332–1335.

(40) Bai, X.; Wang, L.; Zong, R.; Zhu, Y. Photocatalytic Activity Enhanced via g-C_3N_4 Nanoplates to Nanorods. *J. Phys. Chem. C* **2013**, *117* (19), 9952–9961.

(41) Wang, Y.; Wang, X.; Antonietti, M.; Zhang, Y. Facile One-Pot Synthesis of Nanoporous Carbon Nitride Solids by Using Soft Templates. *ChemSusChem* **2010**, *3* (4), 435–439.

(42) Fukasawa, Y.; Takanabe, K.; Shimojima, A.; Antonietti, M.; Domen, K.; Okubo, T. Synthesis of Ordered Porous Graphitic-C_3N_4 and Regularly Arranged Ta_3N_5 Nanoparticles by Using Self-Assembled Silica Nanospheres as a Primary Template. *Chem. - An Asian J.* **2011**, *6* (1), 103–109.

(43) Liang, Q.; Li, Z.; Yu, X.; Huang, Z. H.; Kang, F.; Yang, Q. H. Macroscopic 3D Porous Graphitic Carbon Nitride Monolith for Enhanced Photocatalytic Hydrogen Evolution. *Adv. Mater.* **2015**, *27* (31), 4634–4639.

(44) Zhang, J.; Zhang, M.; Yang, C.; Wang, X. Nanospherical Carbon Nitride Frameworks with Sharp Edges Accelerating Charge Collection and Separation at a Soft Photocatalytic Interface. *Adv. Mater.* **2014**, *26* (24), 4121–4126.

(45) Cui, Y.; Zhang, J.; Zhang, G.; Huang, J.; Liu, P.; Antonietti, M.; Wang, X. Synthesis of Bulk and Nanoporous Carbon Nitride Polymers from Ammonium Thiocyanate for Photocatalytic Hydrogen Evolution. *J. Mater. Chem.* **2011**, *21* (34), 13032–13039.

(46) Gao, X.; Wang, L.; Ma, J.; Wang, Y.; Zhang, J. Facile Preparation of Nitrogen-Doped Graphene as an Efficient Oxygen Reduction Electrocatalyst. *Inorg. Chem. Front.* **2017**, *4* (9), 1582–1590.

(47) Dong, F.; Wu, L.; Sun, Y.; Fu, M.; Wu, Z.; Lee, S. C. Efficient Synthesis of Polymeric g-C_3N_4 Layered Materials as Novel Efficient Visible Light Driven Photocatalysts. *J. Mater. Chem.* **2011**, *21* (39), 15171–15174.

(48) Wang, Y.; Bayazit, M. K.; Moniz, S. J. A.; Ruan, Q.; Lau, C. C.; Martsinovich, N.; Tang, J. Linker-Controlled Polymeric Photocatalyst for Highly Efficient Hydrogen Evolution from Water. *Energy Environ. Sci.* **2017**, *10* (7), 1643–1651.

(49) Han, Q.; Wang, B.; Gao, J.; Cheng, Z.; Zhao, Y.; Zhang, Z.; Qu, L. Atomically Thin Mesoporous Nanomesh of g-C_3N_4 for High-Efficiency Photocatalytic Hydrogen Evolution. *ACS Nano* **2016**, *10* (2), 2745–2751.

(50) Seredych, M.; Bandosz, T. J. Nitrogen Enrichment of S-Doped Nanoporous Carbon by g- C_3N_4: Insight into Photosensitivity Enhancement. *Carbon* **2016**, *107*, 895–906.

(51) Putri, T. W.; Raya, I.; Natsir, H.; Mayasari, E. Chlorella Sp : Extraction of Fatty Acid by Using Avocado Oil as Solvent and Its Application as an Anti-Aging Cream. *J. Phys. Conf. Ser.* **2018**, *979* (1), 2848–2857.

(52) Zhang, J.; Zhao, Z.; Xia, Z.; Dai, L. A Metal-Free Bifunctional Electrocatalyst for Oxygen Reduction and Oxygen Evolution Reactions. *Nat. Nanotechnol.* **2015**, *10* (5), 444–452.

(53) Li, J.; Zhang, X.; Raziq, F.; Wang, J.; Liu, C.; Liu, Y.; Sun, J.; Yan, R.; Qu, B.; Qin, C.; et al. Improved Photocatalytic Activities of g-C_3N_4 Nanosheets by Effectively Trapping

Holes with Halogen-Induced Surface Polarization and 2,4-Dichlorophenol Decomposition Mechanism. *Appl. Catal. B Environ.* **2017**, *218*, 60–67.

(54) Ofer, D.; Crooks, R. M.; Wrighton, M. S. Potential Dependence of the Conductivity of Highly Oxidized Poly Thiophenes, Polypyrroles, and Poly Aniline: Finite Windows of High Conductivity. *J. Am. Chem. Soc.* **1990**, *112* (22), 7869–7879.

(55) Xu, W.; Liu, J.; Zhu, H. Pitting Corrosion of Friction Stir Welded Aluminum Alloy Thick Plate in Alkaline Chloride Solution. *Electrochim. Acta* **2010**, *55* (8), 2918–2923.

(56) Surekha, K.; Murty, B. S.; Prasad Rao, K. Effect of Processing Parameters on the Corrosion Behaviour of Friction Stir Processed AA 2219 Aluminum Alloy. *Solid State Sci.* **2009**, *11* (4), 907–917.

(57) Shen, C.; Zhang, J.; Ge, J. Microstructures and Electrochemical Behaviors of the Friction Stir Welding Dissimilar Weld. *J. Environ. Sci.* **2011**, *23* (SUPPL.), S32–S35.

(58) Tang, L.; Ji, R.; Li, X.; Teng, K. S.; Lau, S. P. Energy-Level Structure of Nitrogen-Doped Graphene Quantum Dots. *J. Mater. Chem. C* **2013**, *1* (32), 4908–4915.

(59) Gao, H.; Yan, S.; Wang, J.; Zou, Z. Inorganic Ions Promoted Photocatalysis Based on Polymer Photocatalyst. *Appl. Catal. B Environ.* **2014**, *158–159*, 321–328.

(60) Li, J.; Shen, B.; Hong, Z.; Lin, B.; Gao, B.; Chen, Y. A Facile Approach to Synthesize Novel Oxygen-Doped g-C_3N_4 with Superior Visible-Light Photoreactivity. *Chem. Commun.* **2012**, *48* (98), 12017–12019.

(61) Moniz, S. J. A.; Shevlin, S. A.; Martin, D. J.; Guo, Z. X.; Tang, J. Visible-Light Driven Heterojunction Photocatalysts for Water Splitting-a Critical Review. *Energy Environ. Sci.* **2015**, *8* (3), 731–759.

(62) Wen, J.; Xie, J.; Chen, X.; Li, X. A Review on g-C_3N_4-Based Photocatalysts. *Appl. Surf. Sci.* **2017**, *391*, 72–123.

(63) Wenderich, K.; Mul, G. Methods, Mechanism, and Applications of Photodeposition in Photocatalysis: A Review. *Chem. Rev.* **2016**, *116* (23), 14587–14619.

(64) Shen, L.; Xing, Z.; Zou, J.; Li, Z.; Wu, X.; Zhang, Y.; Zhu, Q.; Yang, S.; Zhou, W. Black TiO_2 Nanobelts/g-C_3N_4 Nanosheets Laminated Heterojunctions with Efficient Visible-Light-Driven Photocatalytic Performance. *Sci. Rep.* **2017**, *7*.

(65) Meng, J.; Lin, Q.; Wu, S.; Pei, J.; Wei, X.; Li, J.; Zhang, Z. Hybrid CN-MEA Microplates with Enhanced Photocatalytic Hydrogen Evolution under Visible Light Irradiation. *Catal. Sci. Technol.* **2017**, *7* (17), 3777–3784.

(66) Han, C.; Gao, Y.; Liu, S.; Ge, L.; Xiao, N.; Dai, D.; Xu, B.; Chen, C. Facile Synthesis of AuPd/g-C_3N_4 Nanocomposite: An Effective Strategy to Enhance Photocatalytic Hydrogen Evolution Activity. *Int. J. Hydrogen Energy* **2017**, *42* (36), 22765–22775.

(67) Yu, H.; Shi, R.; Zhao, Y.; Bian, T.; Zhao, Y.; Zhou, C.; Waterhouse, G. I. N.; Wu, L. Z.; Tung, C. H.; Zhang, T. Alkali-Assisted Synthesis of Nitrogen Deficient Graphitic Carbon Nitride with Tunable Band Structures for Efficient Visible-Light-Driven Hydrogen Evolution. *Adv. Mater.* **2017**, *29* (16).

(68) Jiang, W.; Ruan, Q.; Xie, J.; Chen, X.; Zhu, Y.; Tang, J. Oxygen-Doped Carbon Nitride Aerogel: A Self-Supported Photocatalyst for Solar-to-Chemical Energy Conversion. *Appl. Catal. B Environ.* **2018**, *236*, 428–435.

(69) Zeng, D.; Wu, P.; Ong, W. J.; Tang, B.; Wu, M.; Zheng, H.; Chen, Y.; Peng, D. L. Construction of Network-like and Flower-like 2H-$MoSe_2$ Nanostructures Coupled with

Porous g-C_3N_4 for Noble-Metal-Free Photocatalytic H_2 Evolution under Visible Light. *Appl. Catal. B Environ.* **2018**, *233*, 26–34.

Chapter 5

5. Synergy of Defect Engineered Graphitic Carbon Nitrides and Upconversion $NaYF_4$: Yb^{3+}, Tm^{3+} Toward Superior Solar Hydrogen Evolution

5.1. Introduction

Solar-to-hydrogen conversion has been regarded as a promising and sustainable strategy to alleviate the steadily worsening energy crisis and environmental issues caused by fossil fuels.[1] To maximize solar utilization, enormous efforts have been a focus on exploiting highly efficient photocatalysts to produce abundant photocarries by extending the light absorption from ultraviolet (UV) to near-infrared (NIR) region and improving charge separation efficiency. Unfortunately, a single photocatalyst alone can hardly satisfy all the above requirements as the NIR-responsive bandgap is generally thought to lack photocatalytic activity or directly convert NIR solar energy into heat. [2] Lanthanide-based upconversion materials possess the ability to convert low NIR photons into high-energy UV and visible photons.[3,4] However, the realization of their photocatalytic activity largely relies on the development of supporting semiconductors. [5,6] Thus, assembling these upconversion materials with UV/vis-responsive nanomaterials is a rational design to broaden the light utilization region. Exhibiting an excellent absorption of UV light, polymerized graphitic carbon nitride (g-C_3N_4), has drawn much attention due to its advantages in low cost, facile synthesis process, stable physicochemical properties, and tailorable electronic structure.[7] Whereas, it is highly desired to optimize the band structure of g-C_3N_4 to overcome the limited light-harvesting and fast photocarrier recombination, [8] and thus

to efficiently absorb the released energy from the upconversion materials. Defect engineering has been demonstrated to be an efficient approach to modify the aforementioned properties. [9] The introduction of impurities, such as dopants, [10,11] vacancies [12,13] in the tri-s-triazine ring, can tune the energy levels and lattice strain of g-C_3N_4, which might give rise to a red shifting in absorption onset or higher charge separation efficiency. [14] However, the defects can also act as recombination centers for photogenerated electron-hole pairs due to the over-strong electron-trapping ability, which would lower the photocatalytic activity.[15] In this case, the precise control on defects supplemented by reasonable structure design on g-C_3N_4 is essential.

Herein, a multiple regulation strategy including upconversion composition, the defect engineering on g-C_3N_4 and three dimension (3D) architecture construction has been developed toward solar H_2 evolution. Both theoretical calculations and experiments were performed to understand how the S dopants and C vacancies affect the electronic structure of defective g-C_3N_4 (DCN). Through precise defect engineering, the induced defect states in DCN extend its visible light response to 590 nm and boost an efficient charge transfer process via a moderate electron-trapping ability. Furthermore, by integrating the upconversion $NaYF_4$: Yb^{3+}, Tm^{3+} (NYF) nanocrystals onto DCN, we successfully achieved a broadband photocatalyst (NYF@DCN) that is able to capture UV, visible, and NIR photons. When irradiated under NIR light, DCN synergetically favors the energy migration from NYF via both enhanced fluorescence re-absorption and excited energy transfer process. Moreover, the subtle integration of well-dispersed hexagonal NYF nanocrystals onto the surface of 3D defective DCN nanocolumns prevents not only structural agglomeration but also provides abundant active sites for efficient mass/energy transfer between nanocomponents. By constructing this

hybrid structure, the photocatalytic performance of the as-developed broadband photocatalyst has been enhanced by 19.3 times compared with bulk g-C_3N_4, which ranks the top among the reported upconversion-based photocatalysis system.

5.2. Experimental Section

5.2.1 Materials

All chemicals were purchased from Sigma-Aldrich and used without further purification.

5.2.2 Synthesis of DCN

DCN was synthesized by the pyrolysis of ethylene glycol (EG)-assisted self-assembled melamine-cyanurate (MCA-EG) via a modified solvothermal reaction.[16] Typically, 10 mmol of melamine and 10 mmol of cyanuric acid were separately dissolved in 60 mL EG under sonication and then heated to 120 ℃. After cooling to ~70 ℃, the solutions were mixed and stirred for another 0.5 h. The white suspension was then poured into an autoclave and heated at 180 °C for 14 h. Afterward, the precipitates were washed, dried, and grounded with sulfur at a mass ratio of 1:1. The resultant light-yellow powder was then transferred to a porcelain boat and sealed with aluminum foil. Afterward, the mixture was heated at 200 °C for 2 h and then at 550 °C for another 4 h in air with a heating rate of 5 °C min^{-1}. Finally, the puffy and brown DCN was obtained. For comparison, bulk g-C_3N_4 (BCN) was prepared directly using melamine as a precursor according to the previous report.[17]

5.2.3 Synthesis of NYF-x@DCN

A series of DCN coupled with NYF ($NaYF_4$:20%Yb, 0.5%Tm) catalysts (NYF-*x*@DCN, where *x* represents the mass percent of NYF at 5%, 35%, 50%) were prepared following a

thermal treatment strategy. To make a good distribution of NYF on the surface of DCN, cyclohexane was chosen as the dispersing solvent. The NYF nanoparticles were synthesized according to the previous report [18] and dissolved in cyclohexane with a concentration of 10 mg mL^{-1}. Afterward, 3.5 mL of the above NYF solution was added to a well-mixed 75 mL of DCN/cyclohexane (1 mg mL^{-1}) suspension and sirred at 40 °C in an oil bath. After evaporation for 4 h, the brown powder was carefully scraped and collected. The resultant composite was subsequently heated at 400 °C for 2 h under N_2 flow with a heating rate of 3 °C min^{-1} to enhance the adhesion. Finally, the sample with 35% mass loading of NYF was obtained after the cooling process and labeled as NYF-35@DCN. Controlled sample of NYF-5@DCN and NYF-50@DCN were prepared via the same process except for the mass loadings of NYF were 5% and 50%, respectively.

5.2.4 Preparation of photoelectrodes

For the synthesis of photoelectrodes, 10 mg of the as-prepared samples were dispersed in 1 mL of ethanol: Nafion (9: 1, by volume) and sonicated for 10 min. Then 30 uL of the suspension was coated on a 10 mm × 15 mm fluorine-doped tin oxide (FTO) conducting glass by a spin coater (Laurell WS-400A-6NPP Lite, USA) within 2 min at 4000 r.p.m. The electrodes were then transferred into a tubular furnace, followed by thermal treatment at 200 °C for 4 h under N_2 atmosphere. [19]

5.2.5 Structural Characterizations

SEM images were collected on a Zeiss Supra 55VP microscope operating at an acceleration voltage of 5~15 kV. HRTEM images were observed using a Tecnai-G2 F30 S-Twin

microscope equipped with an energy-dispersive X-ray spectroscopy spectrometer. X-ray diffraction (XRD) patterns were analyzed by a Bruker D8 diffractometer with Cu Kα radiation (λ = 1.5418 Å). Fourier transform infrared (FT-IR) spectra were acquired by a Nicolet 6700 instrument. N_2 adsorption and desorption isotherms were carried out using a Micromeritics 3 Flex analyzer. X-ray photoelectron spectroscopy (XPS) spectra were studied by an ESCALAB250Xi spectrometer with a monochromatic Al Kα source and all peaks were calibrated at 284.6 eV. UV-visible diffuse reflectance spectra (UV-vis DRS) were investigated by a Perkin Elmer Lambda 950 spectrophotometer. Electron paramagnetic resonance (EPR) was performed on a Bruker A300-10/12 EPR spectrometer with f = 9.853 GHz. The spectral properties of upconversion nanoparticles were measured with a home-built system which a fiber-coupled 980 nm diode laser (BL976-PAG500, controller CLD1015, Thorlabs) worked as the pumping source and a commercial spectrometer (Shamrock 193i, Andor) with an EMCCD (iXon Ultra 888, Andor) as the detector. In addition, the emission signal was filtered by a short pass filter (SPF, FF01-842/SP-25, Semrock).

5.2.6 Photoelectrochemical measurements

The photoelectrochemical measurements were carried out in a standard three-electrode system using a CHI 650D electrochemical workstation (CHI Instrument, USA). The FTO photoelectrode, Pt wire, and Ag/AgCl (saturated KCl) electrode were employed as the working electrode, counter electrode, and reference electrode, respectively. The electrolyte was 0.35 M Na_2S/0.25M Na_2SO_3 aqueous solution. A Xe arc lamp (PLS-SXE300C) equipped with an AM 1.5 G filter or UV-cutoff filter (λ > 420 nm) or bandpass filter (λ=450, 500, 550, 600, and 650) was employed as the light source. The light was illuminated on the backside of the FTO

electrode with an intensity of 100 mW cm^{-2}. Photovoltammogram curves and photocurrents (i-t) were measured in a potential range of -0.4 ~ 0.8 V at a scan rate of 10 mV s^{-1}. Electrochemical impedance spectroscopy (EIS) was measured by applying 5 mV alternative signal over the frequency ranged from 100 kHz to 0.01 Hz. Mott-Schottky plots were measured in 0.5 M Na_2SO_4 aqueous solution (pH=7) and the frequency of 1~3 kHz with an alternating voltage magnitude of 10 mV. The calculated flat potential E_{fp} *vs.* AgCl/Ag can be converted to E'_{fb} *vs.* RHE via the following equation (1): [17]

$$E'_{fp}=E_{fp}+0.197+0.059pH \qquad (1)$$

A series of bandpass light filters were also equipped onto the Xe arc lamp for IPCE (incident photo-to-current efficiency) measurements according to the equation (2): [20]

$$IPCE = (1240\times I)/(\lambda\times J_{light})\times 100 \qquad (2)$$

where I is the current density (mA cm^{-2}), λ is the incident light wavelength (nm), and J_{light} is the density of monochromatic light at a specific wavelength (mW cm^{-2}).

5.2.7 Photocatalytic hydrogen evolution

The photocatalytic activity of the as-prepared samples was evaluated by photocatalytic hydrogen evolution at room temperature. Typically, 80 mg of the catalyst was firstly dispersed in 80 mL of triethanolamine and water solution (volume ratio of 1:9) under sonication. Afterward, a certain amount of H_2PtCl_6 (1 wt% Pt) was added to the solution to act as the co-catalyst. Then the suspension was bubbled with N_2 for 0.5 h to remove the air, and the flask was sealed with silicone rubber and parafilm. A Xe arc lamp (PLS-SXE300C) equipped with

an AM 1.5 G filter or UV-cutoff filter (λ > 420 nm) was employed as the light source to trigger the photocatalytic reaction. The mixture was under continuous magnetic stirring, and the flask was put in front of the lamp where the light intensity was measured at ~ 100 mW cm^{-2}. The amount of generated hydrogen was determined with the gas chromatography (GC2014, Shimadzu) after intermittently taking out 0.2 mL of gas.

5.2.8 Quantum efficiency

The apparent quantum efficiency (AQE) was measured under the identical reaction condition under the illumination of a 300 W Xe lamp with bandpass filters. The apparent QE was calculated according to equation (3): [16]

$$\text{AQE}\ (\%) = \frac{number\ of\ reacted\ electrons}{number\ of\ incident\ photons} \times 100 = \frac{number\ of\ H_2\ molecules \times 2}{number\ of\ incident\ photons} \times 100 \qquad (3)$$

5.2.9 DFT Calculations

To make the proportions of elements in the theoretical model consistent with the experimental one (C: N: S= 39: 56: 1), the 2 × 3 g-C_3N_4 supercells with lattice parameters 14.28 Å and 21.36 Å are used. Two possible synthetic routes and four stable intermediates are taken into account to make the relationship between structure and electronic property clear. A vacuum gap of 15 Å is applied to avoid the effect from the neighboring layer, and the G-centered Monkhorst–Pack grid for the Brillouin zone is 3 × 2 × 1. Optimization stops when the force on each atom is less than 0.05 eV $Å^{-1}$. The optimized configurations containing C defects are buckled. The vacuum energy level for every structure is calculated and set to 0 to make the absolute values of the VBM/CBM comparable. Charge density difference of g-C_3N_4 (DCN and BCN) and $NaYF_4$: Yb^{3+}, Tm^{3+} (NYF) composites were performed by generalized gradient approximation

(GGA) [21] with the Perdew–Burke–Ernzerh of (PBE) [22] functional using the plane-wave basis Vienna Ab-initio Simulation Package (VASP) code. [23] The DFT-D2 method of Grimme, which contains van der Waals corrections are used in electronic structure calculations. The configuration of the (010) facet of the 4*2*1 NYF with lattice parameters of 3.496 Å, 5.914 Å, and 5.937 Å is used in the charge density difference calculation.

5.3. Results and Discussion

As depicted in **Figure 5. 1a**, a series of NYF-x@DCN catalysts (where x represents the mass percentage of NYF nanocrystals) were prepared by the pyrolysis of ethylene glycol (EG)-assisted self-assembled melamine-cyanurate (MCA-EG) and subsequent thermal treatment with NYF. The growth of hexagonal MCA-EG columns was restricted to a size of ~ 1 μm in length and 200 nm in width (**Figure 5. 1b**). While sulfur acts as a morphology protecting agent in the air thermal exfoliation process, which is confirmed by the well-established hexagonal nanocolumns of DCN (**Figure 5. 1c, d**). The NYF upconversion nanocrystals (25 nm) also demonstrate a uniform hexagonal shape and robust thermal stability as their morphology and crystallinity are well preserved even after the post-thermal treatment (**Figure 5. 1e-g**). [18] Benefiting from the 3D scaffold, the NYF nanocrystals (≤35 wt %) are uniformly distributed on the surface of DCN nanocolumns (**Figure 5. 1f**). The high-resolution TEM (HRTEM) image readily shows the well crystalline feature of the as-prepared NYF nanocrystals with interplanar spacing (d) of 0.30 and 0.52 nm for the (110) and (100) crystal planes, respectively (**Figure 5. 1g**). The defective structure and S-doping feature of DCN are evidenced by the amorphous crystalline property of DCN (**Figure 5. 1g**) and the corresponding elemental mapping images (**Figure 5. 1h**).

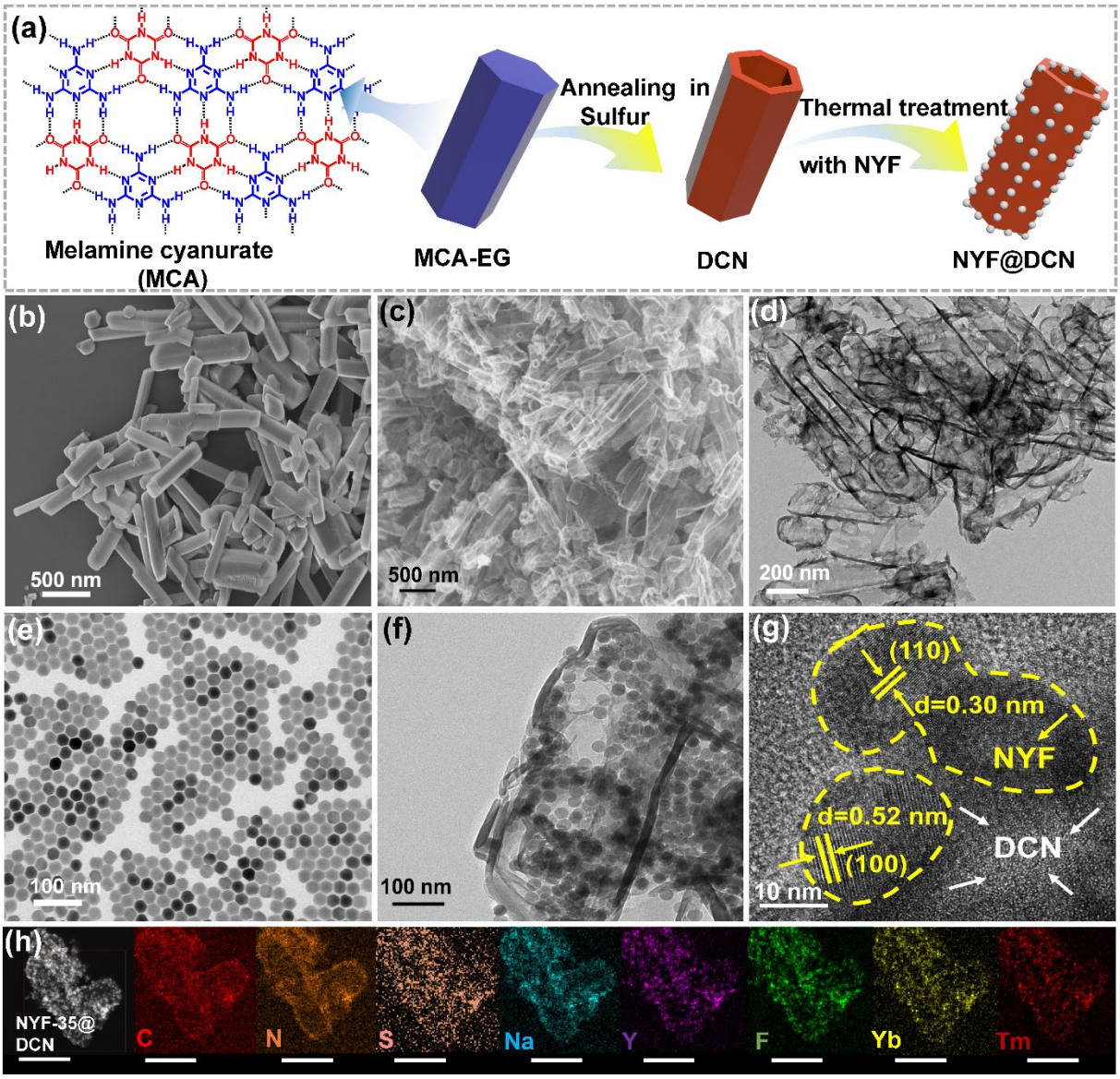

Figure 5.1 (a) Schematic illustration for the fabrication of NYF@DCN; SEM images of **(b)** MCA-EG and **(c)** DCN; TEM images of **(d)** DCN, **(e)** NYF, **(f)** NYF-35@DCN; **(g)** HRTEM image of NYF-35@DCN; **(h)** High-magnification scanning transmission electron microscopy image with the corresponding elemental mapping of C, N, S, Na, Y, F, Yb, and Tm for NYF-35@DCN (scale bar: 500 nm).

X-ray diffraction (XRD) patterns and N_2 absorption-desorption isotherms were further conducted to characterize the crystalline and surface features of the as-prepared NYF@DCN samples (**Figure 5. 2**). The typical XRD patterns of MCA-EG confirm the combination reaction

of melamine and cyanuric acid in EG solvent (**Figure 5. 2a**). [16] After the pyrolysis process, both BCN and DCN show the typical diffraction peaks at around 13.1 and 27.4° (**Figure 5. 2b**), corresponding to the (100) and (002) crystal planes of g-C_3N_4. [24] However, the intensity of DCN is much lower, suggesting its less crystalline feature, which is consistent with the HRTEM image (**Figure 5. 1g**). It has been reported that the less ordered crystalline structure of g-C_3N_4 generally indicates an intensive thermal etching process with abundant defects, which is supposed to facilitate the photocatalytic activity. [24] The distinctive XRD peaks of NYF-5@DCN, NYF-35@DCN, and NYF-50@DCN can be indexed to the hexagonal phases of NYF (JCPDS NO. 016-334), [25] indicating that the thermal coupling of DCN and NYF does not affect their crystalline features. N_2 sorption-desorption isotherms show a significant increase of specific surface area from 20.1 $m^2 g^{-1}$ for BCN to 131.2 $m^2 g^{-1}$ for DCN, suggesting a more porous architecture of the as-prepared DCN (**Figure 5. 2c**). This also can be visually seen from a much higher volume of the brown DCN than BCN with the same weight (insert, **Figure 5. 2c**). For NYF-5@DCN, NYF-35@DCN, and NYF-50@DCN nanocatalysts, the BET surface area reduces to 103.5, 95.8, and 77.9 $m^2 g^{-1}$, respectively, due to the increasing mass loading of NYF (**Table 5. 1**). According to the Barrett-Joyner-Halenda (BJH) pore size distribution profiles (**Figure 5. 2d**), the as-prepared DCN shows a hierarchically mesoporous and macroporous structure with the pore sizes in the range of 2-5 nm and 20-100 nm, respectively. Remarkably, the pronation of melamine and addition of sulfur dramatically expand the pore volume to 0.59 $cm^3 g^{-1}$ of DCN, which is 3.9 times higher than that of BCN, giving rise to better physical confinement of reactants for dynamically facilitating the mass transfer.[23] Such structure engineering significantly eliminates g-C_3N_4 agglomeration, and the

highly porous structure benefits the transfer and separation of photo-generated electrons and holes.

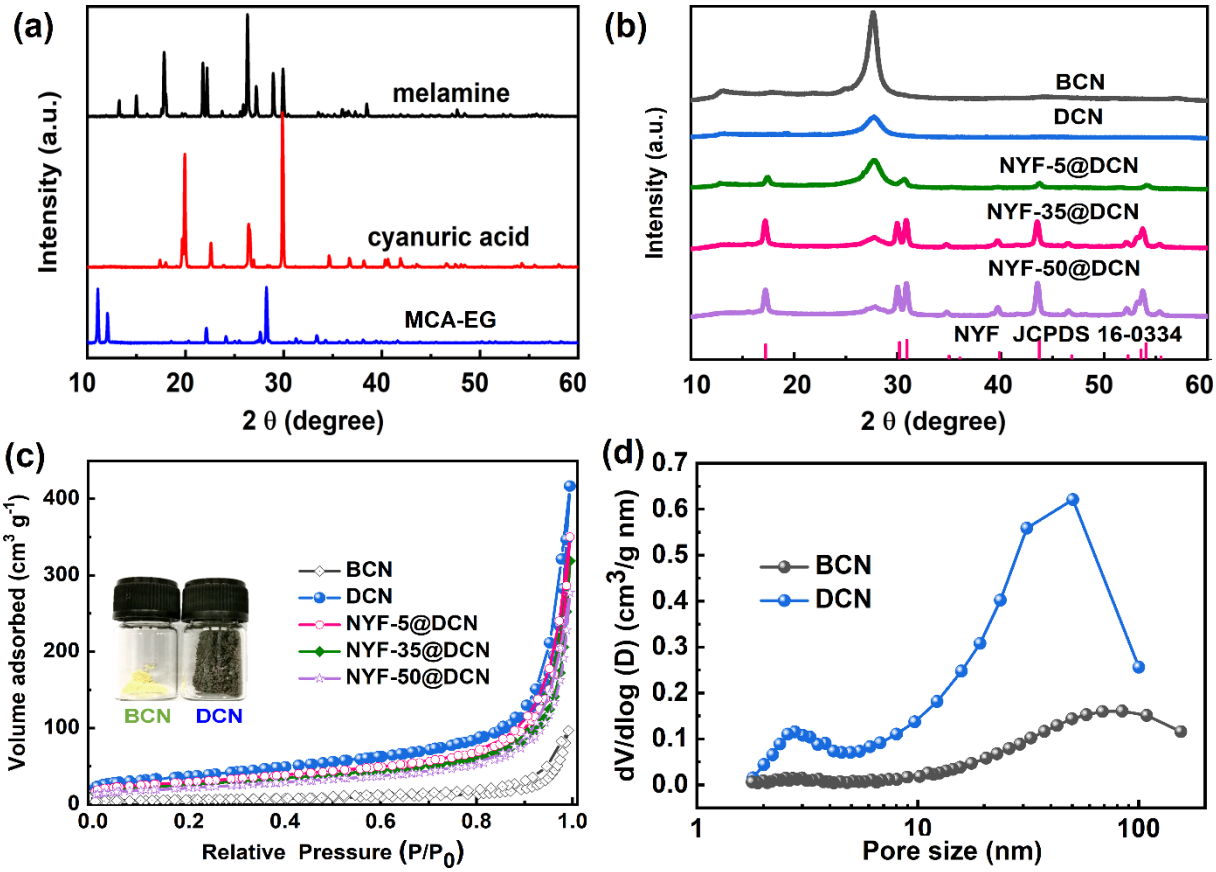

Figure 5.2 XRD patterns of **(a)** melamine, cyanuric acid, and MCA-EG supramolecule; **(b)** BCN, DCN, and NYF@DCN samples; **(c)** N_2 sorption-desorption isotherms (insert: digital photo of BCN and DCN of 50 mg of BCN, DCN, and NYF@DCN; **(d)** Pore size distribution plots of BCN and DCN.

Table 5.1 Physicochemical properties of the as-prepared catalysts.

Sample	BET specific surface area ($m^2 g^{-1}$)	Pore volume ($cm^3 g^{-1}$)
BCN	20.1	0.15
DCN	131.2	0.59
NYF-5@DCN	103.5	0.49
NYF-35@DCN	95.8	0.44
NYF-50@DCN	77.9	0.38

Apart from morphology modification, defect engineering on DCN is also achieved via the in-situ generated S dopants and C vacancies. Based on the X-ray photoelectron spectroscopy (XPS) result, we demonstrate that S atoms substitute the two-coordinated N atoms to form C-S-C bond with an atomic doping-level of 0.55% (**Figure 5. 3a**, **Table 5. 2**). [26] The C vacancies are further confirmed by the electron paramagnetic resonance (EPR) spectra with a reduced g signal intensity at around 2.0042 (**Figure 5. 3b**).[12] The strong vibration modes of Fourier transform infrared (FT-IR) spectra in the range of 3000-3300 cm^{-1} also evidence that the abundant amino groups, accompanied by the C vacancies, are presented in DCN (**Figure 5. 3c**). [12]

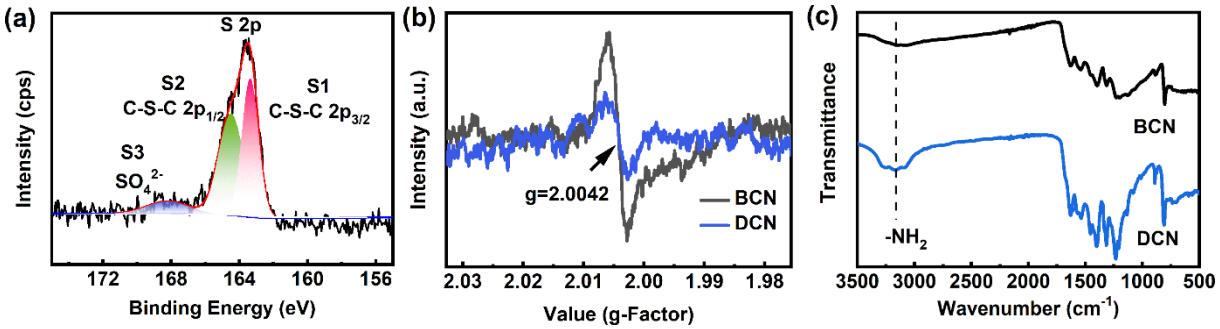

Figure 5.3 (a) Core-level XPS spectrum of S 2p for DCN; **(b)** EPR spectra and **(c)** FT-IR spectra for BCN and DCN.

Table 5.2 Surface compositions of the as-prepared catalysts obtained from XPS analysis (atomic %).

Sample	C	N	O	S	C/N
DCN	39.43	58.65	1.37	0.55	0.67
BCN	40.80	57.12	2.07	--	0.71

DFT calculations and optical experiments were performed to investigate the effect of S dopants and N vacancies on the electronic structure and light-harvesting ability of g-C_3N_4. The negative formation energies of -3.82 and -4.25 eV for g-C_3N_4 with S-dopant (CN*s*) and C-vacancy (CN*c*) further indicate that S and C vacancies are energetically favorable in two- and three-coordinated N sites, respectively (**Figure 5. 4a**). Based on the surface element ratio (Table 5. 2), we propose a DCN calculated model with the atomic C: N: S ratio of 33: 52: 1 (insert in **Figure 5. 4b**). Compared to BCN, DCN shows a narrower bandgap as reflected by the density of states (DOSs) (**Figure 5. 4b-c**). More importantly, for DCN, significant states of N 2p and C 2p around the Fermi level are presented, which implies the generation of defect states and improved electrical conductivity (**Figure 5. 4b**). The existence of defect states in

DCN is further experimentally confirmed by the absorption shoulder around 500 nm and the Urbach tail [10], as reflected in the UV-vis diffusion reflectance absorption spectra (**Figure 5. 4d**). With the contribution of S dopants and C vacancies, the visible light absorption region of DCN is extended from 457 to 520 nm. Based on the Kubelk-Munk function, [8] DCN shows a 0.21 eV lower bandgap of 2.60 eV than BCN (**Figure 5. 4e**), which is in good accordance with the theoretical calculations. The position of defect states is calculated to be 2.10 eV above the valence band (VB), suggesting the utilization of photons excited with much lower energy and an enhanced visible absorption up to 590 nm.

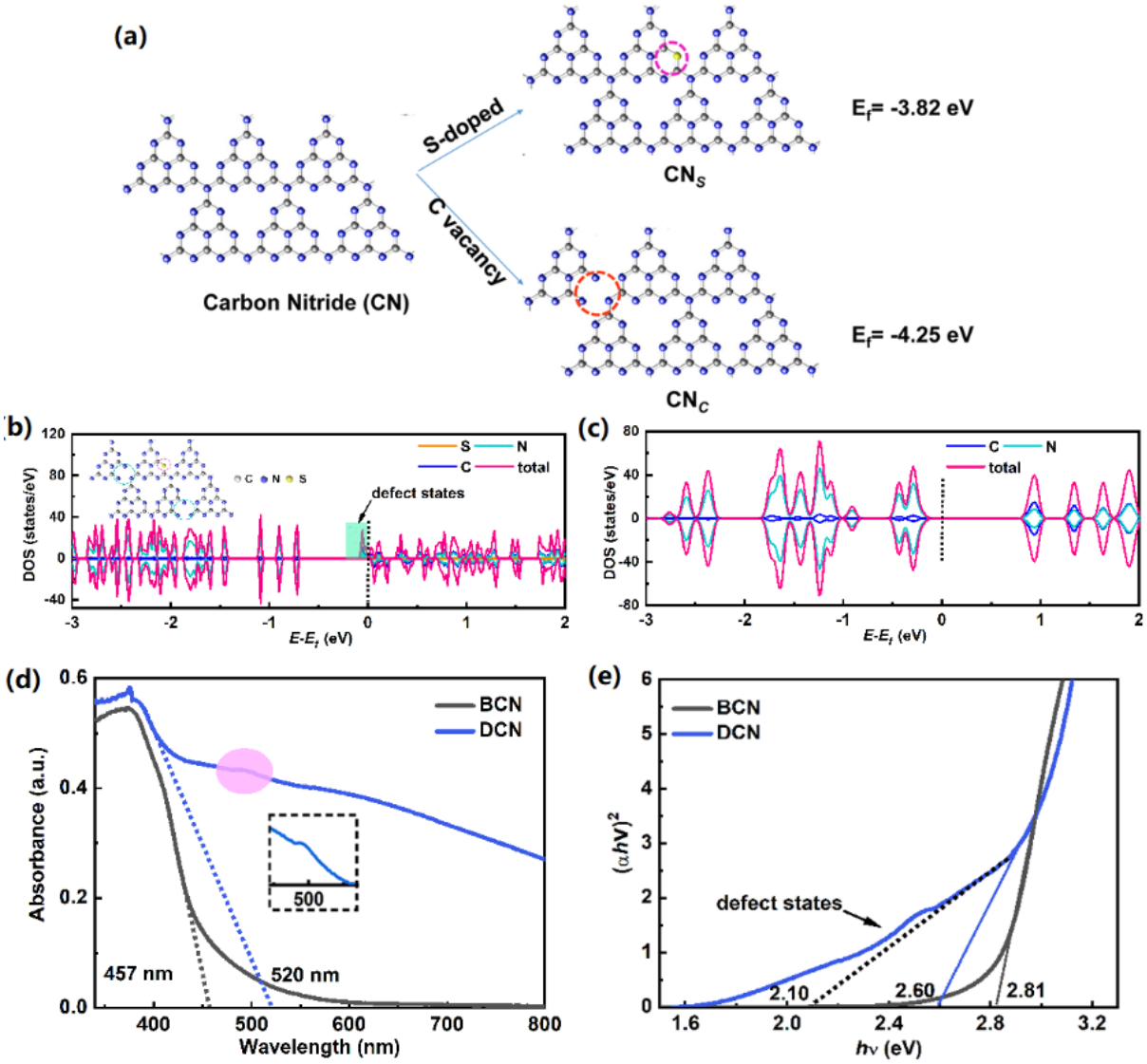

Figure 5.4 (a) The formation energy (E_f) and optimized structure of defective g-C_3N_4 obtained with S dopant or C vacancy: pure g-C_3N_4 (CN); g-C_3N_4 with a S-doped site (CN_S); and g-C_3N_4 with a C vacancy (CN_C); DOSs of **(b)** DCN (insert: proposed structure of DCN) and **(c)** BCN (the Fermi level is defined as 0 eV); **(d)** UV-vis diffusion reflectance absorption spectra of BCN and DCN; **(e)** $(\alpha h\nu)^2$ *vs*. $h\nu$ plots based on Kubelk-Munk method.

To evaluate the photocatalytic performance of the regulations, systematic photoelectrochemical measurements were carried out. Employing a typical three-electrode cell system, the 1 μm thick photoelectrode was back-illuminated under a chopped simulated solar

light. **Figure 5. 5a** shows the transient photocurrents of BCN, DCN, and NYF@DCN catalysts at 0.2 V (*vs.* Ag/AgCl). Specifically, NYF-35@DCN, NYF-50@DCN, NYF-5@DCN, DCN, and BCN, in decreasing order, deliver a photocurrent of 301, 234, 167, 112, and 7 μA cm^{-2}, respectively. This implies an optimized mass loading of NYF nanocrystals is necessary to obtain the highest photocarriers separation efficiency. Noticeably, NYF-35@DCN also displays the highest photocurrents even at a wavelength longer than its bandgap excitation (λ = 476 nm), *i.e.,* 16.0 μA cm^{-2} at 500 nm, 12.55 μA cm^{-2} at 550 nm, and 8.15 μA cm^{-2} at 650 nm (**Figure 5. 5b**, left). This enhanced visible light utilization can be ascribed to the reduced photon-excited energy (< 2.60 eV) caused by the defect states (**Figure 5. 4e**). The contribution of upconversion NYF nanocrystals is further verified by an obvious photocurrent of 8 μA cm^{-2} for NYF-35@DCN with a 980 nm laser (**Figure 5. 5b**, right). Compared to BCN and DCN, NYF-35@DCN shows an overwhelming superiority on incident photon-to-current efficiency (IPCE) over all wavelengths, demonstrating the boosted solar energy conversion after the multiple regulations on carbon nitrides (**Figure 5. 5c**).

Electrochemical impedance spectroscopy (EIS) measurement was then performed to evaluate the migration ability of electrons in photocatalysts. As shown in **Figure 5. 5d**, the fitting curves match well with original EIS data using the equivalent circuit. [27] In dark, NYF-35@DCN shows the lowest charge transfer resistance (R_{ct}) of 9.85×10^4 Ω cm^2, which is half of DCN (1.98×10^5 Ω cm^2, **Table 5. 3**). This is mainly due to its enhanced bulk electrical conductivity induced by defects in DCN and lower intrinsic resistance of NYF. Moreover, under simulated solar irradiation, NYF-35@DCN also presents the lowest R_{ct} value of 3.35×10^4

Ω cm^2, implying the superior photoelectrochemical property and significantly decreased transport obstacle for photocarriers (**Table 5. 4**).

Table 5.3 EIS results of g-C_3N_4 samples measured in the dark.*

	BCN	**DCN**	**NYF-35@DCN**
R_{Sol} (Ω cm^2)	15.72	9.68	10.74
R_t (Ω cm^2)	379790	198410	95772
Q ($Ω^{-1}cm^{-2}$ s^n)	3.35×10^{-6}	2.58×10^{-6}	7.97×10^{-6}
n	0.82	0.92	0.99
R_{ss} (Ω cm^2)	4.80	1.79	7.12

Table 5.4 EIS results of g-C_3N_4 samples measured in simulated solar light. *

	BCN	**DCN**	**NYF-35@DCN**
R_{Sol} (Ω cm^2)	12.52	8.35	12.12
R_t (Ω cm^2)	55389	43808	33506
Q ($Ω^{-1}cm^{-2}$ s^n)	4.40×10^{-6}	2.48×10^{-6}	2.06×10^{-6}
n	0.82	0.73	0.77
C_{ss} (μF cm^{-2})	0.91	8.12	7.54
R_{ss} (Ω cm^2)	1.49	5.10	6.25

***Note:** EIS data were fitted according to the equivalent circuit, where R_{sol} is the solution resistance, R_t is the electron migration resistance; CPE is a constant phase angle element. R_{ss} C_{ss}, and W_{ss} are the electron transfer resistance on the interface and the interface capacitance, and the Warburg resistance caused by the diffusion effect of the electrolyte, respectively.

As we know, defects have pros and cons for photocatalytic activity. [28] Despite the enhanced light absorption, the surface states might be deteriorated with an overstrong electron-trapping ability, thus leading to worse recombination of photocarriers. [29] In this work, the precise control on defects for efficient charge transfer was achieved by a moderate electron-trapping property. The interface capacitance (C_{ss}), a good descriptor to elucidate the accumulation of electrons at the semiconductor/electrolyte interface, was analyzed according to the EIS results. [30] Under solar irradiation, DCN and NYF-35@DCN show a substantial increase of C_{ss} (8.12, and 7.54 μF cm^{-2}) compared to BCN (0.91 μF cm^{-2}), indicating the enhanced charge density of surface states by accommodating the photo-excited electrons from CB or the transited electrons from VB (**Table 5. 4**). To explore the strength of the electron-trapping, the pseudo-first-order recombination rate constant (k) is calculated using the following equation based on the decay profiles of the open-circuit potential (**Figure 5. 5e**): [27]

$$(\mathrm{V} - V_{light})/(V_{dark} - V_{light}) = 1 - \exp(-kt) \qquad (1)$$

where V, $V_{dark,}$ and V_{light} are the open-circuit potential, in the dark and under light irradiation, respectively. As a result, NYF-35@DCN presents the slowest decay kinetics (0.156 s^{-1}) compared to BCN (0.571 s^{-1}), DCN (0.320 s^{-1}), NYF-5@DCN (0.207 s^{-1}) and NYF-50@DCN (0.202 s^{-1}). This means a suppressed recombination and prolonged lifetimes of surface photocarriers for NYF@DCN catalysts, implying the modest electron-trapping ability of defect sites. Thus, our structure engineering strategy greatly balances surface states and electron-trapping.

The photocatalytic activities of the samples were evaluated by hydrogen evolution under simulated solar light irradiation **(Figure 5. 5f)**. Benefiting from the merits of 3D structure and defect engineering, DCN displays an improved H_2 evolution rate of 1872 μmol h^{-1} g^{-1}, which is 12.9 times higher than that of BCN. Remarkably, the upconversion coupling further boosts the NIR energy utilization, leading to enhanced photocatalytic activity. The NYF-35@DCN achieves the highest hydrogen evolution rate of 2799 μmol h^{-1} g^{-1}. Furthermore, NYF-35@DCN exhibits robust stability against photocorrosion as evidenced by the continuous H_2 evolution without noticeable deterioration (**Figure 5. 5h**) and superior apparent quantum efficiency (**Figure 5. 5g**). As an overview of the state-of-the-art, the solar hydrogen evolution performance of NYF-35@DCN not only ranks the top among the g-C_3N_4 based photocatalysts but also exceeds the upconversion particles-based and other traditional photocatalysts (**Figure 5. 5i**). [3,8,31–37]

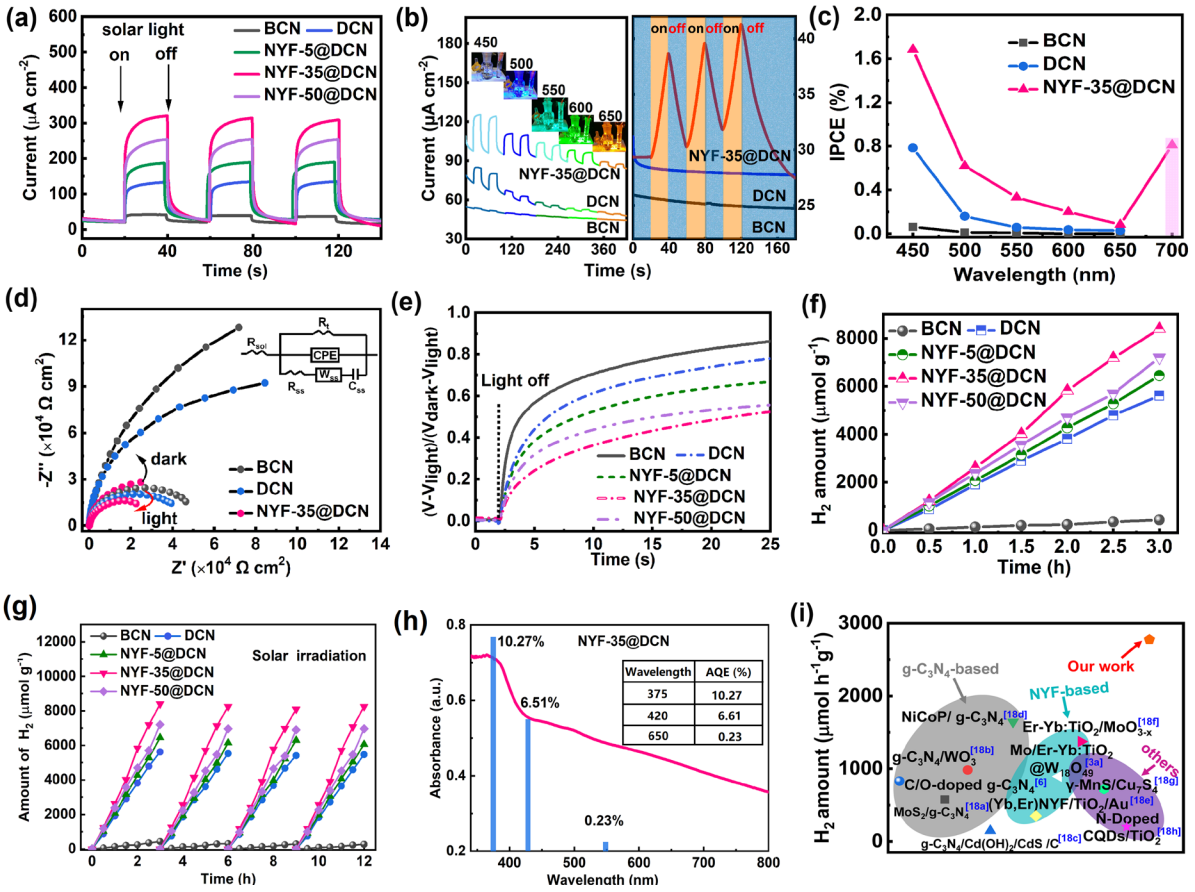

Figure 5.5 (a) Transient photocurrent responses at 0.2 V *vs.* AgCl/Ag electrode; **(b)** Transient photocurrent responses at longer wavelength of 450, 500, 550, 600, 650 (left) and 980 nm (right) for BCN, DCN, and NYF-35@DCN; **(c)** IPCE curves of BCN, DCN, and NYF-35@DCN; **(d)** EIS Nyquist plots (insert: equivalent circuit); **(e)** Open-circuit potential decay curves of BCN, DCN and NYF@DCN samples; **(f)** Typical time course; **(g)** H_2 evolution rate for BCN, DCN, and NYF@DCN hybrids; **(g)** Cycling stability of hydrogen evolution under simulated sunlight for BCN, DCN, and NYF@DCN; **(h)** Apparent quantum efficiency (AQE) of NYF-35@DCN at 375, 420, and 650 nm; **(i)** Comparison of solar H_2 evolution rate of NYF-35@DCN with representative reported photocatalysts.

It is critical to reveal the underlying energy migration of NYF@DCN for the in-depth understanding of the synergistic effect between upconversion and defect engineering toward

solar hydrogen evolution. The photoluminescence spectra show that the hexagonal NYF nanocrystals can upconvert the NIR energy into higher UV and visible light photons, corresponding to the transitions of $^1I_6 \rightarrow {}^3F_4$ (345 nm), $^1D_2 \rightarrow {}^3H_6$ (361 nm), $^1D_2 \rightarrow {}^3F_4$ (451 nm), $^1G_4 \rightarrow {}^3H_6$ (475 nm), $^1G_4 \rightarrow {}^3F_4$ (646 nm) and $^3H_4 \rightarrow {}^3H_6$ (800 nm), respectively (**Figure 5. 6a**). [38] However, the NYF-35@DCN hybrid exhibits negligible UV emissions (345 and 361 nm) and the dramatically reduced-intensity ratio of the blue emissions (451, 475 nm) to yellow emission (650 nm) from 10.9 to 2.4. These weakened emissions are covered in the light absorption region of DCN, and thus they can be theoretically reabsorbed by DCN via the photon transfer process. To provide direct evidence, the transient photocurrent test was performed with a purpose-designed electrode in which BCN and DCN were pasted on the conductive side of FTO glass while NYF was pasted on the non-conductive side (**Figure 5. 6b**). Illuminating NYF with a 980 nm laser, NYF‖FTO‖DCN electrode shows a higher photocurrent (1.01 μA cm^{-2}) than NYF‖FTO‖BCN (0.17 μA cm^{-2}). This confirms that the defect engineered g-C_3N_4 is more favorable in harvesting the upconverted fluorescence. Moreover, the time-resolved fluorescence decay curves recorded by a home-made scanning confocal microscope under a 980 nm pulsed laser show that NYF-35@DCN exhibits a shorter lifetime of 179 μs than NYF of 255 μs at 451 nm (**Figure 5. 6c**). This indicates the upconverted energy can also be transferred via the non-radiative excited-state energy transfer pathway from Tm^{3+} $^1D_2$ excited state to CB/defect states of DCN. Notably, DFT-based charge density difference diagrams shown in **Figure 5. 6d-e** demonstrate a stronger electronic interaction and polarization at the interface of NYF@DCN than that of NYF@BCN, which effectively strengthens the composite affiliation and dynamically facilitates the energy transfer (ET)

process. Thus, defect engineered g-C_3N_4 is more favorable in accepting the photon energy from the upconverted energy from NYF via both photon transfer and excited state energy transfer.

Based on the above analyses, we propose a schematic for the solar light harvesting and charge transfer process for NYF@DCN. According to the calculated bandgap and defect states level (**Figure 5. 4e**), the band structures of BCN and DCN were drawn after measuring their CB positions at -0.70 and -0.59 V *vs.* reference hydrogen electrode (RHE), respectively (**Figure 5. 6f-g**). Under solar light irradiation, the electrons involved in hydrogen evolution are dominantly excited via the following five ways: (1) Under UV and visible light illumination with wavelength < 476 nm, the electrons in the VB of DCN can be excited to the CB (-0.59 V) via a bandgap excitation, simultaneously leaving VB with positive holes to react with scavenger; (2) Due to the defect engineering on DCN, additional electrons will be excited to the defect states level (-0.09 V), which thermodynamically satisfies hydrogen evolution requirement via the sub-gap excitation, extending the visible light absorption region to 590 nm; (3) Acting as an energy buffering level, the defect states of DCN can work as an electrons reservoir and accept the electrons from CB, preventing their rapid recombination with holes in VB; (4) Under NIR light illumination (λ = 980 nm), the photons in NYF are excited to the long-lived $^2F_{5/2}$ level of Yb^{3+} sensitizer and transfer to the activated levels of $^1D_2$, $^1G_4$, $^3F_2$ and $^3H_5$ of Tm^{3+} activator.[39] The upconverted UV and blue emissions centering around 345, 361, 451 and 477 nm are subsequently released and act as a secondary light source to re-excite DCN with extra electrons in CB or defect states via a photon transfer (PT) pathway; (5) While a proportion of excited electrons in $^1I_6$ and $^1D_2$ levels are transferred to DCN via a non-radiative excited state energy transfer (ET) process, generating more electrons for photocatalysis. Due

to the enhanced light-harvesting ability of DCN and enhanced electronic polarization at the interface of NYF@DCN, a fascinating synergetic effect between defect states and upconversion was achieved. This broadband photocatalyst with porous 3D architecture, intimate contact between nanocomponents, and accelerated charge transfer process, ultimately boosts a superior hydrogen evolution performance.

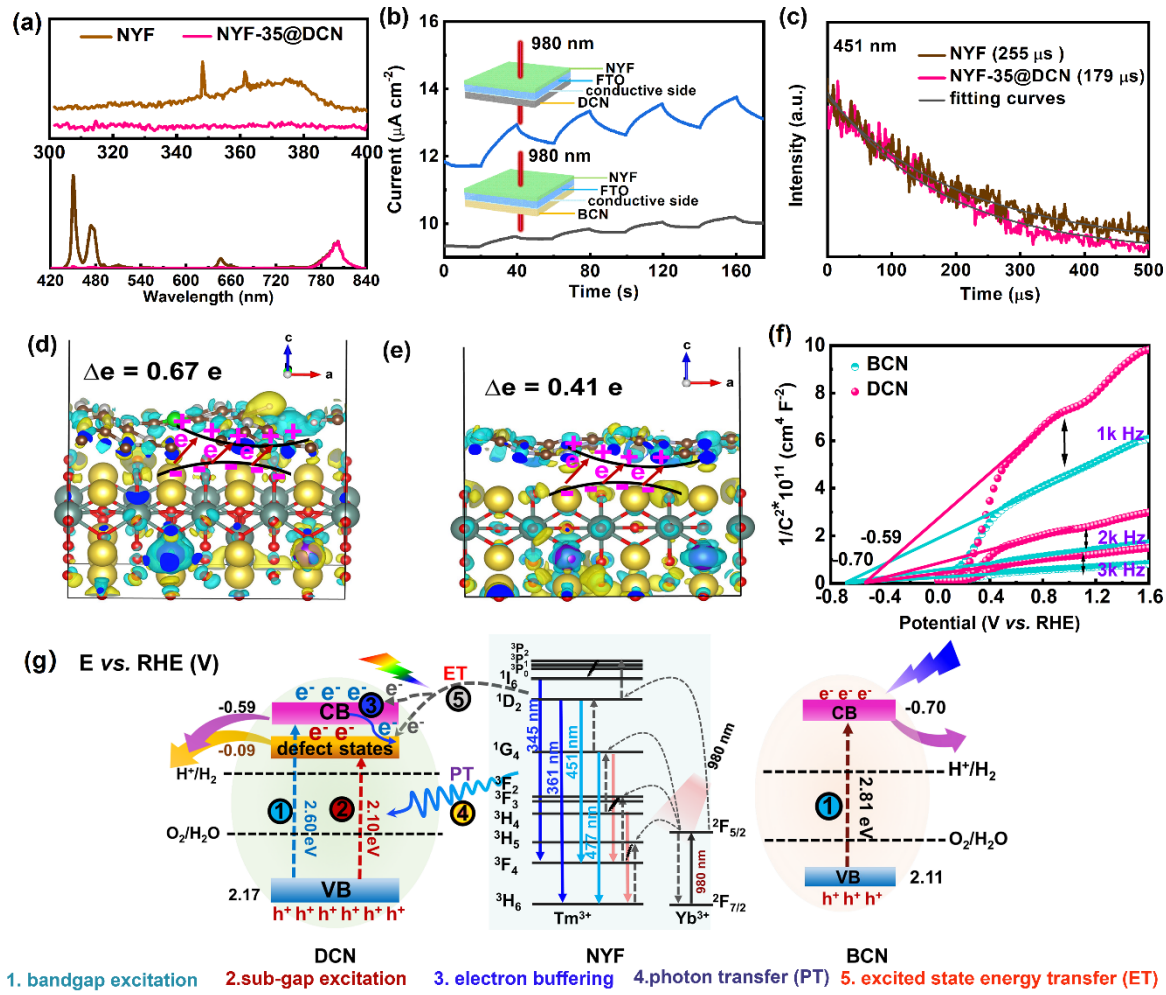

Figure 5.6 (a) Upconversion photoluminescence spectra of NYF and NYF-35@DCN; **(b)** Transient photocurrent responses at 0.2 V *vs.* AgCl/Ag electrode of NYF‖FTO‖DCN (BCN) with laser back-illuminated (from NYF to BCN/DCN); **(c)** Time-resolved fluorescence decay curves of 451 nm emission for NYF and NYF-35@DCN; Differential charge density between

(d) DCN and NYF, and **(e)** BCN and NYF (olive and cyan iso-surfaces represent the region of net electron accumulation and deficit; grey: C, brown: N; green: S; yellow: Na; dark grey: Y; red: F; blue: Yb; purple: Tm); **(f)** Mott-Schottky curves of BCN and DCN under different frequencies in 0.5 M Na_2SO_4; **(g)** Proposed photocatalytic mechanism of NYF@DCN photocatalysts.

5.4. Conclusion

In summary, we have successfully developed a broadband photocatalyst by coupling hexagonal $NaYF_4$: Yb^{3+}, Tm^{3+} upconversion nanocrystals onto the surface of defect engineered DCN nanocolumns. The experimental investigations and DFT calculations show that S dopants and C vacancies jointly to render DCN with defect states, which are effective in extending light absorbance from 441 to 590 nm and suppress the recombined electrons from CB via a narrower bandgap and electron buffering. Moreover, the Yb^{3+} and Tm^{3+} cations further upconvert NIR light into UV/visible light to re-excite the electron-hole pairs in DCN or impart the excited electrons from $^1I_6$ and $^1D_2$ levels to CB of DCN, enabling NYF@DCN a full-solar-spectral photocatalyst for hydrogen evolution. Additionally, a promoted interfacial charge polarization is also realized between DCN and NYF. Therefore, the defective g-C_3N_4 is more favorable to accept the upconverted energy transferred from NYF. The optimization on the porous 3D scaffold significantly enhances a more efficient light absorption, and mass/charge transfer, leading to an increase in solar light utilization. The optimized NYF loading on DCN exhibits a superior H_2 evolution activity of 2799 μmol h^{-1} g^{-1}, ranking the top among the g-C_3N_4 based photocatalysts and upconversion particles-based photocatalysts. This work provides an avenue to boost solar utilization via multiple regulations on broadband photocatalyst.

5.5. References

(1) Witt, H. T.; Müller, A.; Rumberg, B. Experimental Evidence for the Mechanism of Photosynthesis. *Nature* **1961**, *191* (4784), 194–195.

(2) Sang, Y.; Zhao, Z.; Zhao, M.; Hao, P.; Leng, Y.; Liu, H. From UV to Near-Infrared, WS_2 Nanosheet: A Novel Photocatalyst for Full Solar Light Spectrum Photodegradation. *Adv. Mater.* **2015**, *27* (2), 363–369.

(3) Chilkalwar, A. A.; Rayalu, S. S. Synergistic Plasmonic and Upconversion Effect of the (Yb, Er) NYF-TiO_2/Au Composite for Photocatalytic Hydrogen Generation. *J. Phys. Chem. C* **2018**, *122* (46), 26307–26314.

(4) Kang, W.; Deng, N.; Ju, J.; Li, Q.; Wu, D.; Ma, X.; Li, L.; Naebe, M.; Cheng, B. A Review of Recent Developments in Rechargeable Lithium-Sulfur Batteries. *Nanoscale* **2016**, *8* (37), 16541–16588.

(5) Tian, Q.; Yao, W.; Wu, W.; Liu, J.; Wu, Z.; Liu, L.; Dai, Z.; Jiang, C. Efficient UV-Vis-NIR Responsive Upconversion and Plasmonic-Enhanced Photocatalyst Based on Lanthanide-Doped $NaYF_4$/SnO_2/Ag. *ACS Sustain. Chem. Eng.* **2017**, *5* (11), 10889–10899.

(6) Feng, W.; Zhang, L.; Zhang, Y.; Yang, Y.; Fang, Z.; Wang, B.; Zhang, S.; Liu, P. Near-Infrared-Activated $NaYF_4$: Yb^{3+}, Er^{3+}/Au/CdS for H_2 Production: Via Photoreforming of Bio-Ethanol: Plasmonic Au as Light Nanoantenna, Energy Relay, Electron Sink and Co-Catalyst. *J. Mater. Chem. A* **2017**, *5* (21), 10311–10320.

(7) Wang, X.; Maeda, K.; Thomas, A.; Takanabe, K.; Xin, G.; Carlsson, J. M.; Domen, K.; Antonietti, M. A Metal-Free Polymeric Photocatalyst for Hydrogen Production from

Water under Visible Light. *Mater. Sustain. Energy A Collect. Peer-Reviewed Res. Rev. Artic. from Nat. Publ. Gr.* **2010**, *8* (1), 271–275.

(8) Gao, X.; Feng, J.; Su, D.; Ma, Y.; Wang, G.; Ma, H.; Zhang, J. In-Situ Exfoliation of Porous Carbon Nitride Nanosheets for Enhanced Hydrogen Evolution. *Nano Energy* **2019**, *59*, 598–609.

(9) Ma, X.; Wang, L.; Zhang, Q.; Jiang, H. Switching on the Photocatalysis of Metal–Organic Frameworks by Engineering Structural Defects. *Angew. Chemie* **2019**, *131* (35), 12303–12307.

(10) Ran, J.; Ma, T. Y.; Gao, G.; Du, X. W.; Qiao, S. Z. Porous P-Doped Graphitic Carbon Nitride Nanosheets for Synergistically Enhanced Visible-Light Photocatalytic H2 Production. *Energy Environ. Sci.* **2015**, *8* (12), 3708–3717.

(11) Tay, Q.; Kanhere, P.; Ng, C. F.; Chen, S.; Chakraborty, S.; Huan, A. C. H.; Sum, T. C.; Ahuja, R.; Chen, Z. Defect Engineered g-C_3N_4 for Efficient Visible Light Photocatalytic Hydrogen Production. *Chem. Mater.* **2015**, *27* (14), 4930–4933.

(12) Li, Y.; Ho, W.; Lv, K.; Zhu, B.; Lee, S. C. Carbon Vacancy-Induced Enhancement of the Visible Light-Driven Photocatalytic Oxidation of NO over g-C_3N_4 Nanosheets. *Appl. Surf. Sci.* **2018**, *430*, 380–389.

(13) Niu, P.; Liu, G.; Cheng, H. M. Nitrogen Vacancy-Promoted Photocatalytic Activity of Graphitic Carbon Nitride. *J. Phys. Chem. C* **2012**, *116* (20), 11013–11018.

(14) Huang, Z. F.; Song, J.; Pan, L.; Wang, Z.; Zhang, X.; Zou, J. J.; Mi, W.; Zhang, X.; Wang, L. Carbon Nitride with Simultaneous Porous Network and O-Doping for Efficient Solar-Energy-Driven Hydrogen Evolution. *Nano Energy* **2015**, *12*, 646–656.

(15) Henderson, M. A.; White, J. M.; Uetsuka, H.; Onishi, H. Photochemical Charge Transfer and Trapping at the Interface between an Organic Adlayer and an Oxide Semiconductor. *J. Am. Chem. Soc.* **2003**, *125* (49), 14974–14975.

(16) Guo, S.; Deng, Z.; Li, M.; Jiang, B.; Tian, C.; Pan, Q.; Fu, H. Phosphorus-Doped Carbon Nitride Tubes with a Layered Micro-Nanostructure for Enhanced Visible-Light Photocatalytic Hydrogen Evolution. *Angew. Chemie - Int. Ed.* **2016**, *55* (5), 1830–1834.

(17) Zhang, X.; Xie, X.; Wang, H.; Zhang, J.; Pan, B.; Xie, Y. Enhanced Photoresponsive Ultrathin Graphitic-Phase C_3N_4 Nanosheets for Bioimaging. *J. Am. Chem. Soc.* **2013**, *135* (1), 18–21.

(18) Liu, D.; Xu, X.; Du, Y.; Qin, X.; Zhang, Y.; Ma, C.; Wen, S.; Ren, W.; Goldys, E. M.; Piper, J. A.; et al. Three-Dimensional Controlled Growth of Monodisperse Sub-50 Nm Heterogeneous Nanocrystals. *Nat. Commun.* **2016**, *7*, 10254.

(19) Gao, X.; Jiao, X.; Zhang, L.; Zhu, W.; Xu, X.; Ma, H.; Chen, T. Cosolvent-Free Nanocasting Synthesis of Ordered Mesoporous g-C_3N_4 and Its Remarkable Photocatalytic Activity for Methyl Orange Degradation. *RSC Adv.* **2015**, *5* (94), 76963–76972.

(20) Hu, Z. F.; Liu, G.; Chen, X. Q.; Shen, Z. R.; Yu, J. C. Enhancing Charge Separation in Metallic Photocatalysts: A Case Study of the Conducting Molybdenum Dioxide. *Adv. Funct. Mater.* **2016**, *26* (25), 4445–4455.

(21) Perdew, J. P.; Burke, K.; Ernzerhof, M. Generalized Gradient Approximation Made Simple. *Phys. Rev. Lett.* **1996**, *77* (18), 3865–3868.

(22) Perdew, J. P.; Ernzerhof, M.; Burke, K. Rationale for Mixing Exact Exchange with Density Functional Approximations. *J. Chem. Phys.* **1996**, *105* (22), 9982–9985.

(23) Kresse, G.; Furthmüller, J. Efficiency of Ab-Initio Total Energy Calculations for Metals and Semiconductors Using a Plane-Wave Basis Set. *Comput. Mater. Sci.* **1996**, *6* (1), 15–50.

(24) Niu, P.; Zhang, L.; Liu, G.; Cheng, H. M. Graphene-like Carbon Nitride Nanosheets for Improved Photocatalytic Activities. *Adv. Funct. Mater.* **2012**, *22* (22), 4763–4770.

(25) Niu, W.; Wu, S.; Zhang, S. A Facile and General Approach for the Multicolor Tuning of Lanthanide-Ion Doped $NaYF_4$ Upconversion Nanoparticles within a Fixed Composition. *J. Mater. Chem.* **2010**, *20* (41), 9113–9117.

(26) Liu, G.; Niu, P.; Sun, C.; Smith, S. C.; Chen, Z.; Lu, G. Q.; Cheng, H. M. Unique Electronic Structure Induced High Photoreactivity of Sulfur-Doped Graphitic C_3N_4. *J. Am. Chem. Soc.* **2010**, *132* (33), 11642–11648.

(27) Hu, Z.; Shen, Z.; Yu, J. C. Covalent Fixation of Surface Oxygen Atoms on Hematite Photoanode for Enhanced Water Oxidation. *Chem. Mater.* **2016**, *28* (2), 564–572.

(28) Bertoluzzi, L.; Lopez-Varo, P.; Jiménez Tejada, J. A.; Bisquert, J. Charge Transfer Processes at the Semiconductor/Electrolyte Interface for Solar Fuel Production: Insight from Impedance Spectroscopy. *J. Mater. Chem. A* **2016**, *4* (8), 2873–2879.

(29) Kim, H. Il; Monllor-Satoca, D.; Kim, W.; Choi, W. N-Doped TiO_2 Nanotubes Coated with a Thin TaOxNy Layer for Photoelectrochemical Water Splitting: Dual Bulk and Surface Modification of Photoanodes. *Energy Environ. Sci.* **2015**, *8* (1), 247–257.

(30) Bu, Y.; Chen, Z.; Li, W. Using Electrochemical Methods to Study the Promotion Mechanism of the Photoelectric Conversion Performance of Ag-Modified Mesoporous g-C_3N_4 Heterojunction Material. *Appl. Catal. B Environ.* **2014**, *144*, 622–630.

(31) Yuan, Y. J.; Shen, Z.; Wu, S.; Su, Y.; Pei, L.; Ji, Z.; Ding, M.; Bai, W.; Chen, Y.; Yu, Z. T.; et al. Liquid Exfoliation of G-C3N4 Nanosheets to Construct 2D-2D MoS_2/g-C_3N_4 Photocatalyst for Enhanced Photocatalytic H2 Production Activity. *Appl. Catal. B Environ.* **2019**, *246*, 120–128.

(32) Fu, J.; Xu, Q.; Low, J.; Jiang, C.; Yu, J. Ultrathin 2D/2D WO_3/ g-C_3N_4 Step-Scheme H_2-Production Photocatalyst. *Appl. Catal. B Environ.* **2019**, *243*, 556–565.

(33) Aleksandrzak, M.; Baranowska, D.; Kedzierski, T.; Sielicki, K.; Zhang, S.; Biegun, M.; Mijowska, E. Superior Synergy of g-C_3N_4/Cd Compounds and Al-MOF-Derived Nanoporous Carbon for Photocatalytic Hydrogen Evolution. *Appl. Catal. B Environ.* **2019**, *257*.

(34) Bi, L.; Gao, X.; Zhang, L.; Wang, D.; Zou, X.; Xie, T. Enhanced Photocatalytic Hydrogen Evolution of NiCoP/ g-C_3N_4 with Improved Separation Efficiency and Charge Transfer Efficiency. *ChemSusChem* **2018**, *11* (1), 276–284.

(35) Shang, J.; Xu, X.; Liu, K.; Bao, Y.; Yangyang; He, M. LSPR-Driven Upconversion Enhancement and Photocatalytic H_2 Evolution for Er-Yb:TiO_2/MoO_{3-x} Nano-Semiconductor Heterostructure. *Ceram. Int.* **2019**, *45* (13), 16625–16630.

(36) Yuan, Q.; Liu, D.; Zhang, N.; Ye, W.; Ju, H.; Shi, L.; Long, R.; Zhu, J.; Xiong, Y. Noble-Metal-Free Janus-like Structures by Cation Exchange for Z-Scheme Photocatalytic

Water Splitting under Broadband Light Irradiation. *Angew. Chemie - Int. Ed.* **2017**, *56* (15), 4206–4210.

(37) Shi, R.; Li, Z.; Yu, H.; Shang, L.; Zhou, C.; Waterhouse, G. I. N.; Wu, L. Z.; Zhang, T. Effect of Nitrogen Doping Level on the Performance of N-Doped Carbon Quantum Dot/TiO_2 Composites for Photocatalytic Hydrogen Evolution. *ChemSusChem* **2017**, *10* (22), 4650–4656.

(38) Tang, Y.; Di, W.; Zhai, X.; Yang, R.; Qin, W. NIR-Responsive Photocatalytic Activity and Mechanism of $NaYF_4$:Yb,Tm@TiO_2 Core-Shell Nanoparticles. *ACS Catal.* **2013**, *3* (3), 405–412.

(39) Chen, G.; Ohulchanskyy, T. Y.; Kumar, R.; Ågren, H.; Prasad, P. N. Ultrasmall Monodisperse $NaYF_4$:Yb^{3+}/Tm^{3+} Nanocrystals with Enhanced near-Infrared to near-Infrared Upconversion Photoluminescence. *ACS Nano* **2010**, *4* (6), 3163–3168.

Chapter 6

6. Identifying the Strong Charge Polarization Effect Enabled by Surface Oxidized Titanium Nitride for High Performance Lithium-Sulfur Batteries

6.1. Introduction

Lithium-sulfur (Li-S) batteries have been considered as one of the most promising next-generation rechargeable battery systems, which can deliver 5 fold higher energy density (theoretical: 2600 Wh kg^{-1}) than the current interaction-based lithium-ion batteries.[1,2] In particular, the natural abundance, environmental friendliness, and low cost of sulfur make it more competitive for large-scale energy storage applications. [3] However, Li-S batteries have suffered from poor capacity retention and sluggish redox kinetics during the solid-liquid-solid lithiation process. The former mainly arises from the "shuttle effect", which is caused by the dissolution and diffusion of lithium polysulfides (Li_2S_n, $3 \leq n \leq 8$) through the electrolyte, separator, and even the anode. The latter is seriously affected by slow mass and electron transfer process due to the low Li^+ diffusion rate and poor conductivity of S/Li_2S.[4–6]

Many efforts have been devoted to addressing these issues, including cathode modification, [7,8] electrolyte additives, [9,10] interlaid separator, [11,12] and anode protection. [13] In the realm of cathodic structure design, carbonaceous hosts with abundant pores and high pore volume showing the capacity of the physical confinement for lithium polysulfides have attracted extensive attention. [14–17] However, the polysulfides migration driven by concentration diffusion

and electrical field cannot be completely prevented, particularly at low rates and over long-term cycling due to the nonpolar feature of the carbon. Therefore, more attention have been paid on the surface chemistry to strengthen the immobilization and accelerate the redox kinetics of polysulfides. The polar surfaces provided by metal oxides (TiO_2, MnO_2),[18,19] metal nitrides (VN),[20] metal sulfides (Co_9S_8),[21] metal phosphides (CoP, FeP), [22,23] and metal carbides (MXene)[24] endow strong polar-polar chemical interactions via dominant chalcogen-lithium binding and minor metal-sulfur binding.[25] Along with strong chemisorption, the unique electrocatalytic effect also triggers multistep redox reactions, leading to higher capacity and Coulombic efficiency.[23,26,27] Cui's group has systematically examined the catalytic effect of metal sulfides (Ni_3S, SnS_2, FeS, CoS_2, VS_2, and TiS) in eliminating the overpotential and activation energy barriers between the polysulfides and sulfur. [26] Subsequent research works further explored the catalytically enhanced redox mechanism of metallic Pt particles, W_2C,[6] Mo_2C, TiC,[27] VN,[20] and CoP.[23] Recently, transition metal nitrides such as TiN, have been intensively investigated, owing to their superior conductivity compared to their oxides and sulfides counterparts, have been largely focused in recent year.[28,29] They even show metallic characteristics, which would be very beneficial to facilitate the redox reaction kinetics and increase the sulfur utilization efficiency for Li-S batteries. Yet the study of polar and conductive TiN as polysulfides mediator for suppressing shuttle effect and boosting redox kinetics needs further investigation as the surface of TiN usually forms a thin oxidization layer in the ambient condition,[30] increasing the complexity of understanding the surface chemistry towards the polysulfides redox reaction. Therefore, it is crucial to study polysulfides mediator down to a detailed surface interface level.

Herein, we report a rational design on structure and surface chemistry by employing the highly ordered mesoporous carbon (OMC) as matrix and the surface oxidized quantum-dot-size TiN (TiN-O) as polysulfides mediator for suppressing shuttle effect and boosting redox kinetics. The composite with TiN-O embedded in OMC (TiN-O-OMC) not only provides physical confinement for polysulfides via the narrow-ordered carbon mesoporous channels (with ~3.5 nm pore size distraction), but also chemically immobilizes lithium polysulfides due to the polar surface of the embedded TiN. Our density functional theory (DFT) calculations verify the dramatic charge polarization effect between the polysulfides and surface oxidized TiN-O via the S-O-Ti bond, as verified by the transfer of 1.67*e* onto TiN-O. Surprisingly, compared to the pure TiN composite, the surface-oxidized TiN-O-OMC shows a stronger affinity for polysulfides with a higher binding energy of -5.51 eV (*vs.* Li_2S_6). Moreover, the superior charge polarization effect could impart an additional driving force propelling the electrons gained from the anode into the long-chain polysulfides, and attracting lithium-ion onto the TiN surface, giving rise to enhanced electron/charge transfer and thus faster redox kinetics is achieved. The experimental studies show a good consistency that the TiN-O-OMC electrode delivers a superior electrochemical catalytic performance with the lowest overpotential of rarely 271 and 465 mV at 0.2 and 5 C and highest lithium-ion diffusion coefficient of 3.6×10^{-8} cm^2 s^{-1} ($Li_2S_4^{2-}\rightarrow Li_2S$). This rationally designed architecture and surface chemistry of TiN-O leads to a high capacity of 1395 mA h g^{-1} at 0.1 C, a Coulombic efficiency approaching 100% and a high-rate performance of 726 mA h g^{-1} at 5 C. Furthermore, the as-developed sulfur cathode also exhibits great potential for practical applications as demonstrated by the pouch cell with an initial discharge capacity of 845 mA h g^{-1} at 0.2 C and stable cycling

performance of 634 mA h g^{-1} after 120 cycles.

6.2. Experimental Section

6.2.1 Materials

All chemicals were purchased from Sigma-Aldrich and used without further purification.

6.2.2 Synthesis of ordered mesoporous carbon (OMC)

In a typical synthesis, 1 g SBA-15 [31] and 10 g of HTM (Sigma-Aldrich, 99.0%) were well-dispersed in 20 mL of deionized water. The solution was then vacuumed at room temperature for 2 h and stirred for another 3 h. After centrifugation (9,000 rpm, 3 min), the collected paste was further heated at 60 ºC for 12 h and annealed at 750 ºC for 6 h under Ar stream with a heating rate of 3 ºC min^{-1}. Finally, the black carbonaceous product was obtained after a 5% HF (Sigma-Aldrich, 40-45%) solution etching process.

6.2.3 Synthesis of titanium nitride/oxide-carbon composites

Specifically, 100 mg of OMC was added to 4 mL of ethanol (Sigma-Aldrich, 99.8%)/tetrabutyl titanate (Aldrich, 97%) (1:1, volume ratio) solution, followed by sonication for 30 mins. The suspension was then vacuumed for 20 mins to allow a complete infiltration of tetrabutyl titanate. After centrifugation (9,000 rpm, 3 mins), the black paste was spread on a petri dish and exposed to air for 1 day to allow completed hydrolysis of tetrabutyl titanate within OMC matrix. Then, the solid was ground and transferred to a boat with 80 mg of g-C_3N_4 [32] was in the upstream. The mixture was further heated at 800 ºC for 3 h with a heating rate of 3 ºC min^{-1}. The black TiN-O-OMC powder was finally obtained after a cooling process and subsequent air exposure

for 3 days. A control sample of TiN-OMC was immediately collected from the tube furnace and preserved in an air-free glovebox. While TiO_2-OMC was prepared via a similar procedure as that of TiN-O-OMC except for the absence of g-C_3N_4 as N source in the annealing process.

6.2.4 Synthesis of TiN-O-OMC cathodes

In this work, sulfur was loaded by a melt-diffusion strategy. Typically, 25 wt% of TiN-O-OMC and 75 wt% of sulfur (Sigma-Aldrich, 99.5%) was ground together till the mixture show a good color uniformity. The solid was transferred to a small glass tube sealed with polyethylene wrap and heated at 155 ºC for 12 h. Then, 80 mg of the TiN-O-OMC/S composite, 10 mg of acetylene carbon black, and 10 mg of poly(vinylidene fluoride) (PVDF, $(CH_2CF_2)_n$) were mixed with 500 μL of N-methyl-2-pyrrolidone (NMP) to form a uniform slurry. The slurry was coated on an Al foil and then dried in a vacuum oven at 60 ºC overnight. The Al foil was then punched into 12 mm diameter disks, and the sulfur loading was controlled in the range of 1.2-1.6 mg cm^{-2}. For comparison experiments, OMC, TiO_2-OMC, and TiN-OMC electrodes were also prepared under the same condition.

6.2.5 Material Characterization

Field-emission SEM (Zeiss Supra 55VP) and TEM (JEM-2011) were applied to record the morphologies of the samples. XRD patterns (Bruker D8 Discovery) and N_2 adsorption and desorption isotherms (Micromeritics 3 Flex) were obtained to analyze the ordered structure. XPS (ESCALAB250Xi) with a monochromatic Al Kα source and elements mapping were used to probe the chemical compositions of the samples. The thermogravimetric analysis (TGA, SDT2960) was carried out on simultaneous thermal-gravimetry and differential thermal

analysis with a heating rate of 5 °C min^{-1} under N_2 atmosphere. UV-vis absorption spectral analysis (Cary 60) was performed to study the adsorption of Li_2S_6.

6.2.6 Electrochemical Measurements

To evaluate the electrochemical performance of TiN-OMC, 2030-type coin cells were assembled using lithium metal as anode and reference electrode, and Celgard 2300 as the separator. The cells were assembled in an Ar-filled glove box (UniLab, Mbraun, Germany) with low levels of both H_2O and O_2 (0.1 ppm). A freshly prepared solution containing 1 M lithium bis-(tri-fluoromethanesulfonyl) imide (LiTFSI, 99.95%) and 1wt% $LiNO_3$ in DOL/DME (volume ratio 1:1) was used as the electrolyte. The cells were operated in a voltage range of 1.7-2.8 V with Neware battery tester. Cyclic voltammetry was recorded on a Bio-Logic VMP3 electrochemical workstation in the voltage range of 1.7-2.8 V. Electrochemical impendence spectroscopy (EIS) was tested in the frequency range between 0.01 Hz and 100 kHz.

6.2.7 Li_2S_6 adsorption test

The Li_2S_6 solution (5 mM) was prepared by dissolving Li_2S and sulfur in a DOL/DME mixed solution (1:1, volume ratio) with a molar ratio of 1:5 at 80 °C for 24 h. Afterward, 5 mg of the as-prepared samples were added into the Li_2S_6 solution, followed by a soaking, standing process. Finally, 3 mL of the clear upper solution was taken out for the UV-visible adsorption test.

6.2.8 Assembly of Li_2S_6 symmetric cells and measurement

Two identical carbon paper disks (1.2 cm in diameter) were used as current collectors to load

the as-prepared host materials. The well-sonicated suspension of materials and ethanol was drop-cast on carbon paper with a mass loading of 0.35 mg cm^{-2}. Celgard 2300 was used as a separator and 0.5 M Li_2S_6 was used as the electrolyte. Particularly, the TiN-OMC electrodes were prepared in the Ar-filled glove box to prevent the surface oxidation of TiN. Both CV and EIS experiments were performed with a Bio-Logic VMP3 Multi Potentiostat.

6.2.9 Li_2S nucleation measurements

The 0.4 M Li_2S_8 catholyte was firstly synthesized by stirring the Li_2S with sulfur at a molar ratio of 1:7 in tetraglyme in the glovebox for 8 h at room temperature.[29] Accordingly, the cathodes were the same with those as mentioned in the symmetric cells experiment while lithium foils were used as anodes. For the 2030-type coin cell assembly, 20 μL Li_2S_8 catholyte was firstly added to the cathode, followed by a Celgard 2300 separator and another 20 μL Li-S electrolyte on the top. The batteries were galvanostatically discharged to 2.06 V under 0.112 mA and then held at voltage 2.05 V until the current was below 0.01 mA. Based on Faraday's law, the nucleation/growth of Li_2S can be evaluated via the fitting of current-time curves after the second potentiostatically discharge stage.

6.2.10 Assembly of pouch cells

The laminate film with 16×20 cm size was first half-folded and sealed by the hot-sealing machine as the shell of pouch cell. The pouch cell cathode electrodes were prepared with the same procedures as those electrodes prepared for coin cells but with a larger size of 6×8 cm. The Al tab was welded onto the cathode electrode. Then, the cathode was sticked the Celgard 2300 separator by the anti-electrolyte-tape. Afterward, the Li foil anode was pasted on the

separator with anti-electrolyte-tape in the glovebox with a welded Ni tap. Then both the cathode and Li foil anode were put in the laminate film package and side sealed by the hot-sealing machine. Then 1.2 g of Li-S electrolyte was injected into the package through the unsealed side. After that, the package was vacuumed and sealed via the vacuum sealing machine. After standby for 1 day, the pouch cell was pressed by formation machine and activated by discharging and charging to 1.7 V and 2.8 V at a low current density of 0.2 C. After for another 12 h, the pouch cell was electrochemically tested using the Land Workstation.

6.2.11 DFT calculations

The first principle calculations were conducted using spin-polarized Perdew-Burke-Ernzerhof (PBE) exchange-correlation functional by Vienna Ab initio Simulation Package (VASP).[33,34] The Grimme DFT-D2 method was applied to treat the van der Waals force between Li_2S_6 and TiN /TiN-O. There are more than 100 atoms in TiN-O structure with relaxed lattice constants 8.488 Å, and the vacuum gap is more than 20 Å. For the initial structure, many possible stacking patterns and distances between Li_2S_6 and TiN were tested to obtain the stable configuration. The kinetic cutoff energy is set 400 eV, while the Γ-centered Monkhorst–Pack grid is 2×2×1. The convergence of force of each atom was 0.05 eV $Å^{-1}$. The binding energy (E_b) is calculated using Equation (2):

$$E_b=E\ (Li_2S_6+TiN\text{-}O)-E\ (Li_2S_6)-E\ (TiN\text{-}O) \qquad (2)$$

where the E (Li_2S_6+TiN-O) presents the total energy for the optimized configuration of Li_2S_6 and TiN-O complex, and the E (Li_2S_6) and E (TiN-O) present the energies for optimized isolated Li_2S_6 and TiN-O structures, respectively. All the crystal structures and charge density

plots were drawn using ESTA.

6.3. Results and Discussion

Metal nitrides are usually synthesized by using the corrosive and hazardous ammonia gas as nitridizing agent. Herein, we demonstrate a green and facile synthetic approach by using g-C_3N_4 as N source. As illustrated in **Figure 6. 1a**, the highly ordered carbon matrix was first synthesized by a nanocasting process, which employs SBA-15 as the hard template and hexamethylenetetramine (HTM) as the precursor. Then TiO_2 nanoparticles were generated after the hydrolysis of tetrabutyl titanate ($Ti(OC_4H_9)_4$) within the OMC. After that, the resultant dark powders were nitridized using g-C_3N_4 as the upstream N source. Further surface oxidization of TiN was completed by simply exposing the composite in air for 3 days. In addition, control samples carried out without nitriding or natural oxidization process were denoted as TiO_2-OMC and TiN-OMC, respectively. The transmission electron microscopy (TEM) observations reveal that the as-prepared OMC successfully replicated highly ordered mesoporous structure of SBA-15 with pores size of approximately 3.5 nm and ~ 9.9 nm in the wall thickness (**Figure 6. 1b-c**). Meanwhile, the ordered mesoporous structure of OMC was well-reserved by TiN-O-OMC after the nanocoating process, which can be seen from the scanning electron microscopy (SEM) images in **Figure 6. 1d-e**. The narrow-ordered channels within the carbon matrix is speculated to restrain the growth of TiN-O because a homogeneous distribution of quantum-dot-sized TiN-O nanoparticles (3-5 nm) is observed in the high-resolution TEM images (**Figure 6. 1f-g**). Additionally, the non-toxic N-rich g-C_3N_4 is found to be as effective as NH_3 for the nitridization of TiO_2. After 3 days of the air-exposing process, the surface of TiN is easily oxidized as

confirmed by the elemental mapping (**Figure 6. 1h**).

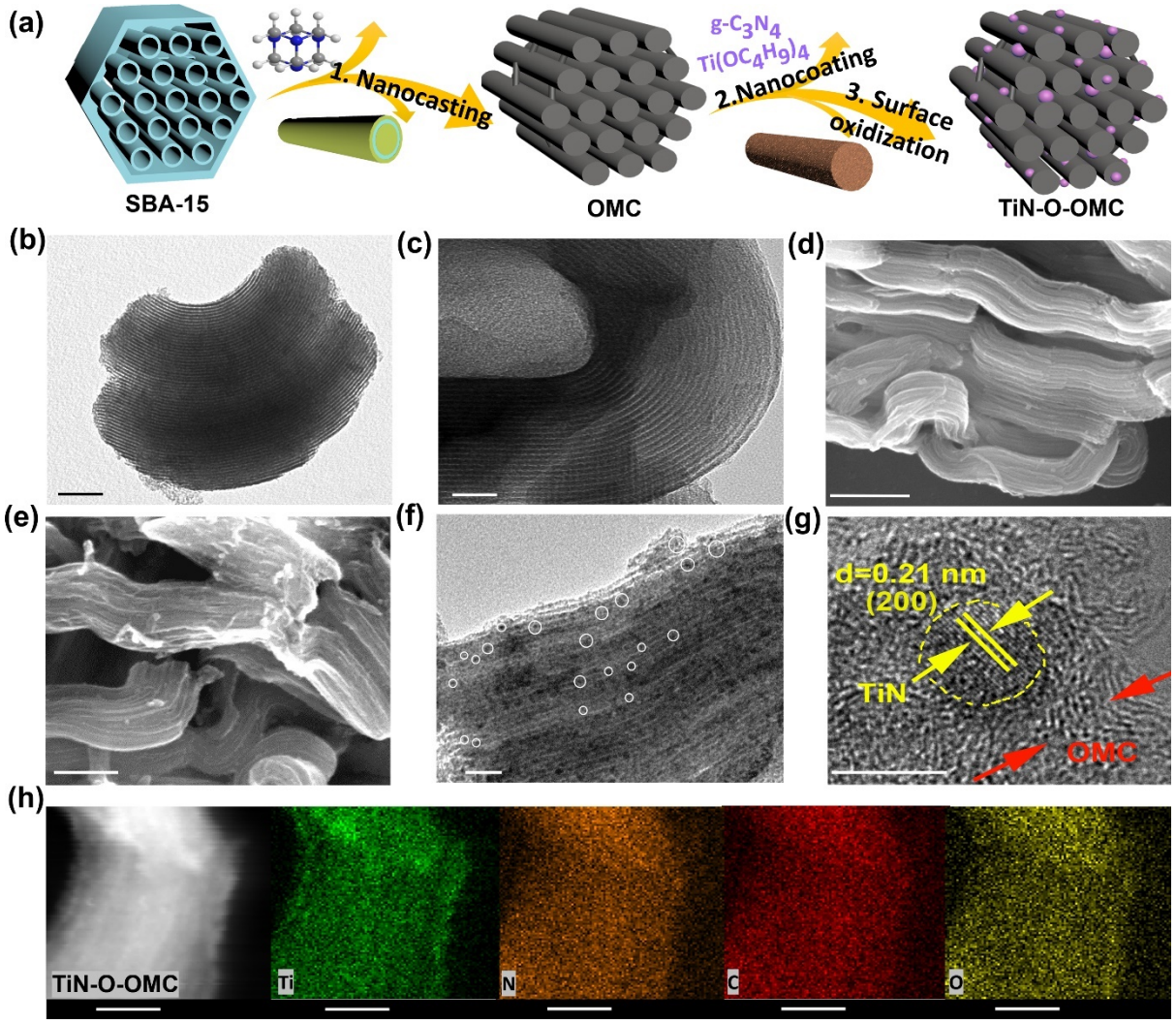

Figure 6.1 (a) Schematic illustration for the fabrication of TiN-O-OMC; TEM images of **(b)** SBA-15 and **(c)** OMC; SEM images of **(d)** OMC and **(e)** TiN-O-OMC; **(f)** TEM image and **(g)** high-resolution TEM image of TiN-O-OMC; **(h)** High-magnification scanning transmission electron microscopy (STEM) image with the corresponding elemental mapping of Ti, N, C, O for TiN-O-OMC.

The sophisticated control of morphology and pore structure was further monitored by small/wide-angle X-ray diffraction (XRD) patterns and N_2 adsorption-desorption isotherms

(**Figure 6. 2**). A distinct diffraction peak indexed to hexagonal (100) reflection is well preserved by TiN-O-OMC after two nanocasting processes (**Figure 6. 2a**), revealing its highly ordered structure. [35] Additionally, the slight shifts of the (100) peak towards the higher angle of TiN-O-OMC is ascribed to the structure shrinkage after annealing at elevated temperature and the removal of the template. [31] From the wide-angle XRD patterns (**Figure 6. 2b**), the typical peaks for both carbon and TiN can be identified, suggesting the successful nitridization with the assistance of the N-rich g-C_3N_4.[36] The mesoporous property was further verified by the capillary condensation characterization as shown in **Figure 6. 2c**. Similar to SBA-15 and OMC, the N_2 adsorption/desorption isotherms of TiN-O-OMC show type IV curve with an H1 hysteresis loop.[37] Additionally, as determined by the Barret-Joyner-Halender (BJH) method, both TiN-O-OMC and OMC demonstrate narrow mesopore size distribution (3.58 and 3.51 nm, respectively), which is consistent with the TEM observation. The control samples, both TiO_2-OMC and TiN-OMC also present a consistency of morphology and pore structure (**Figure 6. 3**). Remarkably, the well-designed TiN-O-OMC shows a high Brunauer-Emmett-Teller (BET) surface area of 355.9 $m^2\ g^{-1}$ and pore volume of 0.95 $cm^3\ g^{-1}$ (**Table 6. 1**), which are critical to providing more active sites and void space to trap and accommodate the sulfur-containing species in Li-S battery. The chemical composition of the TiN-O-OMC surface was identified by X-ray photoelectron spectroscopy (XPS). The molar ratios of 5.8, 9.6, 11.8, and 72.8 % were detected for Ti, N, O, and C, respectively (**Table 6. 2**). After the natural oxidization process, two new peaks assigned to O-Ti-O and O-Ti-N are deconvolved at 458.5, 464.4 eV, and 457.0, 463.1 eV in the Ti 2p spectrum (**Figure 6. 2d**). Based on the different fractions of Ti-containing species (**Table 6. 3**) and previous literature,[30] the chemical structure of surface

oxidized TiN is proposed to contain O-Ti-O top layer, followed by O-Ti-N intermediate layer and pure TiN in the bulk (**Figure 6. 2e**). Additionally, the molar ratio of TiO_2/TiN was calculated to be 12:15, indicating that a high portion of surface TiN has converted to TiO_2 owing to the natural oxidization.

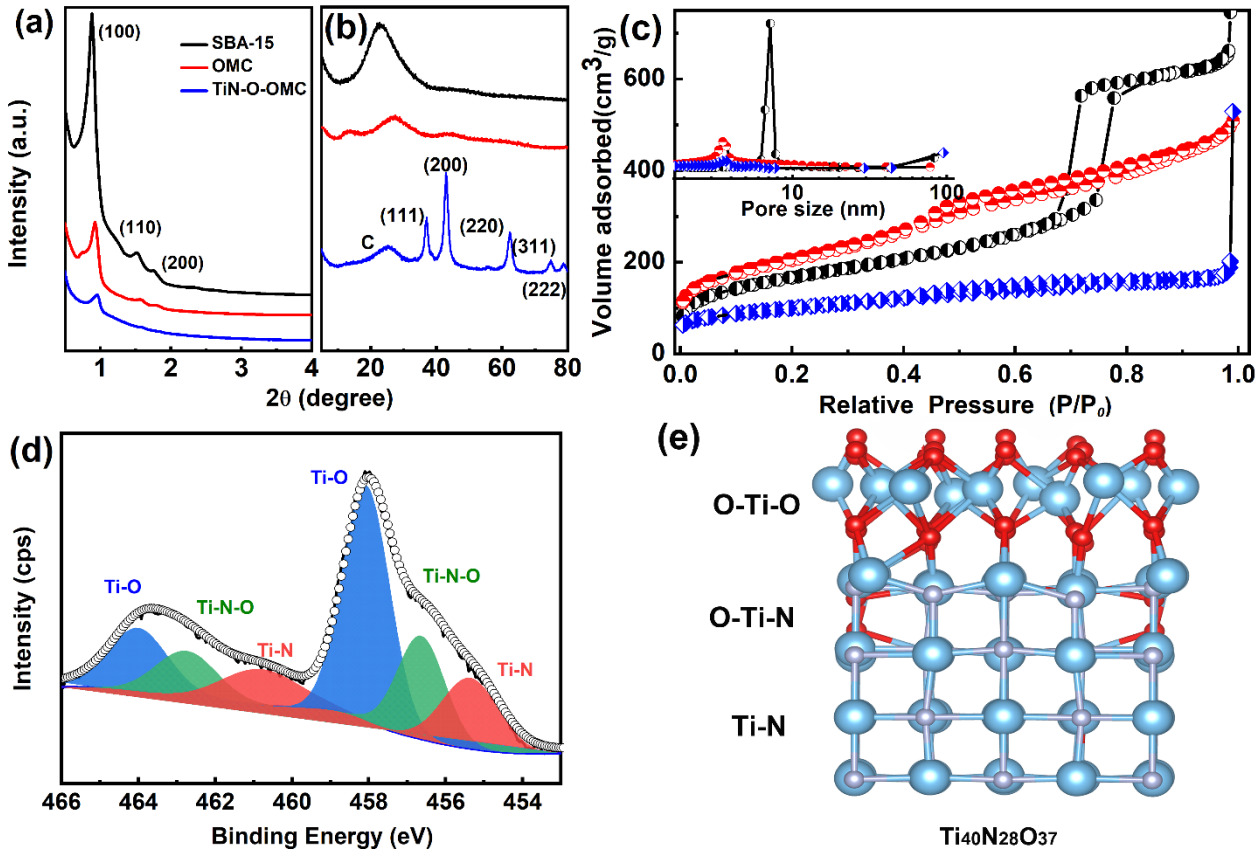

Figure 6.2 (a) Small-angle and **(b)** wide-angle XRD patterns; **(c)** N_2 adsorption-desorption isotherms (insert: pore size distribution plots) of SBA-15, OMC and TiN-O-OMC; **(d)** Core-level XPS spectra of Ti 2p of TiN-O-OMC and **(e)** the proposed chemical structure of surface oxidized TiN.

Controlled experiments were also carried out, which employs the non-oxidized TiN-OMC and TiO_2-OMC as references to identify the superiority of surface oxidized TiN toward polysulfides trapping. As seen from **Figure 6. 3**, similar results on morphology and textural

properties of TiN-OMC and TiO_2-OMC are found in comparison with that of TiN-O-OMC (**Figure 6. 1e-f**, **Figure 6. 2a-c**).

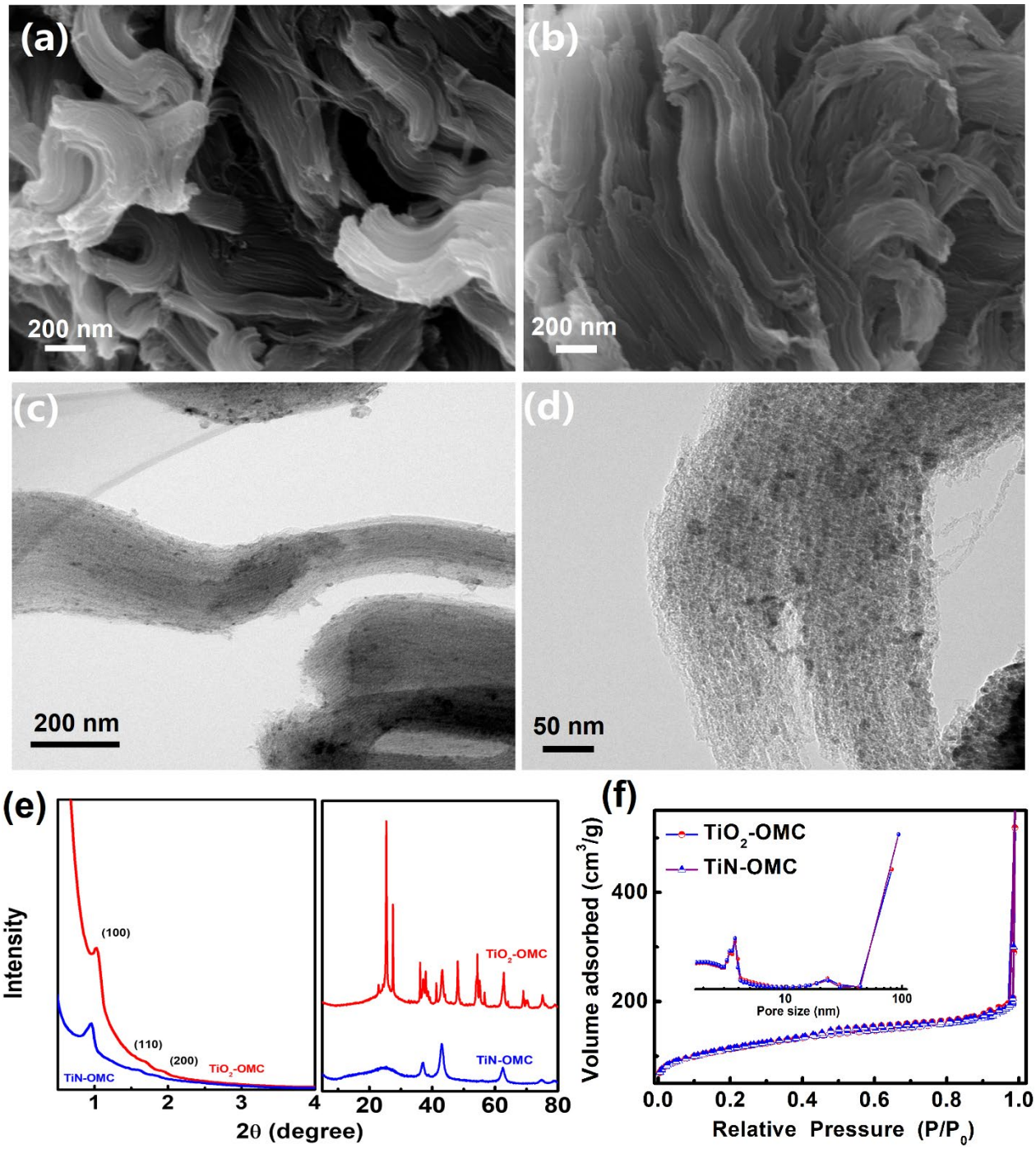

Figure 6.3 SEM images of **(a)** TiO_2-OMC and **(b)** TiN-OMC; TEM images of **(c)** TiO_2-OMC and **(d)** TiN-OMC; **(e)** Small-angle and wide-angle XRD patterns for TiO_2-OMC and TiN-

OMC; **(f)** N_2 sorption-desorption isotherms of TiO_2-OMC and TiN-OMC (insert: pore size distribution plots).

Table 6.1 Comparison of BET surface area, pore volume, and pore size distribution of SBA-15, OMC, TiO_2-OMC, TiN-OMC, and TiN-O-OMC.

Sample	**BET specific surface area** ($m^2\ g^{-1}$)	**Pore volume** ($cm^3\ g^{-1}$)	**Pore size** (nm)
SBA-15	587.1	1.38	6.2-7.8
OMC	726.3	0.78	3.1-4.0
TiO2-OMC	355.9	0.81	3.2-4.1
TiN-OMC	386.1	0.82	3.2-4.2
TiN-O-OMC	355.9	0.88	3.1-4.1

Table 6.2 Elements content of TiN-O-OMC.

Elements	Ti	N	C	O
Content (at. %)	5.79	9.62	72.78	11.81

Table 6.3 Fractions of Ti-containing species for TiN-O-OMC.

Species	O-Ti-O (amorphous)	N-Ti-O	Ti-N	O-Ti-O (amorphous)	N-Ti-O	Ti-N
Content (at. %)	8.8	14.2	9.8	20.7	21.6	24.9
Peak position (eV)	464.4	463.1	461.1	458.5	457.0	455.7

To examine the effect of surface oxidized TiN on battery performance, systematic electrochemical measurements were conducted using OMC, TiO_2-OMC, TiN-OMC, and TiN-O-OMC as cathodes with a sulfur content of 75 wt % (**Figure 6. 4a**). **Figure 6. 4b-e** reveal the typical galvanostatic charge/discharge profiles of the sulfur cathodes at different current densities. Two representative discharge plateaus at around 2.38 and 2.10 V are observed (at 0.1 C current rate, 1C=1675 mA g^{-1}), corresponding to the reduction of sulfur to long-chain lithium polysulfides (Li_2S_x, $3 \leq x \leq 8$) and the subsequent formation of short-chain Li_2S_2/Li_2S, respectively.[17] After introducing polar TiO_2 and TiN into the OMC matrix, the capacity significantly increases from 710 to 980 and 1264 mAh g^{-1}, respectively (**Figure 6. 4b-e**). Remarkably, TiN-O-OMC electrode delivers the highest specific capacity at different current rates (1395, 1264, 1109, 990, 882, and 727 mA h g^{-1} at 0.1, 0.2, 0.5, 1, 2, and 5 C, respectively, **Figure 6. 4b**).

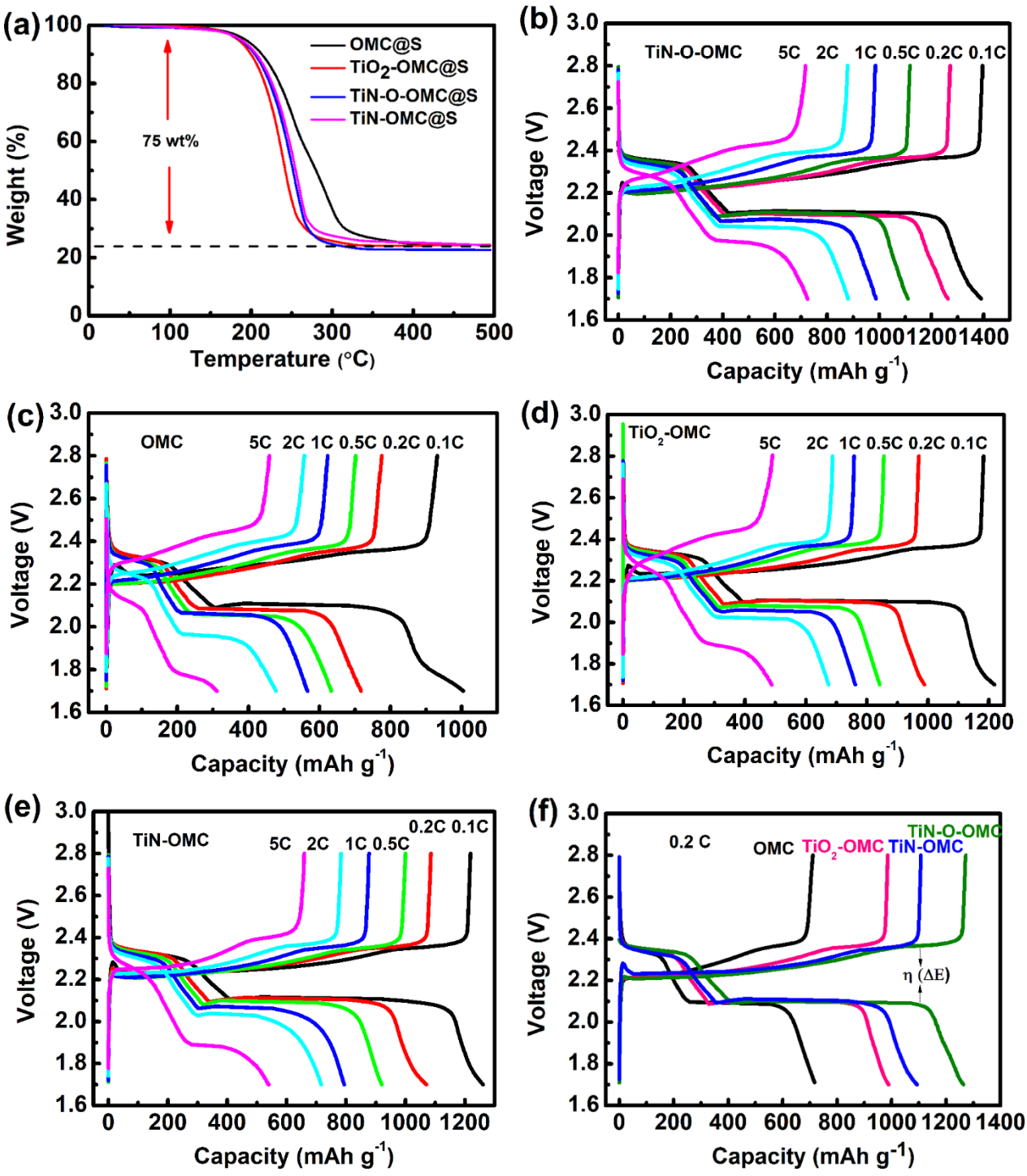

Figure 6.4 (a) TGA curves of OMC@S, TiO_2-OMC@S, TiN-O-OMC@S, and TiN-OMC@S measured under N_2 atmosphere with a heating rate of 10 °C min^{-1} from room temperature to 500 °C; Galvanostatic discharge-charge voltage profiles of **(b)** TiN-O-OMC; **(c)** OMC; **(d)** TiO_2-OMC; and **(e)** TiN-OMC electrodes at various rates from 0.1 to 5 C; **(f)** Galvanostatic

charge/discharge voltage profiles at 0.2 C for OMC, TiO_2-OMC, TiN-OMC, and TiN-O-OMC electrodes within the potential window in the range of 1.7 to 2.8 V.

The surface oxidized TiN is particularly effective in alleviating the electrochemical polarization at a higher current rate. Specifically, at a low current rate of 0.2 C, the voltage hysteresis (η) of TiN-OMC is only 1 mV lower than that of TiN-O-OMC, indicating their similar redox kinetics for the solid-liquid-solid lithiation process (**Figure 6. 5a**). However, at a high current rate of 5 C, η for TiN-OMC, TiO_2-OMC, and OMC electrodes are 72, 99, and 215 mV higher than TiN-O-OMC, respectively. Benefiting from the mesoporous structure and strong trapping affinity with polysulfides, the TiN-O-OMC electrode demonstrates an excellent high rate performance. As shown in **Figure 6. 5b**, the capacity decreases with the increasing current density and can maintain a high capacity up to 718 mA h g^{-1} at 5 C. Furthermore, the capacity can recover to 1284 mA h g^{-1} after abruptly switching the current density back to 0.1 C, implying the remarkable robustness and stability of TiN-O-OMC electrode. However, TiN-OMC, TiO_2-OMC, and OMC cathodes deliver much lower capacities after reversing back to low rates, in decreasing order of 992, 553, and 711 mA h g^{-1}, respectively. For long-term cycling stability at a low current density of 0.2 C (**Figure 6. 5c**), the TiN-O-OMC shows superior cycling stability with a high initial capacity of 1264 mA h g^{-1} and a fading rate of 0.06 % from the second cycle. While the capacity fading rates of OMC, TiO_2-OMC, and TiN-OMC are 0.14%, 0.17%, and 0.13%, respectively. Moreover, at higher current density of 0.5 and 5 C, the capacity of the TiN-O-OMC cathode can maintain at 915 and 612 mA h g^{-1} with a negligible fading rate of 0.06 % and 0.05 % over 200 cycles (**Figure 6. 5d**). The high Columbic efficiency (above 98.2 %) indicates the dramatically suppressed shuttle effect of polysulfides.

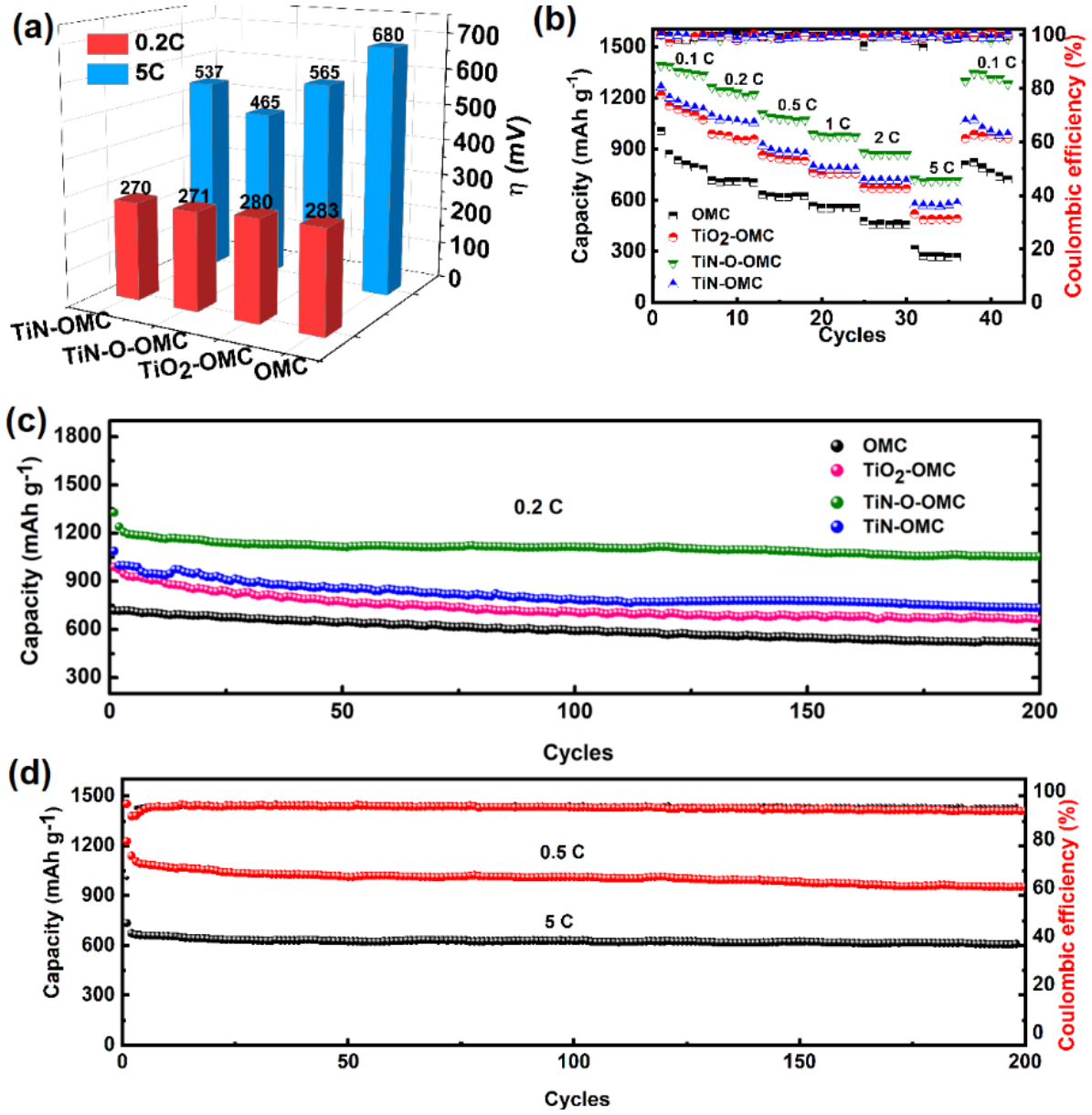

Figure 6.5 (a) The voltage hysteresis (second discharge plateau) of OMC, TiO_2-OMC, and TiN-O-OMC, TiN-OMC electrodes at 0.2 and 0.5 C; **(b)** Comparison of rate performance from 0.1-5 C; **(c)** Comparison of cycling stability at 0.2 C; **(d)** Cycling stability of TiN-O-OMC at 0.5 C and 5 C.

We further evaluated the long-term cycling stability of TiN-O-OMC with high sulfur loading (4.3 mg cm^{-2}). It delivers an initial capacity of 645 mA h g^{-1} and stable cycling to 600 cycles with a capacity fading rate of 0.2 % at a high current density of 5 C (**Figure 6. 6**). The high

capacity retention of TiN-O-OMC cathodes implies the effective immobilization of lithium polysulfides by the well-designed architecture of surface-oxidized polar TiN embedded in the ordered mesoporous carbon matrix.

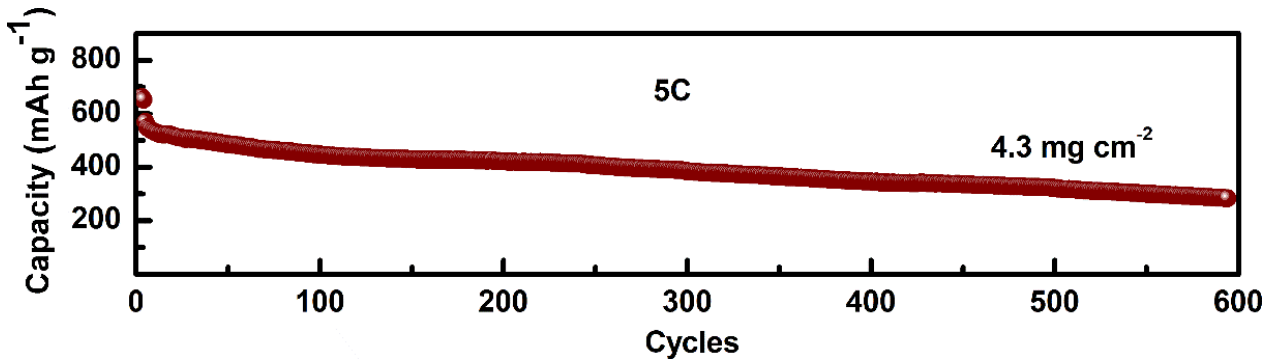

Figure 6.6 Cycling stability of TiN-O-OMC@S electrode at 5 C with a high sulfur mass loading of 4.3 mg cm^{-2}.

Once the polysulfides is anchored on the polar material, it is essential to trigger the subsequent liquid-to-solid (Li_2S_n to Li_2S) conversion, which is the key to improve the rate performance, maximum the utilization of sulfur species and extending the battery lifespan. To this end, cycling voltammogram (CV) scanning, electrochemical impendence spectroscopy (EIS), and Li_2S nucleation experiments were conducted to study how the surface-oxidized TiN affects the electrochemical process (**Figure 6. 7**). As shown in **Figure 6. 7a**, TiN-O-OMC electrode shows two cathodic peaks at 2.32 (C1) and 2.04 V (C2) and two anodic peaks at 2.31 (A1) and 2.38 V (A2) at a scan rate of 0.1 mV s^{-1}, which is consistent with the Galvanostatic charge/discharge profiles. Additionally, C1, C2 peaks locate at higher potential positions than those of OMC, TiO_2-OMC, and TiN-OMC electrodes, whereas A1and A2 shows an opposite tendency (**Figure 6. 7b-d**), which is in good agreement with the η results (**Figure 6. 5a**). The mitigated electrochemical polarization of the TiN-O-OMC electrode is also manifested from

the well-separated cathodic/anodic peaks with approximately double the current density than other electrodes. Furthermore, the Li^+ diffusion coefficient (D_{Li^+}, a good descriptor to evaluate the redox kinetics) was measured by CV under different scanning rates from 0.1 to 0.5 mV s^{-1}. As seen in **Figure 6. 7e**, the cathodic and anodic peaks (I_p) of all the electrodes exhibited a good linear relationship with the square root of scanning rates ($v^{\frac{1}{2}}$), indicating a diffusion-controlled process. Based on the classical Randles-Sevcik Equation (1):

$$I_p = 268600\, n^{\frac{3}{2}} A\, D^{\frac{1}{2}} C\, v^{\frac{1}{2}} \quad (1)$$

D_{Li^+} (cm^2 s^{-1}) can be calculated from the slope of the curve ($I_p/ v^{\frac{1}{2}}$) as the n (number of electrons transferred in the redox reaction), A (electrode area, cm^2), and C (concentration of Li^+ in the cathode, mol cm^{-3}) are unchanged (**Figure 6. 7f**). For TiN-O-OMC cathode, $D_{Li^+}^{C1}$= 1.8×10^{-8}, $D_{Li^+}^{C2}$= 3.6×10^{-8}, $D_{Li^+}^{A1}$= 1.9×10^{-8}, and $D_{Li^+}^{A2}$= 7.9×10^{-8} cm^2 s^{-1} are obtained, which are 1-3 times higher than the values for OMC, TiO_2-OMC, and TiN-OMC. Without any embedded particles, OMC demonstrated the lowest Li^+ diffusivity, indicating its limited surface activity towards the redox reaction.

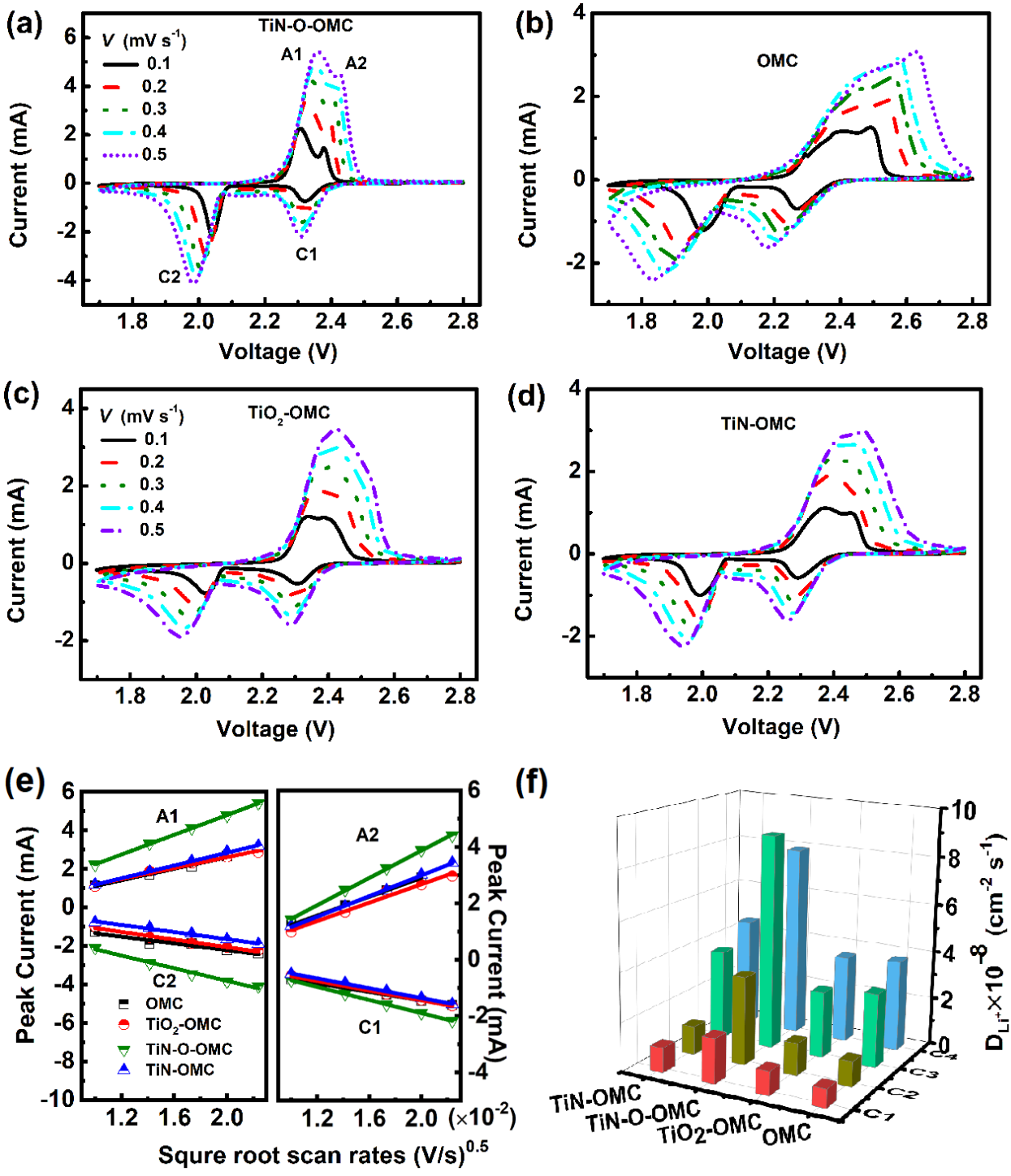

Figure 6.7 CV scans of **(a)** TiN-O-OMC; **(b)** OMC; **(c)** TiO_2-OMC; **(d)** TiN-OMC from 0.1-0.5 mV s^{-1} in a typical Li-S coin cell; **(e)** Peak currents (I_p) versus square root of scan rates ($v^{1/2}$); **(f)** Calculated Li diffusion coefficient of OMC, TiO_2-OMC, TiN-OMC and TiN-O-OMC electrodes.

The inferior performance of the TiO_2-OMC electrode could be ascribed to its large charge transfer resistance confirmed by the EIS result (R_{ct}, 90.8 Ω, **Figure 6. 8a, Table 6. 4**). Surprisingly, although a higher R_{ct} is observed for TiN-O-OMC than TiN-OMC (59.9 Ω vs. 27.3 Ω), the TiN-O-OMC presents higher D_{Li^+} diffusion coefficient than TiN-OMC, which originates from the oxidization layer of TiN. To probe the electrochemical conversion of lithium polysulfides at the electrode/electrolyte interface, symmetric cells employing two identical carbon paper as electrodes (mass loading of 0.4 mg cm^{-2}, without sulfur) and Li_2S_6 as electrolyte (40 μL of 0.4 M) were assembled.[23] The enhanced current density observed in **Figure 6. 8b** proves the fastest lithium polysulfides redox conversion by TiN-O-OMC due to the strong affinity for polysulfides and facilitated ion/electron transport, which has been validated by the adsorption and Li^+ diffusion experiments.

To further study the favorable effect of the surface oxidized TiN on the polysulfides redox reaction at the liquid-solid boundary, Li_2S precipitation experiments on the surface of OMC, TiO_2-OMC, TiN-O-OMC, and TiN-OMC were performed.[38] The deposition was studied under galvanostatic discharge to 2.06 V at a constant current of 0.112 mA, which aims to consume most of the long-chain lithium polysulfides.[39] Then, the potentiostatic conditions were applied to maintain an overpotential of 10 mV at 2.05 V till the current fell below 0.01 mA. The 10 mV of overpotential is necessary to provide the driving force for the nucleation of Li_2S since a surface energy barrier must be overcome.[38] According to the previous report,[38,39] the precipitation of Li_2S begins with the nucleation and is then followed by the growth of impingement, as illustrated by the current peak in **Figure 6. 8c-f**. The potentiostatic curves deliver three important data: (i) the current peak increases in the order of OMC<TiO_2-

OMC<TiN-OMC<<TiN-O-OMC with current densities of 0.12, 0.13, 0.17 and 0.32 mA, (ii) whereas the corresponding disposition time (at current peak) witnesses an opposite tendency of 7489>5160>5151>2709 s, and (iii) the calculated capacities of Li_2S precipitation (yellow section) of 45<59<68<95 mA h g_{sul}^{-1} in the same order. The former two values indicate that the fast conversion rate of Li_2S nucleation process and the last one reveals the enhanced Li_2S deposition process. Therefore, these results clearly elucidate the enhanced electrochemical catalytical property of the naturally oxidized layer of TiN for Li_2S conversion than the pure TiN phase.

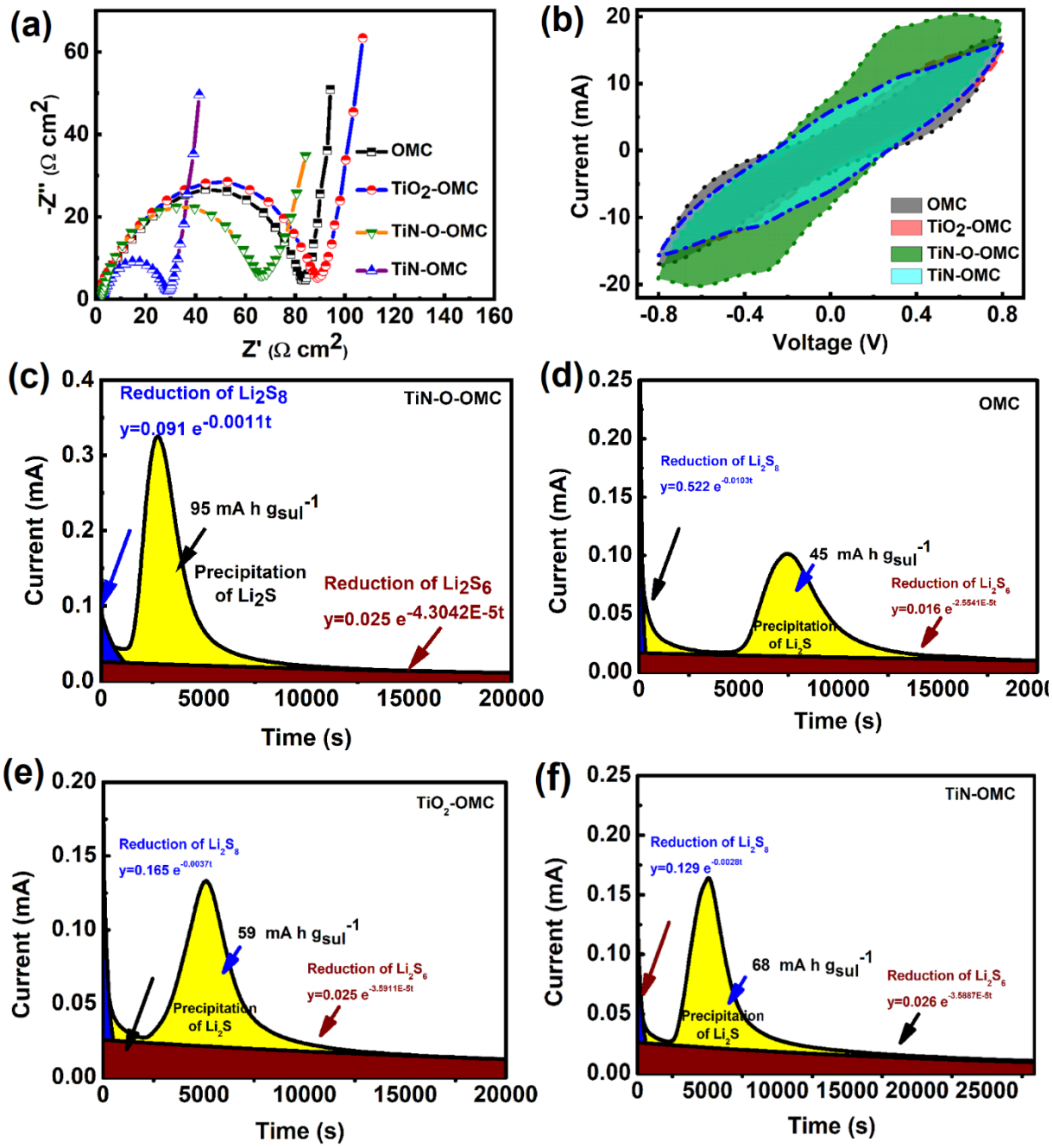

Figure 6.8 (a) EIS spectra of OMC, TiO_2-OMC, TiN-OMC and TiN-O-OMC electrodes; **(b)** CV scans with a 10 mV s^{-1} rate of symmetric cells containing 0.4 M Li_2S_6 in 1,3-dioxolane (DOL)/1,2-dimethoxyethane (DME, volume ratio 1:1) solution as electrolyte and OMC, TiO_2-OMC, TiN-OMC and TiN-O-OMC as the electrodes. Fitting of current *vs.* time curve for potentiostatic discharge at 2.05V of **(c)** TiN-O-OMC; **(d)** OMC; **(e)** TiO_2-OMC; **(f)** TiN-OMC based cathode with Li_2S_8 catholyte.

Table 6.4 Fitting results of EIS of OMC, TiO_2-OMC, TiN-O-OMC and TiN-OMC.*

Resistance / samples	R_s (Ω)	R_{ct} (Ω)
OMC	3.41	84.82
TiO_2-OMC	4.61	90.85
TiN-OMC	2.33	27.29
TiN-O-OMC	2.23	59.97

*Note: EIS result is fitted employing the equivalent circuit (R1+ C1/(R2+W1)). The fitting curves show good consistency with our experimental results. The Nyquist plots consist of two parts, one semicircle in the high- and medium frequency (charge transfer resistance, R_{ct}), and an inclined line in the low frequency (diffusion process). The smallest semicircles for the TiN-O-OMC and TiN-OMC electrodes indicate the reduced charge transfer resistance, demonstrating the higher electronic conductivity of TiN than TiO_2 and pure OMC.

Ultraviolet-visible (UV-vis) absorption spectroscopy was carried out after immersing the cathode host materials in 5 mM Li_2S_6 solution to check the trapping effect of lithium polysulfides for surface oxidized TiN. As shown in **Figure 6. 9a**, TiN-O-OMC, followed by TiN-OMC, displays the lowest adsorption intensity and completely purify the Li_2S_6 solution, exhibiting the strongest adsorption affinity for Li_2S_6. Because of the lower polysulfide binding energy of TiO_2 than that of TiN, TiO_2-OMC shows lower chemisorption ability with a much darker color in Li_2S_6 solution.[40] In contrast, OMC shows the weakest affinity to Li_2S_6 owing to the limited binding effect towards Li_2S_6. Moreover, the strong chemical interaction between

the surface oxidized TiN-O-OMC and polysulfides was further confirmed by the XPS spectra after vacuuming the solvent used in the adsorption experiment. As verified in **Figure 6. 9b-c**, the Ti 2p and O 1s spectra show a significant 0.2~1.0 eV shift to the lower binding energy. The enhanced XPS intensity around 456.5 eV might indicate the formation of S-O-Ti binding. To gain more insights into the oxidization effect of TiN, DFT calculations were performed to study the absorption of typical lithium polysulfides, Li_2S_6, on the TiN (200) crystal facet as reported previously.[29] For comparison, the binding behavior and chemical interaction of Li_2S_6 with the pristine TiN were also studied. As shown in **Figure 6. 9d-e**, the terminal S site of Li_2S_6 tends to locate above the Ti atom while Li atom tends to interact with N atom with the binding lengths of 2.43 and 1.98 Å, respectively. Whereas, for the oxidized TiN, S sites preferentially stand away from the surface while Li atom shows a shorter binding length of 1.89 Å to O atom, predicting a stronger binding affinity. This is further confirmed by the higher binding energy (E_b) of surface oxidized TiN (-5.51 eV) than that of pure TiN (-5.39 eV), which is consistent with the existing experimental observations. Moreover, the O atoms are favorable in the charge polarization effect due to the larger electronegativity of oxygen, which is widely studied in the field of hetero-atom doping.[41,42] As depicted from the charge density difference diagrams (**Figure 6. 9f-g)**, the olive and cyan iso-surfaces represent the region of net electron accumulation and deficit, respectively. In detail, a limited 0.1*e* is transferred from the long-chain Li_2S_6 to pure TiN, whereas 1.67*e* is transferred to the surface oxidized TiN. The significant polarization of electronic density is also in good accordance with the negative shifting (0.2~1 eV) of Ti 2p and O 1s XPS spectra (**Figure 6. 9b-c**). It can be inferred that in the discharge process, the enhanced electronic polarization effect could provide an additional

driving facilitate to profit the electrons transfer from anode to polysulfides, attract Li^+ onto the surface of TiN-O-OMC and accelerate charge/electron transport (as illustrated in **Figure 6. 9h, i**).

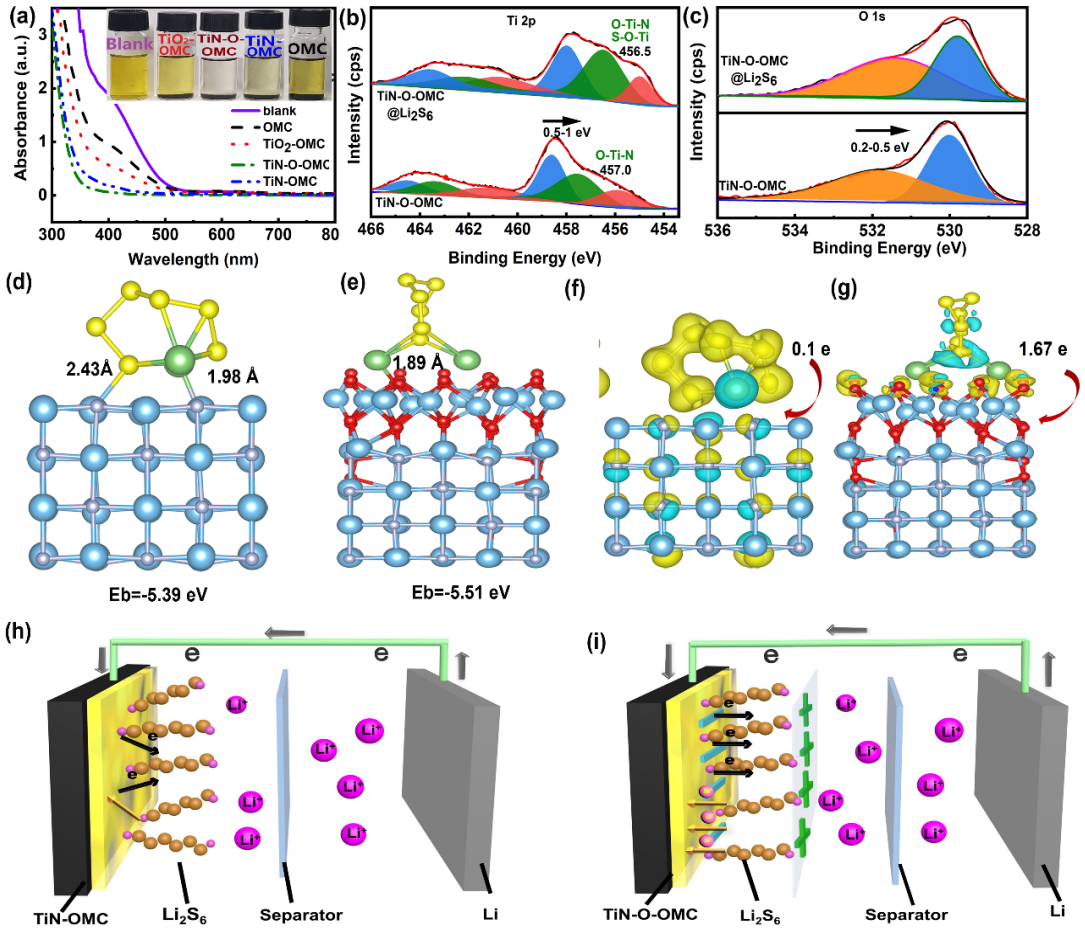

Figure 6.9 (a) Ultraviolet/visible absorption spectra of 5 mM Li_2S_6 in DOL/OME (volume 1:1) after the addition of 5 mg OMC, TiO_2-OMC, TiN-O-OMC and TiN-OMC (insert: digital photo of Li_2S_6 solutions after the addition of host materials); **(b)** High-resolution XPS spectrum of Ti 2p and **(c)** O 1s before and after immersing in 5 mM Li_2S_6 solution acquired from TiN-O-OMC; Optimized configurations for the binding of Li_2S_6 to **(d)** TiN **(e)** TiN-O; Charge density difference diagrams of **(f)** TiN and **(g)** TiN-O. Blue, grey, red, green, and yellow balls represent Ti, N, O, Li and S atoms, respectively; The cyan and yellow colors indicate the regions of

charge loss and gain. **(h-i)** Schematic illustration of the enhanced charge/electron transport of TiN-O-OMC over TiN-OMC.

Motivated by the urgent demand for developing flexible future energy storage devices, herein we manufactured prototype pouch cells, employing the as-prepared TiN-O-OMC as the cathode material with a sulfur loading of ~ 1.4 mg cm^{-2} and a size of 60 mm × 80 mm (**Figure 6. 10a**). This unique pouch cell demonstrates superior flexibility by adapting to different folding movements from 0 to 180° (**Figure 6. 10b**). Benefiting from the enhanced physiochemical adsorption ability for lithium polysulfides and fast redox kinetics, the TiN-O-OMC in pouch cells also shows a high specific capacity of 884, 788, and 727 mA h g^{-1} at 0.1, 0.2, and 0.5 C, and a low η of 239 mV at 0.2 C (**Figure 6. 10c**). In addition, the TiN-O-OMC pouch cell exhibits an excellent rate performance with its capacity can recover to 790 mA h g^{-1} after decreasing the current density from 2 C to 0.2 C **(Figure 6. 10d)**. Notably, the cathode displays a stable cycling performance with a high capacity retention of 634 mA h g^{-1} (at a low fading rate of 0.16 % per cycle) and high Columbic efficiency of 98.5% at 0.2 C (**Figure 6. 10e**).

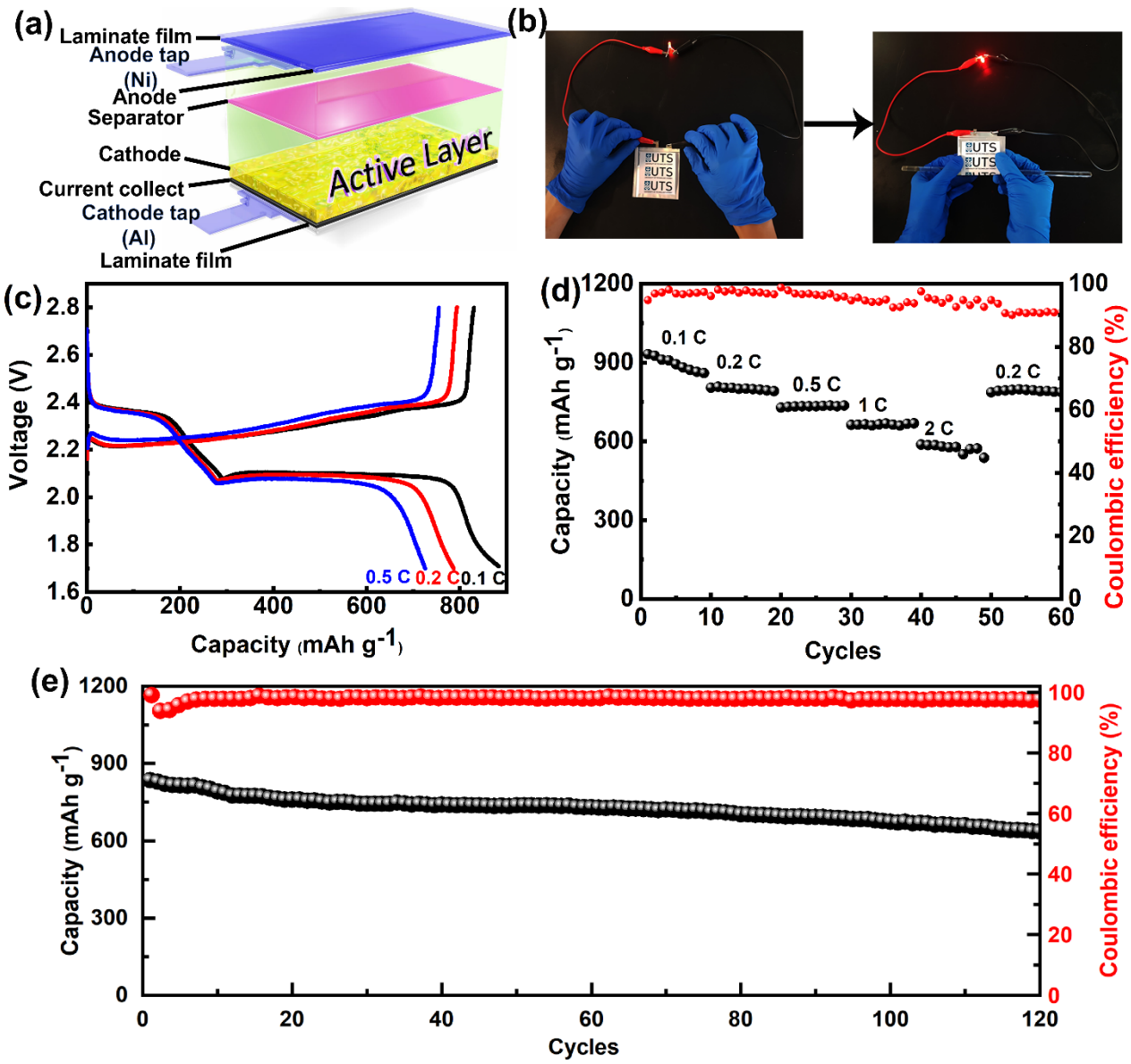

Figure 6.10 (**a**) Schematic of the basic configuration of a proof-of-concept Li-S pouch cell; **(b)** Flexibility test with folding angles from 0 to 180°of the as-prepared TiN-O-OMC pouch cell; **(c)** Galvanostatic charge/discharge profiles at low rates of 0.1, 0.2 and 0.5 C; **(d)** Rate performance and Coulombic efficiency at different current densities; **(e)** Cycling stability and Coulombic efficiency at 0.2 C with a sulfur loading of 1.4 mg cm^{-2}.

6.4. Conclusion

In summary, we successfully developed a technique by employing the highly ordered

mesoporous carbon as matrix and the surface oxidized quantum-dot-size TiN-O as polysulfides mediator to suppress shuttle effect and boost redox kinetics of Li-S batteries. Both the physical confinement and chemical adsorption for the polysulfides of the as-prepared materials facilitate the redox reaction between sulfur and polysulfides. Especially, the surface oxidized TiN-O is more effective in alleviating the polysulfides shuttle effect and boosting the overall redox kinetics, which has been confirmed by both experimental and theoretical studies. The DFT calculations further verified that the surface oxygen renders a charge polarization effect for imparting additional "driving force" to propel both the electrons and Li^+ transportation. Benefiting from the synergetic effects of mesoporous architecture and oxidized surface chemistry, the TiN-O-OMC cathode exhibits significant enhancement on the charge transfer process, lower polarization (271 mV), high lithium-ion diffusion coefficient (7.9×10^{-8} cm^2 s^{-1}) and Li_2S nucleation/deposition conversion. Thus, the TiN-O-OMC electrode achieves high specific capacities of 1395 and 726 mA h g^{-1} at 0.1 and 5 C and high Coulombic efficiencies (~ 100%). The cathode material also delivers excellent rate performance and cycling stability. When assembling to the prototype pouch cells, the as-prepared materials show superior flexibility with high capacity of 890 mA h g^{-1} at 0.2 C and stable cycling performance of 634 mA h g^{-1} after 120 cycles, indicating great potential for practical applications.

6.5. Reference

(1) Seh, Z. W.; Sun, Y.; Zhang, Q.; Cui, Y. Designing High-Energy Lithium-Sulfur Batteries. *Chem. Soc. Rev.* **2016**, *45* (20), 5605–5634.

(2) Li, G.; Wang, X.; Seo, M. H.; Li, M.; Ma, L.; Yuan, Y.; Wu, T.; Yu, A.; Wang, S.; Lu,

J.; et al. Chemisorption of Polysulfides through Redox Reactions with Organic Molecules for Lithium-Sulfur Batteries. *Nat. Commun.* **2018**, *9* (1), 705.

(3) Saha, N. C.; Tompkins, H. G. Titanium Nitride Oxidation Chemistry: An X-Ray Photoelectron Spectroscopy Study. *J. Appl. Phys.* **1992**, *72* (7), 3072–3079.

(4) Hu, C.; Chen, H.; Shen, Y.; Lu, D.; Zhao, Y.; Lu, A. H.; Wu, X.; Lu, W.; Chen, L. In Situ Wrapping of the Cathode Material in Lithium-Sulfur Batteries. *Nat. Commun.* **2017**, *8* (1), 479.

(5) Li, Z.; Jiang, Y.; Yuan, L.; Yi, Z.; Wu, C.; Liu, Y.; Strasser, P.; Huang, Y. A Highly Ordered Meso@microporous Carbon-Supported Sulfur@smaller Sulfur Core-Shell Structured Cathode for Li-S Batteries. *ACS Nano* **2014**, *8* (9), 9295–9303.

(6) Thangavel, N. K.; Gopalakrishnan, D.; Arava, L. M. R. Understanding Heterogeneous Electrocatalysis of Lithium Polysulfide Redox on Pt and WS_2 Surfaces. *J. Phys. Chem. C* **2017**, *121* (23), 12718–12725.

(7) Yang, Y.; Wang, S.; Lin, S.; Li, Y.; Zhang, W.; Chao, Y.; Luo, M.; Xing, Y.; Wang, K.; Yang, C.; et al. Rational Design of Hierarchical TiO_2 /Epitaxially Aligned MoS_2 -Carbon Coupled Interface Nanosheets Core/Shell Architecture for Ultrastable Sodium-Ion and Lithium-Sulfur Batteries. *Small Methods* **2018**, *2* (10), 1800119.

(8) Wang, H.; Adams, B. D.; Pan, H.; Zhang, L.; Han, K. S.; Estevez, L.; Lu, D.; Jia, H.; Feng, J.; Guo, J.; et al. Tailored Reaction Route by Micropore Confinement for Li–S Batteries Operating under Lean Electrolyte Conditions. *Adv. Energy Mater.* **2018**, *8* (21), 1800590.

(9) Huang, J. K.; Li, M.; Wan, Y.; Dey, S.; Ostwal, M.; Zhang, D.; Yang, C. W.; Su, C. J.;

Jeng, U. S.; Ming, J.; et al. Functional Two-Dimensional Coordination Polymeric Layer as a Charge Barrier in Li-S Batteries. *ACS Nano* **2018**, *12* (1), 836–843.

(10) Liu, X.; Li, X.; Li, H.; Wu, H. Bin. Recent Progress of Hybrid Solid-State Electrolytes for Lithium Batteries. *Chem. - A Eur. J.* **2018**, *24* (69), 18293–18306.

(11) Jeong, Y. C.; Kim, J. H.; Nam, S.; Park, C. R.; Yang, S. J. Rational Design of Nanostructured Functional Interlayer/Separator for Advanced Li–S Batteries. *Adv. Funct. Mater.* **2018**, *28* (38), 1707411.

(12) He, J.; Chen, Y.; Manthiram, A. Vertical Co_9S_8 Hollow Nanowall Arrays Grown on a Celgard Separator as a Multifunctional Polysulfide Barrier for High-Performance Li-S Batteries. *Energy Environ. Sci.* **2018**, *11* (9), 2560–2568.

(13) Pang, Q.; Shyamsunder, A.; Narayanan, B.; Kwok, C. Y.; Curtiss, L. A.; Nazar, L. F. Tuning the Electrolyte Network Structure to Invoke Quasi-Solid State Sulfur Conversion and Suppress Lithium Dendrite Formation in Li–S Batteries. *Nat. Energy* **2018**, *3* (9), 783–791.

(14) Xin, S.; Gu, L.; Zhao, N. H.; Yin, Y. X.; Zhou, L. J.; Guo, Y. G.; Wan, L. J. Smaller Sulfur Molecules Promise Better Lithium'sulfur Batteries. *J. Am. Chem. Soc.* **2012**, *134* (45), 18510–18513.

(15) Li, D.; Han, F.; Wang, S.; Cheng, F.; Sun, Q.; Li, W. C. High Sulfur Loading Cathodes Fabricated Using Peapodlike, Large Pore Volume Mesoporous Carbon for Lithium-Sulfur Battery. *ACS Appl. Mater. Interfaces* **2013**, *5* (6), 2208–2213.

(16) Liang, X.; Nazar, L. F. In Situ Reactive Assembly of Scalable Core-Shell Sulfur-MnO_2 Composite Cathodes. *ACS Nano* **2016**, *10* (4), 4192–4198.

(17) Ji, X.; Lee, K. T.; Nazar, L. F. A Highly Ordered Nanostructured Carbon-Sulfur Cathode for Lithium-Sulfur Batteries. *Nat. Mater.* **2009**, *8* (6), 500–506.

(18) Qiu, J.; Zhang, P.; Ling, M.; Li, S.; Liu, P.; Zhao, H.; Zhang, S. Photocatalytic Synthesis of TiO_2 and Reduced Graphene Oxide Nanocomposite for Lithium-Ion Battery. *ACS Appl. Mater. Interfaces* **2012**, *4* (7), 3636–3642.

(19) Kong, W.; Yan, L.; Luo, Y.; Wang, D.; Jiang, K.; Li, Q.; Fan, S.; Wang, J. Ultrathin MnO_2/Graphene Oxide/Carbon Nanotube Interlayer as Efficient Polysulfide-Trapping Shield for High-Performance Li–S Batteries. *Adv. Funct. Mater.* **2017**, *27* (18), 1606663.

(20) Song, Y.; Zhao, W.; Kong, L.; Zhang, L.; Zhu, X.; Shao, Y.; Ding, F.; Zhang, Q.; Sun, J.; Liu, Z. Synchronous Immobilization and Conversion of Polysulfides on a VO_2-VN Binary Host Targeting High Sulfur Load Li-S Batteries. *Energy Environ. Sci.* **2018**, *11* (9), 2620–2630.

(21) Chen, T.; Ma, L.; Cheng, B.; Chen, R.; Hu, Y.; Zhu, G.; Wang, Y.; Liang, J.; Tie, Z.; Liu, J.; et al. Metallic and Polar Co_9S_8 Inlaid Carbon Hollow Nanopolyhedra as Efficient Polysulfide Mediator for Lithium−sulfur Batteries. *Nano Energy* **2017**, *38*, 239–248.

(22) Huang, S.; Lim, Y. Von; Zhang, X.; Wang, Y.; Zheng, Y.; Kong, D.; Ding, M.; Yang, S. A.; Yang, H. Y. Regulating the Polysulfide Redox Conversion by Iron Phosphide Nanocrystals for High-Rate and Ultrastable Lithium-Sulfur Battery. *Nano Energy* **2018**, *51*, 340–348.

(23) Zhong, Y.; Yin, L.; He, P.; Liu, W.; Wu, Z.; Wang, H. Surface Chemistry in Cobalt Phosphide-Stabilized Lithium-Sulfur Batteries. *J. Am. Chem. Soc.* **2018**, *140* (4), 1455–1459.

(24) Bao, W.; Su, D.; Zhang, W.; Guo, X.; Wang, G. 3D Metal Carbide@Mesoporous Carbon Hybrid Architecture as a New Polysulfide Reservoir for Lithium-Sulfur Batteries. *Adv. Funct. Mater.* **2016**, *26* (47), 8746–8756.

(25) Pang, Q.; Liang, X.; Kwok, C. Y.; Nazar, L. F. Advances in Lithium-Sulfur Batteries Based on Multifunctional Cathodes and Electrolytes. *Nat. Energy* **2016**, *1* (9), 16132.

(26) Zhou, G.; Tian, H.; Jin, Y.; Tao, X.; Liu, B.; Zhang, R.; Seh, Z. W.; Zhuo, D.; Liu, Y.; Sun, J.; et al. Catalytic Oxidation of Li2S on the Surface of Metal Sulfides for Li-S Batteries. *Proc. Natl. Acad. Sci. U. S. A.* **2017**, *114* (5), 840–845.

(27) Zhou, F.; Li, Z.; Luo, X.; Wu, T.; Jiang, B.; Lu, L. L.; Yao, H. Bin; Antonietti, M.; Yu, S. H. Low Cost Metal Carbide Nanocrystals as Binding and Electrocatalytic Sites for High Performance Li-S Batteries. *Nano Lett.* **2018**, *18* (2), 1035–1043.

(28) Cui, Z.; Zu, C.; Zhou, W.; Manthiram, A.; Goodenough, J. B. Mesoporous Titanium Nitride-Enabled Highly Stable Lithium-Sulfur Batteries. *Adv. Mater.* **2016**, *28* (32), 6926–6931.

(29) Zhou, T.; Lv, W.; Li, J.; Zhou, G.; Zhao, Y.; Fan, S.; Liu, B.; Li, B.; Kang, F.; Yang, Q. H. Twinborn TiO_2-TiN Heterostructures Enabling Smooth Trapping-Diffusion-Conversion of Polysulfides towards Ultralong Life Lithium-Sulfur Batteries. *Energy Environ. Sci.* **2017**, *10* (7), 1694–1703.

(30) ESAKA, F.; SHIMADA, H.; IMAMURA, M.; MATSUBAYASHI, N.; SATO, T.; NISHIJIMA, A.; KAWANA, A.; ICHIMURA, H.; KIKUCHI, T.; FURUYA, K. Surface Oxidation of Chromium Nitride Films Studied by Means of X-Ray Photoelectron Spectroscopy and X-Ray Absorption Spectroscopy Using Synchrotron

Radiation. *Hyomen Kagaku* **1995**, *16* (7), 428–433.

(31) Gao, X.; Jiao, X.; Zhang, L.; Zhu, W.; Xu, X.; Ma, H.; Chen, T. Cosolvent-Free Nanocasting Synthesis of Ordered Mesoporous g-C_3N_4 and Its Remarkable Photocatalytic Activity for Methyl Orange Degradation. *RSC Adv.* **2015**, *5* (94), 76963–76972.

(32) Wang, X.; Maeda, K.; Thomas, A.; Takanabe, K.; Xin, G.; Carlsson, J. M.; Domen, K.; Antonietti, M. A Metal-Free Polymeric Photocatalyst for Hydrogen Production from Water under Visible Light. *Mater. Sustain. Energy A Collect. Peer-Reviewed Res. Rev. Artic. from Nat. Publ. Gr.* **2010**, *8* (1), 271–275.

(33) Perdew, J. P.; Burke, K.; Ernzerhof, M. Generalized Gradient Approximation Made Simple. *Phys. Rev. Lett.* **1996**, *77* (18), 3865–3868.

(34) Kresse, G.; Furthmüller, J. Efficient Iterative Schemes for Ab Initio Total-Energy Calculations Using a Plane-Wave Basis Set. *Phys. Rev. B - Condens. Matter Mater. Phys.* **1996**, *54* (16), 11169–11186.

(35) Park, S. S.; Chu, S. W.; Xue, C.; Zhao, D.; Ha, C. S. Facile Synthesis of Mesoporous Carbon Nitrides Using the Incipient Wetness Method and the Application as Hydrogen Adsorbent. *J. Mater. Chem.* **2011**, *21* (29), 10801–10807.

(36) Sun, P.; Lin, R.; Wang, Z.; Qiu, M.; Chai, Z.; Zhang, B.; Meng, H.; Tan, S.; Zhao, C.; Mai, W. Rational Design of Carbon Shell Endows TiN@C Nanotube Based Fiber Supercapacitors with Significantly Enhanced Mechanical Stability and Electrochemical Performance. *Nano Energy* **2017**, *31*, 432–440.

(37) Chen, J.; Takanabe, K.; Ohnishi, R.; Lu, D.; Okada, S.; Hatasawa, H.; Morioka, H.;

Antonietti, M.; Kubota, J.; Domen, K. Nano-Sized TiN on Carbon Black as an Efficient Electrocatalyst for the Oxygen Reduction Reaction Prepared Using an Mpg-C_3N_4 Template. *Chem. Commun.* **2010**, *46* (40), 7492–7494.

(38) Fan, F. Y.; Carter, W. C.; Chiang, Y. M. Mechanism and Kinetics of Li_2S Precipitation in Lithium-Sulfur Batteries. *Adv. Mater.* **2015**, *27* (35), 5203–5209.

(39) Xu, J.; Zhang, W.; Fan, H.; Cheng, F.; Su, D.; Wang, G. Promoting Lithium Polysulfide/Sulfide Redox Kinetics by the Catalyzing of Zinc Sulfide for High Performance Lithium-Sulfur Battery. *Nano Energy* **2018**, *51*, 73–82.

(40) Wang, Y.; Zhang, R.; Pang, Y. chao; Chen, X.; Lang, J.; Xu, J.; Xiao, C.; Li, H.; Xi, K.; Ding, S. Carbon@titanium Nitride Dual Shell Nanospheres as Multi-Functional Hosts for Lithium Sulfur Batteries. *Energy Storage Mater.* **2019**, *16*, 228–235.

(41) Gao, X.; Wang, L.; Ma, J.; Wang, Y.; Zhang, J. Facile Preparation of Nitrogen-Doped Graphene as an Efficient Oxygen Reduction Electrocatalyst. *Inorg. Chem. Front.* **2017**, *4* (9), 1582–1590.

(42) Jiang, L.; Yuan, X.; Pan, Y.; Liang, J.; Zeng, G.; Wu, Z.; Wang, H. Doping of Graphitic Carbon Nitride for Photocatalysis: A Reveiw. *Appl. Catal. B Environ.* **2017**, *217*, 388–406.

Chapter 7

7. General Conclusions and Outlook

7.1. General Conclusions

In this doctoral thesis work, the recent development of g-C_3N_4 nanomaterials in photocatalytic hydrogen evolution was first summarized in the following aspects: 1) morphology controls to increase the amount of reactive sites; 2) defect engineering to modify the electronic structure; 3) hybrid coupling to boost the photocarrier separation and maximize solar utilization. Bearing this in mind, C/O-doped g-C_3N_4 ultrathin nanosheets and S-doped/C vacant g-C_3N_4 nanocolumn coupled with $NaYF_4$, Yb^{3+}, Tm^{3+} nanocrystals were fabricated to boost photocatalytic activity.

1) For the C/O-doped g-C_3N_4 ultrathin nanosheets, the target material combines the synergic contribution of textural and defects, which not only provide abundant reactive sites for redox reaction but also render an optimized electronic structure for the charge transport. On the one hand, C dopants are demonstrated to induce the delocalized π bonds, which favor the bulk electronic conductivity and thus fast charge transfer process. On the other hand, the O dopants contribute to the electron polarization and shortened band length, further accelerating the charge transfer and reducing the electron diffusion pathway. As a result, the resultant NCN shows a superior hydrogen evolution rate of 830.1 and 115.5 μmol g^{-1} h^{-1} under solar- and visible-light irradiation, respectively.
2) For the broadband S-doped/C vacant g-C_3N_4 nanocolumn coupled with NaYF4, Yb^{3+}, Tm^{3+} photocatalyst, the target material combines the merits of morphology modification, defect engineering as well as hybrid coupling. The S dopants and C vacancies render DCN with

defect states to effectively extend the visible light absorption to 590 nm and boost charge transfer. While a promoted interfacial charge polarization between DCN and NYF favors the upconverted excited energy transfer from NYF onto DCN, maximizing the solar energy utilization. As a result, the NYF@DCN catalyst exhibits a high solar H_2 evolution rate of 2799 μmol h^{-1} g^{-1}, which ranks the top among the reported upconversion-based system.

The g-C_3N_4 derivative, TiN, is also prepared for the cathodic sulfur host in Li-S batteries, which works in another way to address current environmental and energy concerns.

3) The surface oxidized TiN embedded in the ordered mesoporous carbon matrix was synthesized using the g-C_3N_4 as N source. Our experimental results show that surface oxidized TiN plays an important role in suppressing polysulfides shutting effect and boosting the conversion dynamics. When tested in soft-package cells, the cathodes show high capacity and excellent cycling performance compared to the pure TiN cathodes.

7.2. Outlook

Despite huge success has been made for g-C_3N_4 toward H_2 evolution, there are several challenges remained to be resolved, and the following are the possible solutions:

1) First, the g-C_3N_4-based photocatalytic systems generally involve the use of cocatalyst (Pt) and alcohols-based sacrificial agents, setting the obstacles for future commercialization.

   ⟹ Developing alternative cheap and efficient cocatalysts such as MPx (M=Ni, Co, Fe, x=0.5-1), which can improve bulk conductivity and selectively produce H_2.

2) Second, the long wavelength light absorption, particularly the NIR light absorption of g-C_3N_4 is still weak even through upconversion nanocrystals can improve solar utilization. However, the enhancement is limited due to the narrow valid range of ~980 nm.

⟹ Constructing with NIR-driven photocatalyst with strong light absorption such as Ag_2S/Ag_3PO_4, Sb_2S_3, quantum dots, and plasma metals.

3) Third, complex synthetic procedures are required to prepare broadband photocatalyst or TiN.

⟹ Developing facile, one-step method to synthesize g-C_3N_4 based materials.

⟹ Fabricating other metallic nitrides using bulk g-C_3N_4 and metal acetate salt ($M(ac)_2$: M= Ni, Co, Fe) as starting materials.

In general, we believe that a clear understanding of the photocatalytic mechanism and energy transfer mechanism between g-C_3N_4 and cocatalyst/semiconductors will undoubtedly guide the design of future g-C_3N_4-based materials. Energy materials based on g-C_3N_4 should be developed particularly in the research area of metal-sulfur batteries and metal anode applications. The future research plan will pay more attention to this point.

Appendix A: Publications

(1) **Gao, X.**; Feng, J.; Su, D.; Ma, Y.; Wang, G.; Ma, H.; Zhang, J. In-Situ Exfoliation of Porous Carbon Nitride Nanosheets for Enhanced Hydrogen Evolution. *Nano Energy* **2019**, *59*, 598–609.

(2) **Gao, X.**; Zhou, D.; Chen, Y.; Wu, W.; Su, D.; Li, B.; Wang, G. Strong Charge Polarization Effect Enabled by Surface Oxidized Titanium Nitride for Lithium-Sulfur Batteries. *Commun. Chem.* **2019**, *2* (1), 66.

(3) **Gao, X.**; Wang, L.; Ma, J.; Wang, Y.; Zhang, J. Facile Preparation of Nitrogen-Doped Graphene as an Efficient Oxygen Reduction Electrocatalyst. *Inorg. Chem. Front.* **2017**, *4* (9), 1582–1590.

(4) **Gao, X.**; Li, S.; Li, T.; Li, G.; Ma, H. g-C_3N_4 as a Saturable Absorber for the Passively Q-Switched Nd:LLF Laser at 1.3 μm;M. *Photonics Res.* **2017**, *5* (1), 33–36.

(5) **Gao, X.**; Jiao, X.; Zhang, L.; Zhu, W.; Xu, X.; Ma, H.; Chen, T. Cosolvent-Free Nanocasting Synthesis of Ordered Mesoporous g-C_3N_4 and Its Remarkable Photocatalytic Activity for Methyl Orange Degradation. *RSC Adv.* **2015**, *5* (94), 76963–76972.

(6) X. Luo, X. Lu, X. Chen, C. Yu, N. Wang, D. Su, **X. Gao,*** G. Wang,* L. Cui,* A robust flame retardant fluorinated polyimide nanofiber separator for high-temperature lithium-sulfur batteries, ***Journal of Materials Chemistry A,*** 2020.

(7) Zhang, F.; Guo, X.; Xiong, P.; Zhang, J.; Song, J.; Yan, K.; **Gao, X.**; Liu, H.; Wang, G. Interface Engineering of MXene Composite Separator for High-Performance Li–Se and Na–Se Batteries. *Adv. Energy Mater.* **2020**, 2000446.

(8) Yu, X.; Yu, Z.-Y.; Zhang, X.-L.; Li, P.; Sun, B.; **Gao, X.**; Yan, K.; Liu, H.; Duan, Y.; Gao, M.-R. Highly Disordered Cobalt Oxide Nanostructure Induced by Sulfur Incorporation for Efficient

Overall Water Splitting. *Nano Energy* **2020**, 104652.

(9) Wang, S.; Xiong, P.; Guo, X.; Zhang, J.; **Gao, X.**; Zhang, F.; Tang, X.; Notten, P. H. L.; Wang, G. A Stable Conversion and Alloying Anode for Potassium-Ion Batteries: A Combined Strategy of Encapsulation and Confinement. *Adv. Funct. Mater.* **2020**, 2001588.

(10) Zhou, D.; Tang, X.; Guo, X.; Li, P.; Shanmukaraj, D.; Liu, H.; **Gao, X.**; Wang, Y.; Rojo, T.; Armand, M.; et al. Polyolefin–Based Janus Separator for Rechargeable Sodium Batteries. *Angew. Chemie Int. Ed.* **2020**, *n/a* (n/a). https://doi.org/10.1002/anie.202007008.

(11) Yang, W.; Yang, W.; Dong, L.; **Gao, X.**; Wang, G.; Shao, G. Enabling Immobilization and Conversion of Polysulfides through a Nitrogen-Doped Carbon Nanotubes/Ultrathin MoS_2 Nanosheet Core-Shell Architecture for Lithium-Sulfur Batteries. *J. Mater. Chem. A* **2019**, *7* (21), 13103–13112.

(12) Chen, Y.; Choi, S.; Su, D.; **Gao, X.**; Wang, G. Self-Standing Sulfur Cathodes Enabled by 3D Hierarchically Porous Titanium Monoxide-Graphene Composite Film for High-Performance Lithium-Sulfur Batteries. *Nano Energy* **2018**, *47*, 331–339.

(13) Zhang, L.; Jia, C.; He, S.; Zhu, Y.; Wang, Y.; Zhao, Z.; **Gao, X.**; Zhang, X.; Sang, Y.; Zhang, D.; et al. Hot Hole Enhanced Synergistic Catalytic Oxidation on Pt-Cu Alloy Clusters. *Adv. Sci.* **2017**, *4* (6).

(14) Liu, L.; Qi, W.; **Gao, X.**; Wang, C.; Wang, G. Synergistic Effect of Metal Ion Additives on Graphitic Carbon Nitride Nanosheet-Templated Electrodeposition of Cu@CuO for Enzyme-Free Glucose Detection. *J. Alloys Compd.* **2018**, *745*, 155–163.

(15) Huang, H.; Zhu, W.; **Gao, X.**; Liu, X.; Ma, H. Synthesis of a Novel Electrode Material Containing Phytic Acid-Polyaniline Nanofibers for Simultaneous Determination of Cadmium

and Lead Ions. *Anal. Chim. Acta* **2016**, *947*, 32–41.

(16) Fan, M.; Li, T.; Zhao, S.; Li, G.; **Gao, X.**; Yang, K.; Li, D.; Kränkel, C. Multilayer Black Phosphorus as Saturable Absorber for an Er:Lu_2O_3 Laser at ~3 μm;M. *Photonics Res.* **2016**, *4* (5), 181–186.

(17) Zhu, W.; Huang, H.; **Gao, X.**; Ma, H. Electrochemical Behavior and Voltammetric Determination of Acetaminophen Based on Glassy Carbon Electrodes Modified with Poly(4-Aminobenzoic Acid)/Electrochemically Reduced Graphene Oxide Composite Films. *Mater. Sci. Eng. C* **2014**, *45*, 21–28.

(18) Ma, X.; Miao, T.; Zhu, W.; **Gao, X.**; Wang, C.; Zhao, C.; Ma, H. Electrochemical Detection of Nitrite Based on Glassy Carbon Electrode Modified with Gold-Polyaniline-Graphene Nanocomposites. *RSC Adv.* **2014**, *4* (101), 57842–57849.

(19) Fan, M.; Li, T.; Zhao, S.; Li, G.; Ma, H.; **Gao, X.**; Kränkel, C.; Huber, G. Watt-Level Passively Q-Switched Er:Lu_2O_3 Laser at 2.84 μm Using MoS_2. *Opt. Lett.* **2016**, *41* (3), 540–543.

Appendix B: Conferences

1. *International Coalition for Energy Storage and Innovation*, Australia, Sydney, 1-4 March 2020 (Oral Presentation).
2. *Preliminary program of 2019 International Symposium on Frontier Materials*, Australia, Sydney, 17-18 November 2019.
3. *2019 International Conference on Electrochemical Energy*, Australia, Sydney, 4-8 August 2019 (Poster).
4. *International Conference for Energy Storage and Conversion*, Australia, Sydney, 16-18 July 2018.
5. *Second International Symposium on Renewable Energy Technologies*, Australia, Sydney, 30-November-4 December 2016.
6. "The excellent photoelectric response of ordered mesoporous g-C_3N_4 (ompg-C_3N_4) and its application on the degradation of methyl orange", *The 18th National Conference on Electrochemistry*, China, Harbin, 9 August 2015 (Youth Report).

Appendix C: Scholarship & Awards

1. 2016-2020: UTS International Research (IRS) scholarship, Australia.
2. 2016-2019: Arena Project Scholarship, Australia.
3. 2019-2020: ARC Discovery Project, Australia.
4. 2015.11: Outstanding Paper Award, New Energy Material Postgraduate's Forum of Shanghai, China.
5. 2015.10: Wanhua Scholarship of Shandong University, China.